PhD-FSTM-2025-093
The Faculty of Sciences, Technology and Communication

Dissertation

Defence held on 29/08/2025 in Luxembourg

to obtain the degree of

Docteur de l'Université du Luxembourg en Sciences de l'Ingenieur

by

André Blumer Sanchez
Born on 10th October 1990 in Campinas (Brazil)

Design of Biomechanical Test Bench for Femoral Nails Using Numerical Simulations and Factorial Analyses

Dissertation Defence Committee

Dr. Eng. Stefan MAAS, Dissertation Supervisor
Professor, Université du Luxembourg

Dr. Eng. Slawomir KEDZIORA, Chairman
Professor, Université du Luxembourg

Dr. Eng. Numa Joy BERTOLA
Professor, Université du Luxembourg

Dr. Med. Jens KELM
Professor, Universitätsklinikum des Saarlandes

Dr. Med. Torsten GERICH
Professor, Centre Hospitalier de Luxembourg

Abstract

Understanding the mechanics behind the stability of a fracture is of great importance to surgeons, potentially providing them with valuable information to assist in the treatment planning process. By running biomechanical studies, consisting of numerical simulations and experimental testing, several implant configurations and different scenarios can be explored to obtain quantitative results of their performance. However, accurately replicating the mechanical behaviour of a fractured bone is a complex endeavour that requires many compromises and simplifications. Generally, biomechanical studies of the femur simplify its intricate original loading by neglecting the effects of muscle forces and applying a single force to the femoral head, usually representative of a single leg stance.

This work proposes an alternative approach, the design of an advanced test setup that not only takes into account the contribution of the muscles alongside the hip joint force, but that is also capable of replicating multiple different body movement scenarios. The development process of the proposed experimental setup followed a methodology that makes use of musculoskeletal and finite element models combined with statistical analyses, with the goal of assessing the significance of individual muscle and defining multi-load configurations that allow for the realistic reproduction of the physiological loading of the femur in a laboratory setting.

Acknowledgement

I would like to take the opportunity here to commit a few paragraphs expressing my gratitude to everyone that contributed in one way or another to the completion of this research project, whether it was through active collaboration throughout its development or providing some much needed personal support during these four years.

Firstly, I wish to express gratitude to my academic supervisor Prof. Dr. Eng. Stefan Maas, for not only entrusting me with this project, but also for patiently encouraging and guiding me through it. Furthermore, I thank the chairman Prof. Dr. Eng. Slawomir Kedziora, for always contributing with his technical expertise through much appreciated constructive feedback. My academic experience at the University of Luxembourg was undoubtedly enriched by the knowledge they shared with me.

I am thankful for the contribution of our medical partners Prof. Dr. Torsten Gerich from Centre Hospitalier de Luxembourg and Prof. Dr. Jens Kelm from Universitätsklinikum des Saarlandes. Their collaboration and clinical expertise was fundamental for the development of this project.

A very sincere thank you to the administrative and technical teams of the University of Luxembourg, whose valuable support and contribution have never passed unnoticed. Furthermore, I would like to demonstrate my deep appreciation for Claude Collé, Vicente Reis Adonis and Daniel Warnimont, who were responsible for the actual realization of the testing equipment.

I'm glad to have had many wonderful colleagues to share my PhD experiences with and I can only hope that I was as supportive and pleasant to them as they were to me. Their friendship, advises and company helped me to overcome the ups and downs encountered during our journey together.

Last but not least, I am extremely grateful for the unconditional support I got from my family and partner. I would not be here today if not for the hard work of my mother and father providing a privileged upbringing that allowed me to carry out a higher education. Likewise, my sister and role model always inspired me to reach ever higher and was the one paving the way that brought me to Luxembourg.

To Geralda Maria Queiroz Sanchez, who was a teacher and valued education.

Contents

Nomenclature

Acronyms

AMMR	AnyBody Managed Model Repository
AO/OTA	AO Foundation/Orthopaedic Trauma Association
BMD	Bone Mineral Density
CT	Computed Tomography
DHS	Dynamic Hip Screw
DIC	Digital Image Correlation
DOE	Design of Experiments
DTW	Dynamic Time Warping
EMG	Electromyography
FE	Finite Element
GN	Gamma Nail
HA	Hydroxyapatite
HU	Hounsfield Unit
LSD	Left Step Down Motion
LSU	Left Step Up Motion
Mocap	Motion Capture
NG	Normal Walking Motion
NURBS	Non-Uniform Rational B-Spline
OFAT	One-Factor-at-a-Time

PFN	Proximal Femoral Nail
PFNA	Proximal Femoral Nail Antirotation
QCT	Quantitative Computed Tomography
RSD	Right Step Down Motion
RSU	Right Step Up Motion
SD	Sitting Down Motion
STL	Stereolithography Format
SU	Standing Up Motion
TLEM	Twente Lower Extremity Model
UTM	Universal Testing Machine

Variables

E	Elasticity Modulus
ρ_{ash}	Ash Density
$\vec{F}$	Force Vector
m	Mass
$\vec{v}$	Translational Velocity Vector
$\vec{a}$	Translational Acceleration Vector
$\vec{M}$	Moment Vector
I	Moment of Inertia
$\vec{\omega}$	Rotational Velocity Vector
$\vec{F}_J$	Net Joint Force Vector
$\vec{M}_J$	Net Joint Moment Vector
$\vec{m}_f$	Foot Mass
$\vec{I}_f$	Foot Moment of Inertia
$\vec{r}_J$	Joint Force Lever Arm Vector
$\vec{r}_{grf}$	Ground Reaction Force Lever Arm Vector

$\vec{v}_f$	Foot Translational Velocity Vector
$\vec{a}_f$	Foot Translational Acceleration Vector
$\vec{\omega}_f$	Foot Rotational Velocity Vector
$\vec{\alpha}_f$	Foot Rotational Acceleration Vector
$\vec{F}_{grf}$	Ground Reaction Force Vector
$\vec{M}_{grf}$	Ground Reaction Force Moment Vector
$\vec{F}_c$	Articular Contact Force Vector
$\vec{M}_c$	Articular Contact Moment Vector
$\vec{r}_c$	Articular Contact Force Lever Arm Vector
$\vec{F}_l$	Ligament Force Vector
$\vec{M}_l$	Ligament Moment Vector
$\vec{r}_l$	Ligament Force Lever Arm Vector
$\vec{F}_m$	Muscle Force Vector
$\vec{M}_m$	Muscle Moment Vector
$\vec{r}_m$	Muscle Force Lever Arm Vector
A_m	Muscle Physiological Cross-Section
F	Quantity of Input Factors
L	Quantity of Factor Levels
N	Quantity of Test Runs
Y	Output
Ef	Effect on Output
$\overline{Y}$	Average of Specific Output
C	Input Factor Coefficient
Y'	Predicted Output
$\overline{\overline{Y}}$	Overall Average of Outputs
Ef_{std}	Standardized Effect

SE	Coefficient's Standard Error
MSE_R	Mean Squared Error of Residuals
k	Sampling Size

Introduction

With age, the integrity of human bones deteriorates, decreasing their strength while increasing their brittleness, consequently making them more susceptible to fractures. Therefore, as the population ages and the elderly community grows, bone injuries become progressively more frequent and more concerning. Proximal femoral fractures are among the most recurrent bone traumas, which is a type of hip damage that can cause mobility impairment. When not properly treated, it can lead to the formation of blood clots, infection, pulmonary embolism, and consequently death.

Medical treatment for proximal femoral fractures is typically performed by surgical insertion of an implant to support the bone and stabilise the fracture. Implant failure or further bone collapse requires additional surgical intervention, which can be life threatening for patients in an advanced age group. Therefore, biomechanical studies of these injuries can provide surgeons with verified quantitative information to optimise implant selection prior to operation, potentially reducing the risk of failure. Therefore, this research aims to create a methodology capable of investigating fracture stability.

The workflow established to achieve such an objective is based on a musculoskeletal model, finite element simulations, and experimental validations. The musculoskeletal model is capable of estimating the forces acting on the bone based on motion capture recordings from human subjects. These forces are then introduced into a computed tomography-based finite element model, to analyse its mechanical behaviour under load.

To finalise, an experimental setup was designed to validate the numerical models, but since the loading of the femur is very complex and contains 23 muscles acting directly on it, this is a significantly challenging process. This intricate configuration of forces cannot be realistically replicated in the laboratory and thus requires a more simplified loading case. This work proposes a systematic methodology based on statistical studies of large batches of finite element simulations to define a simplified loading configuration that still generates a realistic stress state in the fracture section of the femur.

Research Motivation and Objective

Provide improved chance of recovery to fracture patients, by developing a numerical model and experimental setup capable of identifying optimal implant configuration.

Chapter 1

Literature Review

1.1 Fundamentals of Anatomy

To properly study, model, and analyse the biomechanics of the lower limbs, it is necessary first and foremost to be familiarised with the fundamental concepts of the human body. Thus, this chapter is dedicated to establishing the foundation of femur anatomy, defining the terminology used to describe its parts, and introducing its osteology and myology.

1.1.1 Anatomic References

When studying the human body, anatomical planes and axes are used to describe movements and locate body parts. Traditionally, the body is sectioned by three planes of motion and intersected by three axes of rotation, as depicted in Figure 1.1 and detailed below:

- **Sagittal/Medial Plane:** Vertical plane that passes through the midline of the body, dividing it into right and left sections.
- **Frontal/Coronal Plane:** Vertical plane perpendicular to the Sagittal plane that divides the body into anterior and posterior sections.
- **Transverse/Horizontal Plane:** Horizontal plane perpendicular to the body's length that divides it into superior and inferior sections.
- **Anteroposterior/Frontal Axis:** Axis normal to the Frontal plane, formed by the intersection between Sagittal and Transverse planes.
- **Mediolateral/Sagittal Axis:** Axis normal to the Sagittal plane, formed by the intersection between Frontal and Transverse planes.
- **Craniocaudal/Longitudinal Axis:** Axis normal to the Transverse plane, formed by the intersection between Frontal and Sagittal planes.

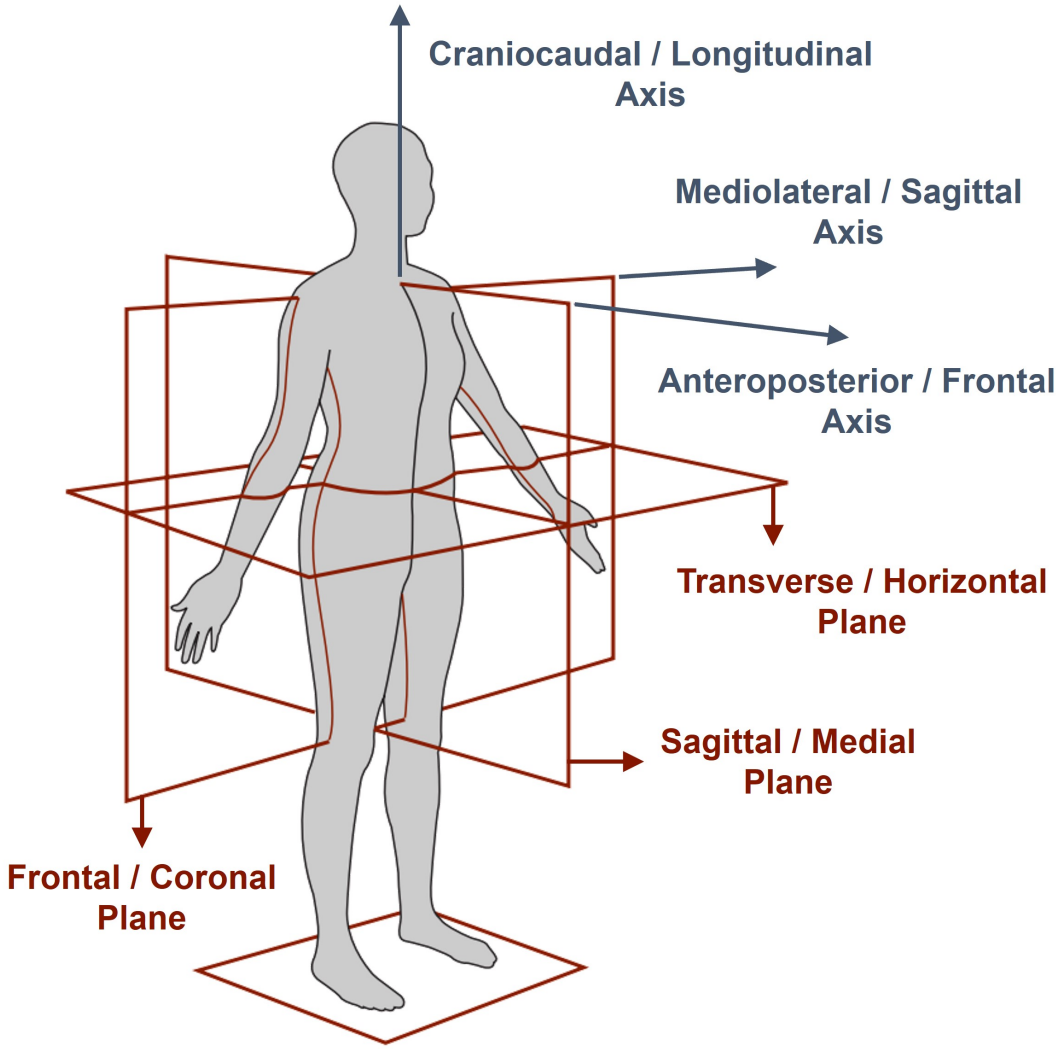

Figure 1.1: Anatomic Planes and Axes of the Human Body [1]

Furthermore, there are orientational terms that are used to define the location of a body part in relation to another, assuming as a reference the human body positioned in the standard anatomical stance (standing erect, facing forward, with arms on the sides), as depicted in Figure 1.2 and detailed below:

- **Anterior:** Described part is located towards the front of the human body.
- **Posterior:** Described part is located towards the back of the human body.
- **Superior:** Described part is located towards the head.
- **Inferior:** Described part is located towards the feet.
- **Medial:** Described part is located towards the midline of the body.
- **Lateral:** Described part is located away from the midline of the body.
- **Proximal:** Described part is located closer towards the torso.
- **Distal:** Described part located away from the torso.

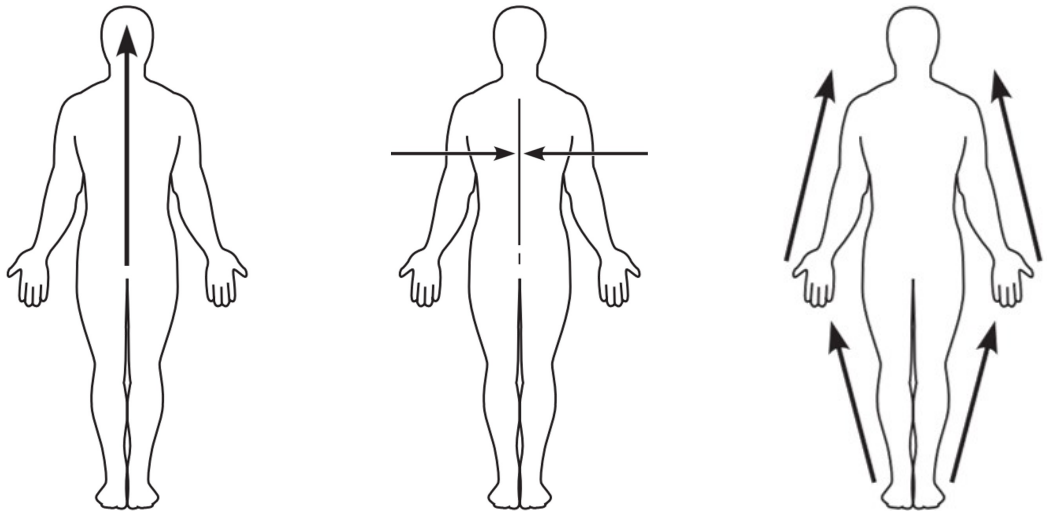

(a) Superior **(b)** Medial **(c)** Proximal

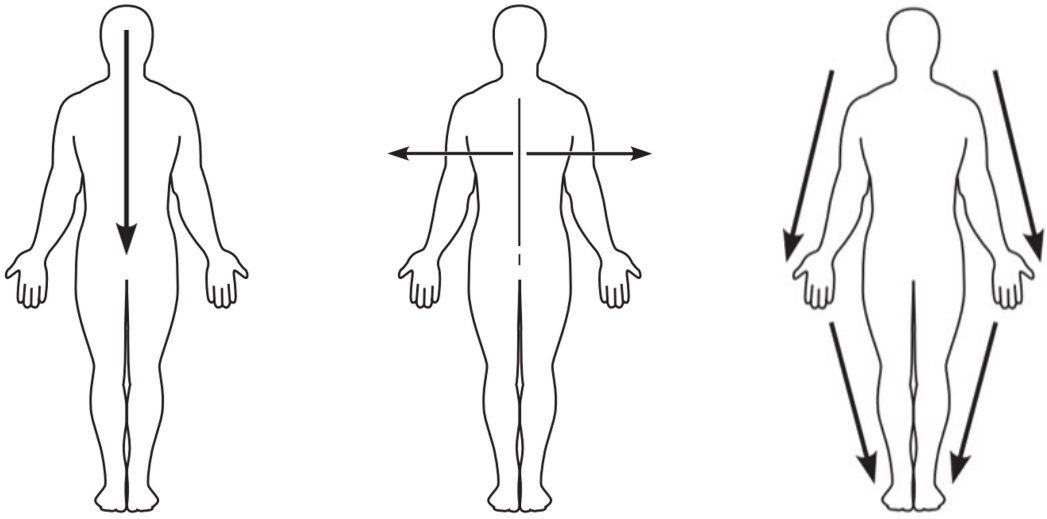

(d) Inferior **(e)** Lateral **(f)** Distal

Figure 1.2: Anatomic Directions of the Human Body [2]

1.1.2 Osteology of the Femur

The femur is the only bone in the thigh and the longest one in the human body, accounting for an average of 27% of a person's height [3]. At both extremities of the bone it expands into epiphysis, a section composed of bony protrusions that form the femur joints and muscle attachment points, such as the femoral head, epicondyles, and trochanters, as depicted in Figure 1.3. The region between the epiphyses is called the diaphysis and consists of the femoral shaft [2].

The skeleton is composed of two types of osseous tissue, the porous and spongy core called trabecular/cancellous bone, and the denser external surface known as cortical/compact bone. The epiphyses are composed of trabecular bone covered by a thin layer of cortical bone, while the diaphysis is a hollow section of only cortical bone [4].

The basic structural unit of cortical bone, called an osteon, is made up of layers of concentric lamellae around a central canal, as presented in Figure 1.4. Usually, osteons are formed parallel to one another and aligned with the longitudinal axis of long bones. Blood vessels and nerves run through the inner cavity of the central canals, while the outer surface of the bone diaphysis is covered by a hard fibrous membrane called the periosteum [2], [4], [5].

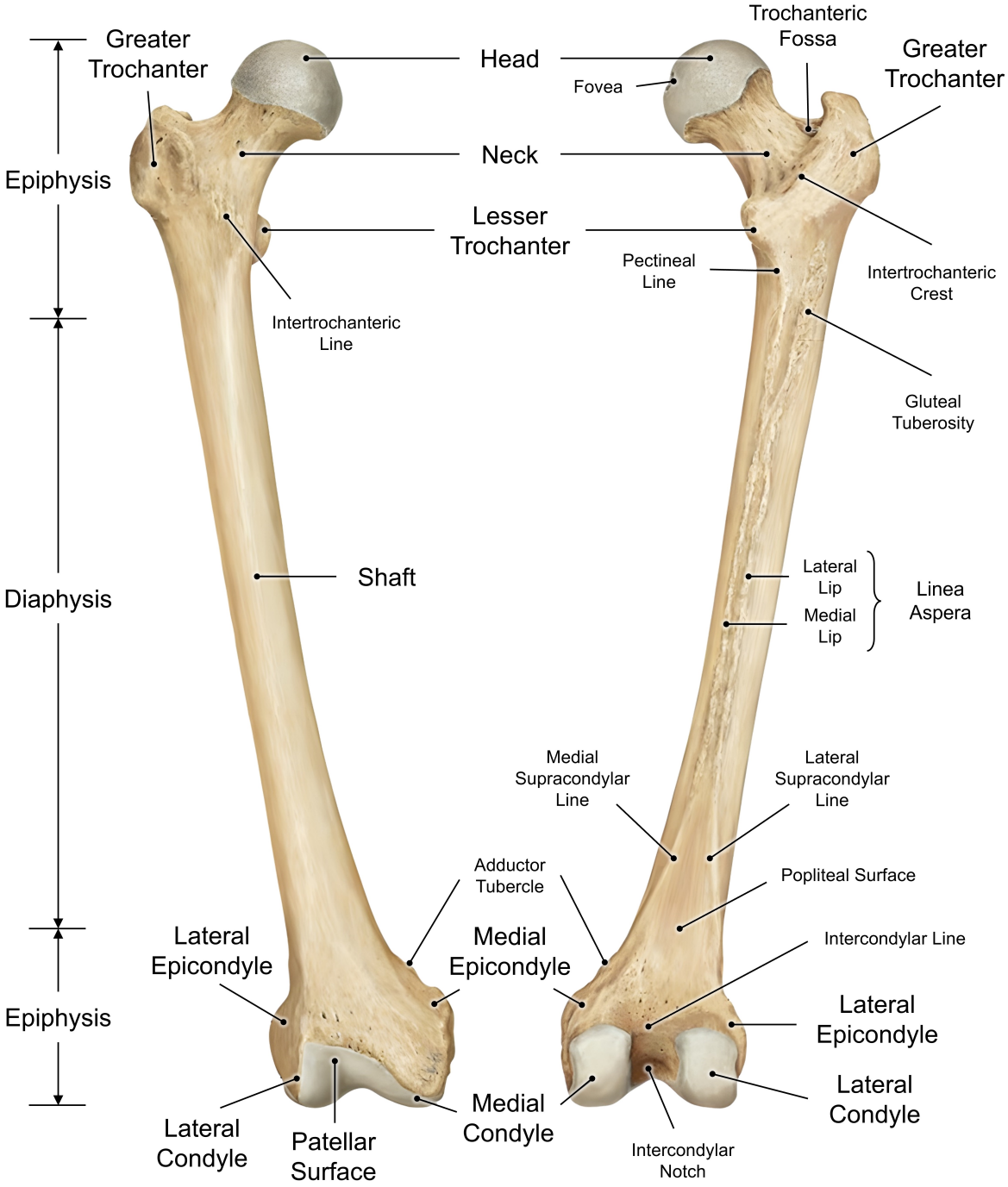

Figure 1.3: Osteology of the Femur (Adapted from [6])

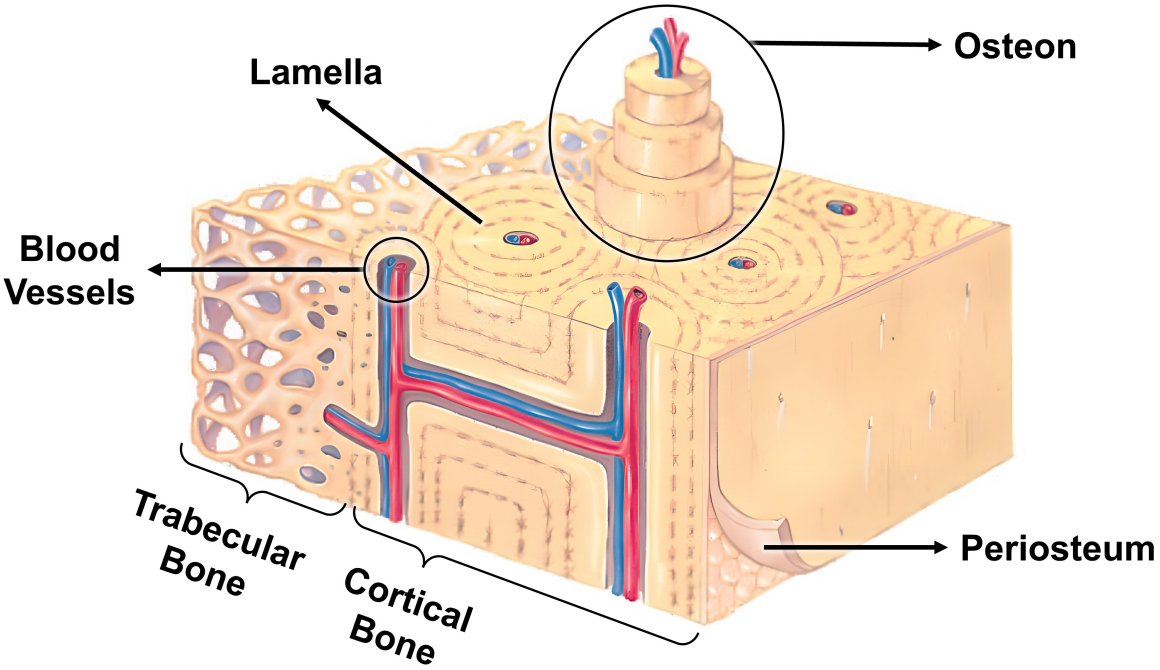

Figure 1.4: Bone Microstructure (Adapted from [2])

In contrast, trabecular bone is formed by branching segments of curved slivers separated by irregular spaces, known as trabeculae [2], [5]. The trabecula become thicker and denser as they approach the cortical bone. They can even contain small osteons close to the transition threshold, but no blood vessels lie within the trabeculae [5], as depicted in Figure 1.4. Furthermore, the thickness, orientation, and spacing of the segments of the trabeculae vary widely, especially between different locations of the bone, as shown in Figure 1.5 for different parts of the same femur.

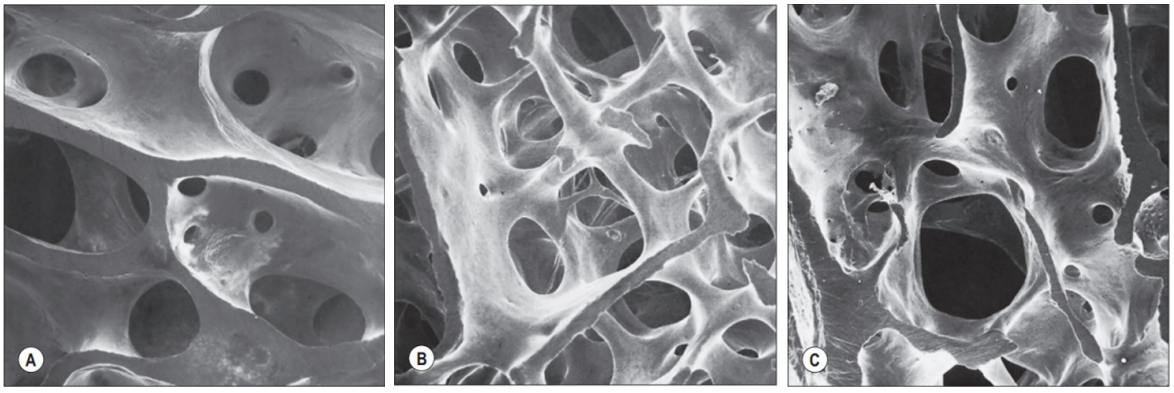

(a) Subcapital Neck **(b)** Greater Trochanter **(c)** Head Rim

Figure 1.5: Variation of Thickness, Orientation and Spacing of the Femoral Trabeculae [5]

The femur articulates at the hip joint by its proximal extremity and at the knee joint by the distal end, making it fundamental for the standing support and locomotion of the human body. The hip works as a ball-and-socket type of joint with the femoral head

articulating within the acetabulum of the pelvis, which gives it the ability to perform the movements of flexion/extension, abduction/adduction and medial/lateral rotations as presented in Figures 1.6a, 1.6b and 1.6c. On the other hand, the knee joint in the lower extremity of the femur works as a hinge type of joint, thus its main movements are flexion and extension, as shown in Figure 1.6d [4], [5].

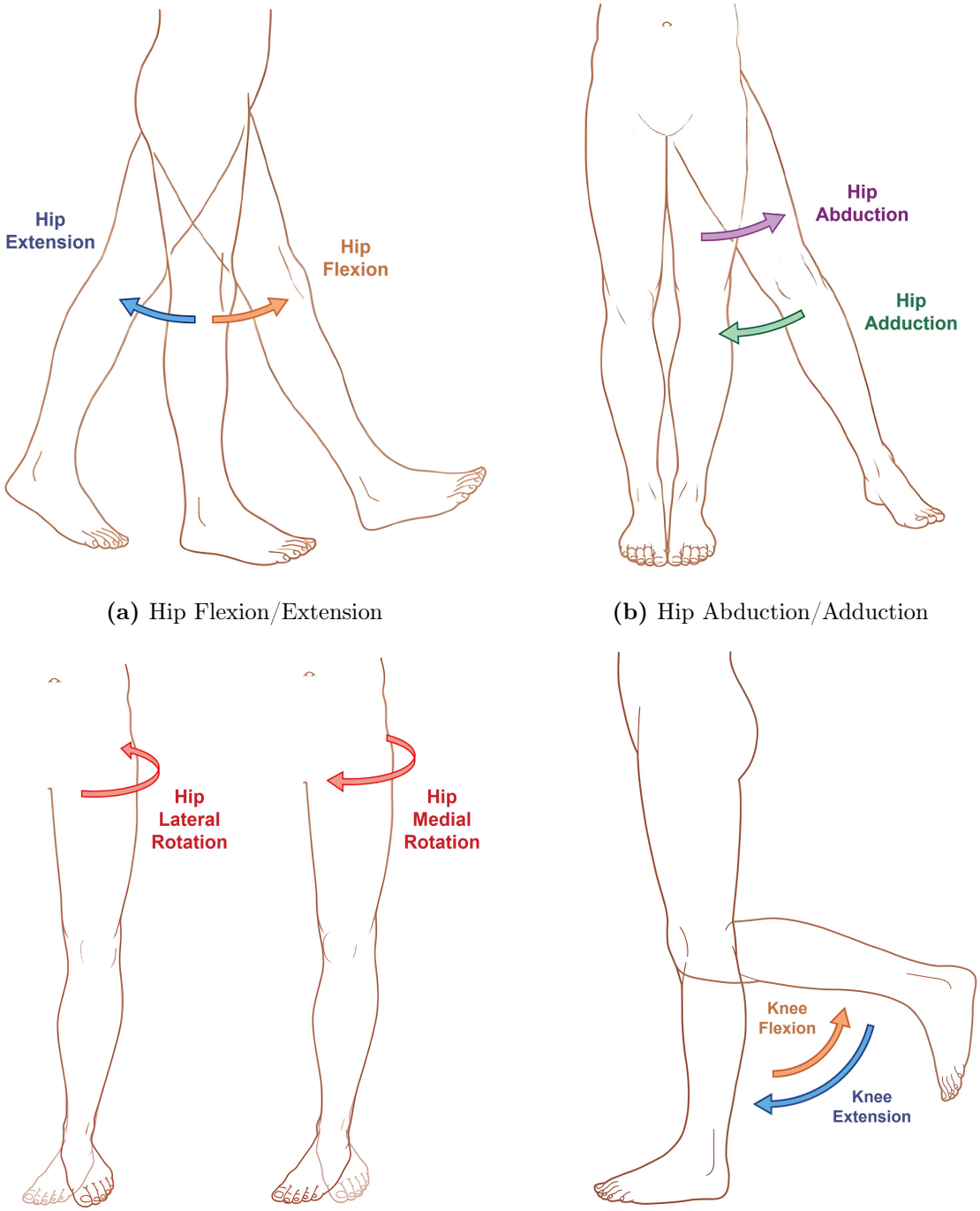

(a) Hip Flexion/Extension

(b) Hip Abduction/Adduction

(c) Hip Medial/Lateral Rotation

(d) Knee Flexion/Extension

Figure 1.6: Movements of the Hip and Knee Joints (Adapted from [5])

1.1.3 Myology of the Thigh

A total of 23 muscles act directly on the femur, the majority connecting it to the pelvis or to the tibia. Figures 1.7 and 1.8 illustrate all the muscles and their respective attachment points, while Tables 1.1 and 1.2 detail the actions they perform when activated [6].

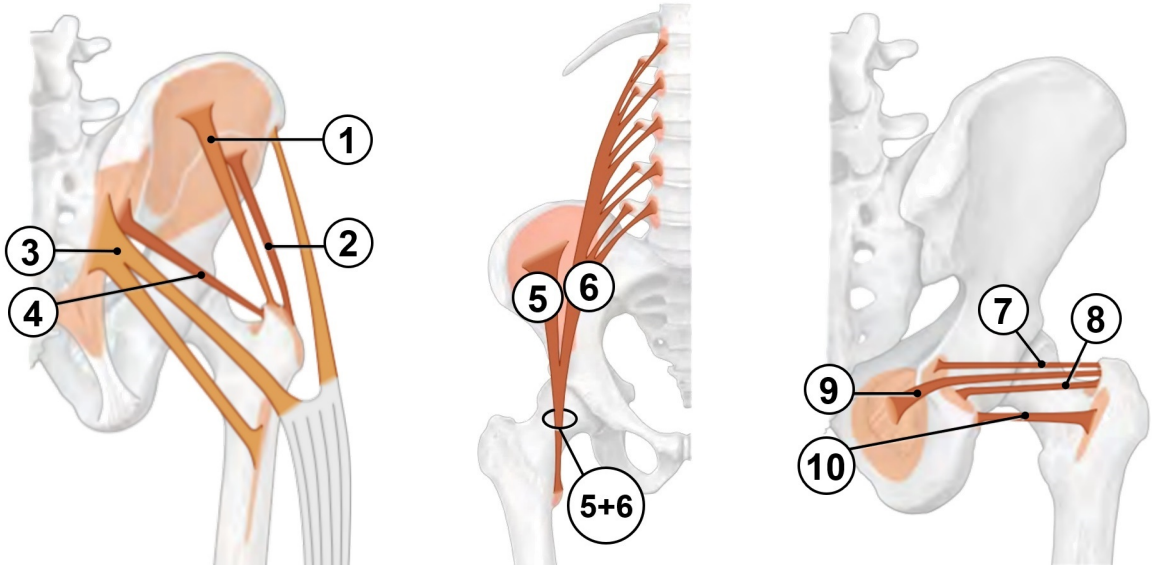

(a) Posterior View **(b)** Anterior View **(c)** Posterior View

Figure 1.7: Muscles of the Hip (Adapted from [6])

Table 1.1: Details of the Hip Muscles

#	Muscle	Attachment Location	Actions
1	Gluteus Medius	Lateral Greater Trochanter	Hip Abduction, Extension, Flexion, Medial and Lateral Rotation
2	Gluteus Minimus	Lateral Greater Trochanter	Hip Abduction, Extension, Flexion, Medial and Lateral Rotation
3	Gluteus Maximus	Gluteal Tuberosity	Hip Extension, Abduction, Adduction and Lateral Rotation
4	Piriformis	Greater Trochanter Apex	Hip Extension, Abduction and Lateral Rotation
5	Iliacus	Lesser Trochanter	Hip Flexion and Lateral Rotation
6	Psoas Major	Lesser Trochanter	Hip Flexion and Lateral Rotation
7	Gemellus Superior	Medial Greater Trochanter	Hip Lateral Rotation, Extension and Abduction
8	Gemellus Inferior	Medial Greater Trochanter	Hip Lateral Rotation, Extension and Abduction
9	Obturator Internus	Medial Greater Trochanter	Hip Lateral Rotation, Extension and Abduction
10	Quadratus Femoris	Intertrochanteric Crest	Hip Lateral Rotation

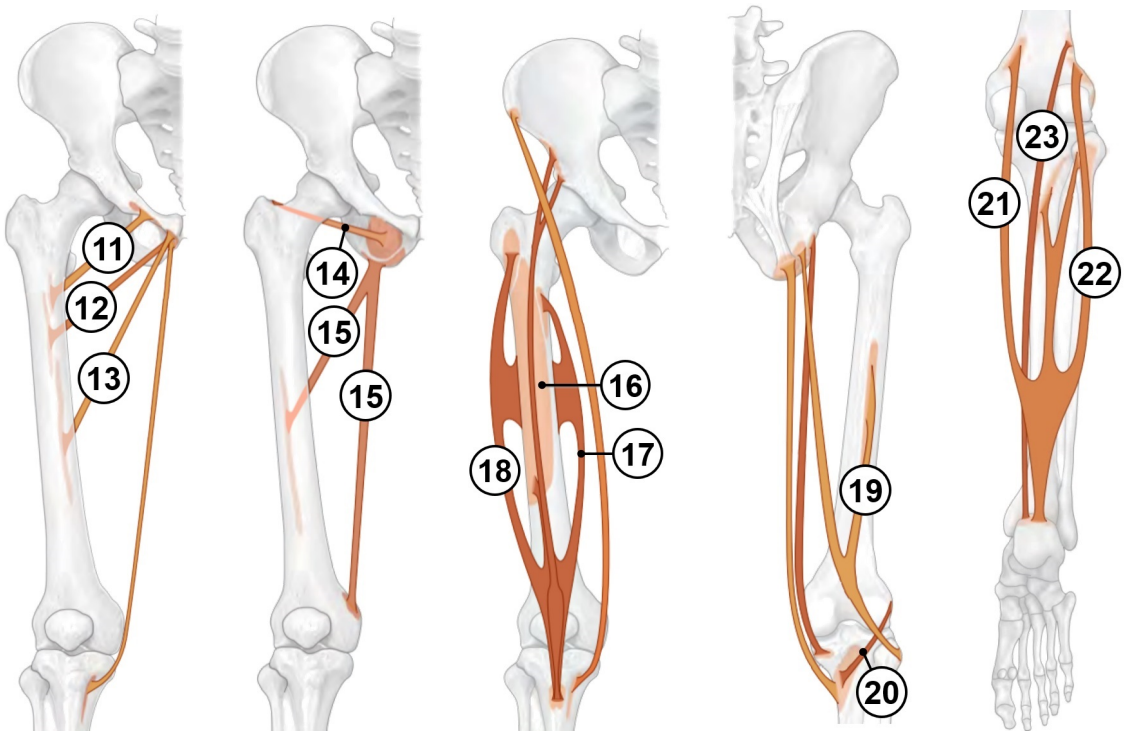

(a) Superficial **(b)** Deep Muscles **(c)** Anterior Muscles **(d)** Posterior Muscles **(e)** Distal Muscles

Figure 1.8: Muscles of the Thigh (Adapted from [6])

Table 1.2: Details of the Tight Muscles

#	Muscle	Attachment Location	Actions
11	Pectineus	Pectineal Line	Hip Adduction, Lateral Rotation and Flexion
12	Adductor Brevis	Linea Aspera Medial Lip	Hip Adduction, Flexion and Extension
13	Adductor Longus	Linea Aspera Medial Lip	Hip Adduction, Flexion and Extension
14	Obturator Externus	Trochanteric Fossa	Hip Adduction and Lateral Rotation
15	Adductor Magnus	Linea Aspera Medial Lip and Adductor Tubercle	Hip Adduction, Extension and Flexion
16	Vastus Intermedius	Anterior Shaft	Knee Extension
17	Vastus Medialis	Linea Aspera Medial Lip	Knee Extension
18	Vastus Lateralis	Linea Aspera Lateral Lip	Knee Extension
19	Biceps Femoris	Linea Aspera Lateral Lip	Knee Flexion, Hip Extension and Lateral Rotation
20	Popliteus	Lateral Epicondyle	Knee Flexion
21	Gastrocnemius Medialis	Superior Medial Condyle	Knee Flexion
22	Gastrocnemius Lateralis	Superior Lateral Condyle	Knee Flexion
23	Plantaris	Superior Lateral Epicondyle	Knee Flexion

1.1.4 Proximal Femoral Fractures

The proximal femur is defined as the section above a transverse line passing through the lower edge of the lesser trochanter. According to the classification of the AO Foundation/Orthopaedic Trauma Association (AO/OTA), fractures in this segment of the femur, known as proximal femoral fractures (AO/OTA fracture code 31), are subcategorised into three types, which are identified according to the topographic region in which they appear [7], [8]:

- **Trochanteric Fractures (31A):** Between the transverse line passing through the lower edge of the lesser trochanter and the intertrochanteric line, Figure 1.9a.
- **Neck Fractures (31B):** Between the intertrochanteric line and the line passing through the distal edge of the articular cartilage of the femoral head, Figure 1.9b.
- **Head Fractures (31C):** At the portion of the femoral head covered with the articular cartilage, Figure 1.9c.

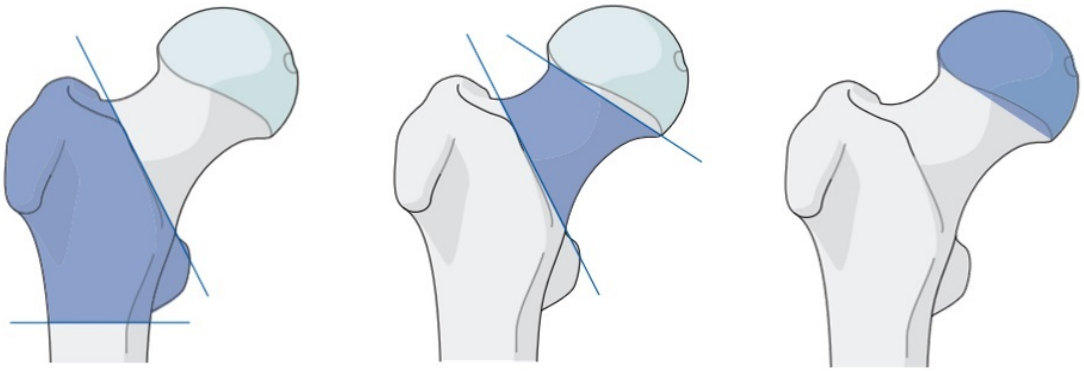

(a) Trochanteric **(b)** Neck **(c)** Head

Figure 1.9: Regional Subdivision of Proximal Femoral Fractures [7]

The focus of this study is on fractures that occur in the trochanteric region. That being said, when examining these fractures closer, it is possible to divide them into three subgroups.

- **Simple Pertrochanteric Fractures (31A1):** Fractures with only one fragment or with the lateral wall not compromised, detailed in Figure 1.10.
- **Multifragmentary Pertrochanteric Fractures (31A2):** Pertrochanteric fractures shattered into multiple fragments, detailed in Figure 1.11.
- **Intertrochanteric Fractures (31A3):** Fracture across the greater and lesser trochanter, detailed in Figure 1.12.

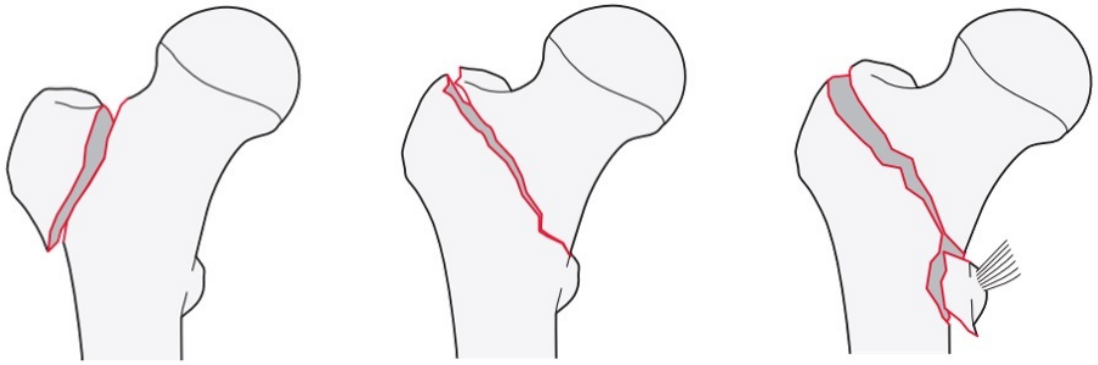

(a) Isolated Trochanter (31A1.1) **(b)** Two Part (31A1.2) **(c)** Lateral Wall Intact (31A1.3)

Figure 1.10: Types of Simple Pertrochanteric Fractures [7]

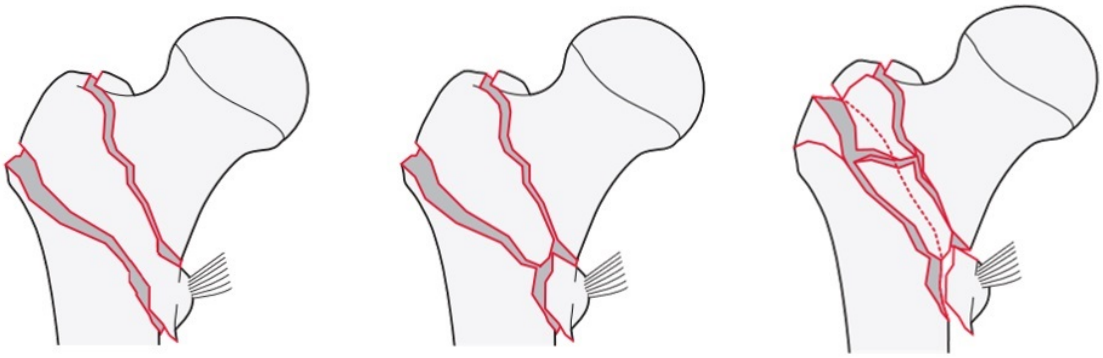

(a) Large Fragment (31A2.1) **(b)** Intermediate Fragment (31A2.2) **(c)** Several Fragments (31A2.3)

Figure 1.11: Types of Multifragmentary Pertrochanteric Fractures [7], [9]

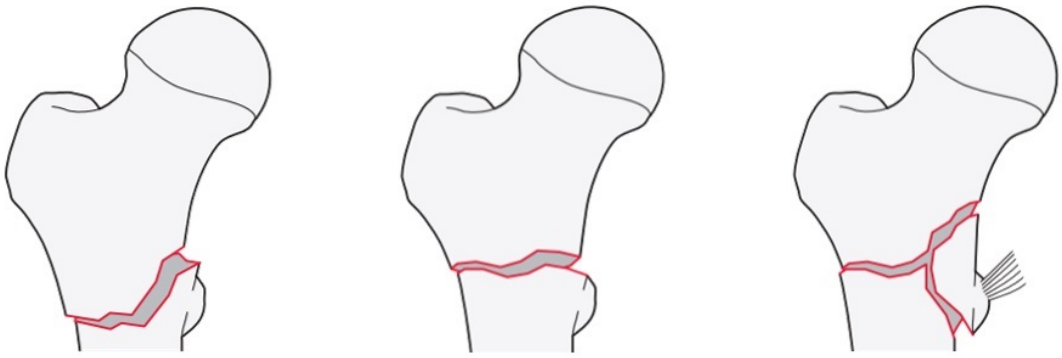

(a) Simple Oblique (31A3.1) **(b)** Simple Transverse (31A3.2) **(c)** Multifragmentary (31A3.3)

Figure 1.12: Types of Intertrochanteric Fractures [7]

Treatments for these fractures include options with extramedullary or intramedullary fixations. The most typical example of an extramedullary implant is the dynamic hip screw (DHS), a head-sparing orthopaedic device consisting of a large lag screw that goes through the neck and is held in place by a lateral femoral plate [10], as presented in Figure 1.13a.

In cases of more unstable fractures, intramedullary implants such as Gamma Nail (GN) and Proximal Femoral Nails (PFN) can provide better results [10]. These osteosynthetic devices consist of a tapered intramedullary nail, slightly bent to accommodate the morphology of the proximal diaphysis, and distally locked in place by small screws. For the GN, a single large lag screw goes through the femoral neck, while in the case of the PFN an additional antirotation screw is present, as shown in Figures 1.13b and 1.13c respectively. Similarly, Proximal Femoral Nail Antirotation (PFNA) is fixed intramedullarily. However, it has a helical blade instead of an additional antirotation or lag screws, as depicted in Figure 1.13d.

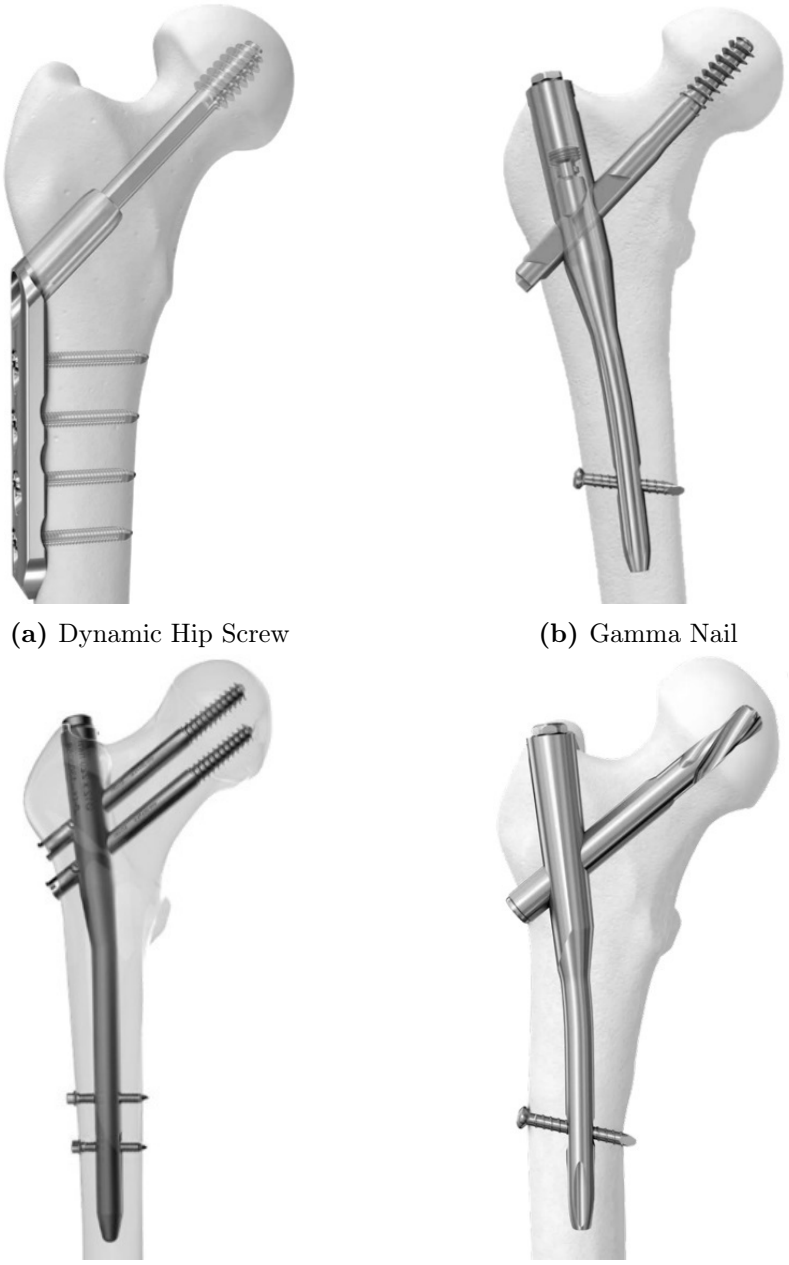

(a) Dynamic Hip Screw **(b)** Gamma Nail

(c) Proximal Femoral Nail **(d)** Proximal Femoral Nail Antirotation

Figure 1.13: Examples of Trochanteric Fractures Implants (Adapted from [11])

1.1.5 Normal Gait Cycle

Gait is defined as the movement pattern performed by the lower limbs during locomotion. It is the result of a complex combination of interactions between the hip, knee, and ankle joints that produces a smooth body motion that minimises the vertical fluctuation of the body's centre of gravity [5]. Naturally, the gait cycle differs with the speed of movement and from person to person. Since walking is such an essential and routine body movement, it is frequently used in biomechanical studies. That being said, it is necessary to define guidelines to describe a normal gait that can be used as a standard to study and assess the walking pattern of human subjects.

Normal walking is characterised as the method of locomotion involving the use of the two legs to provide support and propulsion to the human body, with at least one foot in contact with the ground at all times. The last detail of this definition is responsible for distinguishing the walking gait cycle from the running gait cycles [12]. The normal gait cycle is defined by one full period of the repetitive event of walking. Generally, the heel strike of the leading leg is considered as the start of the cycle, therefore the cycle ends when the same heel hits the ground again, as presented in Figure 1.14.

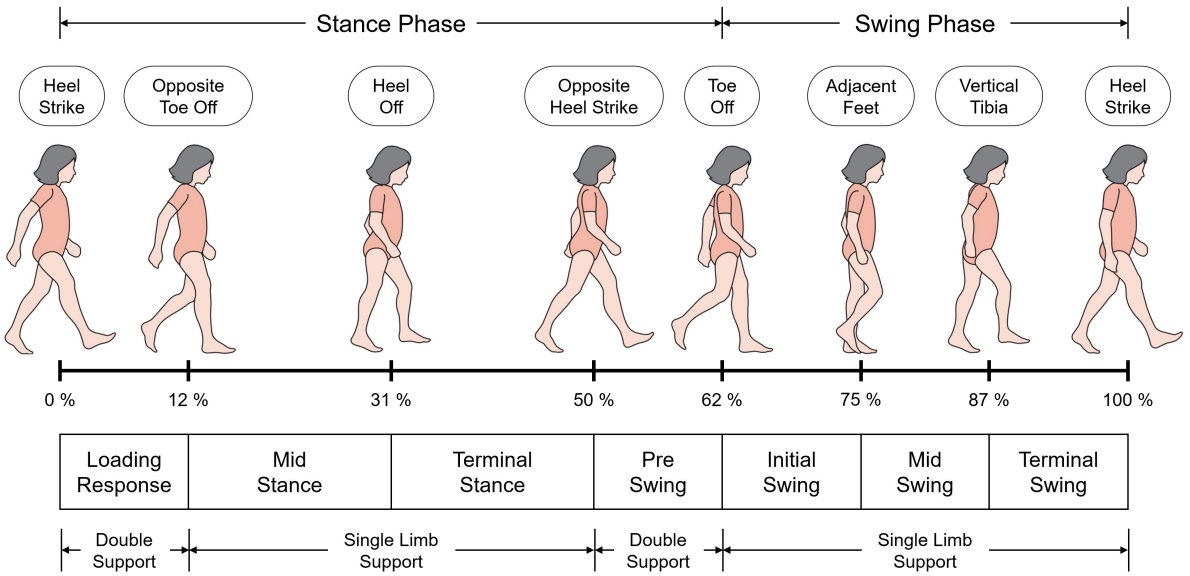

Figure 1.14: Normal Gait Cycle (Adapted from [13])

The full cycle is subdivided into seven events. The first four occur while the foot is in contact with the ground, known as the stance phase, and the last for the initial 60% of the cycle. The following three occur while the leading leg hangs off the ground, known as the swing phase, and it finishes when the heel makes contact and the cycle is completed. Naturally, the opposite leg goes through the same process, but offset by half a cycle [12]–[14].

During the stance phase, there are two moments when both feet are in contact with the ground, the loading response, and pre-swing events. These double support periods usually last for 10% of the gait cycle, however, this varies with the speed of walking. As the pace ramps up, the swing phase becomes proportionately longer while the stance phase and double support period get shorter. The transition from walking to running is marked by the disappearance of double support periods, which turns into a float period when neither foot is in contact with the ground [12].

1.2 Biomechanical Testing

Studies of the biomechanical behaviour of bones under physiological loading are important to better understand the mechanics of a fracture and to determine the appropriate requirements for the favourable long-term functioning of a bone-implant system. This can be achieved by mechanically testing bone samples, using either cadaveric specimens or artificial bones, in experimental setups that can recreate equivalent loading conditions.

1.2.1 Experimental Configuration

In the literature, studies dedicated to mechanically testing the response of the femur predominantly use experimental systems with simplified loading conditions. These setups usually apply a single vertical force to the femoral head of the bone while its distal extremity is fixed, aiming to replicate the loading condition during single leg stance. The main idea of this configuration is to replicate only the contact force of the hip joint, as this is the most dominant load acting on the femur.

In general, all these systems make use of a Universal Testing Machine (UTM) to apply the vertical force, as they are versatile and contain most of the capabilities required to perform these types of mechanical tests. Thus, the main distinguishing characteristics of the experimental setups found in the literature lie in the fixture system and the instrumentation of the specimen. Since the UTM actuator works only vertically, the fixture system plays an important role in the test by being responsible for positioning the bone and consequently establishing the correct orientation for the force.

Some works follow a straightforward approach by placing the base supporting the specimen fixed at the desired angle for the study [15]–[17], as exemplified in Figure 1.15. However, this design does not allow for any flexibility, requiring a completely new fixture to alter the orientation of the force. Other works opt for an adjustable base that allows for variation of the inclination angle on one or more axes [18]–[20], as shown by the examples in Figure 1.16.

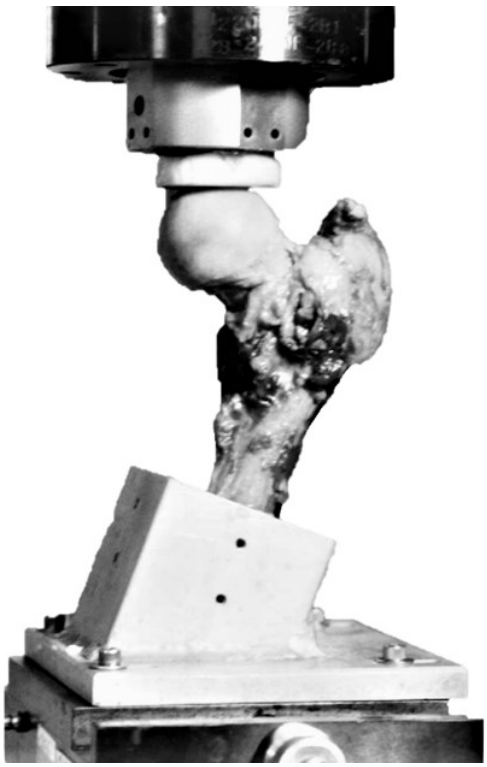

(a) Keyak Setup (Adapted from [17])

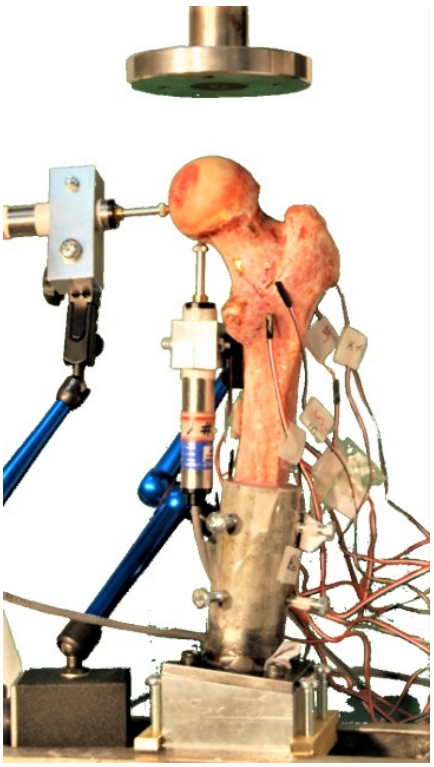

(b) Yosibash Setup (Adapted from [21])

Figure 1.15: Experimental Systems with Fixed Femoral Angle

(a) Trabelsi Setup (Adapted from [19])

(b) Mirzaei Setup (Adapted from [18])

Figure 1.16: Experimental Systems with Adjustable Femoral Angle

Another approach is to introduce additional forces, alongside the hip joint contact force, to represent some of the muscles that act on the femur. These additional forces are complementary to and operate in collaboration with the predominant force applied to the femoral head. This testing configuration is seldom found in the literature, as it greatly increases the complexity of the experimental setup.

One method of adding supplementary loading to the system is by introducing force actuators that operate simultaneously and independently of the UTM's actuator [22]. This active approach provides for more flexibility and control over the individual forces. However, it is more resource intensive and requires the synchronisation between the actuators and the UTM.

It is also possible to follow a passive approach by making use of levers and pulleys to distribute a single force (from the UTM's actuator) to different points of application [23]–[26], as exemplified by the two distinctive concepts found in the literature and presented in Figure 1.17. This method excludes the need for additional actuators and substantially reduces the complexity introduced to the experimental setup. Furthermore, since all loads are generated by a single source of force, they are all inherently synchronised.

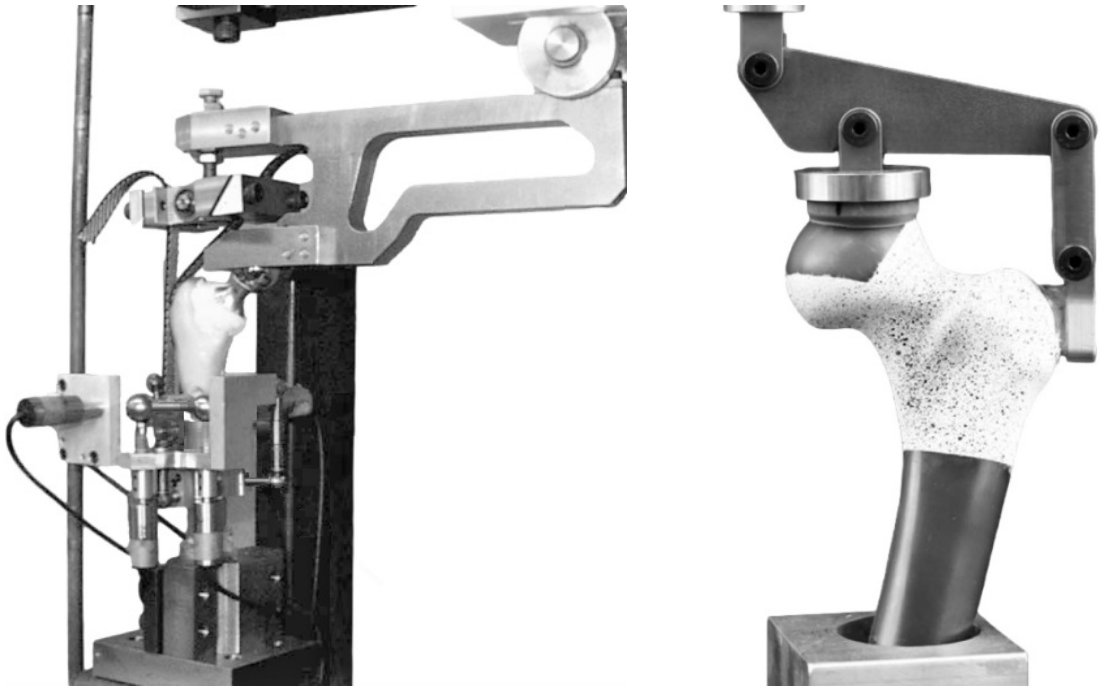

(a) Briton Setup (Adapted from [25])

(b) Dickinson Setup (Adapted from [26])

Figure 1.17: Experimental Systems with Multiple Forces

On the other hand, the passive approach lacks flexibility, since the individual forces cannot be adjusted independently. In order to change the intensity or orientation of the forces, it is necessary to alter the dimension and positioning of the levers and pulleys, requiring a complete redesign of the loading distribution system.

The representative loading of the muscle forces, either generated by the independent actuators of the active approach or the resultant of the loading distribution system from the passive method, are applied to the specimen through cables, ropes, or straps that are glued to the surface of the bone at the muscle's anatomical region of attachment.

In contrast to these mechanical tests that aim to recreate the loading condition during gait, there are works in the literature focused on experimentally recreating the conditions of a sideways fall, an accident that often leads to femoral fractures [27]–[30]. In these cases, the tests are also mostly performed using a UTM, however, the femoral head is loaded in the medio-lateral direction instead of vertically, as depicted in the examples in Figure 1.18 .

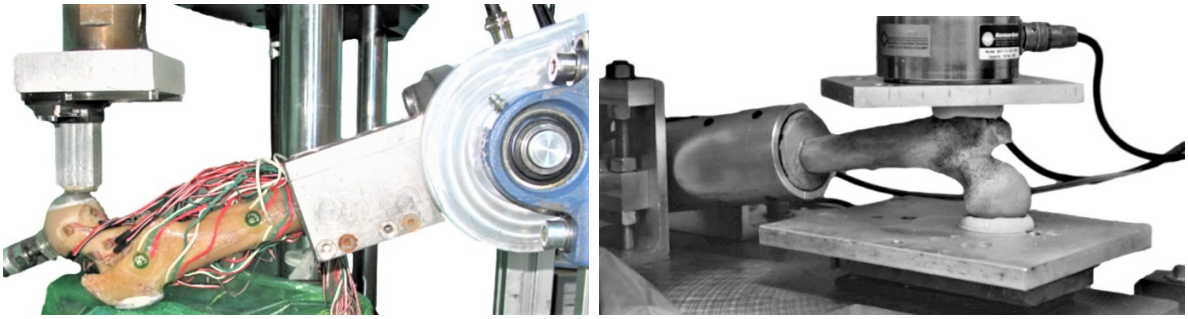

(a) Grassi Setup (Adapted from [29]) **(b)** Nishiyama Setup (Adapted from [28])

Figure 1.18: Experimental Systems for Sideways Fall

1.2.2 Instrumentation

An essential aspect of biomechanical tests is the instrumentation of the experimental setup. The loading axis of UTMs is already equipped with force and displacement sensors, allowing for the acquisition of these physical quantities. Depending on the nature of the study, collecting only these measurements could be sufficient, such as in cases only interested in fracture load or overall stiffness of the bone [17], [31], [32].

However, in order to validate the FE model more accurately based on the experimental results, it is necessary to collect additional data directly on the specimens. Most studies in the literature usually measure the total displacement of a specific landmark or its local strain values. The macro motions that occur on the bone can be obtained using displacement transducers or optical markers, while the superficial strain values are measured using digital image correlation (DIC) or strain gauges.

Most earlier works in the literature relied on strain gauges to measure strain values generated on the surface of the femur under load [16], [19], [22], [24], however, strain gauges are limited to localised measurements. Therefore, the most recent works use DIC [15], [26], [33]–[36], which allows measurement of full-field strain levels throughout a complex geometry, such as the surface of the proximal femur, as shown in Figure 1.19.

(a) Equipment Setup (Adapted from [33])

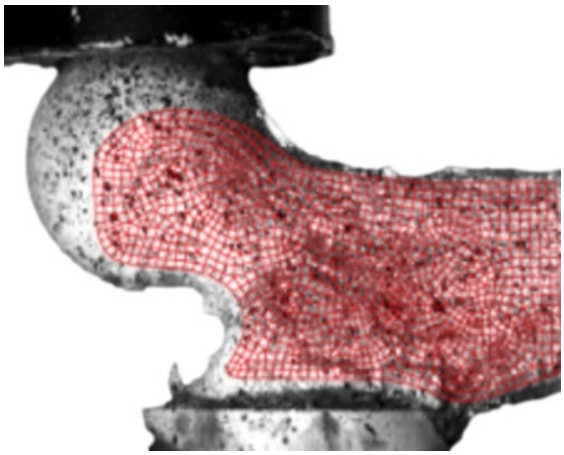

(b) Speckle Pattern (Adapted from [35])

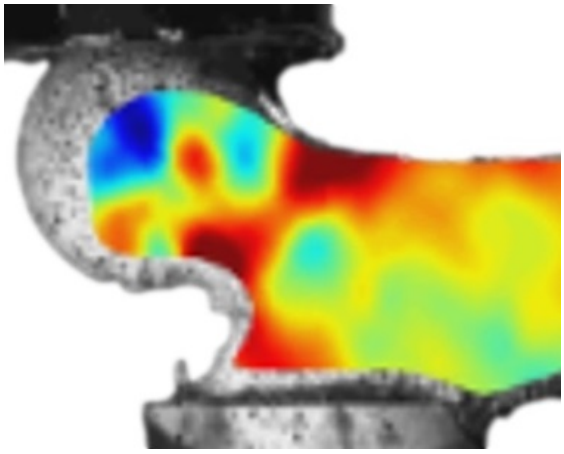

(c) Strain Results (Adapted from [35])

Figure 1.19: Examples of Digital Image Correlation (DIC) Applications

1.3 Numerical Simulations

Studying the behaviour of a femoral fracture solely empirically, by conducting compression tests of individual bone specimens, presents the limitation that the same specimen cannot be tested multiple times for different scenarios. This constraint can be addressed by recreating the bone geometry from computed tomography (CT) scans and modelling it using the finite element (FE) method. Additionally, this technique allows for patient-specific assessment in a non-invasive manner.

1.3.1 Material Properties

To setup a reliable FE model, it is essential not only to accurately recreate the geometry of the bone but also realistically model its material properties. As previously detailed in Chapter 1.1.2, the cortical and trabecular bones are formed by heterogeneous microstructures, which are characterised as non-homogeneous and orthotropic.

However, assigning the properties of the material spatially orientated to the principal axes of orthotropy is an extremely complex process, especially for the intricate geometry of the trabecular bone. When dealing with small bone specimens, the definition of orthotropic orientation has an important effect on the results, while for global analyses of the proximal femur this can be neglected, as long as the material is modelled considering its non-homogeneities [37].

1.3.1.1 Cadaveric Bones

To properly model the material property, taking into consideration the non-homogeneities of the bone, many researchers have established mathematical relationships between density and elasticity modulus. Thus, the material property can be assigned to the geometry at a local level, deriving the elasticity moduli of each element of the mesh from its own local density [38]. This localised densitometric characteristics of a bone can be measured by quantitative computed tomography (QCT), by simultaneously scanning the body part and a calibration phantom, as shown in Figure 1.20.

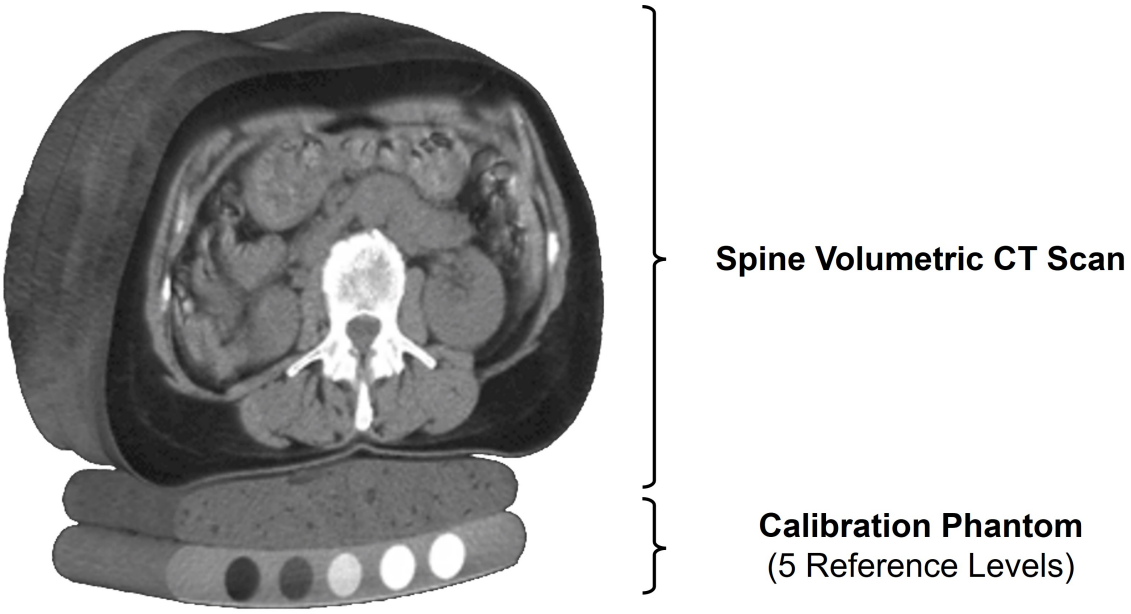

Figure 1.20: Quantitative Computed Tomography (QCT) (Adapted from [39])

The calibration phantom is a reference standard that is used to convert the radiodensity measurement to bone mineral density (BMD). To achieve this purpose, the phantom is composed of cylinders filled with different mixtures of substances with varying concentrations to represent distinct levels of BMD, usually the substance used is dipotassium phosphate (K_2HPO_4) or hydroxyapatite (HA) [40].

A regular uncalibrated CT image measures the radiodensity in Hounsfield units (HU) based on the Hounsfield scale, which uses water and air as references for the values of 0 HU and -1000 HU respectively.

In the case of a QCT scan, the captured radiodensity measurement uses the densities contained in the calibration phantom (at $mg_{K_2HPO_4}/cm^3$ or mg_{HA}/cm^3) as the scale. The density of the substances enclosed within the phantom has been linearly related to the ash density of the bone, allowing the direct conversion from x-ray attenuation data to the physical property of the bone [38].

The measured ash density must then be converted into a material property. This can be done by establishing an empirical relationship between the density and the elasticity modulus of the physical specimen. Thus, a continuous function ($E = \alpha\rho^{\beta}$) can be fitted to the curve of the experimental data, allowing the Elasticity Modulus (E) to be calculated from the ash density (ρ_{ash}) using the fitting parameters α and β [41]

1.3.1.2 Artificial Bones

This process of introducing the non-homogeneities of the material into the FE model is very important when dealing with real human bones. However, in the field of biomechanics, a common alternative to cadaveric specimens is to use artificial bones as test samples. These composite bones are designed to replicate the biomechanical properties of real bones. Furthermore, the use of artificial bones mitigates many of the shortcoming of the cadaveric option, such as high inconsistency between specimens, their cost, availability, and the inconvenient preservation effort required by them [42].

Sawbones is a manufacturer of such artificial bones, and it is widely used and well regarded within the field of biomechanical studies. Their 4^{th} generation of composite bones are manufactured using a cortical shell of short fibre-filled epoxy and a trabecular core of solid rigid polyurethane foam [43], as depicted by the cut section in Figure 1.21.

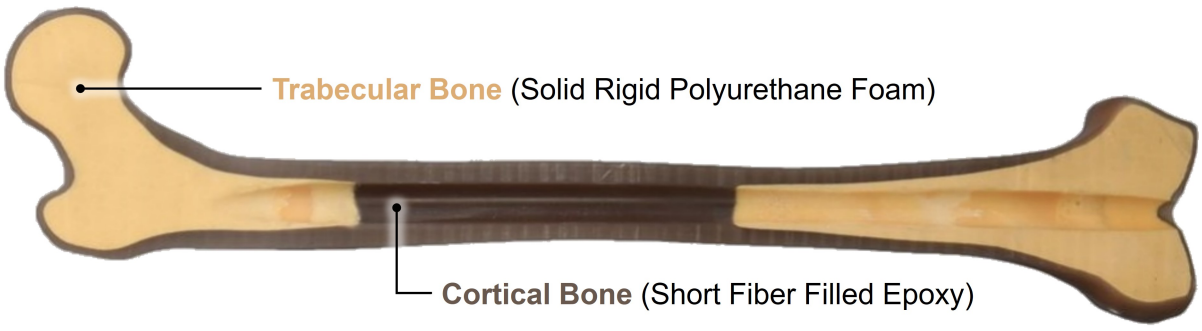

Figure 1.21: Cut Section of Artificial Bone from Sawbones (Adapted from [43])

These materials are reasonably homogeneous, making their modelling process and assignment of the material properties much simpler than real human bones. The cortical layer and the trabecular core can be modelled as separate geometries that interact through a bonded contact, each defined by their own respective homogeneous material properties (detailed in Table 1.3 according to the manufacturer's specification).

Table 1.3: Compressive Material Properties of Artificial Bones [43]

Material	Density (g/cm^3)	Strength (MPa)		Modulus (GPa)	
		Tensile	Compressive	Tensile	Compressive
Cortical Bone (Short Fiber Filled Epoxy)	1.64	106	157	16.0	16.70
Trabecular Bone (Solid Rigid Polyurethane Foam)	0.27	-	6	-	0.155

1.3.2 Loading Measurement

The forces acting on the femur are plenty, aside from the joint contact forces of the hip and knee, there are 23 different muscles that act directly along the bone, as previously detailed in Chapter 1.1.3. Assigning these forces to the FE model in a realistic manner is essential to recreate the accurate biomechanical behaviour of the bone, however, the real challenge lies in determining the magnitude and direction of the forces.

The loading that acts on human joints can be measured by using instrumented implants, which are equipped with sensors and make use of telemetry to remotely collect measured data. For instance, the database made available by the OrthoLoad team is a compilation of joint loads acquired in vivo, at the Julius Wolff Institute of Charité in Berlin, for different routine and sportive activities [44]. Three different models of instrumented hip implants, used in the OrthoLoad project, are shown in Figure 1.22.

(a) One 4-Channel Transmitter **(b)** Two 8-Channel Transmitters **(c)** One 9-Channel Transmitter

Figure 1.22: Instrumented Hip Implants [44]

In the case of muscle forces, it is not possible to measure them directly in the fibres of the muscle itself. The electric potential generated by muscle cells can be measured by electromyography (EMG). However, the EMG signal is a measure of muscle activity and alone does not provide quantitative values of muscle forces [45].

1.3.3 Musculoskeletal Simulation

Muscle and joint forces are usually mathematically estimated from numerical models using inverse dynamics. This method indirectly determines the forces and moments acting on a moving rigid-body from its kinematic and inertial properties [46]. Thus, by creating an anatomical model of the human body, known as a musculoskeletal model, where the limbs act as segments interconnected by joints that are actuated by muscles, it is possible to derive the forces necessary to recreate a specific movement.

1.3.3.1 3D Kinematics

In order to define the kinematics of a specific body movement and use it as input for the inverse dynamics simulation, it is necessary to capture and measure the motion that happens in the physical world and recreate it digitally. This is usually done through motion capture recordings (Mocap), a process that uses cameras to track retroreflective markers placed on key body landmarks of a human subject [47].

Analysing the captured image, it is possible to quantify the position of the markers by measuring the spatial coordinates of their centres. To locate 3D coordinates, two cameras are required; however, since markers can get blocked by body parts, a multi-camera system is used to guarantee that all markers are visible by at least two cameras throughout the movement [46], as illustrated in Figure 1.23a. The markers used are spherical because on a sphere the centre is the same for every camera at any viewing angle. Additionally, they are covered with retroreflective material, which enhances their brightness, makes their edges clearer and consequently easier to identify [47], as shown in Figure 1.23b.

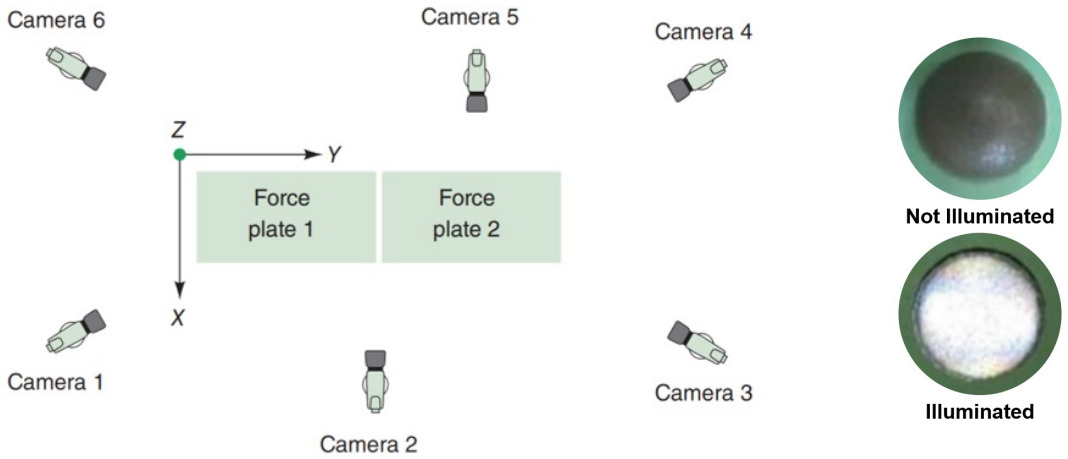

(a) Camera Arrangement [46] **(b)** Reflective Marker [47]

Figure 1.23: Motion Capture Setup of 3D Kinematics

The correct positioning of the markers on the human body is essential for an accurate digital recreation of the motion being captured. Usually, they are placed at the

pivoting points of the segments involved in the movement of interest [46]. In the case of normal gait for instance, which is widely studied in the field of biomechanics, there are standard protocols that define the positioning of the markers.

1.3.3.2 Inverse Dynamics

Traditional or forward dynamics describes the motion of a body for a given input force and initial conditions. Inverse dynamics, on the other hand, uses a recorded motion to define the forces and moments responsible for describing the given movement. This is achieved using the Newton-Euler equations of motion, as presented in Equations 1.1 and 1.2, which respectively states that the rate of change of momentum of a rigid body equals the sum of all the forces acting on it and the rate of change of its angular momentum equals the sum of all the acting moments.

$$\sum \vec{F} = \frac{\mathrm{d}}{\mathrm{d}t}(m \cdot \vec{v}) = m \cdot \vec{a} \tag{1.1}$$

$$\sum \vec{M} = \frac{\mathrm{d}}{\mathrm{d}t}(I \cdot \vec{\omega}) \tag{1.2}$$

A 3D inverse dynamics analysis of a rigid body has six equations of motion, each one related to a degree of freedom, three translational, and three rotational. However, when analysing a body segment with multiple muscles, as the foot depicted in Figure 1.24a, there are more than six unknown variables and the solution is indeterminate. In order to solve this problem, the sum of all effective forces acting on an anatomical joint can be represented as a net joint force ($\vec{F}_J$) and a net joint moment ($\vec{M}_J$).

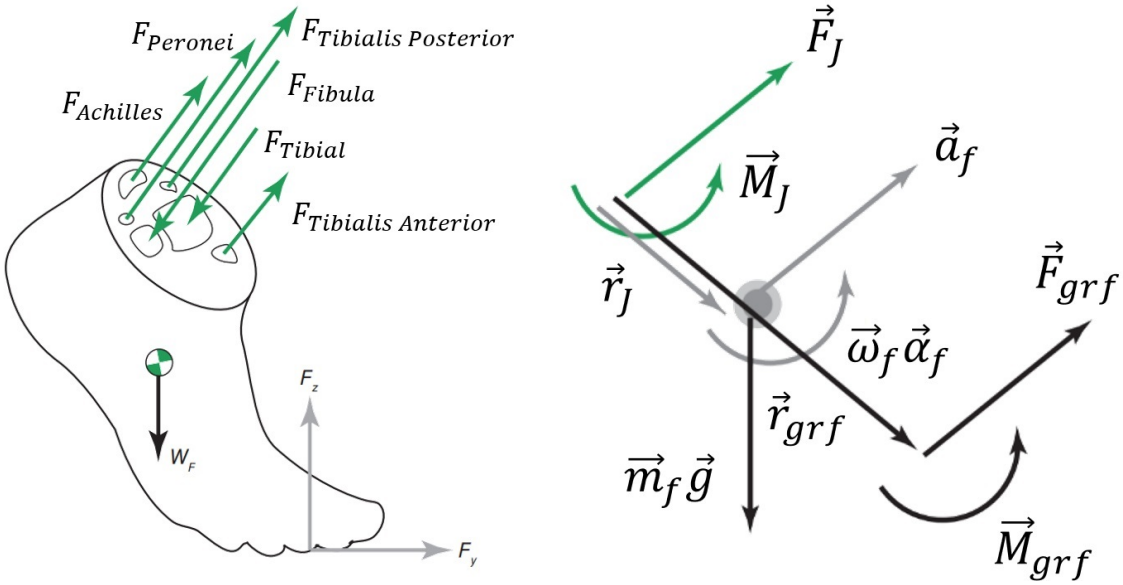

(a) Foot Including all Effective Forces **(b)** Foot Free-Body Diagram

Figure 1.24: Forces Acting on the Foot (Adapted from [46])

Considering that the foot is a one link segment pivoting at the ankle joint, it can be represented by the free-body diagram shown in Figure 1.24b. The net joint force and moment are the output of the equations of motion derived from the free-body diagram, while the following three case specific parameters act as input:

- **Inertial Characteristics:** Mass (m_f), moment of inertia (I_f) and lever arms ($\vec{r}_J$ and $\vec{r}_{grf}$) of the foot, defined from the anthropometric characteristics of the human subject.
- **Kinematic Variables:** Translational velocity ($\vec{v}_f$) and acceleration ($\vec{a}_f$), rotational velocity ($\vec{\omega}_f$) and acceleration($\vec{\alpha}_f$), values derived from motion capture data.
- **External Forces:** Ground reaction force ($\vec{F}_{grf}$) and its moment ($\vec{M}_{grf}$), values obtained, using force plates, simultaneously with the acquisition of the motion capture data.

Once the net joint force and moment are calculated, the muscle forces necessary to produce the given movement of the joint can be determined by calculating the equilibrium of forces and moments at the joint. For instance, a simplified model of the human elbow can be represented by the arm and forearm segments, interconnected and articulating at the elbow joint of one degree of freedom, being driven by three muscles, as illustrated in Figure 1.25.

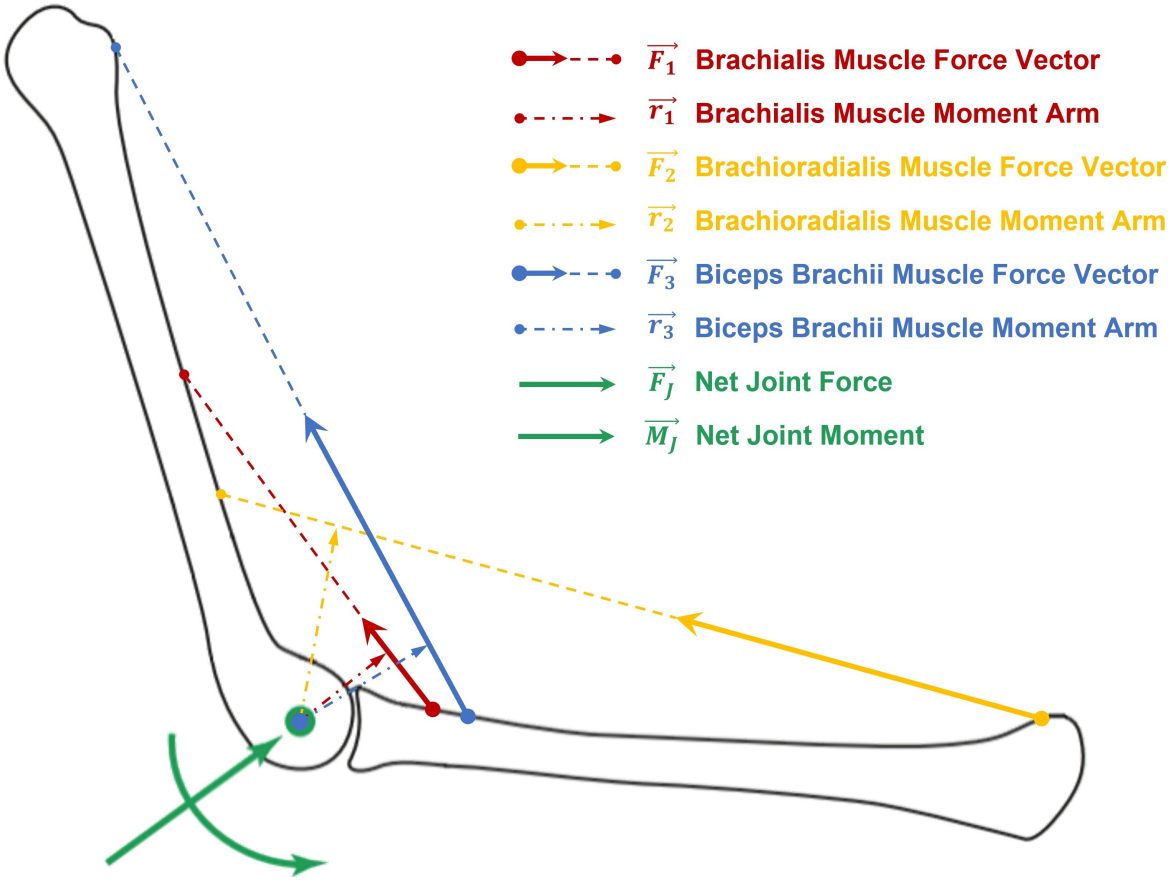

Figure 1.25: Musculoskeletal Model of the Human Elbow (Adapted from [46])

The net joint force ($\vec{F}_J$) and moment ($\vec{M}_J$), calculated using inverse dynamics to perform a given motion of the elbow, is equal to the vector sum of all the forces of internal muscles ($\vec{F}_m$), ligaments ($\vec{F}_l$) and articular contact ($\vec{F}_c$), as detailed in Equations 1.3 and 1.4.

$$\vec{F}_J = \sum_{i=1}^{m} \vec{F_{mi}} + \sum_{i=1}^{l} \vec{F}_{li} + \sum_{i=1}^{c} \vec{F}_{ci} \tag{1.3}$$

$$\vec{M}_J = \sum_{i=1}^{m} (\vec{r_{mi}} \times \vec{F_{mi}}) + \sum_{i=1}^{l} (\vec{r}_{li} \times \vec{F}_{li}) + \sum_{i=1}^{c} (\vec{r_{ci}} \times \vec{F}_{ci}) \tag{1.4}$$

Making the simplifying assumptions that the ligament forces are negligible when the joint is positioned in the middle of its range of motion, and that the articular contact forces pass through the joint pivot point ($\vec{r_c} = 0$), Equations 1.3 and 1.4 can be reduced to 1.5 and 1.6.

$$\vec{F}_J = \sum_{i=1}^{m} \vec{F_{mi}} + \sum_{i=1}^{c} \vec{F}_{ci} \tag{1.5}$$

$$\vec{M}_J = \sum_{i=1}^{m} (\vec{r_{mi}} \times \vec{F_{mi}}) \tag{1.6}$$

There are an infinite number of combinations of the three muscle forces that satisfy the equilibrium of the Equation 1.6, however, a physiologically reasonable solution can be found when a compromise that reduces the stresses on the muscles is achieved. Thus, an additional constraint must be applied as the cost function of this optimisation problem, presented in Equation 1.7, with (A_m) representing the physiological cross-section of the muscle [46].

$$Minimize = \sum_{i=1}^{3} \left(\frac{F_{mi}}{A_{mi}} \right)^3 \tag{1.7}$$

Despite the simplicity of this example, it adequately describes the principle of the process and can be similarly applied for other more complex joints of the human body with more degrees of freedom and acting muscles. In a larger scale, the musculoskeletal model of the complete body is a system based on the human anatomy, where the whole skeleton is recreated as rigid-bodies driven by all the muscles acting at their origin and insertion locations, making it able to recreate realistic full body movements [46], as depicted in Figure 1.26.

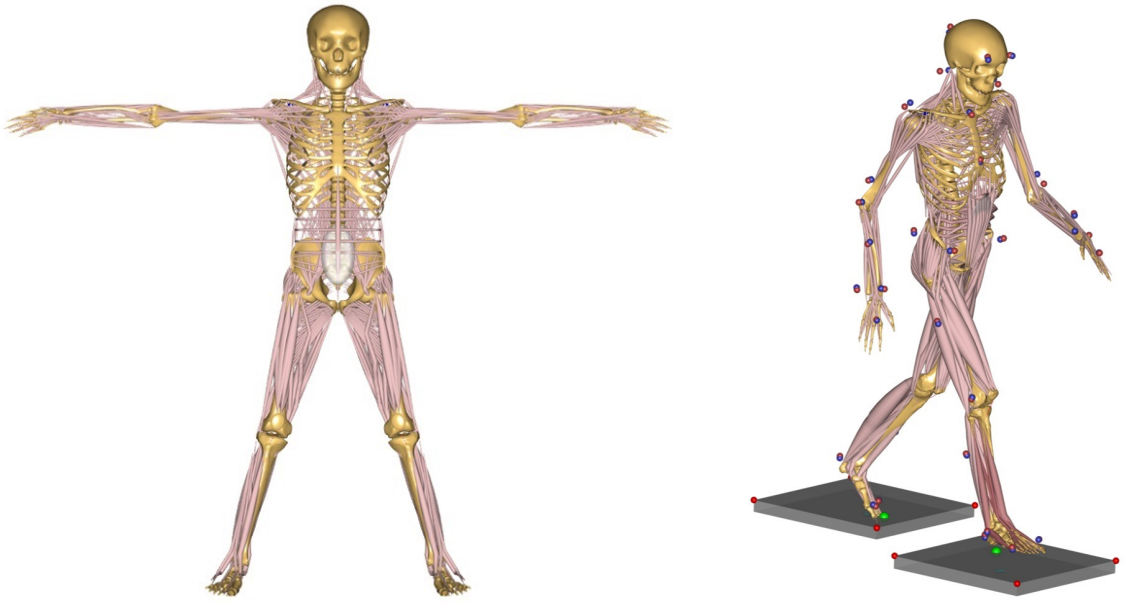

(a) AMMR Musculoskeletal Model [48] **(b)** AnyBody Gait Simulation [49]

Figure 1.26: Musculoskeletal Model from AnyBody Managed Model Repository (AMMR) [48]

1.3.4 Finite Element Simulation

The prediction of bone strength through finite element methods have been widely used over the years, however, the workflow defined in the Chapter 1.3 is not the only existing strategy to model and simulate this type of problems. Many different approaches to developing an image-based FE model of bone structures can be found in the literature, and they usually differ in four main aspects: the geometry creation, the material modelling, the loading condition, and the failure criteria [50]. This Section will go through some of these modelling strategies while highlighting the reasoning behind the techniques chosen to be used in this work.

1.3.4.1 Geometry Creation

The recreation of the bone geometry is widely done based on computed tomography scans, since the X-ray attenuation in bone is much higher than in soft tissue, resulting in images with well contrast edges. However, capturing the complex anatomic shape of the bone is just the first step of the geometry creation process, the conversion of these layered images into its respective 3D model can be done using different techniques.

Voxel-based discretization is a fast and automated method that generates a 3D geometry by converting each bone containing voxel of the CT images into a brick element, as depicted in Figure 1.27a. This approach was used in early biomechanic studies [17], [31], [32] due to its simplicity. However, the jagged surface inherent in this process causes superficial stress concentrations that impact the accuracy of the model.

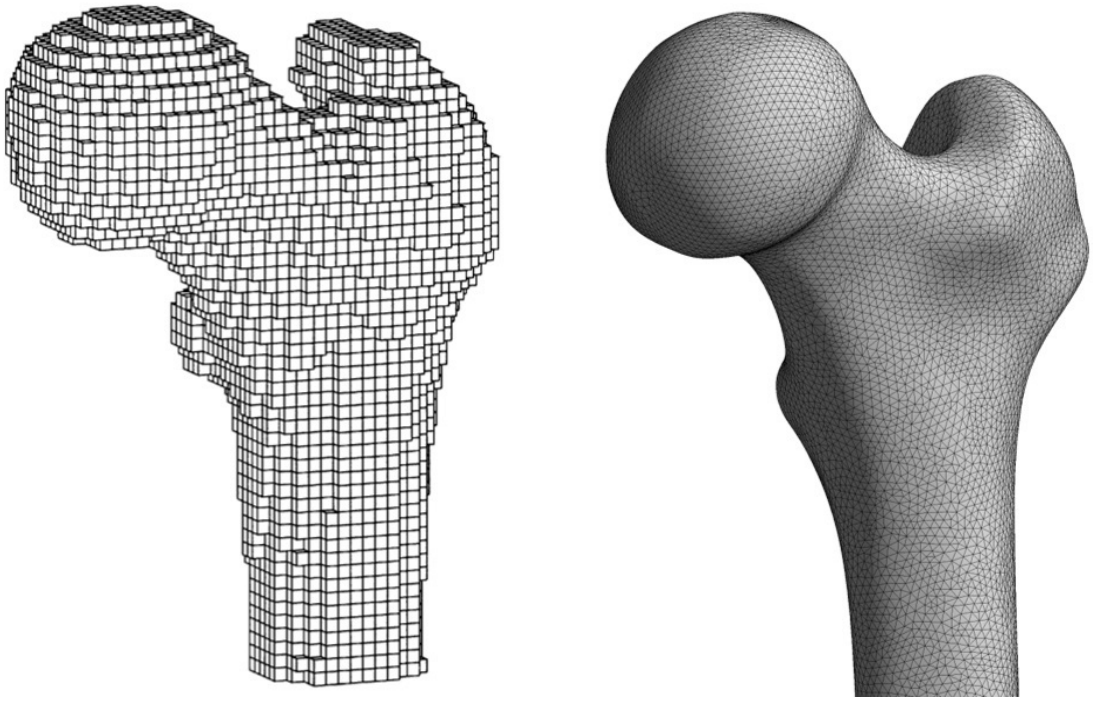

(a) Voxel Based Femur Geometry [31] **(b)** CT Image Segmentation Based Geometry

Figure 1.27: Comparison of Geometry Creation Methods

Alternatively, a faceted 3D model that is smoother than voxel-based geometry, as shown in Figure 1.27b, can be created by treating the digital images of the CT scan using image segmentation. This procedure makes use of image processing techniques, such as edge detection and thresholding, to identify and isolate the contour of the bone.

This outline is then used as a reference to define and create the three-dimensional surfaces of the digital model of the bone. Due to its accuracy, this method is the gold standard for recreating 3D bone geometries, being the predominant approach used in the literature [50], and the one chosen for this work.

1.3.4.2 Material Modelling

Most of the FE models of the femur found in the literature are based on cadaveric bones, therefore, their material properties are modelled as isotropic and heterogeneous [16]–[20], [31], [32], [51], [52]. In these cases, the heterogeneity of the material is defined according to the grey scale values of the CT images (Hounsfield units), as previously detailed in Section 1.3.1.1.

Studies based on artificial femurs are not as prevalent in the literature and some are only limited to their experimental testing [22], [24], [25]. The works that create FE models derived from these bones divide the geometry into cortical and trabecular portions, each with its own isotropic and homogeneous material properties [15], as detailed in Section 1.3.1.2 and used in this work.

1.3.4.3 Loading Condition

The main boundary condition, used in the literature to simulate physiological loading during gait, considers that a single force is applied to the femoral head at varying angles [15]–[20], [31], [32]. This load is usually derived from the hip joint contact force generated by a single leg stance. The constraining of the body is regularly done at the distal extremity of its diaphysis, after cutting the distal epiphysis of the bone, as exemplified in Figure 1.28.

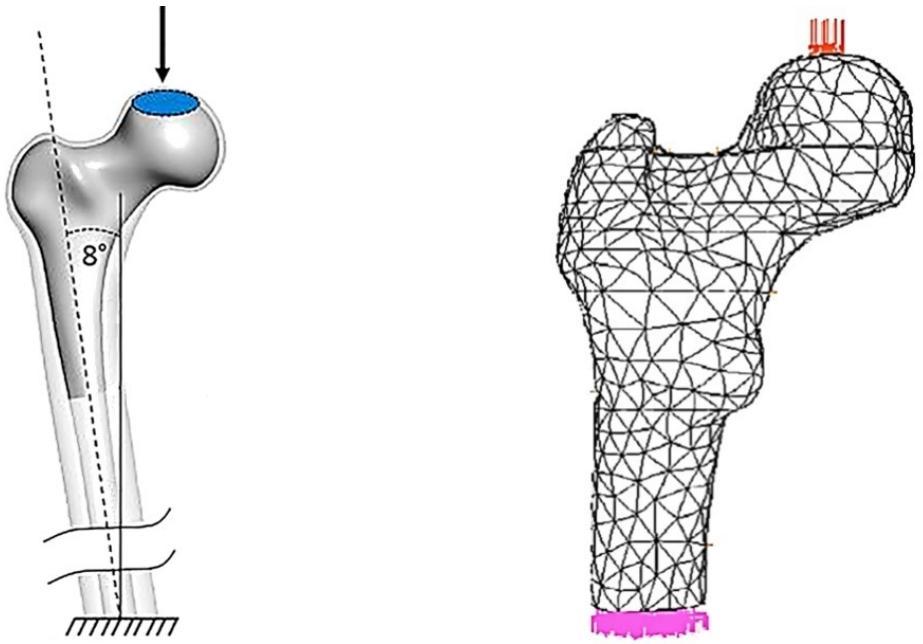

(a) Levadnyi Model (Adapted from [15]) **(b)** Yosibash Model (Adapted from [53])

Figure 1.28: Typical Gait Boundary Conditions Found in the Literature

A minority of works introduce a more complex loading configuration, which ranges from including just a few up to all the muscles forces that act on the femur [51], [52], [54], [55]. However, these studies are usually limited only to the numerical simulation, not encompassing the validation of the model through experimental testing.

Alternatively, there are studies that attempt to recreate the loading conditions that arise from a sideways fall, a common accident that usually leads to a femoral fracture. In these cases, the force is either applied to the greater trochanter while the femoral head is supported along the loading direction [28], [30], as illustrated in Figure 1.29a, or the force is applied to the femoral head and the greater trochanter is supported [27], [29], depicted in Figure 1.29b.

This work proposes to simulate the gait condition using a complete FE model that includes all the active muscle of the femur in addition to the hip joint contact force. Then, a corresponding model with a single equivalent force should be derived from the results obtained from the model with the complete loading condition.

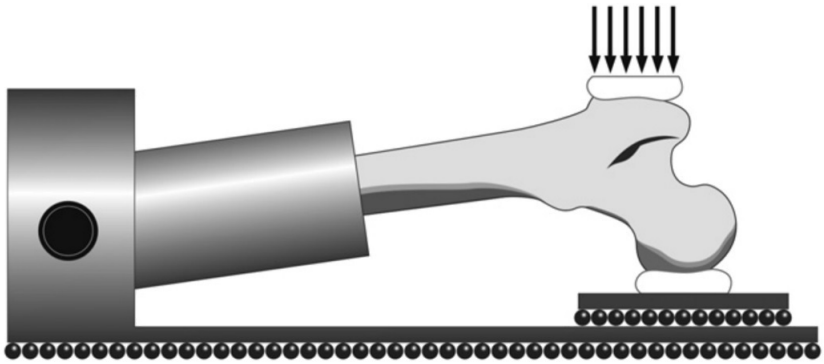

(a) Nishiyama Model (Adapted from [28])

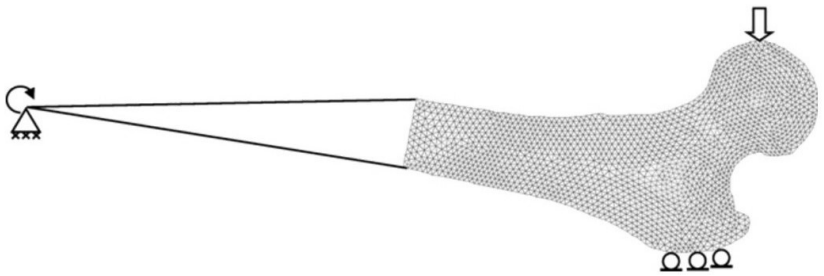

(b) Dragomir Model (Adapted from [56])

Figure 1.29: Typical Sideways Fall Boundary Conditions Found in the Literature

1.3.4.4 Stress Assessment

In the literature, there is no consensus on which criterion best describes the failure mechanism of bone, different criteria have been used to assess femoral failure [50]. A commonly used stress-based criterion is the equivalent von Mises stress [17], [31], [32]. However, for this work, the material used to manufacture artificial bones (short fibre-filled epoxy) has a brittle behaviour, identified by its low elongation at break (1.4%) presented in Figure 1.30. Therefore, it is recommended to assess its failure using the Mohr-Coulomb criterion based on the principal stresses instead of equivalent von Mises.

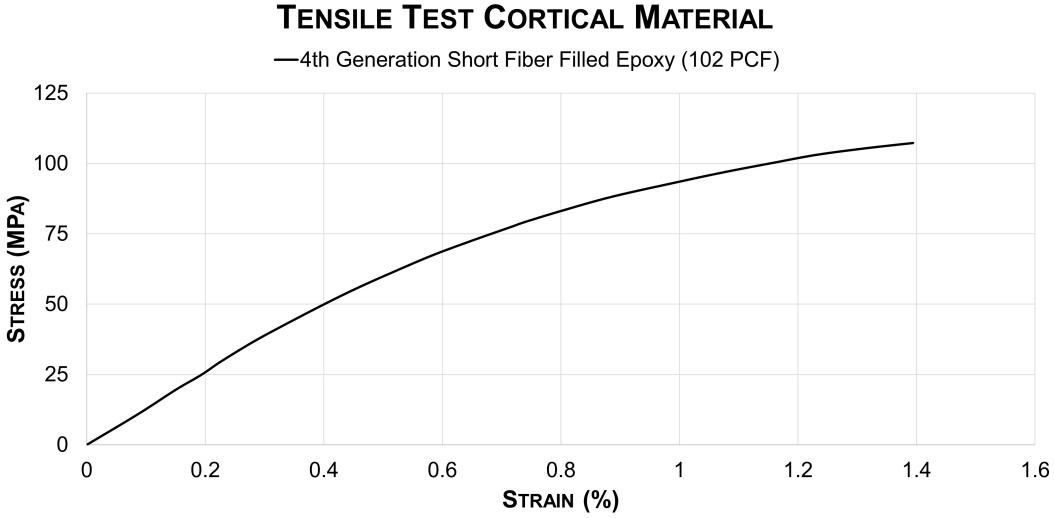

Figure 1.30: Tensile Test of the Short Fiber Filled Epoxy Material [43]

1.4 Design of Experiments

Design of experiments (DOE) is a data analysis tool capable of creating a data collection strategy for a given experiment, performing controlled tests while manipulating the input variables to evaluate how they might affect the output of the tests. In its simplest form, this method can be applied by varying the levels of one of the inputs while keeping the others at a constant value, known as the one-factor-at-a-time (OFAT) method.

As the number of variables increases, so does the number of test runs required, rendering the OFAT approach inefficient for a higher number of input parameters. Therefore, methods capable of altering multiple variables simultaneously have been developed and are widely used.

1.4.1 Full Factorial Analysis

Factorial analysis is a methodology used to design an experiment consisting of two or more input variables (known as Factors) that vary between different values (known as Levels). This approach changes multiple factors in each test run, making it capable of evaluating not only the effects of each factor by itself, but also the effects of interactions between them. The effect of a factor can be defined as the response of the output variable due to a change in the level of that given factor.

Assuming a simple experiment as an example, composed of two **factors** ($F = 2$), factor A and B, both varying between two different **levels** ($L = 2$), a lower ($-$) and an upper level ($+$). In this case, there are four combinations between factors and levels, which consequently requires the same number of **test runs** ($N = 4$) to measure all possible output **responses** (Y^{++}, Y^{+-}, Y^{-+}, Y^{--}) as shown in Table 1.4.

Table 1.4: Two-Factor Factorial Experiment Table

Run	A	B	AB	Response
1	$+$	$+$	$+$	Y^{++}
2	$+$	$-$	$-$	Y^{+-}
3	$-$	$+$	$-$	Y^{-+}
4	$-$	$-$	$+$	Y^{--}

Considering that the number of test runs increases exponentially according to the number of factors, this process becomes very costly in cases with large quantities of input variables or a large number of levels. To accommodate experiments with a higher number of factors and/or levels, other methodologies are usually used, keeping the number of test runs within a manageable amount. For starters, a subset of the full

factorial design can be selected, known as a fractional factorial design, by eliminating potentially redundant experiments while trying to focus on the most important features of the problem.

1.4.2 Plackett-Burman Design

The Plackett-Burman design is a method developed to analyse experiments with a high number of factors and/or levels, while using a limited amount of test runs. This is achieved by guaranteeing that the combination of levels (+ +, + -, - +, - -) for any pair of factors appears the same number of times within the design, as exemplified in Table 1.5 [57].

Table 1.5: Plackett-Burman Design with 12 Test Runs for 11 Factors with 2 levels

Run	$\mathbf{F}_1$	$\mathbf{F}_2$	$\mathbf{F}_3$	$\mathbf{F}_4$	$\mathbf{F}_5$	$\mathbf{F}_6$	$\mathbf{F}_7$	$\mathbf{F}_8$	$\mathbf{F}_9$	$\mathbf{F}_{10}$	$\mathbf{F}_{11}$
1	+	+	+	+	+	+	+	+	+	+	+
2	-	+	-	+	+	+	-	-	-	+	-
3	-	-	+	-	+	+	+	-	-	-	+
4	+	-	-	+	-	+	+	+	-	-	-
5	-	+	-	-	+	-	+	+	+	-	-
6	-	-	+	-	-	+	-	+	+	+	-
7	-	-	-	+	-	-	+	-	+	+	+
8	+	-	-	-	+	-	-	+	-	+	+
9	+	+	-	-	-	+	-	-	+	-	+
10	+	+	+	-	-	-	+	-	-	+	-
11	-	+	+	+	-	-	-	+	-	-	+
12	+	-	+	+	+	-	-	-	+	-	-

Following this approach, it is possible to detect the main effects of a large number of factors with only a few dozens of test runs, as opposed to the hundreds necessary when using a full factorial design. That said, working with fewer data points means that interactions between factors are neglected, which makes this method great for screening many factors and narrowing them down before performing a full factorial analysis.

1.4.3 Assessment of Statistical Significance

In order to assess how significantly each factor is capable of affecting the target output response, it is necessary to establish quantifiable values for their effects (Ef), which are defined as the sum of the average responses ($\overline{Y}$) for both the upper level (+) and the lower level (−). Considering a simple two-factor experiment design, as presented

in Table 1.4, the main effects are calculated by Equations 1.8 and 1.9 [58]. The same applies to the effect of the interaction between factor A and factor B, defined in Equation 1.10.

$$Ef_A = \overline{Y_A^+} + \overline{Y_A^-} = \frac{(1) \times Y^{++} + (1) \times Y^{+-}}{2} + \frac{(-1) \times Y^{-+} + (-1) \times Y^{--}}{2} \tag{1.8}$$

$$Ef_B = \overline{Y_B^+} + \overline{Y_B^-} = \frac{(1) \times Y^{++} + (1) \times Y^{-+}}{2} + \frac{(-1) \times Y^{+-} + (-1) \times Y^{--}}{2} \tag{1.9}$$

$$Ef_{AB} = \overline{Y_{AB}^+} + \overline{Y_{AB}^-} = \frac{(1) \times Y^{++} + (1) \times Y^{--}}{2} + \frac{(-1) \times Y^{+-} + (-1) \times Y^{-+}}{2} \tag{1.10}$$

From the effects, it is possible to write a general linear model equation for the predicted response (Y'), considering the halves of the effects ($\frac{Ef_A}{2}$, $\frac{Ef_B}{2}$ and $\frac{Ef_{AB}}{2}$) as the coefficients (C_A, C_B and C_{AB}) for their respective factors and the response average ($\overline{\overline{Y}}$) as the intercept value, elaborated according to the Equation 1.11.

$$Y' = \overline{\overline{Y}} + C_A \times A + C_B \times B + C_{AB} \times AB \tag{1.11}$$

To check the statistical significance of the effects, it is necessary to standardize the prediction coefficients, taking into consideration their standard error (SE), as defined on Equations 1.12. This standardization of the effect turns it on a unit-less value (Ef_{std}) that can be used on a statistical null hypotheses test to verify its significance.

$$Ef_{std} = \frac{C}{SE} \tag{1.12}$$

The coefficient's standard error (SE) is derived from the standard error of the regression (prediction model), which in turn can be calculated from the mean squared error of the residuals (MSE_R) and the sampling size (k), as shown on Equation 1.13

$$SE = \sqrt{\frac{MSE_R}{k}} \tag{1.13}$$

Chapter 2

Musculoskeletal Model

2.1 Lower Extremity Modelling

As previously detailed in Chapter 1.3.3.2, the musculoskeletal model is a digital replica of the human body, capable of recreating a given body movement and determining the muscle and joint forces required to perform it. There are a variety of solutions on the market for simulating musculoskeletal models; this work uses the AnyBody modelling system (software version 7.3) [49].

An open library of musculoskeletal models is available and ready to be used with the AnyBody modelling system, known as the AnyBody Managed Model Repository (AMMR) [48]. This library contains not only customisable human body models, but also application examples of common daily activities.

The full-body plug-in-gait model (AMMR version 2.4.1) from the repository was used, which consists of the Twente Lower Extremity Model 2.1 (TLEM 2.1), developed based on cadaveric anatomical data at the University of Twente in the Netherlands [59], [60]. It is composed of 6 degrees of freedom and 169 segments of muscle, as depicted in Figure 2.1.

The muscles are modelled as multiple separate segments in the AnyBody system, as illustrated in Figure 2.2 for the adductor longus. Consequently, the 23 muscles acting directly on the femur, previously defined in Chapter 1.1.3, are divided into the 122 individual segments detailed in Table 2.1.

Before entering the muscles forces obtained from the musculoskeletal simulation in the finite element model, the 122 individual forces were restored to the original 23 complete muscles, with the aim of reducing the complexity of the model. This was done by calculating the total force of each of the muscles as the sum of the forces of their individual segments, then assigning the total loading to the equivalent surface of origin/insertion of the full muscle.

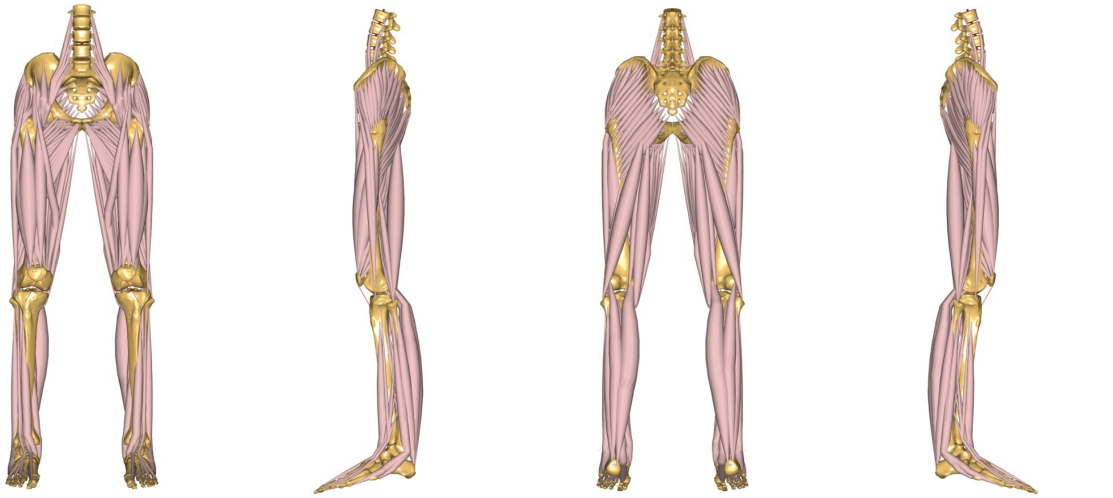

(a) Anterior View **(b)** Left Lateral View **(c)** Posterior View **(d)** Right Lateral View

Figure 2.1: Twente Lower Extremity Musculoskeletal Model TLEM 2.1 [49]

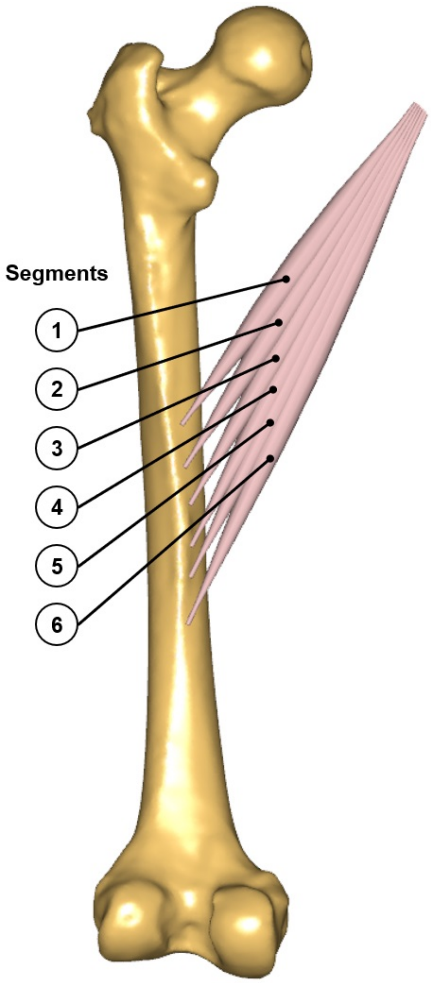

Figure 2.2: Adductor Longus Segmentation

Table 2.1: Femoral Muscles Segmentation

Muscle	Segments
Gluteus Medius	12
Gluteus Minimus	3
Gluteus Maximus	12
Piriformis	1
Iliacus	6
Psoas Major	11
Gemellus Superior	1
Gemellus Inferior	1
Obturator Internus	6
Quadratus Femoris	4
Pectineus	4
Adductor Brevis	6
Adductor Longus	6
Obturator Externus	5
Adductor Magnus	13
Vastus Intermedius	6
Vastus Medialis	8
Vastus Lateralis	8
Biceps Femoris	3
Popliteus	3
Gastrocnemius Medialis	1
Gastrocnemius Lateralis	1
Plantaris	1
Total	122

2.2 Motion Capture Data

In order to estimate the muscle and joint forces acting on the bone for a given body movement, it is necessary to have a motion capture recording of the movement to drive the musculoskeletal model. In this study, an existing human movement database, published by Liang *et al.* (2020) on Nature's open data journal *Scientific Data*, was used [61].

This database is composed of motion capture recordings for seven different human subjects performing multiple simple body movements. The participants were a mix of healthy male and female subjects with no prior neurological or medical conditions, as detailed in Table 2.2.

Table 2.2: Participants Demographics and Anthropometrics [61]

Participant	**1**	**2**	**3**	**4**	**5**	**6**	**7**
Age	41-50	41-50	61-70	21-30	31-40	31-40	51-60
Gender	Male	Female	Female	Male	Male	Male	Male
Mass (kg)	69.9	52.9	59.0	75.1	60.2	65.4	77.3
Height (m)	1.81	1.64	1.61	1.82	1.66	1.69	1.78

When importing the data to be used with the AMMR musculoskeletal model, some adjustments were necessary to guarantee compatibility. Mainly, the marker placement protocol was adapted, the force plate configuration was altered, and gravity direction was reoriented.

The marker protocol used for these recordings follows a placement set that contains 84 markers, detailed in Figure 2.3. While the marker placement of the AMMR musculoskeletal model [48] is based on the Vicon Plug-In Gait protocol [62], consisted of only 40 markers, as detailed in Figure 2.4.

To ensure compatibility between both protocols, an equivalent correlations was created, containing 36 points, where the markers non-existent on AnyBody were deactivated. Active and inactive markers are represented in Figure 2.5, in darker and lighter shades, respectively.

Lastly, Anybody's AMMR musculoskeletal model is configured by default with three type 4 force plates, which are capable of measuring the forces and moments in each direction (X, Y, and Z). The data set, on the other hand, was recorded using two type 3 force plates, which measures a combinations of X, Y, and Z forces at eight different points of the plate. However, since the mocap framework of AnyBody supports all force plate types (1-4), the model can be easily configured to work with the motion capture recordings from Liang *et al.*.

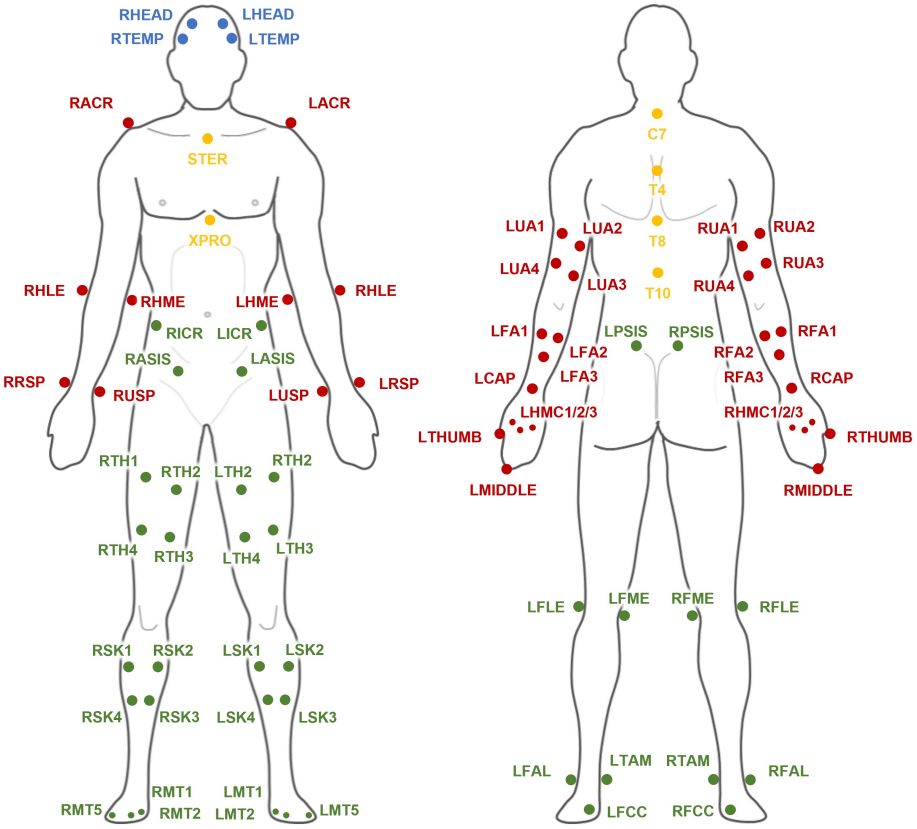

Figure 2.3: Liang *et al.* Marker Protocol

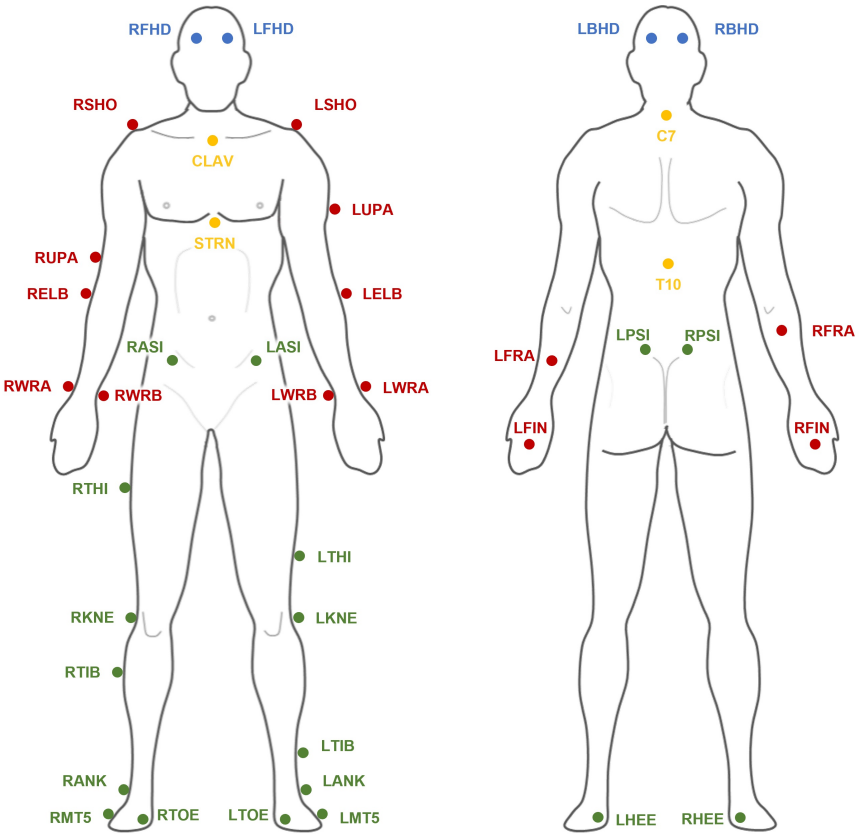

Figure 2.4: AnyBody Marker Protocol

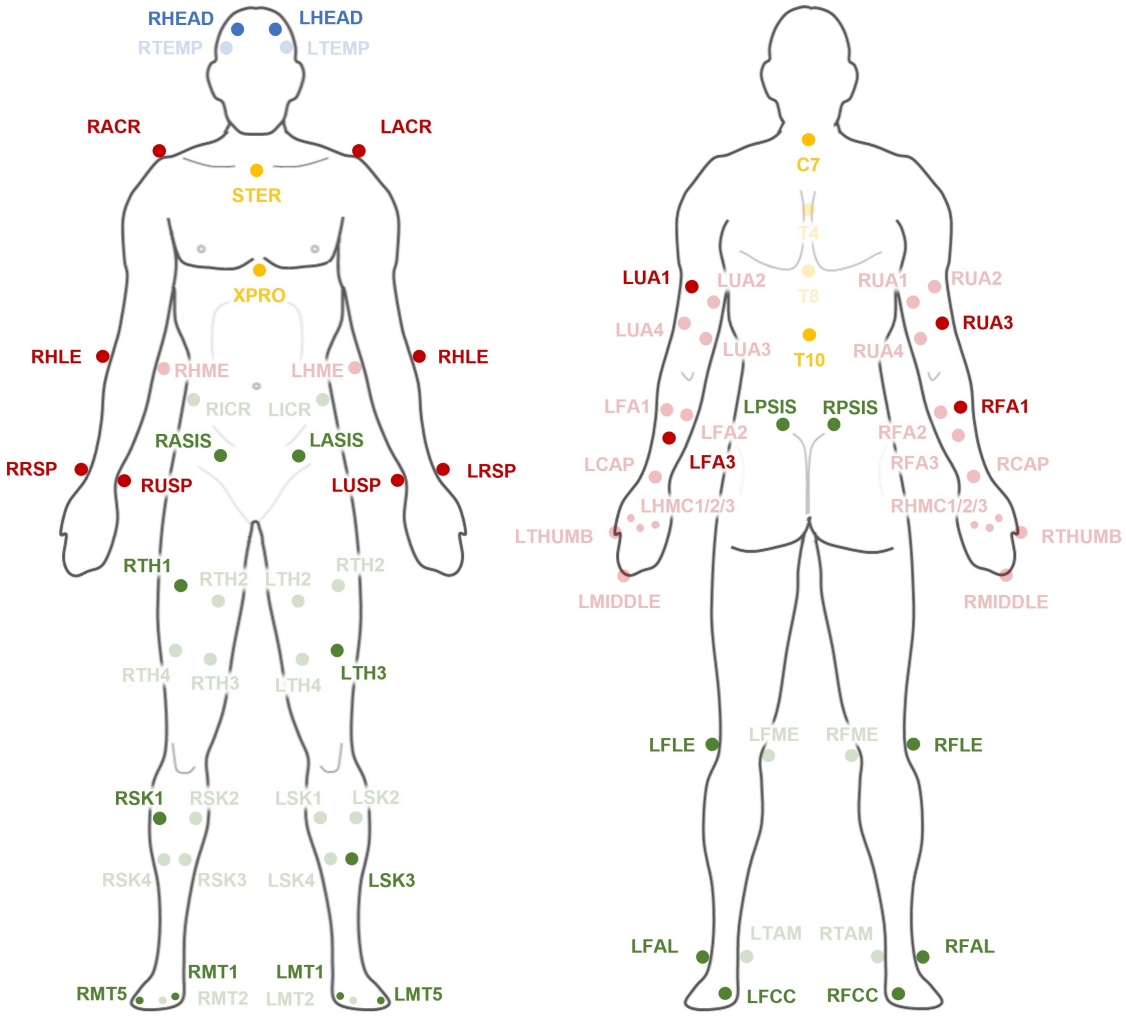

Figure 2.5: Equivalent Marker Placement

2.2.1 Movement Scenarios

When trying to meticulously recreate the physiological conditions of a fractured bone, it is important to take into account the different loading scenarios it might be under. These loading cases that the bone undergoes on a daily basis are defined by the body movements that are being performed. Considering postoperative patients, it is a reasonable assumption that their main daily activities can be summarised into simple actions such as walking, climbing stairs, and sitting.

The walking motion is simply defined by one cycle of normal gait, however the sitting action involves the motion of sitting down and standing up, illustrated on 2.6. Similarly, stair climbing can be subdivided into four different motions, as the act of stair walking not only encompasses moving up and down the stairs, but also differs if the movement is led by the right or left leg, as shown in Figure 2.7. Thus, the three defined movement scenarios (walking, sitting and stair climbing) were subdivided into the following seven body motions to be analysed:

- **Walking Scenario**
  - Normal Gait (NG)
- **Sitting Scenario**
  - Sitting Down (SD)
  - Standing Up (SU)
- **Stair Climbing Scenario**
  - Left Step Up (LSU)
  - Right Step Up (RSU)
  - Left Step Down (LSD)
  - Right Step Down (RSD)

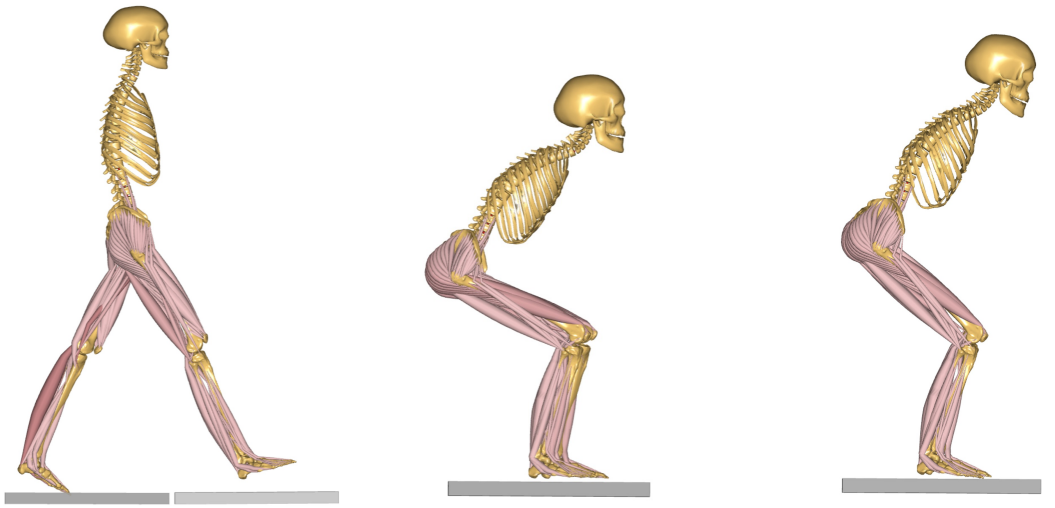

(a) Normal Gait **(b)** Standing Up **(c)** Sitting Down

Figure 2.6: Motion Subdivisions of Walking and Sitting Movement Scenario

(a) Left Step Up **(b)** Left Step Down **(c)** Right Step Up **(d)** Right Step Down

Figure 2.7: Motion Subdivisions of Stair Climbing Movement Scenario

2.3 Simulation Results

In order to take into account the results from the musculoskeletal simulations of all human subjects, an average set of muscle and joint forces must be estimated. However, since these results are temporal series and each subject has its own cadence of movement, they vary in length and do not align. Therefore, averaging them together in that way would result in misleading results.

When repeating a body movement, there is always a difference from one motion to another, that being in trajectory, speed, or rhythm. However, similarities between each motion exist and a repeatable pattern can be identified, even if they do not temporally align [63].

2.3.1 Time Series Matching

A common practice applied while studying time series that vary due to difference speed between samples, such as in the field of speech recognition, is to distort one temporal series to match another. Dynamic Time Warping (DTW) is a well-known algorithm that identifies similar patterns between temporal series and then aligns them by minimising the Euclidean distance of the original signals to warp them into alignment [64].

Using the computing platform MATLAB, a subroutine can be created to average together into a single set of forces the muscle and joint loads estimated by the musculoskeletal simulations of each human subject, using the DTW function. The averaging of all muscle and joint forces for the Normal Gait motion is presented in Figures 2.8. The results of all the additional movement scenarios are included in the Appendices, where Figures A.1, A.9, A.17, A.25, A.33, A.41 present the average forces plots for the respective motions of Sitting Down, Standing Up, Left Step Up, Right Step Up, Left Step Down and Right Step Down.

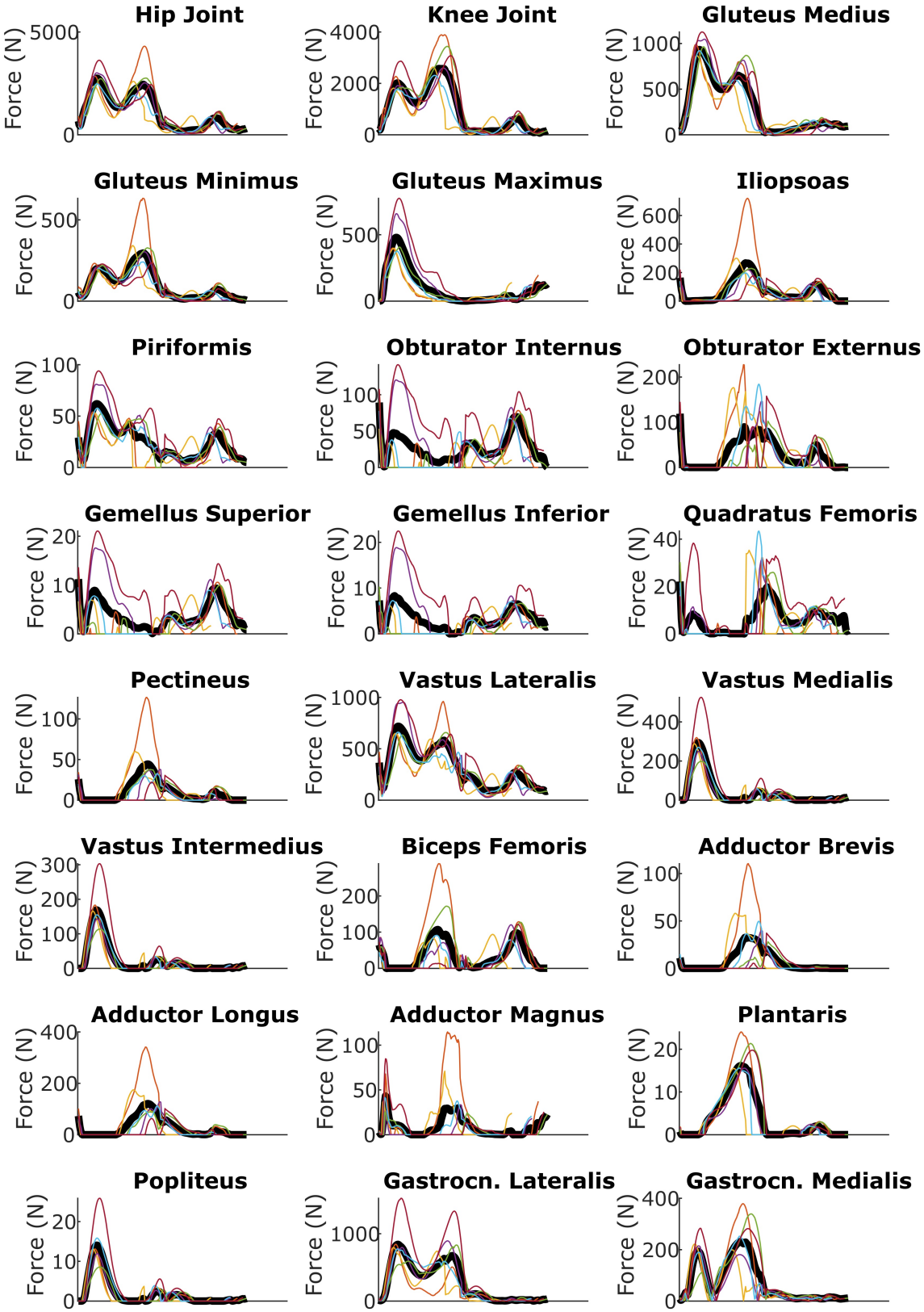

Figure 2.8: DTW Averaging of Normal Gait Forces

2.3.2 Validation

Considering that muscle forces cannot be measured directly, there are no empirical values to compare against and consequently validate the estimations from the musculoskeletal simulations. Joint forces, on the other hand, have been measured, as previously detailed in Section 1.3.2. Therefore, by verifying the results of the calculated joint forces, the overall musculoskeletal model can be validated.

As a reference point, the hip joint contact force estimated for each movement by the musculoskeletal simulations was compared to the empirical measurements gathered in vivo by the OrthoLoad project described in Section 1.3.2 [44]. The comparison was done to the data collected from subject H7R, using the files H7R_221113_1_162 for the walking scenario, H7R_140912_1_55 for the sitting scenario and H7R_300615_1_35 for the stair climbing scenario.

Observing the comparison graphs presented in Figures 2.9, 2.10, 2.11, it is possible to notice that the hip joint contact for both the simulations and the references (OrthoLoad data) follows a similar profile with comparable magnitudes, showing that the results are within a realistic range.

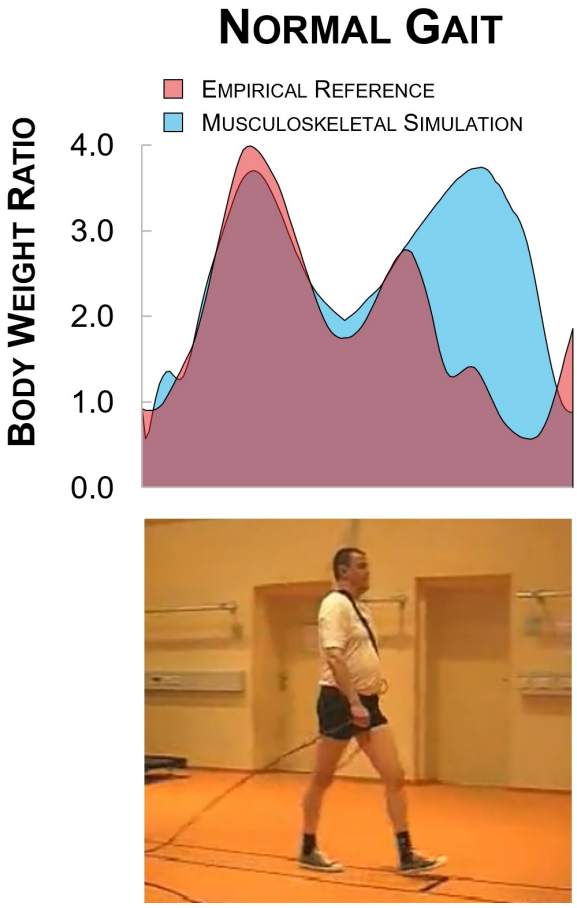

Figure 2.9: Walking Hip Joint Force Validation (H7R_221113_1_162) [44]

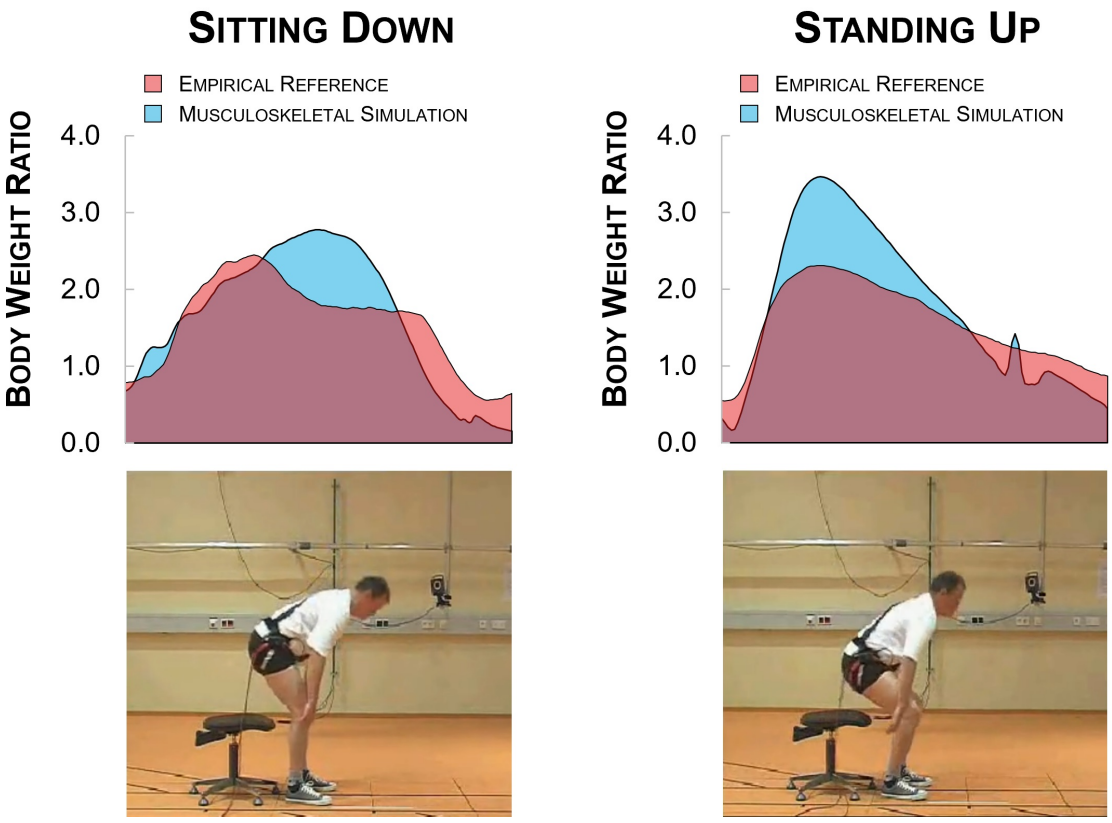

Figure 2.10: Sitting Hip Joint Force Validation (H7R_140912_1_55) [44]

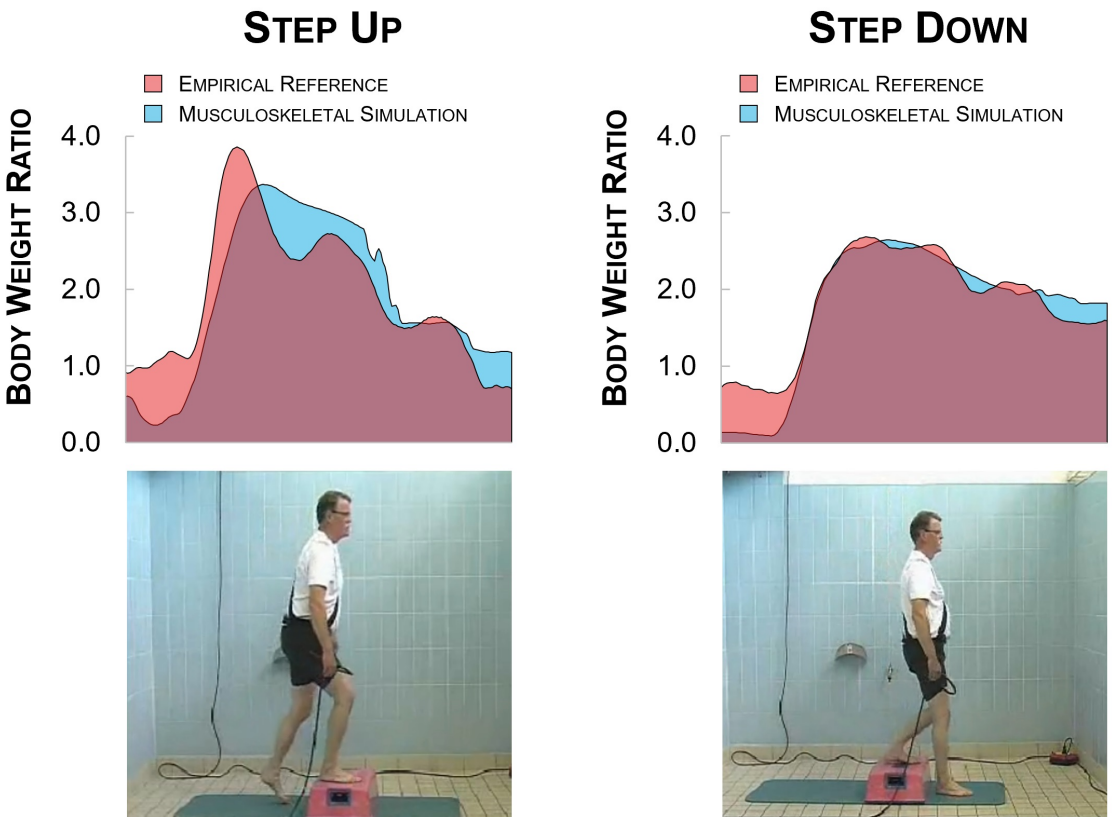

Figure 2.11: Stair Climbing Hip Joint Force Validation (H7R_300615_1_35) [44]

Chapter 3

Finite Element Simulation

The finite element model of the femur was created based on computed tomography scan images of artificial bones and forces estimated with the musculoskeletal model, using Ansys Workbench (software version 2021 R1) [65]. The materials were modelled as isotropic and homogeneous, following the methodology detailed in Section 1.3.4.2 and using the material properties of Section 1.3.1.2.

For each movement scenario defined in Section 2.2.1, a different simulation was created. By discretising the simulations into multiple steps, with varying muscle and joint forces, the stress results covered the complete cycle of each movement scenario. Once the whole movement is simulated, the position where peak stresses occur can be identified.

3.1 Geometry

The artificial bones used in this work were the medium-size left femur with a cancellous core of 17 PCF (pound per cubic foot) and an intramedullary canal of 13 mm (catalogue number #3403), to represent non-osteoporotic patients, shown in Figure 3.1. While an osteoporotic version with a thinner cortical shell, a 10 PCF cancellous core, and an intramedullary canal of 16 mm (catalogue number #3503) can be used to represent patients with osteoporosis, as depicted in Figure 3.2.

Figure 3.1: Sawbones Medium Femur #3403 [43]

Figure 3.2: Sawbones Osteoporotic Medium Femur #3503 [43]

Both bones were CT scanned using a slice thickness of 0.7 mm and an image matrix of 512 x 512 pixels with an in-plane spatial resolution of approximately 0.41 mm x 0.41 mm, show in Figure 3.3. The images were processed using InVesalius software [66], which allows the recreation of the bone geometry as a 3D model in stereolithography format (STL) using image segmentation, as presented in Figure 3.4.

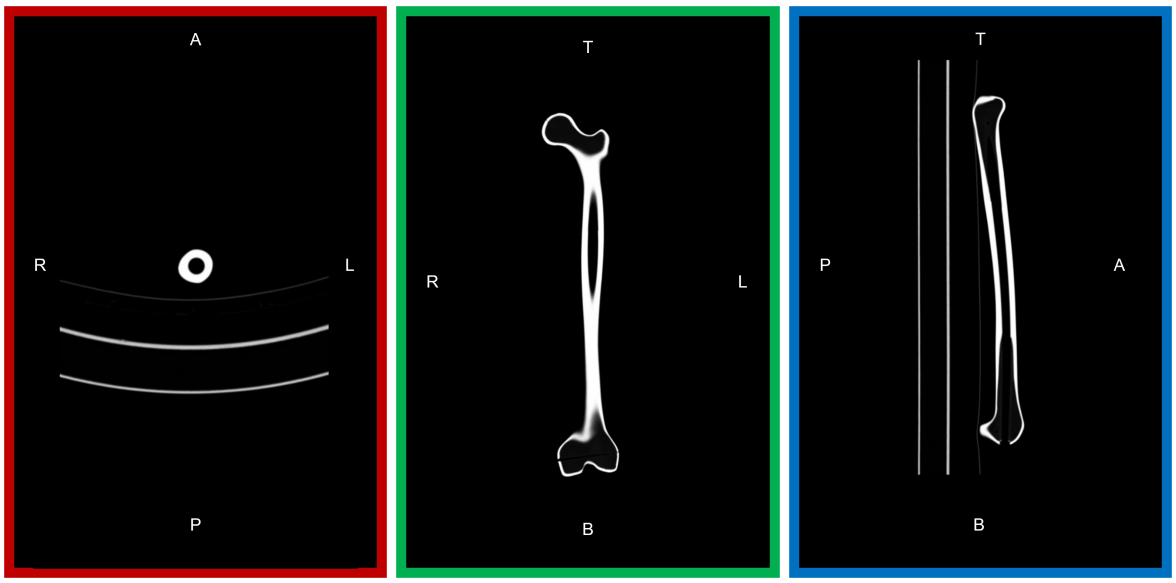

(a) Transverse Plane **(b)** Coronal Plane **(c)** Sagittal Plane

Figure 3.3: CT Scan Images of the Femur

The surface of 3D models generated from the segmentation process is not smooth and presents many imperfections inherent to the resolution and voxel nature of the scan. Geometry clean-up was performed using the modelling software Meshmixer [67], resulting in a smoother and high-fidelity 3D mesh of the physical bone, as shown in Figure 3.5a.

Nevertheless, the STL model is still composed of a triangular mesh and, consequently, it is not truly smooth. Using this faceted geometry to create the FE model is inconvenient, as it limits the manipulation of the surface and makes meshing more difficult. Thus, this geometry was converted into a spline-based model using Non-Uniform Rational B-Spline (NURBS) in the 3D modelling software SpaceClaim [68], depicted in Figure 3.5b.

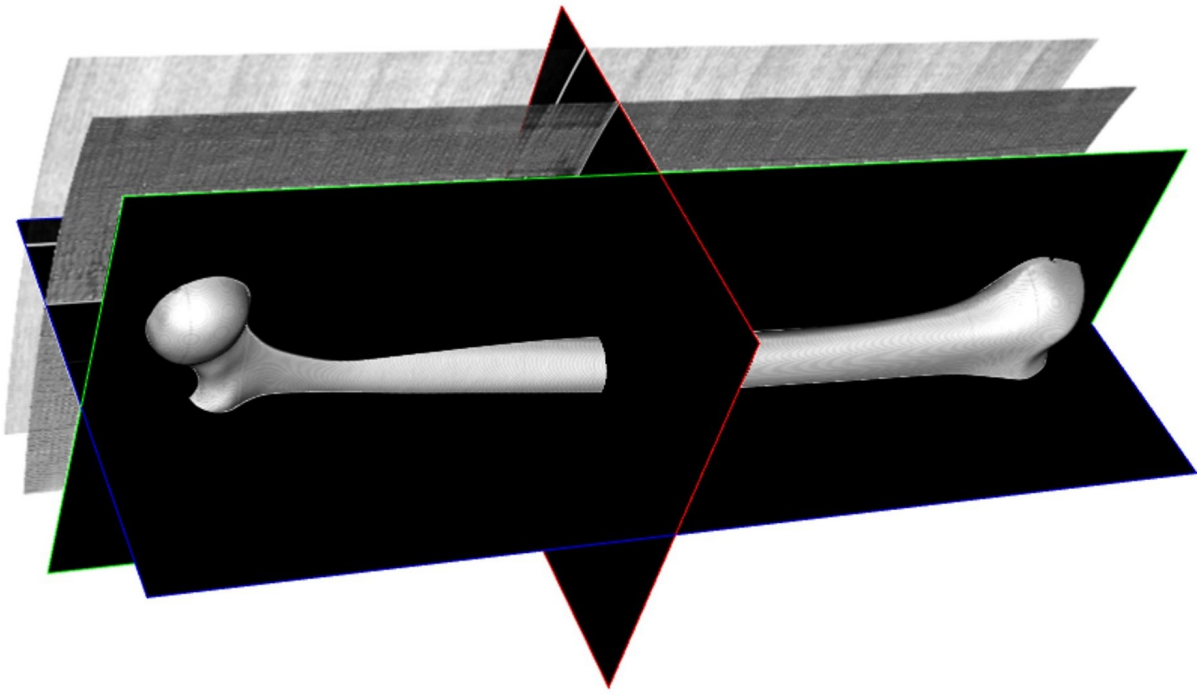

Figure 3.4: 3D Geometry from CT Scan Segmentation

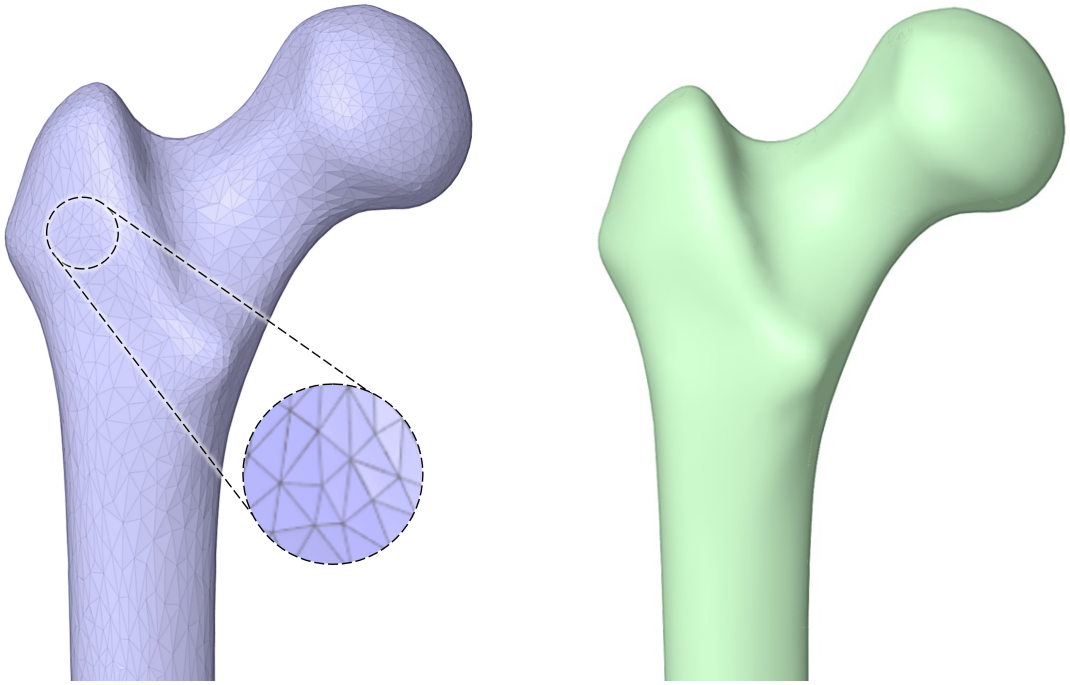

(a) STL Faceted Geometry **(b)** NURBS Geometry

Figure 3.5: Process of Geometry Creation

Finally, the cortical and trabecular portions of the femur geometry are included in the FE model as two separate bodies interfaced by bounded contact and meshed, as shown in Figure 3.6. Then, each body is assigned its respective material properties and meshed, as shown in Figure 3.7

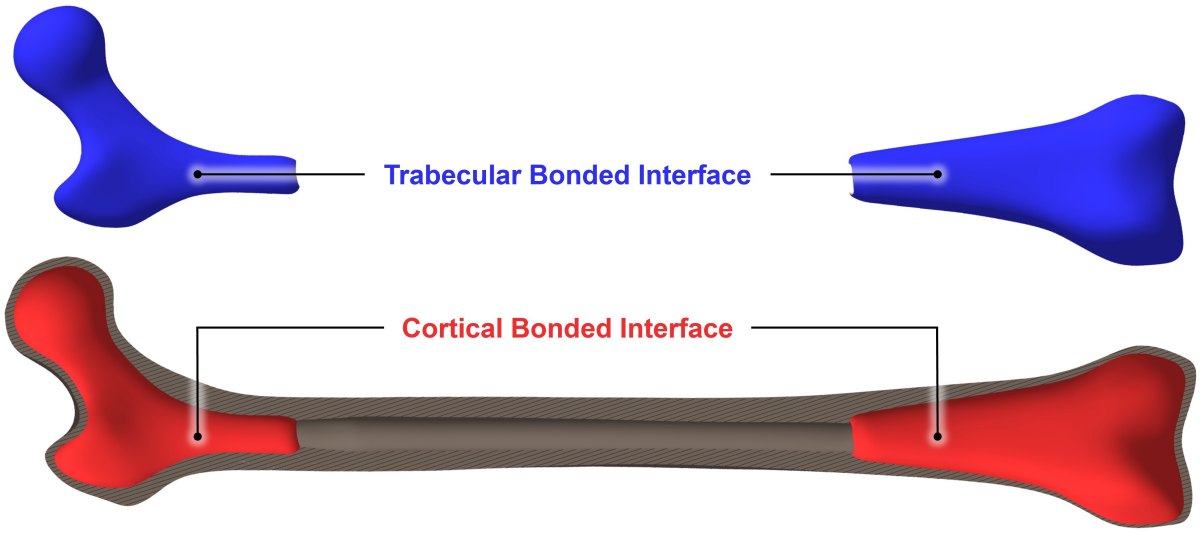

Figure 3.6: Bonded Contact Surfaces

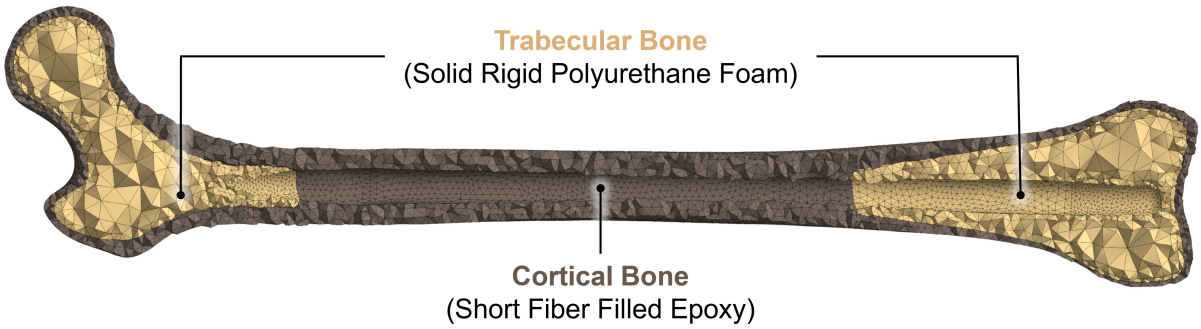

Figure 3.7: Finite Element Mesh

3.2 Boundary Conditions

The model was constrained by creating a spherical joint at the articulation point of the knee, locking the translation of the body in all directions. This was achieved using three stiff springs ($10^6\ N/mm$) to remotely attach the surface of the meniscus to the environment, at the centre of rotation of the knee, as presented in Figure 3.8. In addition, another set of springs was added to limit the potential rotation of the body and stabilise the system. These weak springs ($100\ N/mm$) were attached to a short section of the inner surface of the medullary cavity to the environment, detailed in Figure 3.8.

The muscle and joint forces calculated by the musculoskeletal simulation are then applied to an estimated area of their respective origin or insertion points on the surface of the femur, following anatomical drawings as reference [5], [6], [69], [70], as represented in Figures 3.9 for the Normal Gait motion.

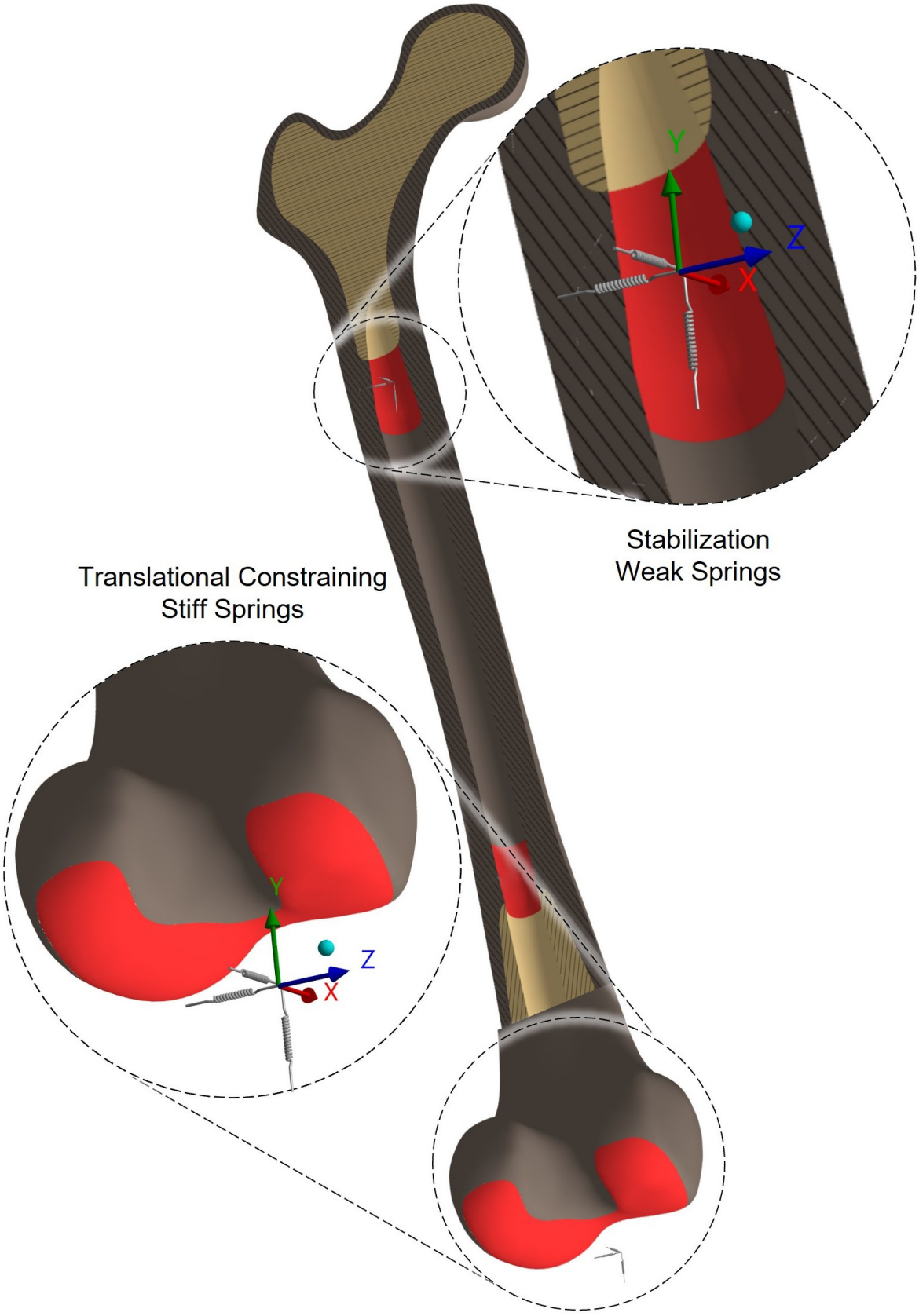

Figure 3.8: Detail of Constraining Springs

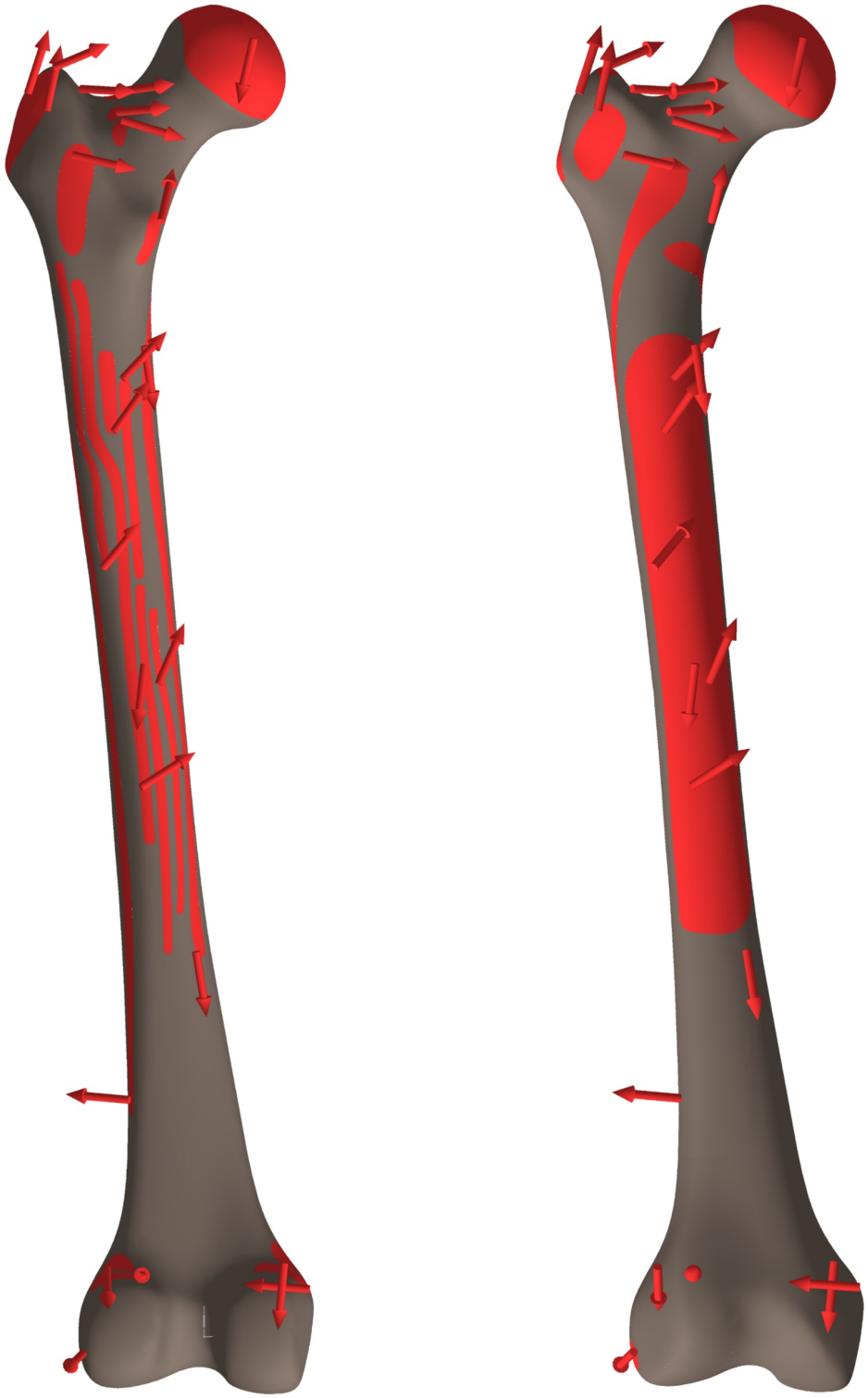

(a) Posterior View **(b)** Anterior View

Figure 3.9: Normal Gait Scenario Forces

The boundary conditions of all the additional movement scenarios are included in the Appendices, where Figures A.2, A.10, A.18, A.26, A.34 and A.42 detail the inputted forces of the respective motions of Sitting Down, Standing Up, Left Step Up, Right Step Up, Left Step Down and Right Step Down.

3.3 Simulation Results

The inverse dynamics simulation performed using the musculoskeletal model is capable of estimating the joint and muscle forces acting on the femur throughout the complete cycle of each body movement scenario. Therefore, the forces applied to the finite element model can be discretized into multiple time steps, covering the whole range of each motion, providing a glance at the progression of the stress state throughout the full cycle.

By examining the principal stresses generated in the proximal region of the femur, the position in the movement cycle can be identified when the peak condition occurs. For the movement scenario of Normal Gait, peak stresses are observed right before the heel strike of the leading leg, when the entire body weight is supported by the back leg, shown in Figure 3.10.

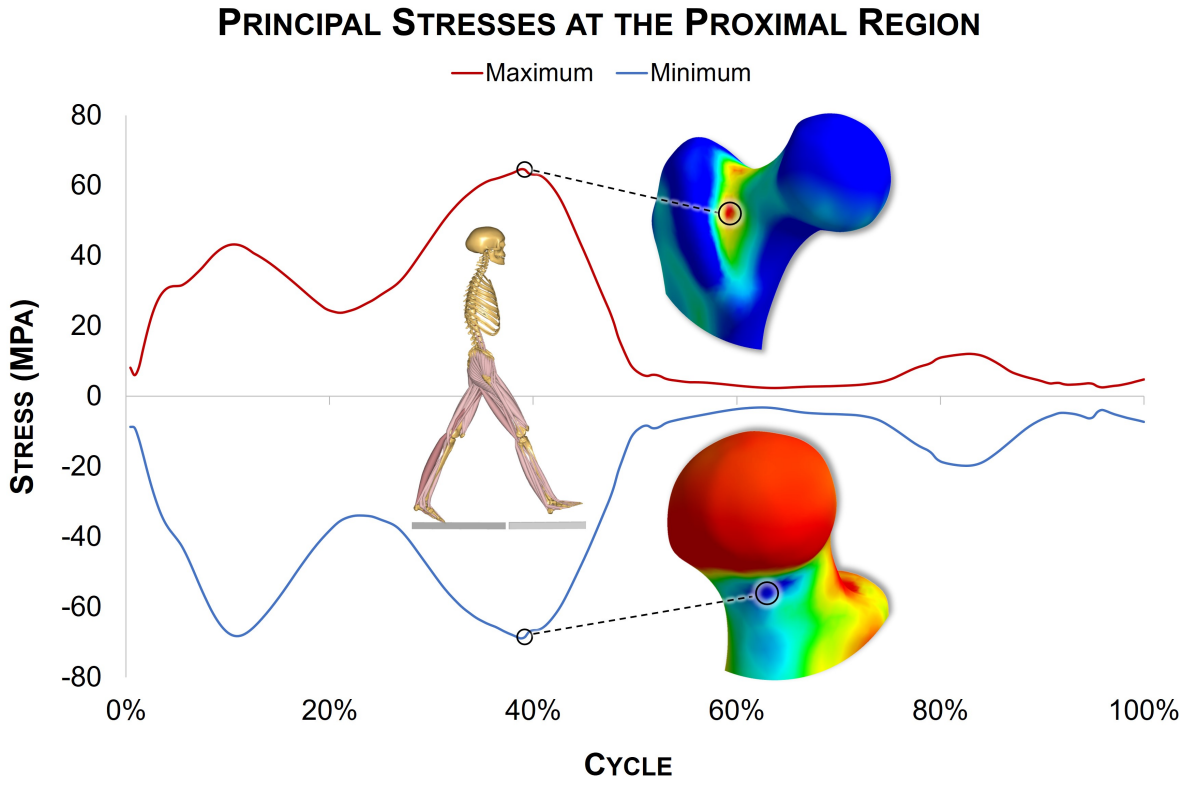

Figure 3.10: Position of Peak Stresses of the Normal Gait Movement Cycle

For the sitting scenario, both the motion of Standing Up and Sitting Down display peak stresses at a similar position, which happens at the midway point between fully seated and straight up. These results are shown in Figures 3.11 and 3.12 for Standing Up and Sitting Down respectively.

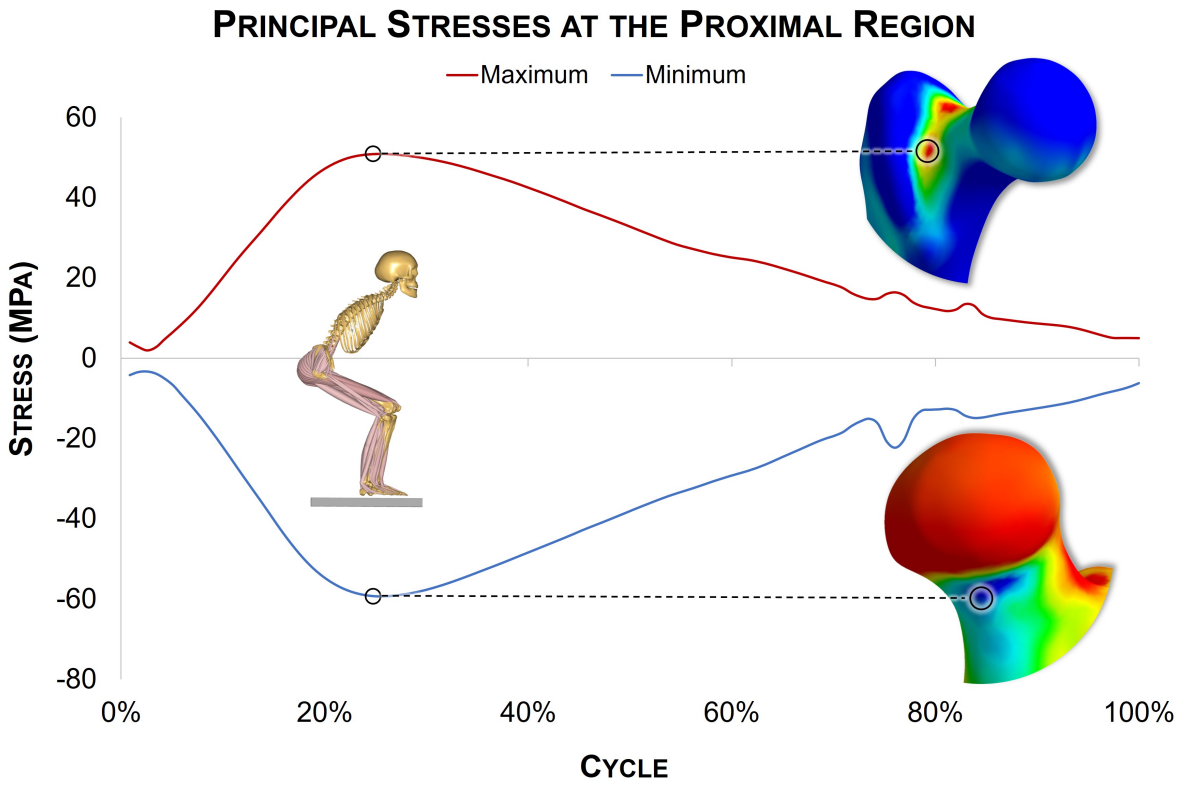

Figure 3.11: Position of Peak Stresses of the Standing Up Movement Cycle

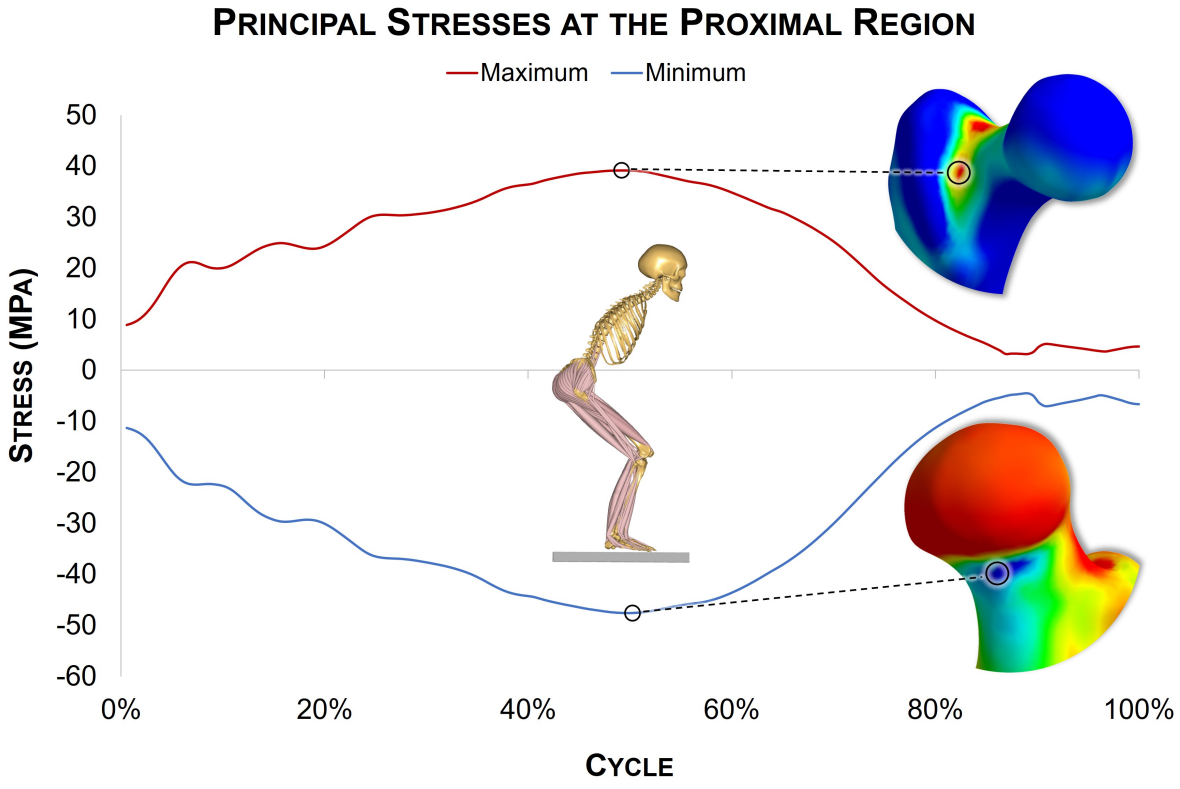

Figure 3.12: Position of Peak Stresses of the Sitting Down Movement Cycle

In the stair climbing scenario, the position of peak stresses will depend on the leg leading the motion since the analysis is always done focusing on the left leg. Therefore, peak stresses happens when the body weight is being solely supported by the left leg. For Left Step Up, peak condition is observed when the right leg leaves the lower step, while for Right Step Up it happens slightly before the right leg touches the step above, as shown in Figures 3.13 and 3.14 respectively.

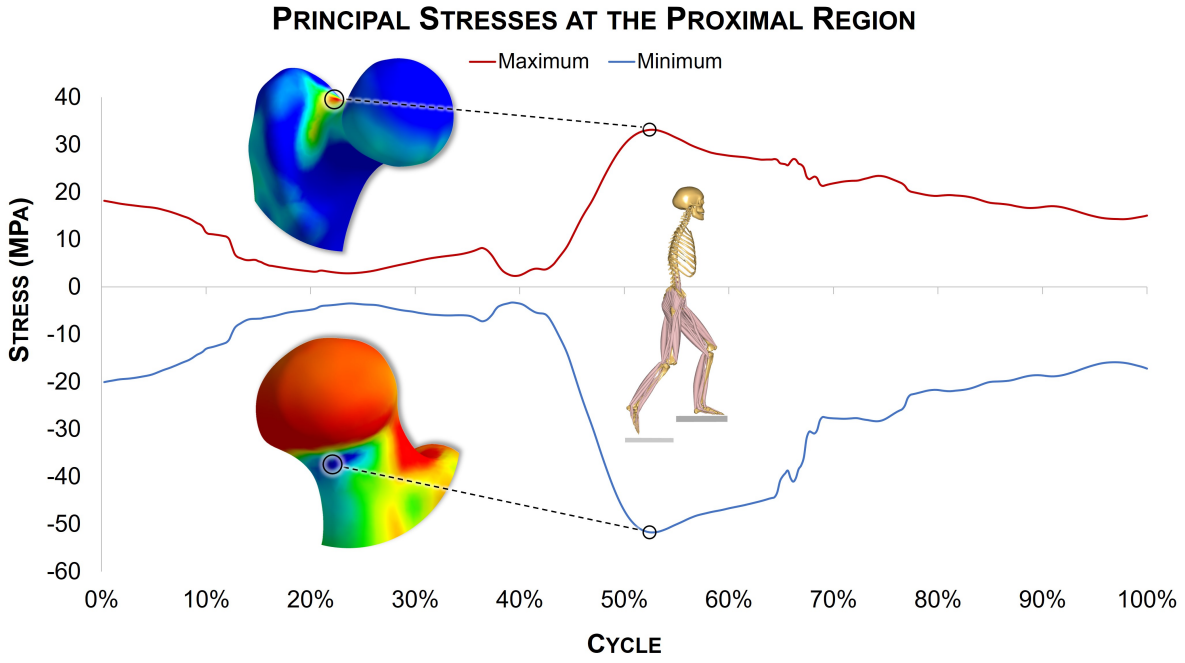

Figure 3.13: Position of Peak Stresses of the Left Step Up Movement Cycle

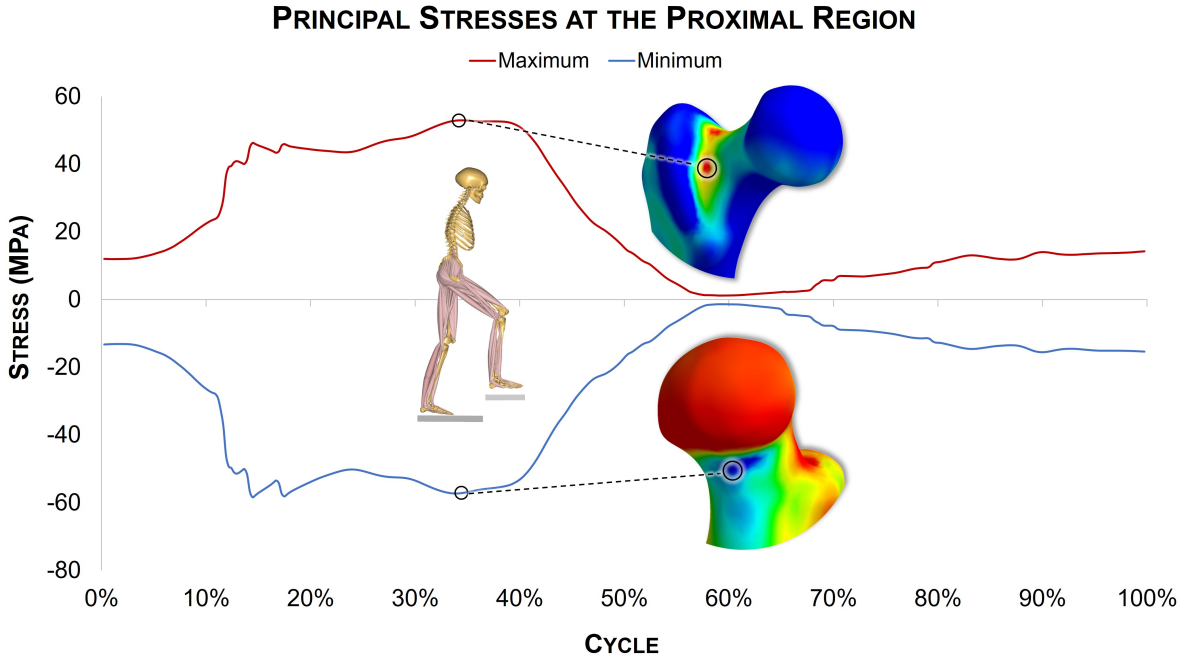

Figure 3.14: Position of Peak Stresses of the Right Step Up Movement Cycle

Similarly, during Left Step Down, the highest stresses are noticed when the left leg is supporting the complete weight of the body as the right leg leaves the step behind, presented in Figure 3.15. Finally, for the Right Step Down motion, the peak condition happens slightly before the right leg touches the step below, shown in Figure 3.16.

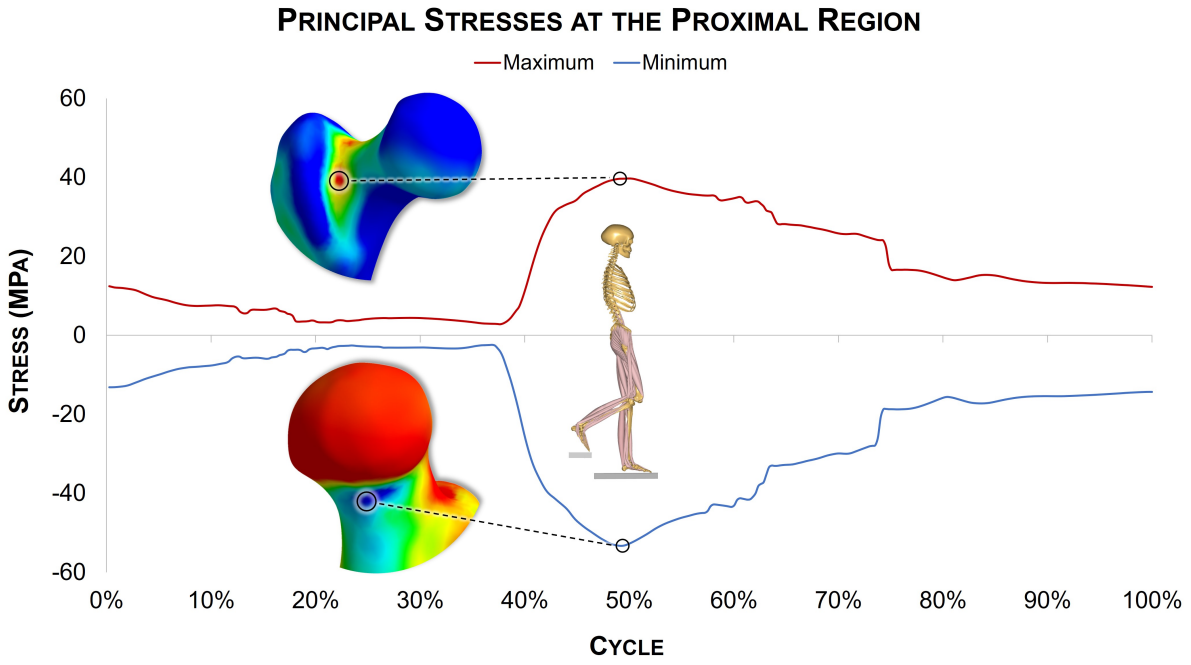

Figure 3.15: Position of Peak Stresses of the Left Step Down Movement Cycle

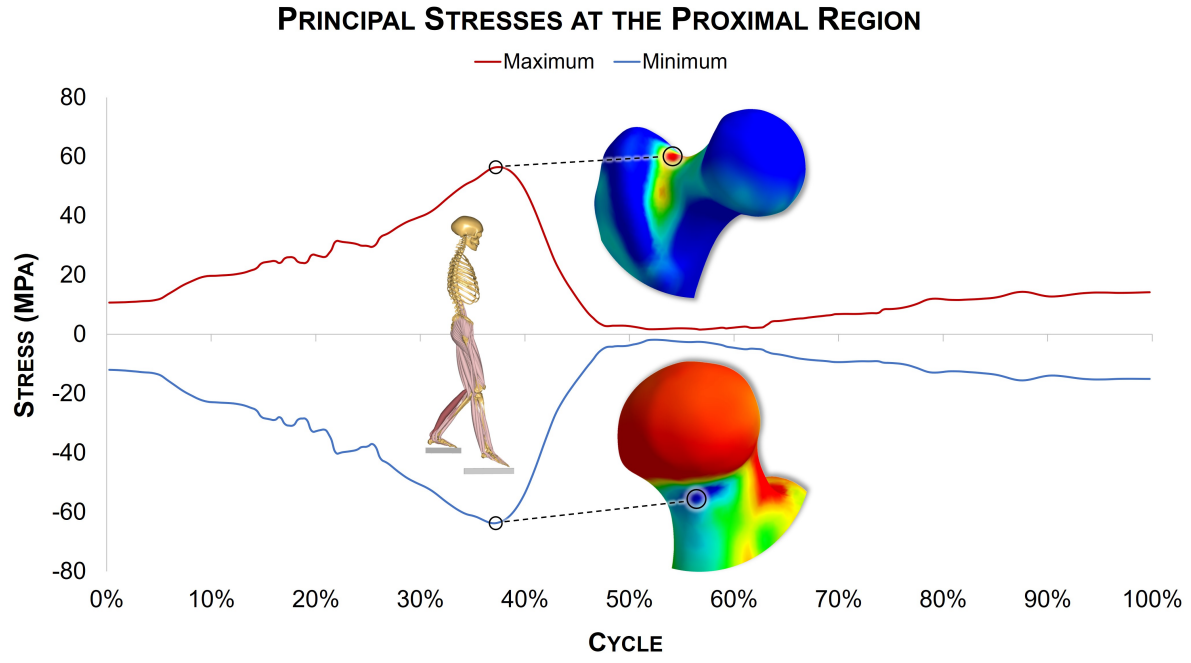

Figure 3.16: Position of Peak Stresses of the Right Step Down Movement Cycle

Observing the stress profiles generated at the position of peak condition for all the movement scenarios, presented in detail in Figures 3.17, 3.18, 3.19, 3.20, 3.21, 3.22 and 3.23, it is noticeable that the stress states follow a very similar pattern around the proximal region of the femur.

When analysing the maximum principal stresses, the hotspot is distributed at the Basicervical region of the femoral neck. The peak minimum principal stresses are concentrated below the medial most side of the femoral head, at the Subcapital region. Considering that the most significant load on the femur is the hip joint contact force, acting downwards at the femoral head, these results are logical. The overwhelming vertical force applied to the head should generate compression below the head while tensile stresses rise at the opposite extremity of the neck.

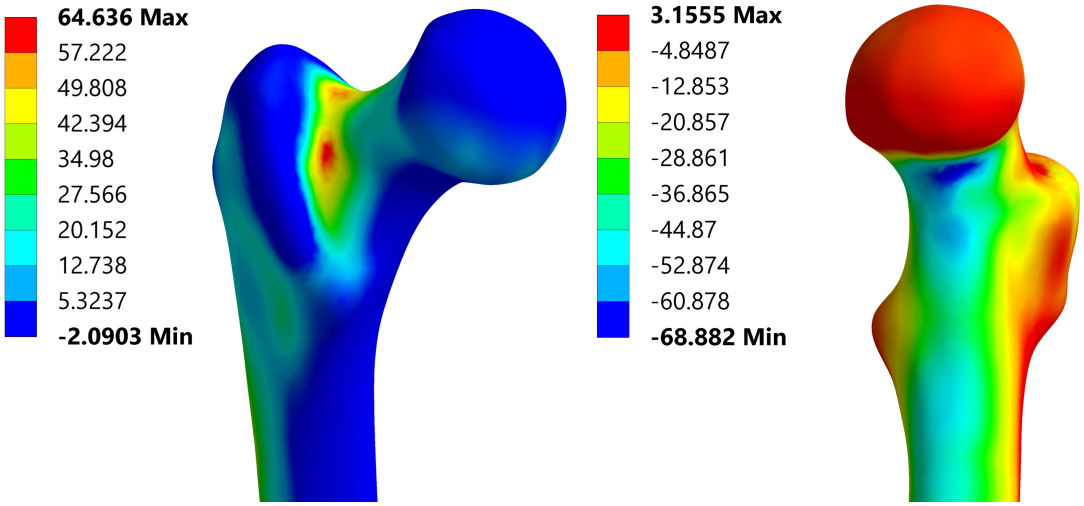

(a) Maximum Principal Stress **(b)** Minimum Principal Stress

Figure 3.17: Normal Gait Peak Principal Stresses

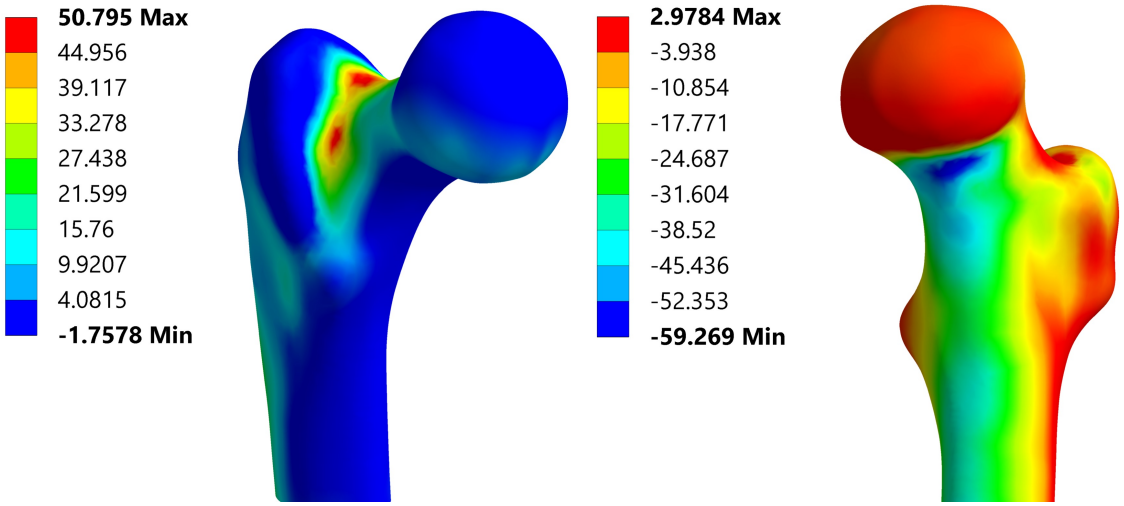

(a) Maximum Principal Stress **(b)** Minimum Principal Stress

Figure 3.18: Standing Up Peak Principal Stresses

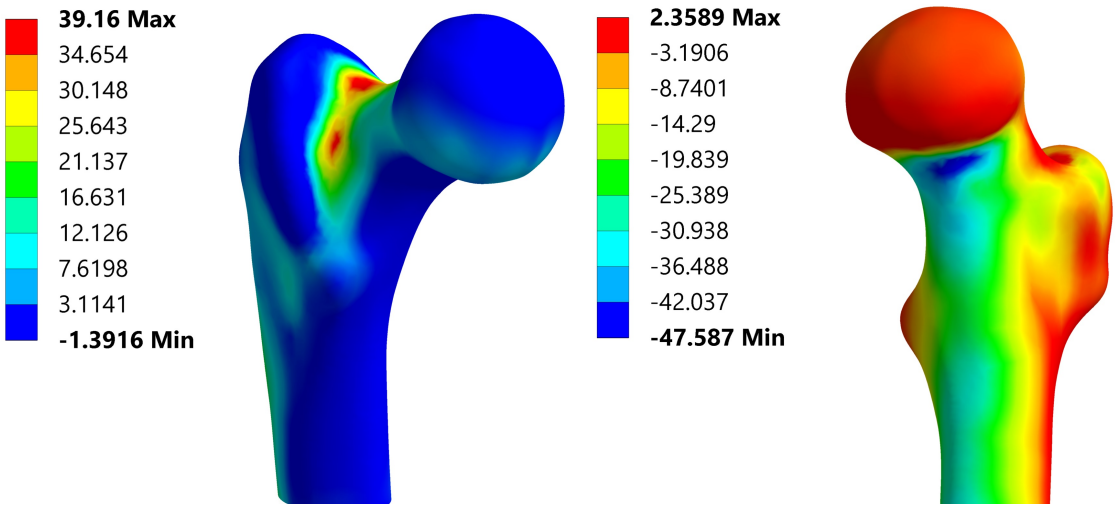

(a) Maximum Principal Stress **(b)** Minimum Principal Stress

Figure 3.19: Sitting Down Peak Principal Stresses

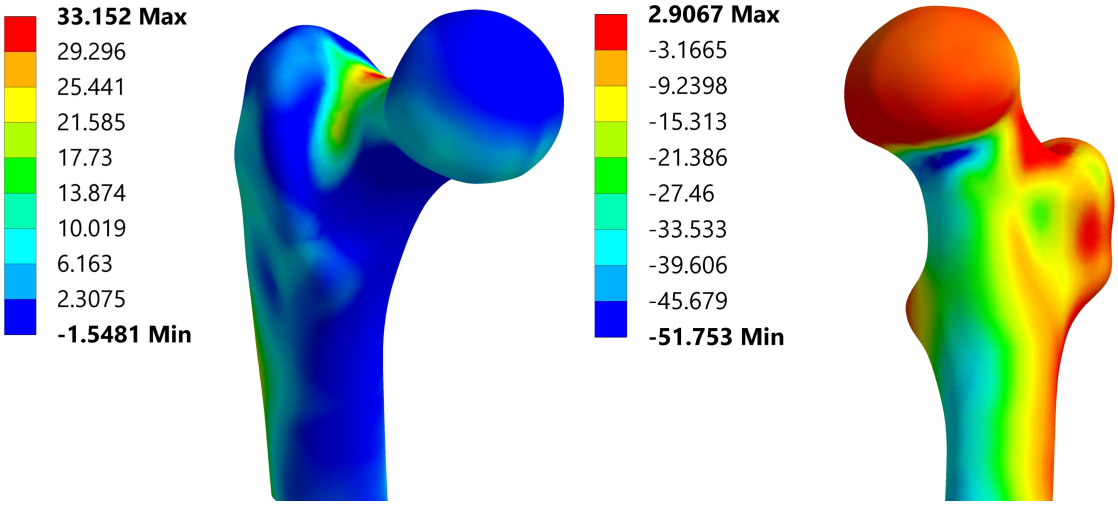

(a) Maximum Principal Stress **(b)** Minimum Principal Stress

Figure 3.20: Left Step Up Peak Principal Stresses

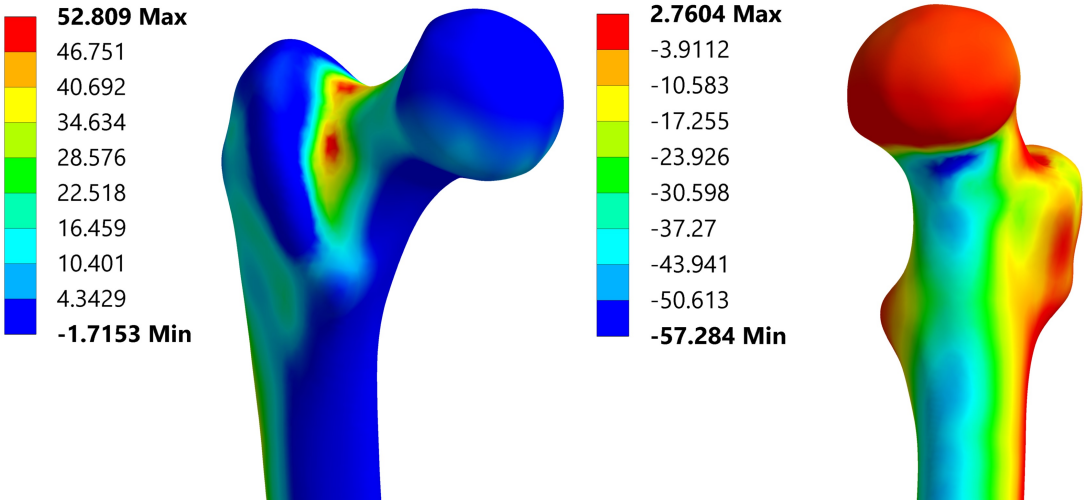

(a) Maximum Principal Stress **(b)** Minimum Principal Stress

Figure 3.21: Right Step Up Peak Principal Stresses

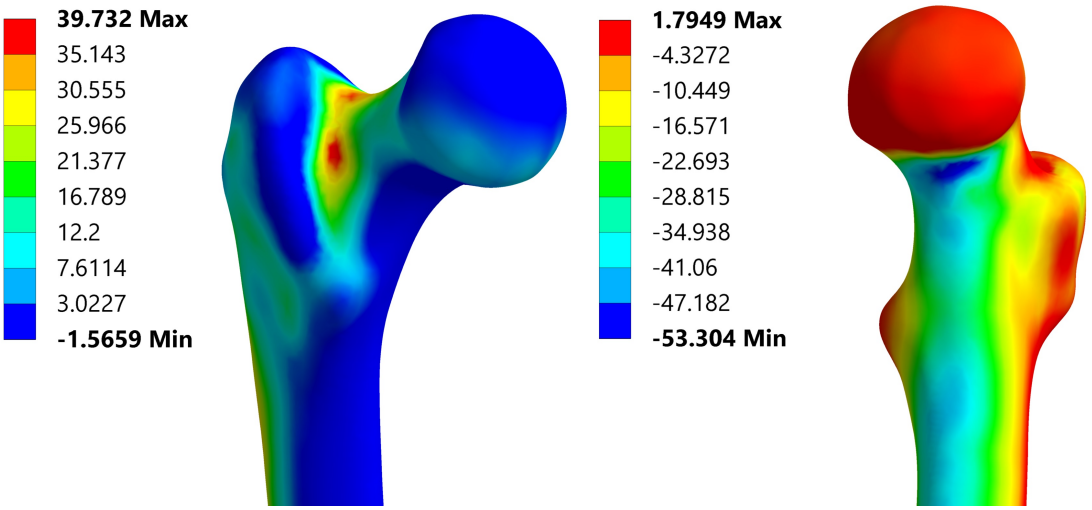

(a) Maximum Principal Stress **(b)** Minimum Principal Stress

Figure 3.22: Left Step Down Peak Principal Stresses

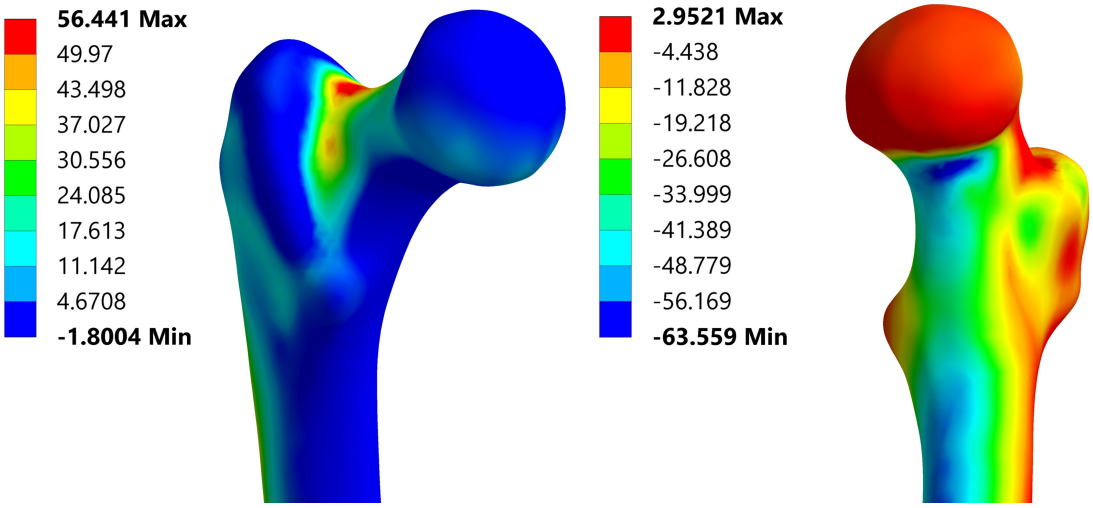

(a) Maximum Principal Stress **(b)** Minimum Principal Stress

Figure 3.23: Right Step Down Peak Principal Stresses

Chapter 4

Force Significance Study

There are 23 muscles that act directly on the femur, as detailed in Section 2.1, and recreating this complex loading condition within an experimental setting is unrealistic. Thus, a simplified loading configuration that can be replicated in the laboratory and is also capable of generating an equivalent mechanical behaviour needs to be defined.

Compared to hip joint force, the most dominant load acting on the proximal femur, the contribution of the muscles is not as impactful. This fact is noticeable in the literature, since most biomechanical tests of the proximal femur disregard all force inputs from the muscles, as discussed in Section 1.3.4.3. However, an analysis should be performed to verify the magnitude of the impact that omitting muscle forces could have on the accuracy of the results of the experimental tests.

This process could be done manually using trial and error, by simply running several simulations while varying the input forces and observing their effect on the output. But due to the high number of variables and possible permutations, a more systematic method is desirable. Therefore, a multi-step statistical study was performed, composed of a preliminary factorial analysis to identify the most relevant forces and a subsequent detailed factorial analysis focusing on the relevant forces.

This study was performed using the DOE tools from the statistical analysis program Minitab (software version 22.3), to create several factorial designs capable of correlating variation of input factors to their respective effect on output variables [71].

4.1 Study Parameters

The preliminary factorial analysis was established considering each force source as a factor that varies between two levels, active or inactive, thus not modifying the directions of the forces, only their magnitudes. The responses of the study, selected to be observed as the affected output of the input factor variation, were the sectional forces and moments at the fracture region.

This region was defined as a sectional cut of the proximal femur, representing an internal surface of an average pertrochanteric fracture, as illustrated in Figure 4.1a. The sectional cut was based on a 3D mapping of fracture lines [72], shown in Figure 4.1b.

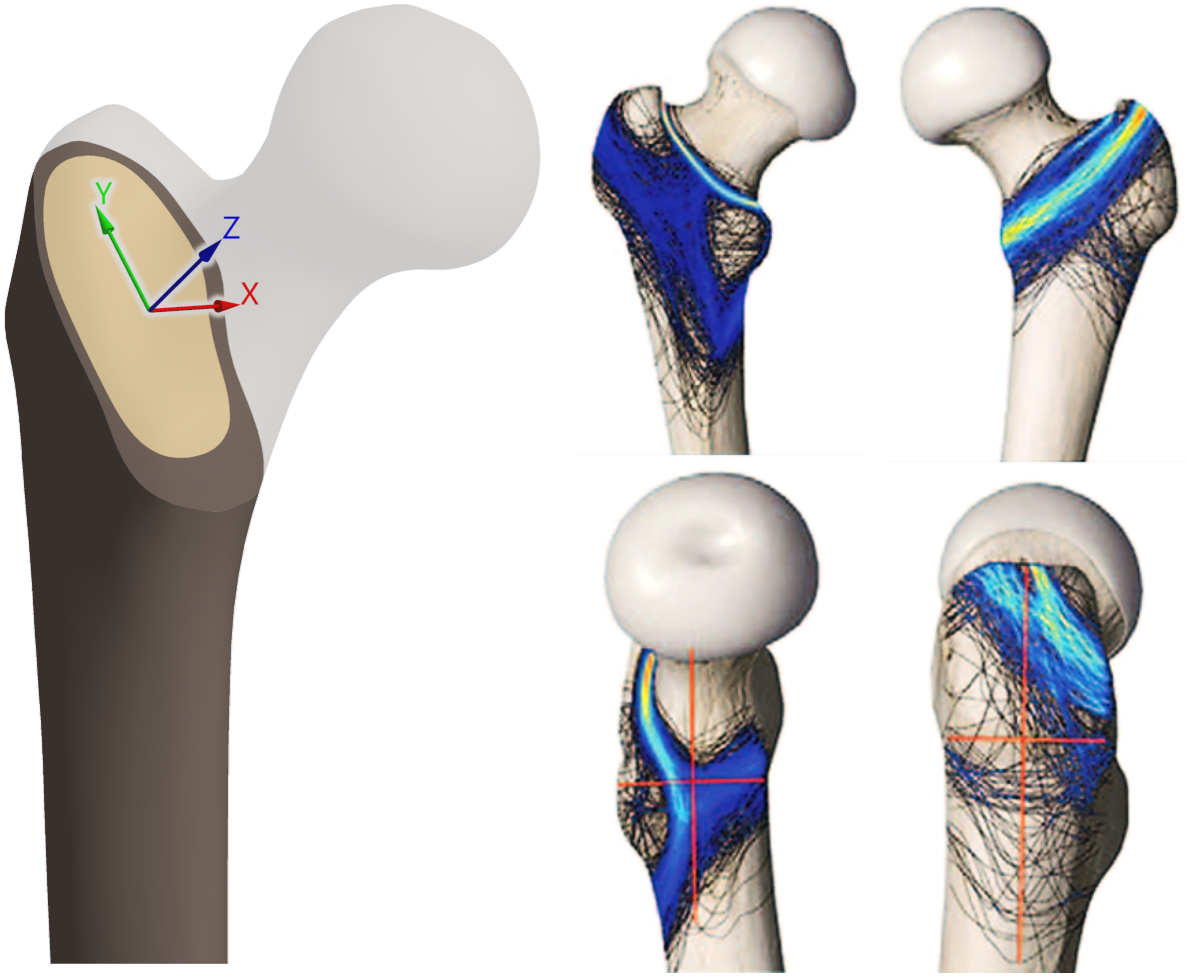

(a) Fracture Section Analysed **(b)** Fracture Line Mapping [72]

Figure 4.1: Definition of the Average Fracture Section

Since the region of interest is located at the proximal end of the femur, to reduce the number of varying factors, the muscles acting at the distal extremity (Popliteus, Plantaris, Gastrocnemius Medialis and Lateralis) were left out of the study due to their neglectable effect on the reactions generated at the selected sectional surface. Furthermore, of the remaining muscle forces, only those above 100 N were considered.

Due to narrowing down of the number of factors resulted from the primary study, it was possible to break down the input variables of the detailed factorial analysis into their respective X, Y and Z components. By varying the individual force components within a upper and lower level, the study results can be examined based not only on the variation of the magnitude of the forces, but also of its direction.

4.2 Preliminary Factorial Analysis

Running a Plackett-Burman factorial analysis for each movement scenario at the position of peak stresses, it is possible to quantify the effect of every single force source (Factors) and their respective contributions to the sectional forces and moments (Responses) from large batches of FE simulations.

The force sources acting on the bone at the moment of peak stresses for each one of the movement cycles are shown in the Tables 4.2, 4.3, 4.4, 4.5, 4.6, 4.7 and 4.8. The forces that were included as factors in the study are presented in black while greyed out ones were left off the analysis due to the criteria previously established in Section 4.1.

Observing the results presented by the Pareto charts in Figures 4.3, 4.5, 4.7, 4.9, 4.11, 4.13 and 4.15, it is evident that the hip joint force is the most dominant as expected. However, it also shows the statistical significance of at least one muscle to the moments being generated at the fracture region, that being the Gluteus Medius for the movements scenarios of Normal Gait (NG), Left Step Up (LSU), Right Step Up (RSU), Left Step Down (LSD), Right Step Down (RSD) and the Obturator Externus for Sitting Down (SD) and Standing Up (SU), as highlighted in Table 4.1. These results show that even though the effects of the muscle forces do not significantly affect the sectional forces at the fracture, they should not be completely disregarded, since it is also shown that some muscles in fact impact the sectional moments.

Table 4.1: Factorial Analysis Results Summary

Standardized Effect of Sectional Force (E_{F_R}) and Moment (E_{M_R})														
Factors	**NG**		**LSU**		**RSU**		**LSD**		**RSD**		**SD**		**SU**	
	E_{F_R}	E_{M_R}	E_{F_R}	E_{M_R}	E_{F_R}	E_{M_R}	E_{F_R}	E_{M_R}	E_{F_R}	E_{M_R}	E_{F_R}	E_{M_R}	E_{F_R}	E_{M_R}
Hip Joint	**75**	**43**	**55**	**452**	**56**	**143**	**57**	**311**	**62**	**72**	**166**	**271**	**191**	**337**
Gluteus Medius	0.0	**9.3**	0.2	**89**	0.3	**57**	0.5	**52**	0.4	**19**	-	-	-	-
Gluteus Minimus	0.2	0.4	0.0	1.1	0.1	0.9	0.5	0.4	0.2	0.5	-	-	-	-
Gluteus Maximus	1.0	0.8	-	-	1.0	0.7	-	-	-	-	0.6	0.7	0.7	0.7
Obturator Externus	-	-	-	-	-	-	-	-	-	-	5.6	**65**	4.7	**56**
Vastus Lateralis	0.4	0.5	0.9	3.0	0.4	3.7	1.0	0.2	0.5	1.2	1.3	3.2	1.5	3.5
Vastus Medialis	1.0	0.9	-	-	-	-	0.0	0.3	1.0	0.7	0.4	0.6	0.4	0.6
Vastus Intermedius	1.2	1.1	-	-	-	-	0.5	1.2	1.0	1.1	0.3	2.7	0.7	2.8
Adductor Longus	-	-	-	-	-	-	-	-	-	-	0.6	0.4	0.5	0.5
Adductor Magnus	-	-	-	-	-	-	-	-	-	-	0.7	0.7	0.8	0.7

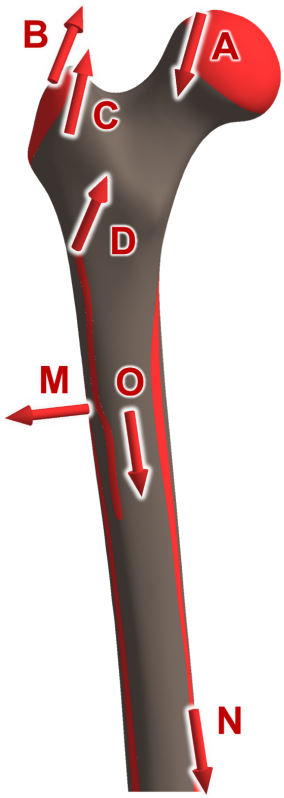

Figure 4.2: NG Loading

Table 4.2: NG Forces at Peak Stresses Position

	Source	Force (N)			
		X	**Y**	**Z**	**R**
A	Hip Joint	-304	-2629	-742	2748
B	Gluteus Medius	327	800	319	921
C	Gluteus Minimus	3	194	45	199
D	Gluteus Maximus	-199	397	168	475
E	Iliopsoas	1	2	0	2
F	Piriformis	-13	37	47	62
G	Obturator Internus	-27	13	34	45
H	Obturator Externus	0	0	0	0
I	Gemellus Superior	-5	3	6	8
J	Gemellus Inferior	-5	3	5	8
K	Quadratus Femoris	-3	2	5	7
L	Pectineus	0	0	0	0
M	Vastus Lateralis	-204	-77	-677	711
N	Vastus Medialis	54	-286	43	294
O	Vastus Intermedius	30	-165	24	169
P	Biceps Femoris	0	0	0	0
Q	Adductor Brevis	0	0	0	0
R	Adductor Longus	0	0	0	0
S	Adductor Magnus	-3	10	2	11

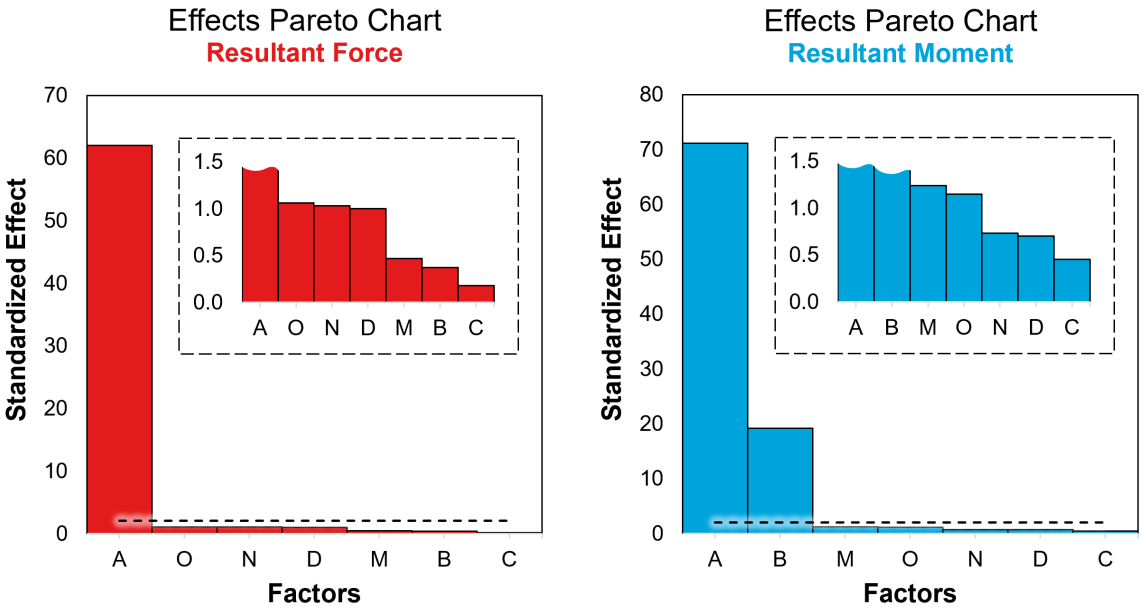

(a) Standardized Effects to Sectional Force **(b)** Standardized Effects to Sectional Moment

Figure 4.3: NG Statistical Significance of Loading Sources

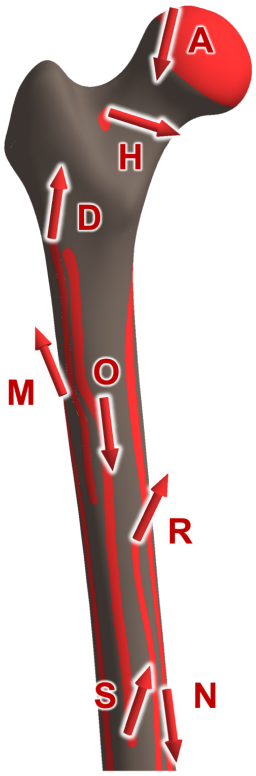

Figure 4.4: SU Loading

Table 4.3: SU Forces at Peak Stresses Position

	Source	Force (N)			
		X	**Y**	**Z**	**R**
A	Hip Joint	35	-2104	-503	2164
B	Gluteus Medius	59	19	41	74
C	Gluteus Minimus	2	31	5	31
D	Gluteus Maximus	-170	733	101	759
E	Iliopsoas	0	0	0	0
F	Piriformis	4	4	9	10
G	Obturator Internus	-6	21	25	33
H	Obturator Externus	-16	-39	124	131
I	Gemellus Superior	0	1	1	1
J	Gemellus Inferior	-1	12	9	14
K	Quadratus Femoris	-27	75	59	99
L	Pectineus	-3	14	15	21
M	Vastus Lateralis	159	963	-394	1053
N	Vastus Medialis	90	-726	96	738
O	Vastus Intermedius	34	-391	47	395
P	Biceps Femoris	0	0	0	0
Q	Adductor Brevis	-13	38	32	51
R	Adductor Longus	-19	94	45	105
S	Adductor Magnus	-74	249	83	273

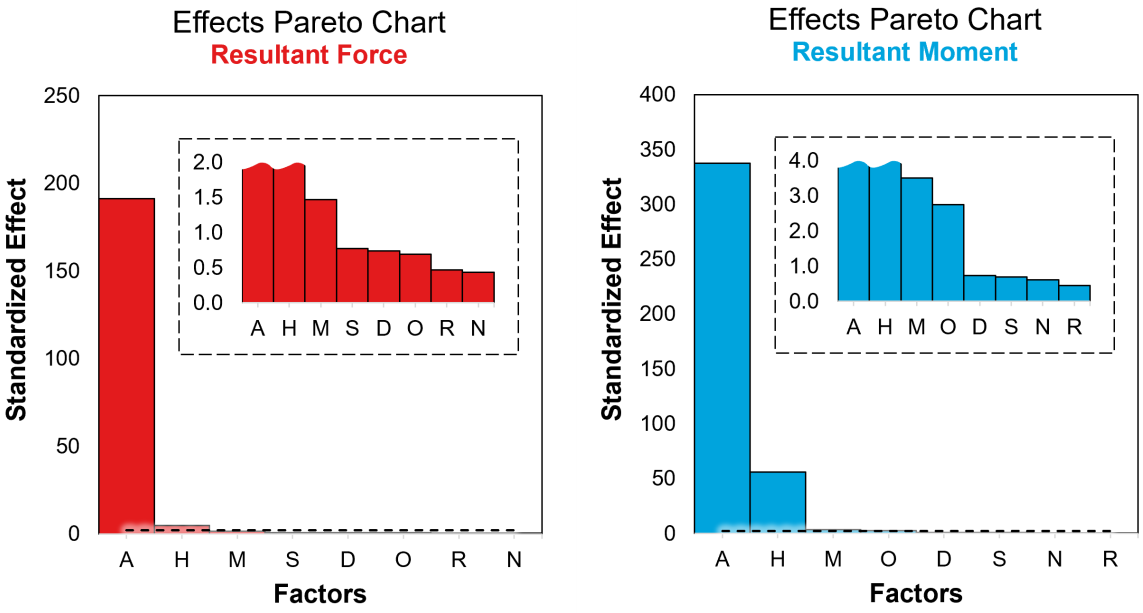

(a) Standardized Effects to Sectional Force **(b)** Standardized Effects to Sectional Moment

Figure 4.5: SU Statistical Significance of Loading Sources

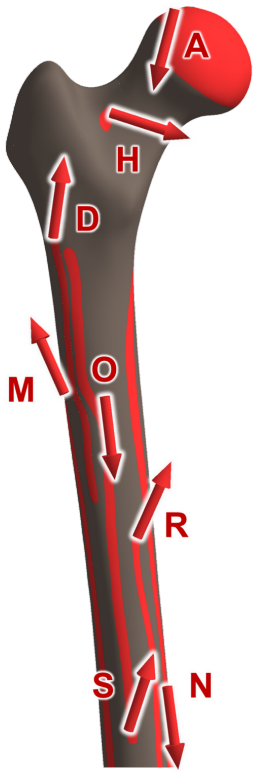

Figure 4.6: SD Loading

Table 4.4: SD Forces at Peak Stresses Position

	Source	Force (N) X	Y	Z	R
A	Hip Joint	-10	-1721	-450	1779
B	Gluteus Medius	66	9	37	76
C	Gluteus Minimus	3	82	15	83
D	Gluteus Maximus	-139	545	75	567
E	Iliopsoas	0	0	0	0
F	Piriformis	5	3	7	9
G	Obturator Internus	-4	-43	133	141
H	Obturator Externus	-17	-43	133	141
I	Gemellus Superior	0	0	0	0
J	Gemellus Inferior	-1	6	5	8
K	Quadratus Femoris	-20	59	46	78
L	Pectineus	-3	16	15	23
M	Vastus Lateralis	95	808	-357	888
N	Vastus Medialis	76	-616	82	626
O	Vastus Intermedius	29	-331	40	335
P	Biceps Femoris	0	0	0	0
Q	Adductor Brevis	-13	38	30	50
R	Adductor Longus	-18	90	41	102
S	Adductor Magnus	-61	211	69	231

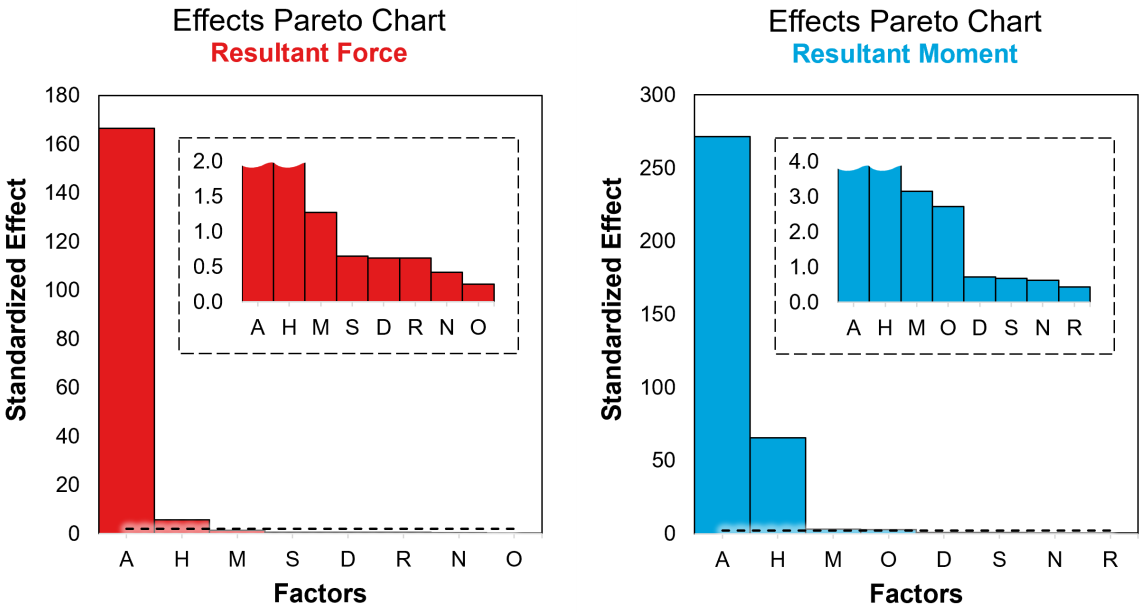

(a) Standardized Effects to Sectional Force **(b)** Standardized Effects to Sectional Moment

Figure 4.7: SD Statistical Significance of Loading Sources

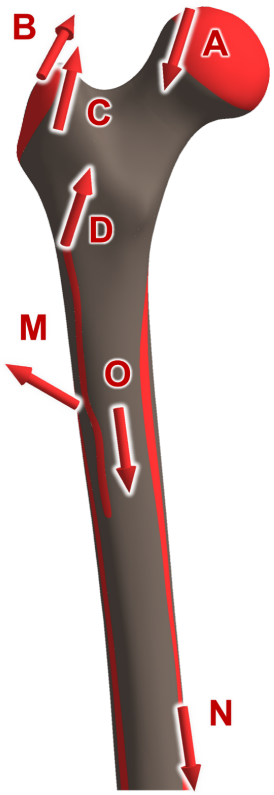

Figure 4.8: LSU Loading

Table 4.5: LSU Forces at Peak Stresses Position

	Source	Force (N)			
		X	**Y**	**Z**	**R**
A	Hip Joint	-294	-2043	-652	2164
B	Gluteus Medius	362	460	246	635
C	Gluteus Minimus	1	110	27	113
D	Gluteus Maximus	-200	504	165	567
E	Iliopsoas	0	0	0	0
F	Piriformis	-2	33	41	52
G	Obturator Internus	-38	27	54	71
H	Obturator Externus	0	0	1	1
I	Gemellus Superior	-5	5	7	10
J	Gemellus Inferior	-7	7	8	13
K	Quadratus Femoris	-14	11	21	27
L	Pectineus	0	0	0	0
M	Vastus Lateralis	-191	329	-569	685
N	Vastus Medialis	66	-455	65	464
O	Vastus Intermedius	33	-262	34	266
P	Biceps Femoris	0	0	0	0
Q	Adductor Brevis	0	0	0	0
R	Adductor Longus	0	0	0	0
S	Adductor Magnus	-21	58	14	64

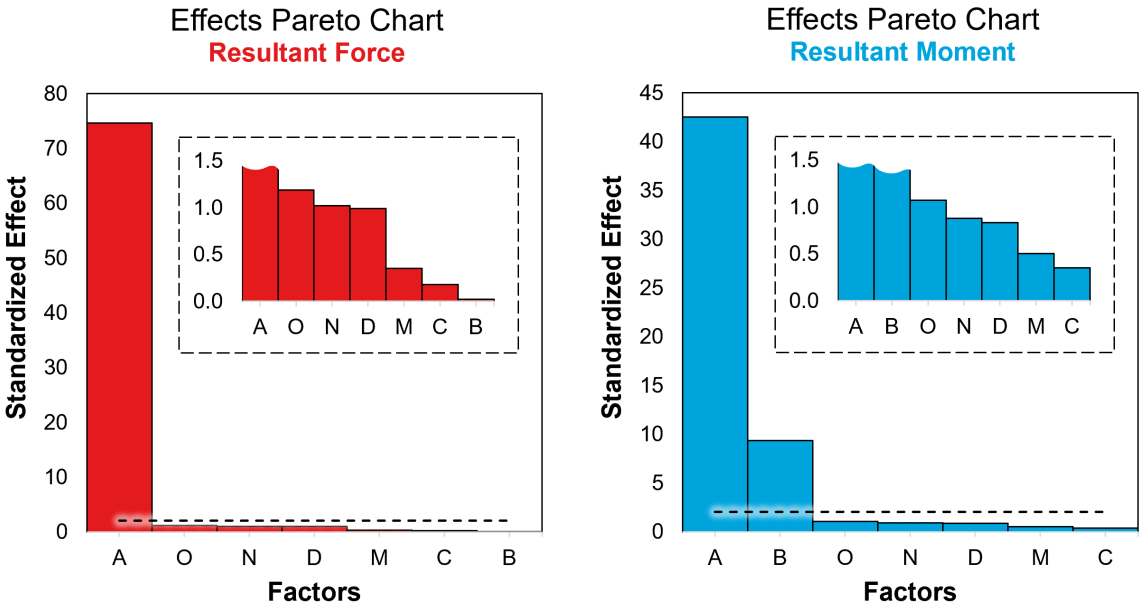

(a) Standardized Effects to Sectional Force **(b)** Standardized Effects to Sectional Moment

Figure 4.9: LSU Statistical Significance of Loading Sources

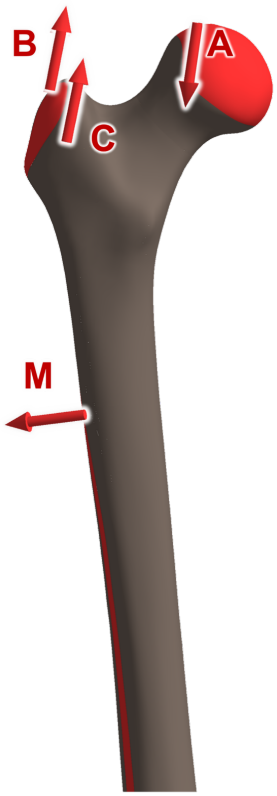

Figure 4.10: RSU Loading

Table 4.6: RSU Forces at Peak Stresses Position

	Source	Force (N)			
		X	**Y**	**Z**	**R**
A	Hip Joint	55	-1911	-275	1931
B	Gluteus Medius	-10	676	132	689
C	Gluteus Minimus	5	147	30	150
D	Gluteus Maximus	-49	67	38	91
E	Iliopsoas	9	12	2	15
F	Piriformis	-4	5	7	9
G	Obturator Internus	0	0	0	0
H	Obturator Externus	0	0	0	0
I	Gemellus Superior	-1	0	1	1
J	Gemellus Inferior	0	0	0	0
K	Quadratus Femoris	0	0	0	0
L	Pectineus	0	0	0	0
M	Vastus Lateralis	89	-33	-256	273
N	Vastus Medialis	10	-47	7	48
O	Vastus Intermedius	5	-27	4	28
P	Biceps Femoris	-3	-16	-2	17
Q	Adductor Brevis	0	0	0	0
R	Adductor Longus	0	0	0	0
S	Adductor Magnus	0	0	0	0

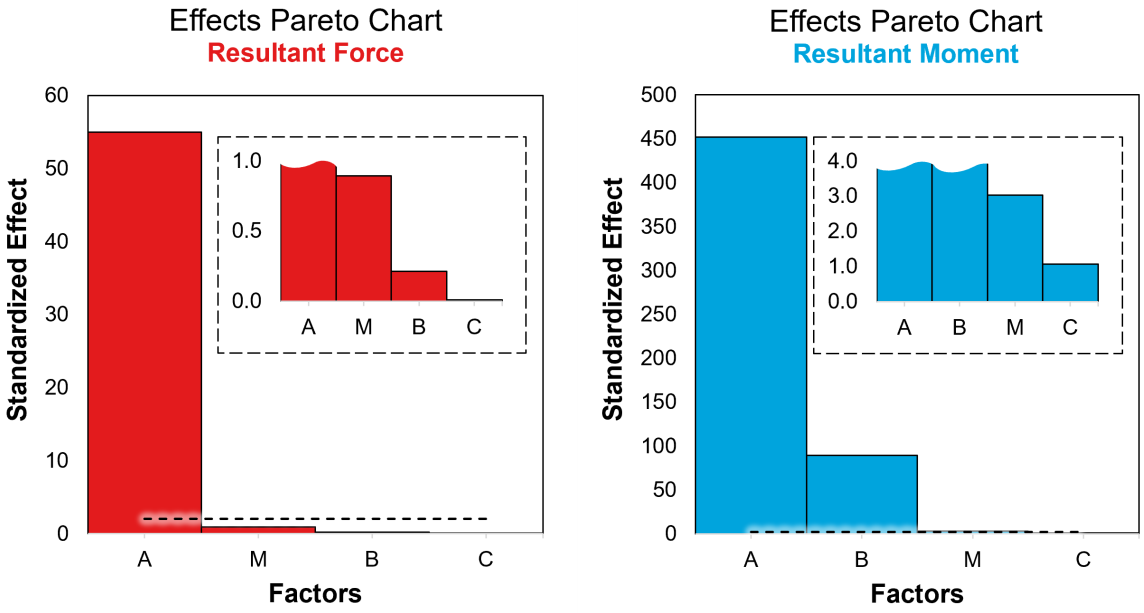

(a) Standardized Effects to Sectional Force **(b)** Standardized Effects to Sectional Moment

Figure 4.11: RSU Statistical Significance of Loading Sources

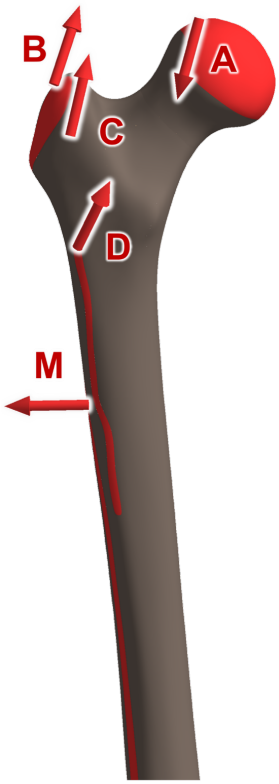

Figure 4.12: LSD Loading

Table 4.7: LSD Forces at Peak Stresses Position

	Source	Force (N)			
		X	**Y**	**Z**	**R**
A	Hip Joint	0	-1963	-534	2035
B	Gluteus Medius	115	686	225	731
C	Gluteus Minimus	3	166	38	170
D	Gluteus Maximus	-112	191	94	241
E	Iliopsoas	19	26	3	32
F	Piriformis	-17	27	36	48
G	Obturator Internus	-29	5	38	49
H	Obturator Externus	0	0	0	0
I	Gemellus Superior	-5	2	6	8
J	Gemellus Inferior	-4	2	5	7
K	Quadratus Femoris	-1	0	3	3
L	Pectineus	0	0	0	0
M	Vastus Lateralis	31	-9	-518	519
N	Vastus Medialis	7	-35	5	36
O	Vastus Intermedius	4	-20	3	20
P	Biceps Femoris	-5	-34	-4	35
Q	Adductor Brevis	0	0	0	0
R	Adductor Longus	0	0	0	0
S	Adductor Magnus	0	0	0	0

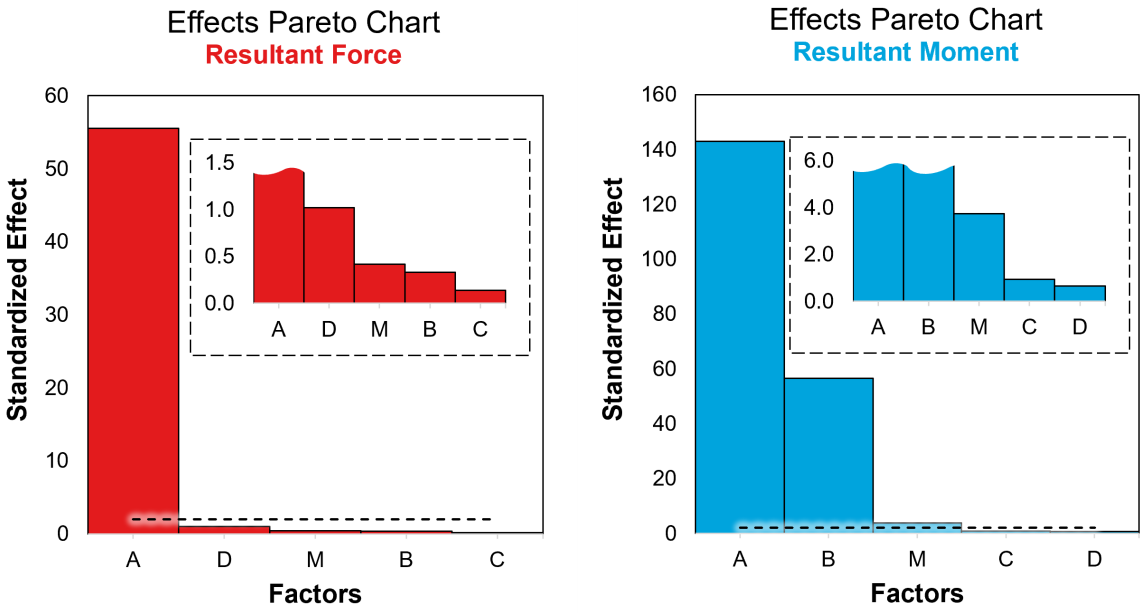

(a) Standardized Effects to Sectional Force **(b)** Standardized Effects to Sectional Moment

Figure 4.13: LSD Statistical Significance of Loading Sources

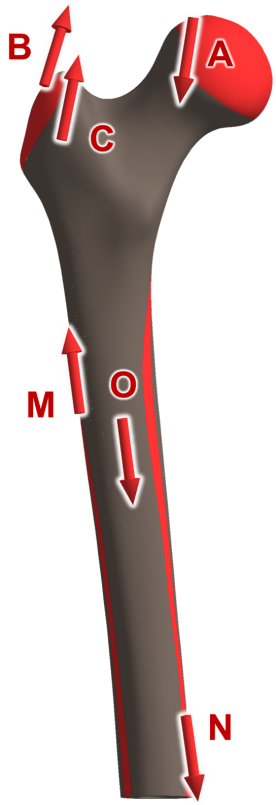

Figure 4.14: RSD Loading

Table 4.8: RSD Forces at Peak Stresses Position

	Source	Force (N) X	Y	Z	R
A	Hip Joint	-152	-2098	-329	2129
B	Gluteus Medius	136	567	168	607
C	Gluteus Minimus	6	170	34	174
D	Gluteus Maximus	-28	53	25	65
E	Iliopsoas	15	21	3	26
F	Piriformis	-1	2	2	3
G	Obturator Internus	0	0	0	0
H	Obturator Externus	0	0	0	0
I	Gemellus Superior	0	0	0	0
J	Gemellus Inferior	0	0	0	0
K	Quadratus Femoris	0			0
L	Pectineus	1	1	1	2
M	Vastus Lateralis	37	1203	-157	1213
N	Vastus Medialis	138	-1047	146	1066
O	Vastus Intermedius	61	-589	75	597
P	Biceps Femoris	0	0	0	0
Q	Adductor Brevis	0	0	0	0
R	Adductor Longus	0	0	0	0
S	Adductor Magnus	-9	34	8	36

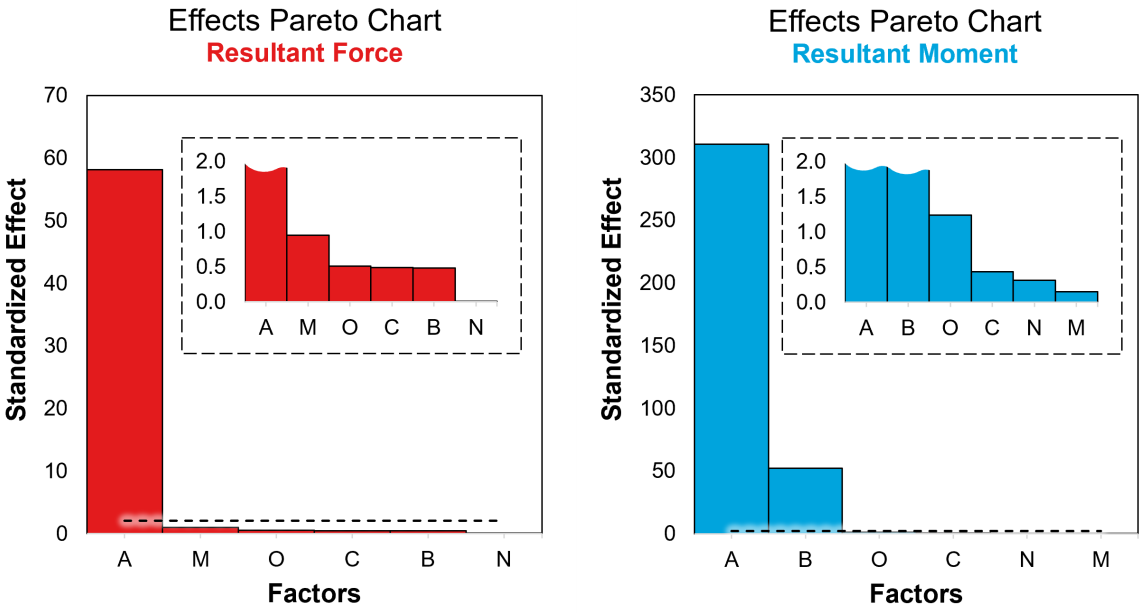

(a) Standardized Effects to Sectional Force **(b)** Standardized Effects to Sectional Moment

Figure 4.15: RSD Statistical Significance of Loading Sources

4.3 Detailed Factorial Analysis

The results from the preliminary factorial analysis were capable of narrowing down the number of forces to only two for each of the movement scenarios. Therefore, even after breaking down each one of them into their respective X, Y and Z components, it only totals 6 factors. The manageable number of input factors allows for an in depth full factorial analysis to be performed, considering the factors varying within an upper and lower range of the peak condition values of its original forces, presented on Tables 4.9 and 4.10.

Table 4.9: Original Gluteus Medius and Hip Joint Forces

Movement	**Hip Joint** (N)			**Gluteus Medius** (N)		
Scenario	**X**	**Y**	**Z**	**X**	**Y**	**Z**
Normal Gait	-304	-2629	-742	327	800	319
Left Step Up	-294	-2043	-652	362	460	246
Right Step Up	55	-1911	-275	-10	676	132
Left Step Down	0	-1963	-534	115	686	225
Right Step Down	-152	-2098	-329	136	567	168

Table 4.10: Original Obturator Externus and Hip Joint Forces

Movement	**Hip Joint** (N)			**Obturator Externus** (N)		
Scenario	**X**	**Y**	**Z**	**X**	**Y**	**Z**
Standing Up	35	-2104	-503	-16	-39	124
Sitting Down	-10	-1721	-450	-17	-43	133

Moreover, this secondary detailed analysis not only follows the same output response of the preliminary study (reaction force and moment at the fracture section), but it additionally expands on it by considering their individual X, Y and Z components instead of simply their resultant. Therefore, the effects of each component can be investigated separately, allowing for adjustment of force orientation and consequently achieving a better match to the complete loading condition.

By adjusting the force components following the regression model generated by the factorial analysis, it is possible to obtain sectional force and moment values that approach more closely the results produced when considering all the muscle forces. The adjusted forces are presented on Tables 4.11 and 4.12.

Table 4.11: Adjusted Gluteus Medius and Hip Joint Forces

Movement	**Hip Joint** (N)			**Gluteus Medius** (N)		
Scenario	**X**	**Y**	**Z**	**X**	**Y**	**Z**
Normal Gait	-306	-2606	-618	123	904	50
Left Step Up	-307	-2018	-543	181	710	123
Right Step Up	59	-1939	-335	6	710	293
Left Step Down	0	-1939	-388	-80	795	-88
Right Step Down	-138	-2043	-268	104	764	-50

Table 4.12: Adjusted Obturator Externus and Hip Joint Forces

Movement	**Hip Joint** (N)			**Obturator Externus** (N)		
Scenario	**X**	**Y**	**Z**	**X**	**Y**	**Z**
Standing Up	45	-2152	-442	-15	146	100
Sitting Down	30	-1620	-253	-34	-48	-50

That being said, when observing the results from the detailed factorial analysis, it is easily noticeable the sensitivity of each output response to the variation of each one of components of the input factors. The factorial plots presented in Figures 4.16 and 4.17 show the change caused to the each individual component of the sectional force and moment when each of the input factors components vary. For instance, a steeper slop signifies that the variation of its factor will results on a stronger change of its respective output response.

The factorial plots of all the additional movement scenarios are included in the Appendices in Figures A.3, A.4, A.11, A.12, A.19, A.20, A.27, A.28, A.35, A.36 A.43 and A.44 for the respective motions of Sitting Down, Standing Up, Left Step Up, Right Step Up, Left Step Down and Right Step Down.

4.4 Experimental Loading Cases

Once the muscle forces considered statistically significant to the sectional forces and moments at the fracture section were identified, a comparative study was performed to assess the actual difference between simplified and more complex loading cases. By simulating each movement scenario using four different loading cases, the effect of neglecting muscle forces can be observed throughout the complete cycle of the motions and an optimised simplification of the loading of the femur can be conceived. The four loading cases established for this comparative analysis are as follows:

- **Complete Loading:** Includes all muscles forces and the hip joint, generating the most thorough and closest-to-reality results. This loading is used as a reference point and as a target result.
- **Single Force Loading:** Includes only the hip joint force, neglecting effect from muscle forces. The most simplified loading case, what is usually employed in biomechanical testing.
- **Significant Loading:** Includes only the forces deemed statistically significant by the preliminary factorial analysis, bridging the gap between the Complete and the Single Force Loading cases.
- **Experimental Loading:** Includes the same forces from the Significant Loading, but with their magnitude and directions adjusted to generate results even closer to the Complete Loading.

The sectional forces and moments at the fracture section are presented in Figures 4.19, 4.24, 4.29, 4.34, 4.39, 4.44 and 4.49 for their respective movements NG, LSU, RSU, LSD, RSD and the Obturator Externus for SD and SU. When observing these results, it is apparent that disregarding muscle forces (represented by the **red** curve) generates higher reaction forces and lower reaction moments in the fracture section.

When the significant muscle forces are added (represented by the **blue** curve), it is possible to observe both the sectional forces and sectional moments shifting towards the reference point (represented by the **black** curve). Going further, the magnitudes and directions of these forces can then be adjusted to achieve a better match to the reference (represented by the **green** curve). Table 4.13 summarises the comparison between the Single Force and Experimental Loading case, highlighting their respective percentage deviation from the Complete Loading case.

Table 4.13: Loading Cases Comparison Summary

Sectional Force F_R (N) and Moment M_R (N/m)														
Factors	**NG**		**LSU**		**RSU**		**LSD**		**RSD**		**SD**		**SU**	
	F_R	M_R	F_R	M_R	F_R	M_R	F_R	M_R	F_R	M_R	F_R	M_R	F_R	M_R
Complete Loading	2417	61	1884	46	1706	54	1743	44	1828	58	1694	34	2035	45
Single Force Loading	2748	47	2164	36	1932	45	2035	28	2129	50	1779	26	2164	35
Difference (%)	14	-23	15	-22	13	-17	17	-36	16	-13	5	-24	6	-23
Experimental Loading	2417	59	1884	46	1738	54	1743	44	1832	58	1696	34	2035	46
Difference (%)	0	-2	0	-1	2	0	0	0	0	0	0	-1	0	3

Furthermore, when comparing the principal stresses that are being generated at the fracture section during the position of peak stresses of each movement scenario, it is noticeable that a closer match to the reference point is achieved when the Experimental Loading case is used instead of the Single Force Loading case.

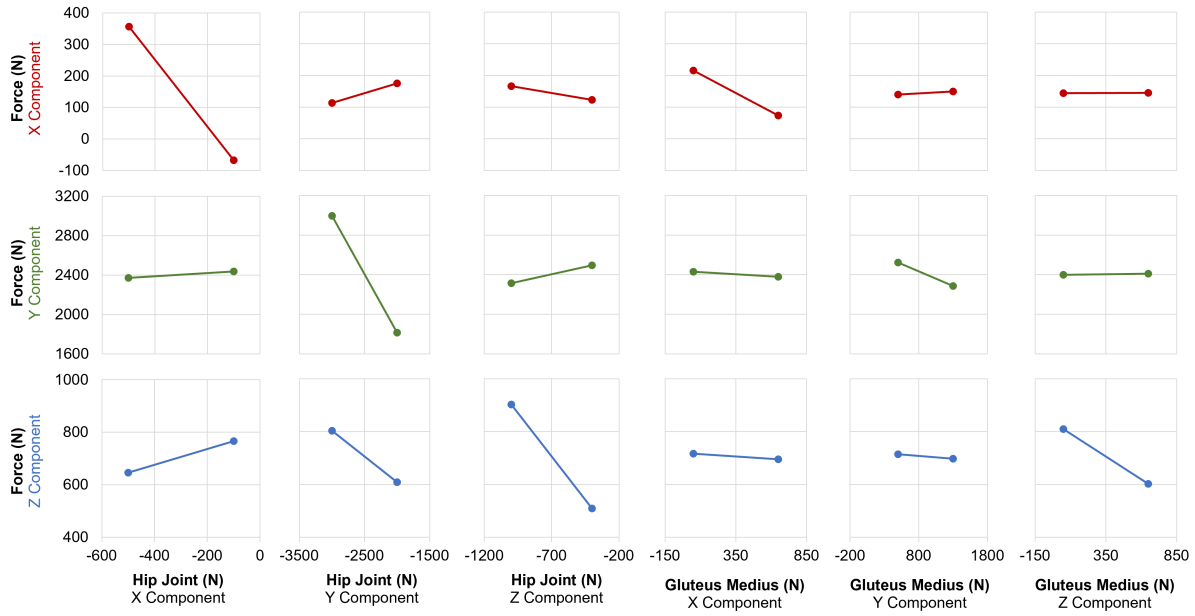

Figure 4.16: Sectional Force Factorial Plots of Normal Gait Movement Scenario

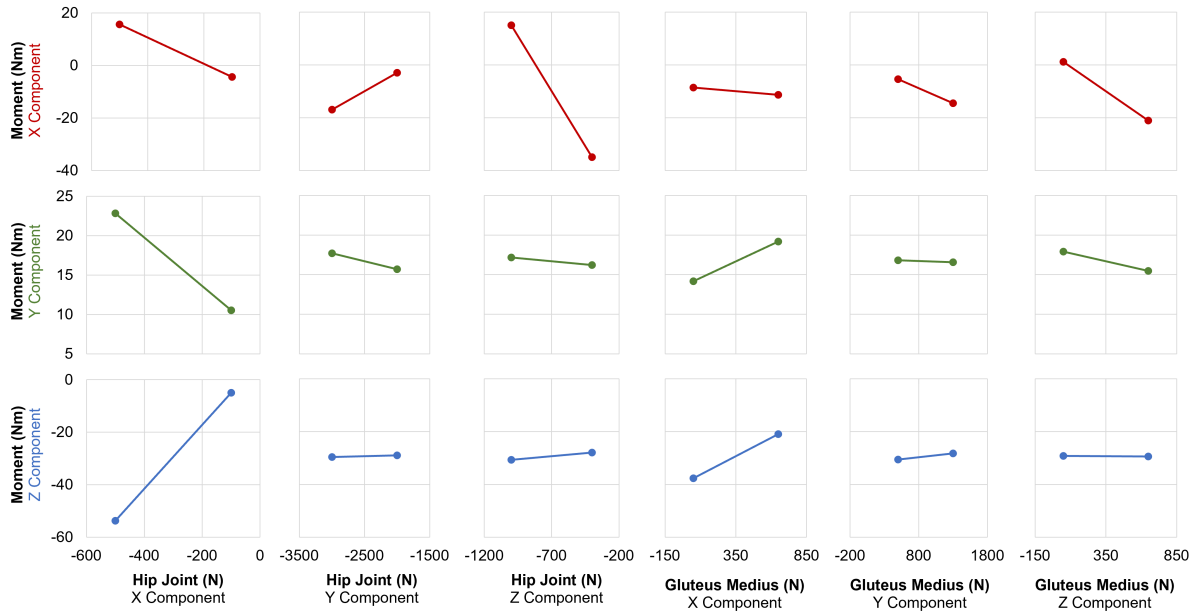

Figure 4.17: Sectional Moment Factorial Plots of Normal Gait Movement Scenario

4.4.1 Normal Gait (NG)

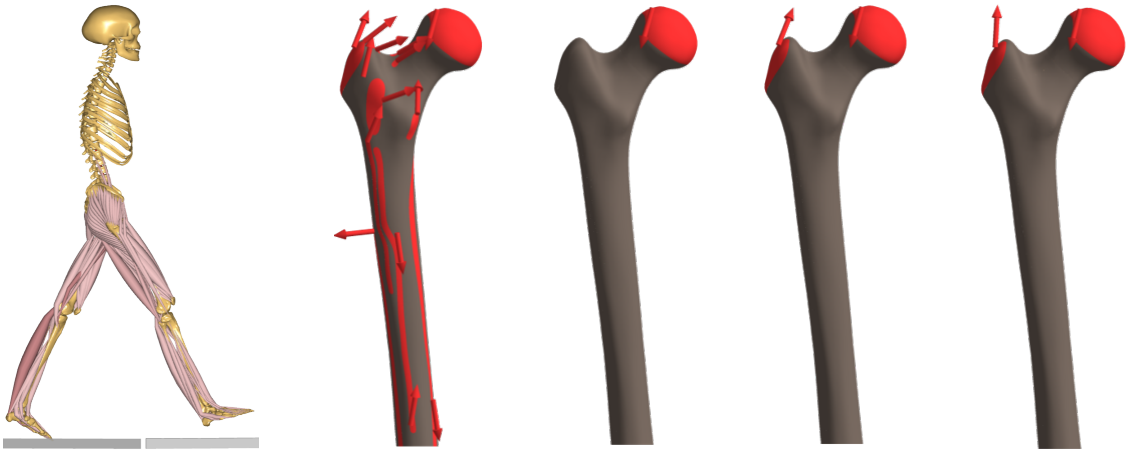

(a) Peak Stresses Position (b) Complete (c) Single (d) Significant (e) Equivalent

Figure 4.18: Normal Gait Loading Cases for the Position of Peak Stresses

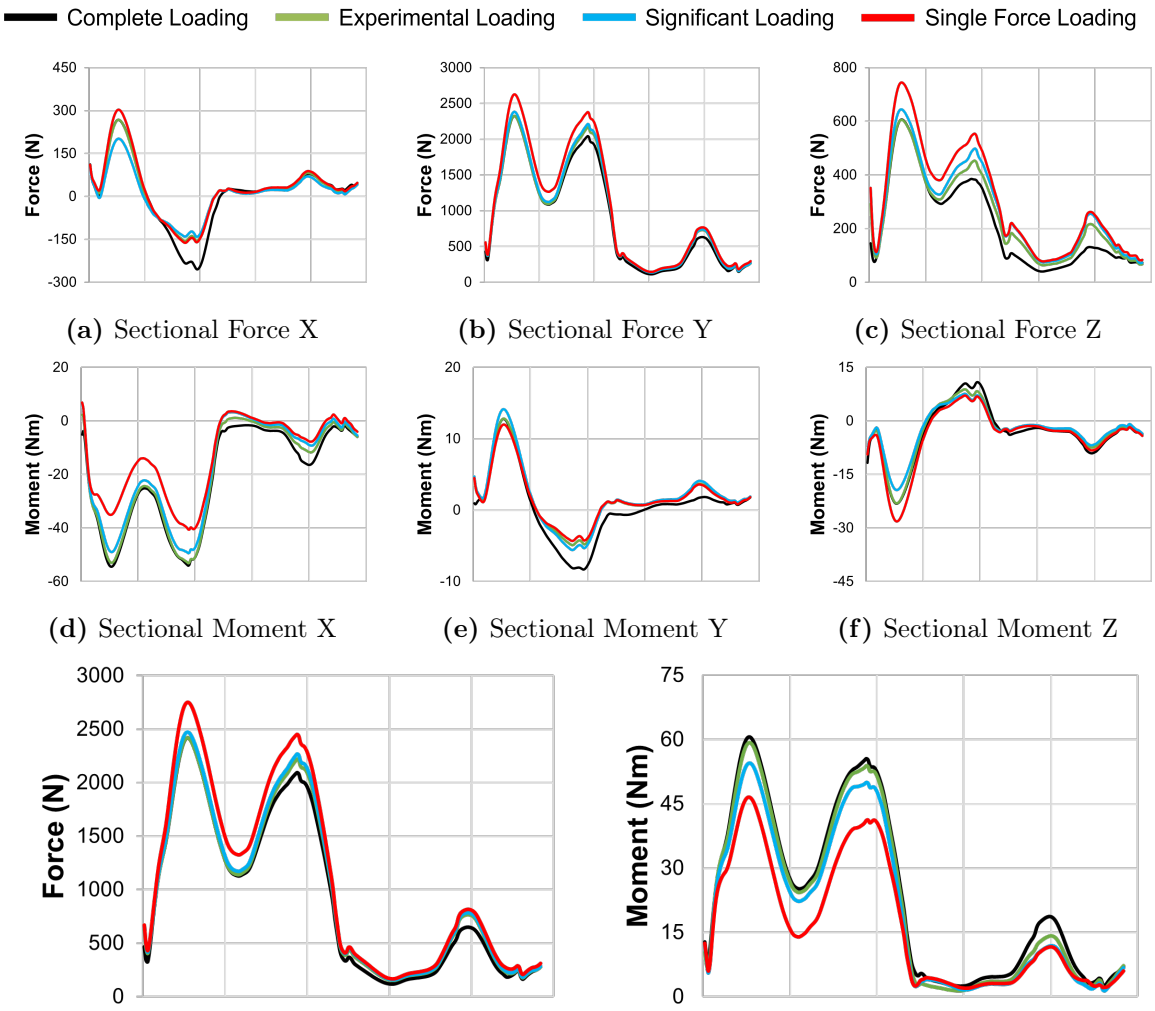

(a) Sectional Force X (b) Sectional Force Y (c) Sectional Force Z

(d) Sectional Moment X (e) Sectional Moment Y (f) Sectional Moment Z

(g) Sectional Force Resultant (h) Sectional Moment Resultant

Figure 4.19: Normal Gait Sectional Forces and Moments Comparison

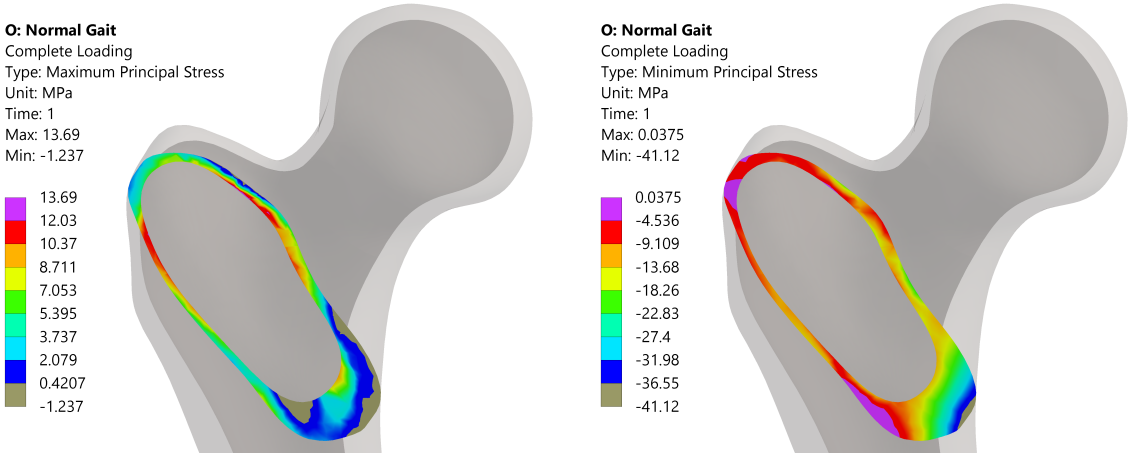

(a) Maximum Principal Stress **(b)** Minimum Principal of Stress

Figure 4.20: Peak Principal Stresses of Complete Loading Case During Normal Gait

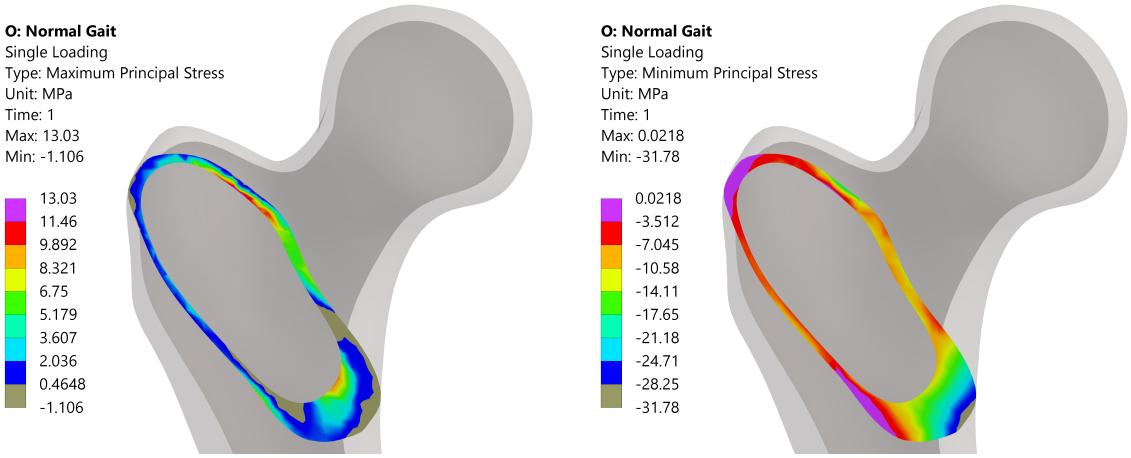

(a) Maximum Principal Stress **(b)** Minimum Principal Stress

Figure 4.21: Peak Principal Stresses of Single Force Loading Case During Normal Gait

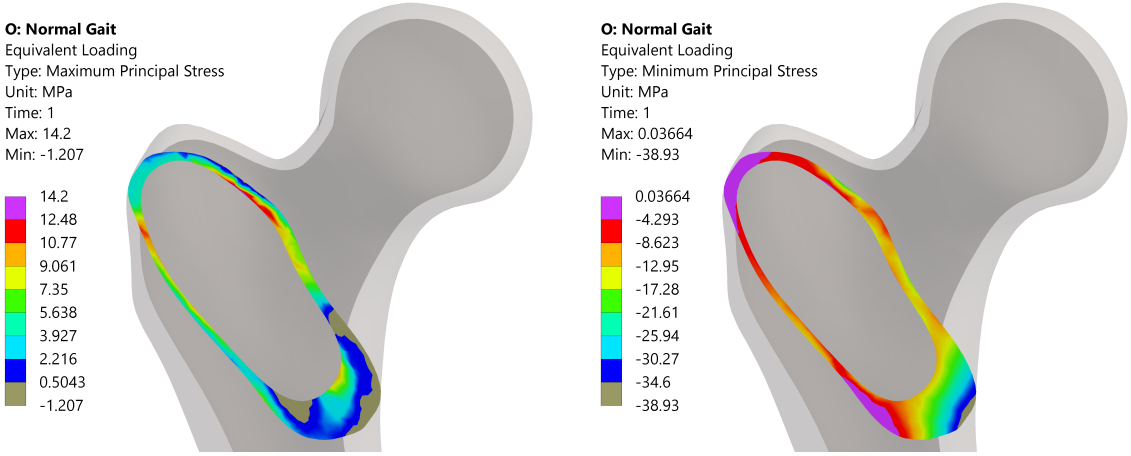

(a) Maximum Principal Stress **(b)** Minimum Principal Stress

Figure 4.22: Peak Principal Stresses of Experimental Loading Case During Normal Gait

4.4.2 Standing Up (SU)

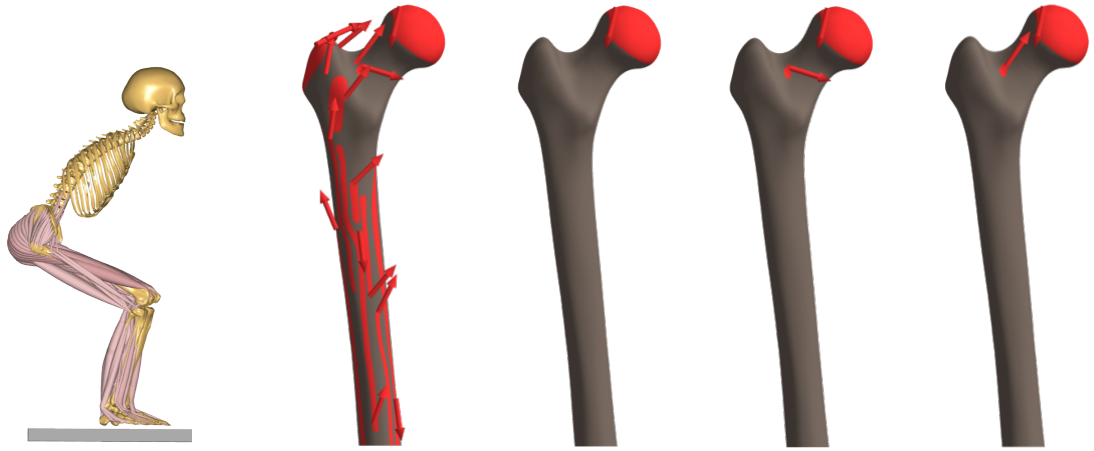

(a) Peak Stresses Position (b) Complete (c) Single (d) Significant (e) Equivalent

Figure 4.23: Standing Up Loading of the Left Femur at the Peak Streeses Position

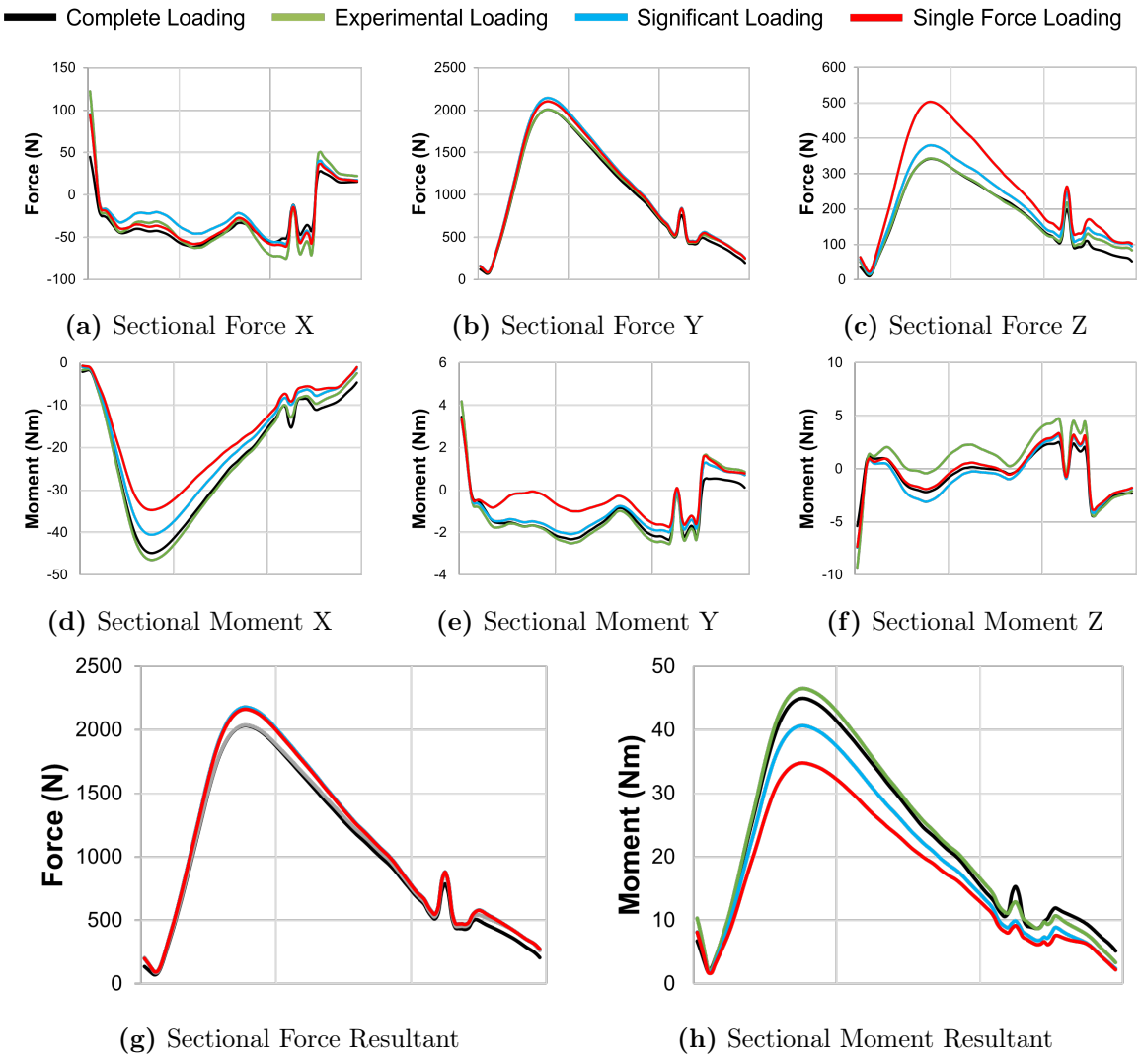

(a) Sectional Force X (b) Sectional Force Y (c) Sectional Force Z

(d) Sectional Moment X (e) Sectional Moment Y (f) Sectional Moment Z

(g) Sectional Force Resultant (h) Sectional Moment Resultant

Figure 4.24: Standing Up Sectional Forces and Moments Comparison

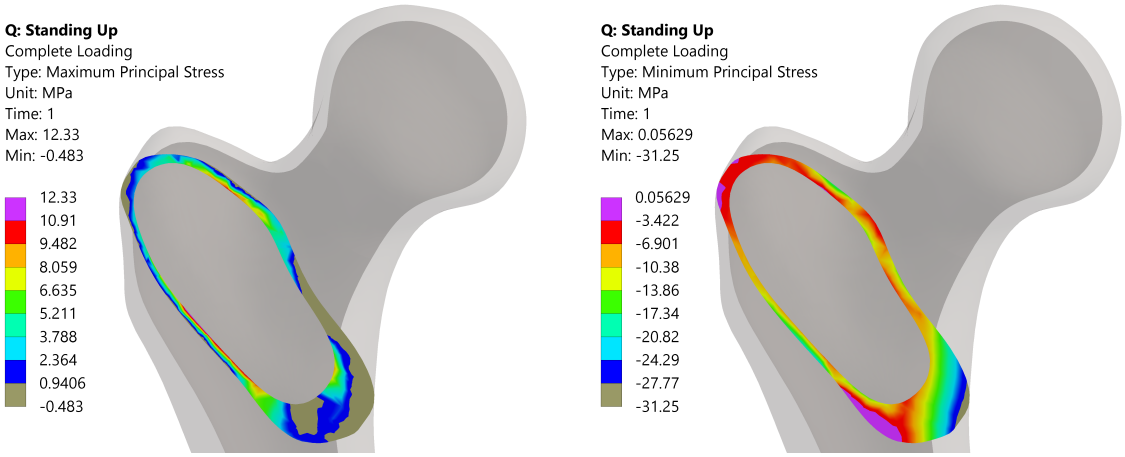

(a) Maximum Principal Stress **(b)** Minimum Principal of Stress

Figure 4.25: Peak Principal Stresses of Complete Loading Case During Standing Up

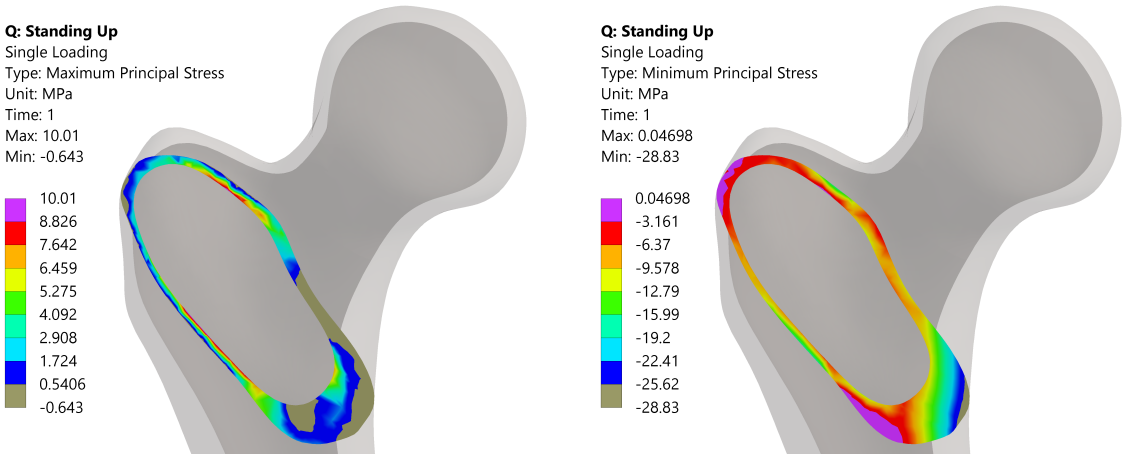

(a) Maximum Principal Stress **(b)** Minimum Principal Stress

Figure 4.26: Peak Principal Stresses of Single Force Loading Case During Standing Up

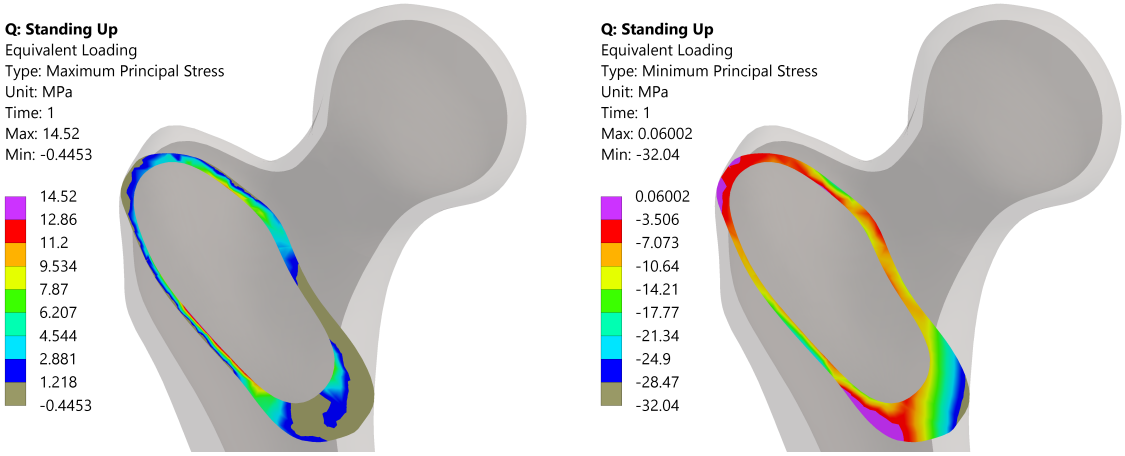

(a) Maximum Principal Stress **(b)** Minimum Principal Stress

Figure 4.27: Peak Principal Stresses of Eqxperimental Loading Case During Standing Up

4.4.3 Sitting Down (SD)

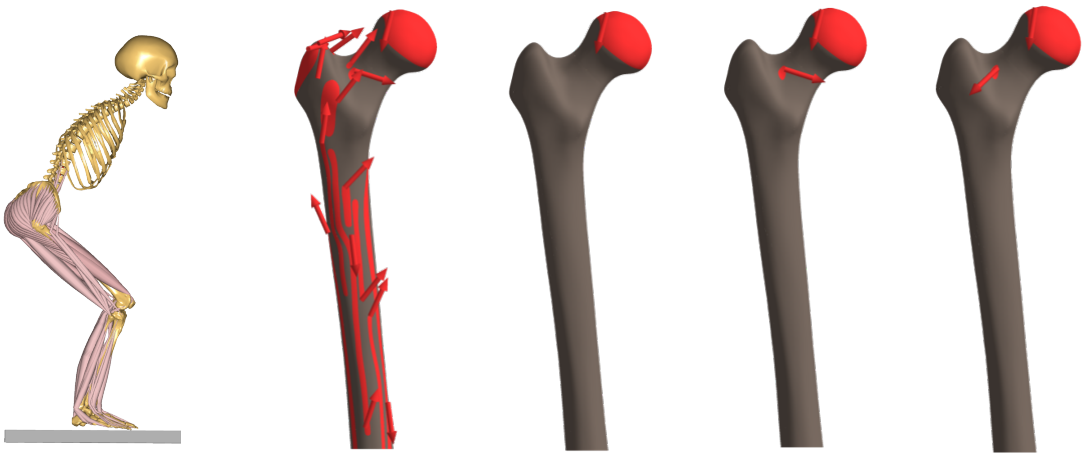

(a) Peak Stresses Position (b) Complete (c) Single (d) Significant (e) Equivalent

Figure 4.28: Sitting Down Loading of the Left Femur at the Peak Streeses Position

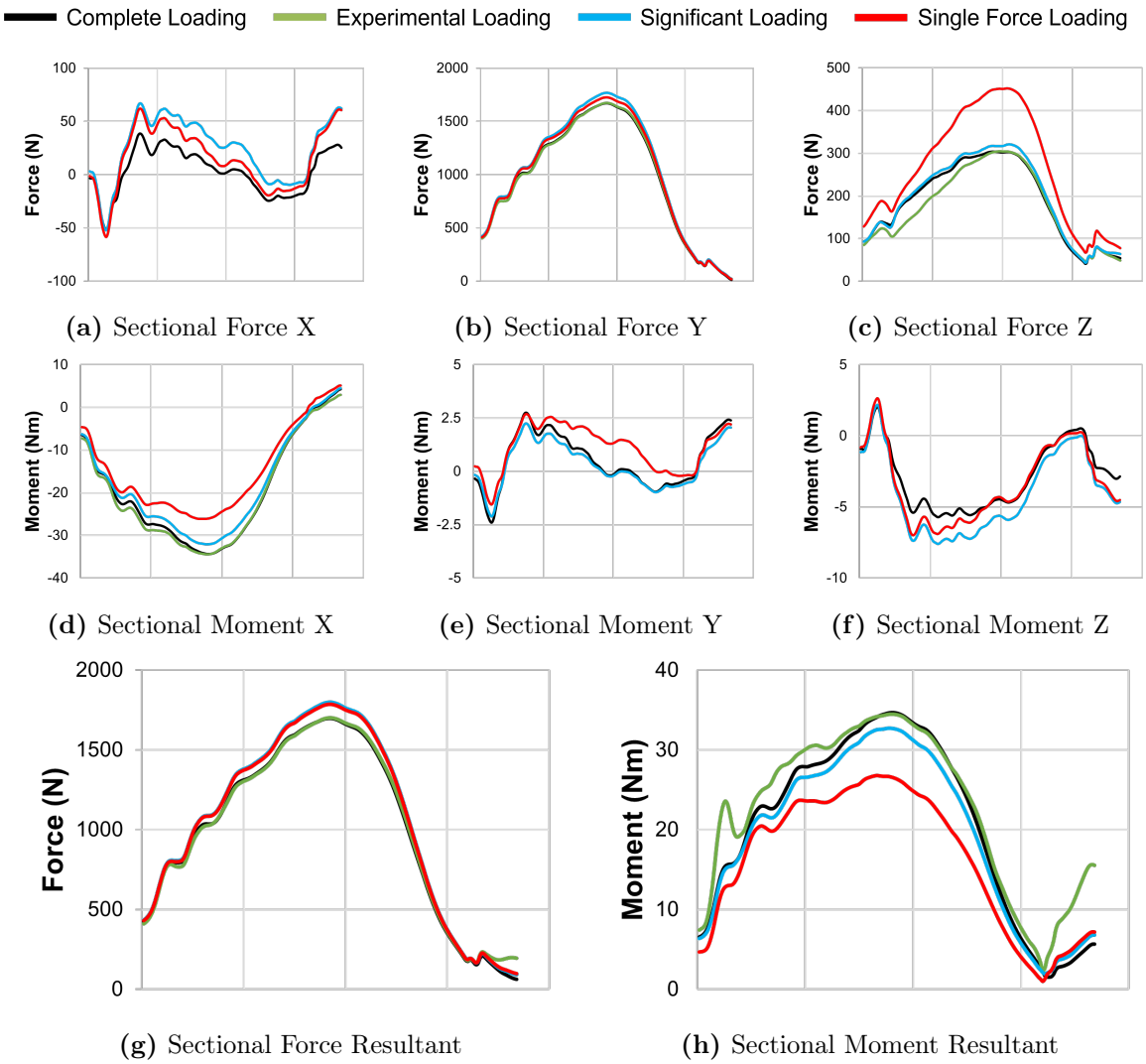

(a) Sectional Force X (b) Sectional Force Y (c) Sectional Force Z

(d) Sectional Moment X (e) Sectional Moment Y (f) Sectional Moment Z

(g) Sectional Force Resultant (h) Sectional Moment Resultant

Figure 4.29: Sitting Down Sectional Forces and Moments Comparison

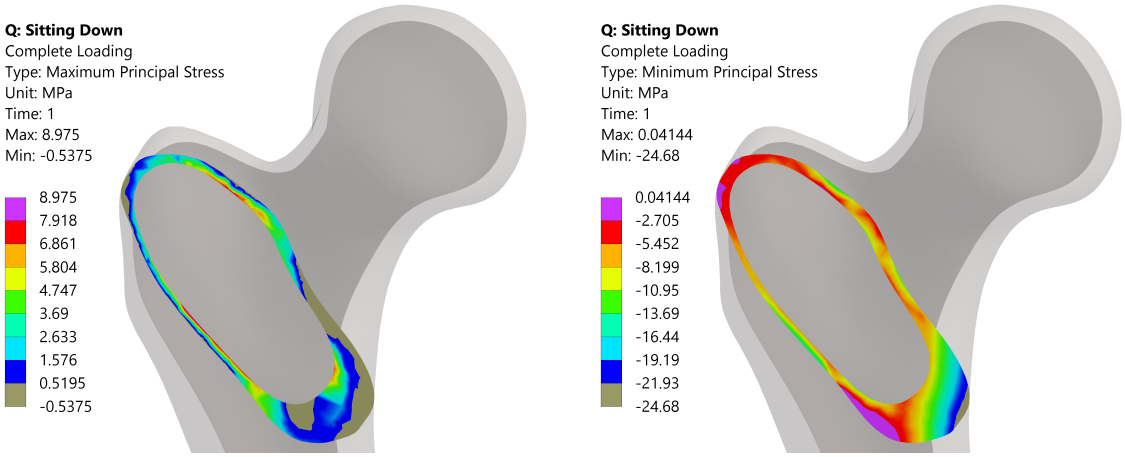

(a) Maximum Principal Stress **(b)** Minimum Principal of Stress

Figure 4.30: Peak Principal Stresses of Complete Loading Case During Sitting Down

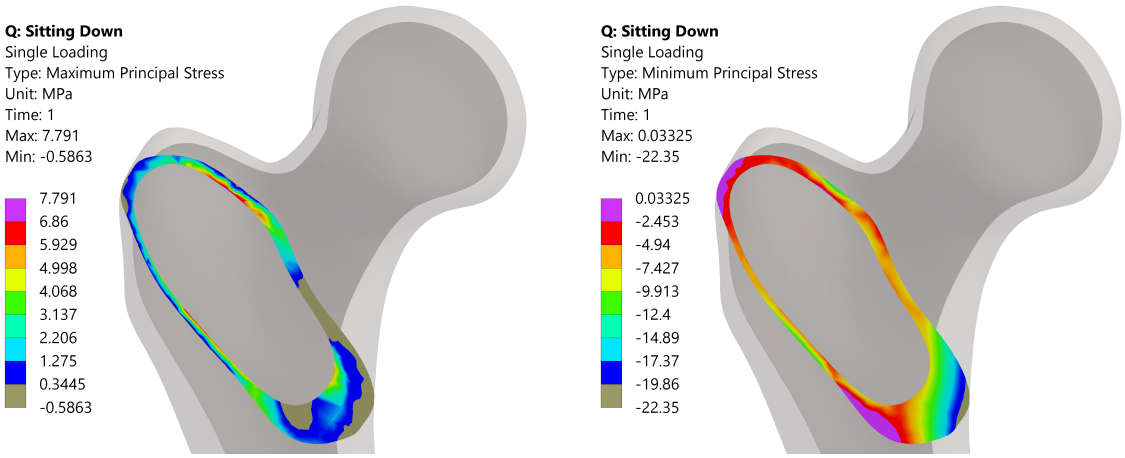

(a) Maximum Principal Stress **(b)** Minimum Principal Stress

Figure 4.31: Peak Principal Stresses of Single Force Loading Case During Sitting Down

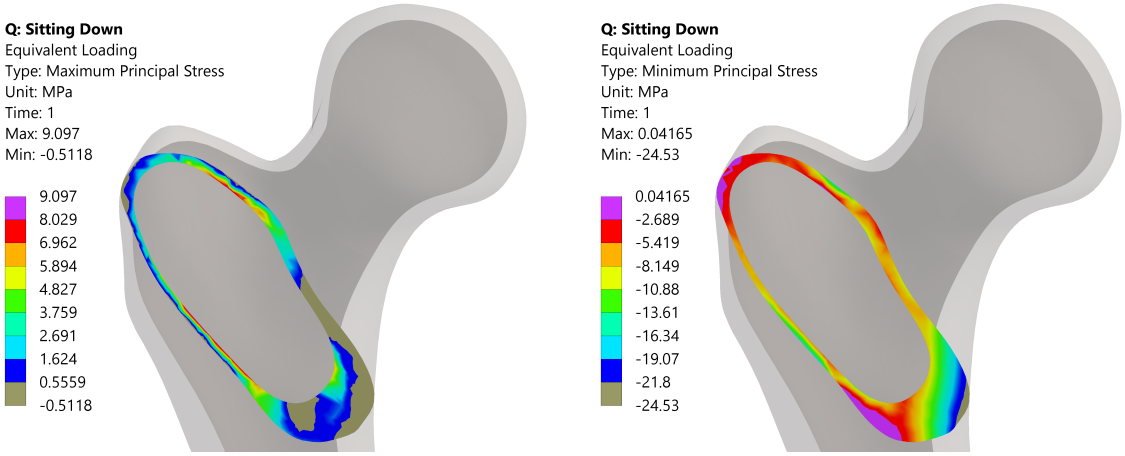

(a) Maximum Principal Stress **(b)** Minimum Principal Stress

Figure 4.32: Peak Principal Stresses of Experimental Loading Case During Sitting Down

4.4.4 Left Step Up (LSU)

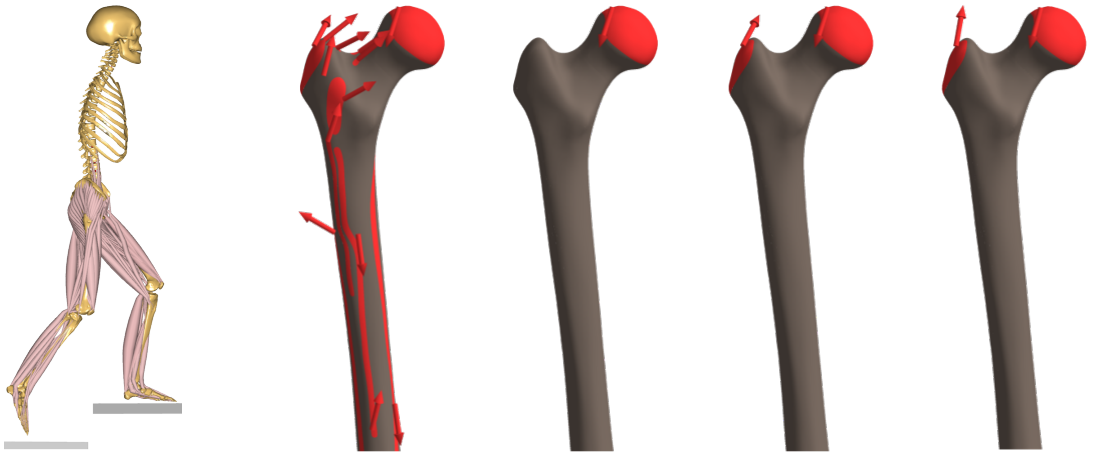

(a) Peak Stresses Position **(b)** Complete **(c)** Single **(d)** Significant **(e)** Equivalent

Figure 4.33: Left Step Up Loading Cases for the Position of Peak Stresses

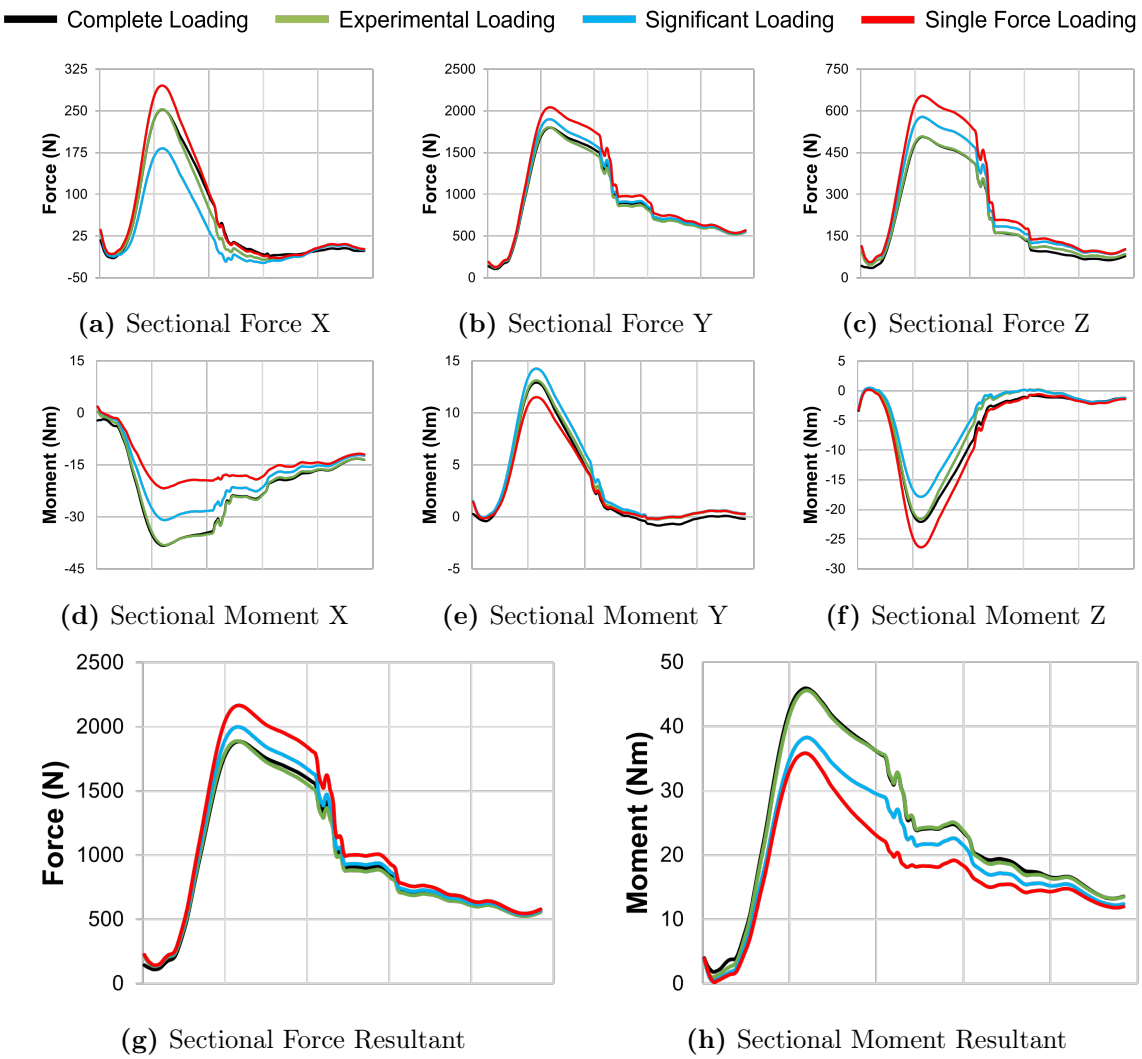

(a) Sectional Force X **(b)** Sectional Force Y **(c)** Sectional Force Z

(d) Sectional Moment X **(e)** Sectional Moment Y **(f)** Sectional Moment Z

(g) Sectional Force Resultant **(h)** Sectional Moment Resultant

Figure 4.34: Left Step Up Sectional Forces and Moments Comparison

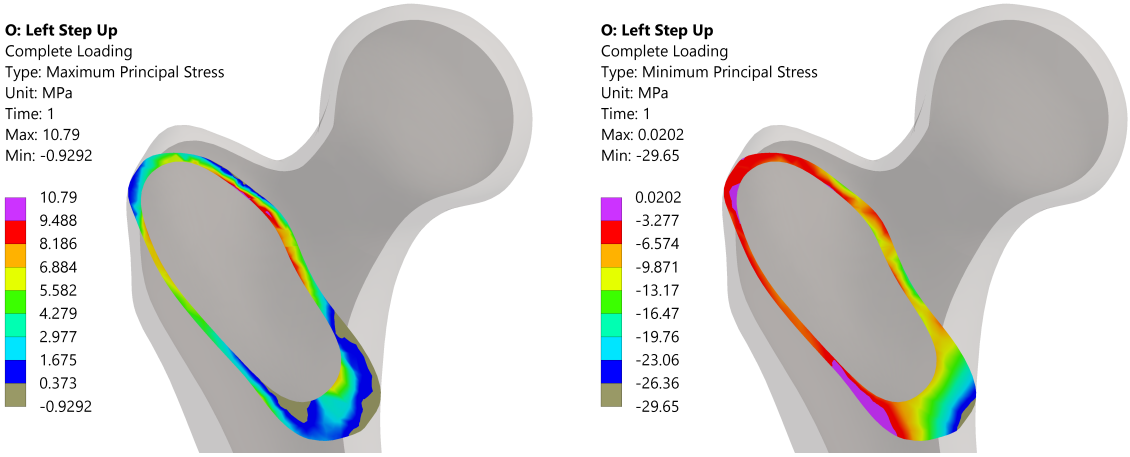

(a) Maximum Principal Stress **(b)** Minimum Principal of Stress

Figure 4.35: Peak Principal Stresses of Complete Loading Case During Left Step Up

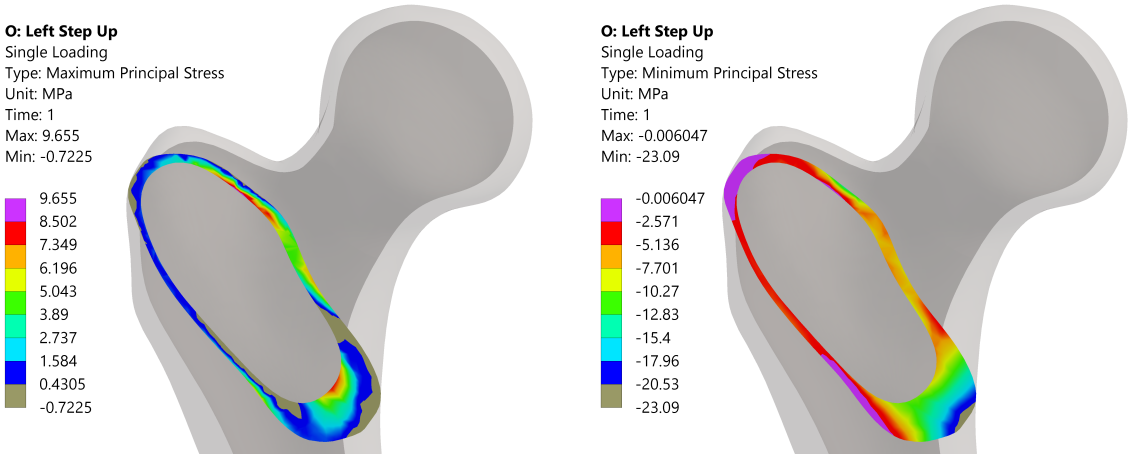

(a) Maximum Principal Stress **(b)** Minimum Principal Stress

Figure 4.36: Peak Principal Stresses of Single Force Loading Case During Left Step Up

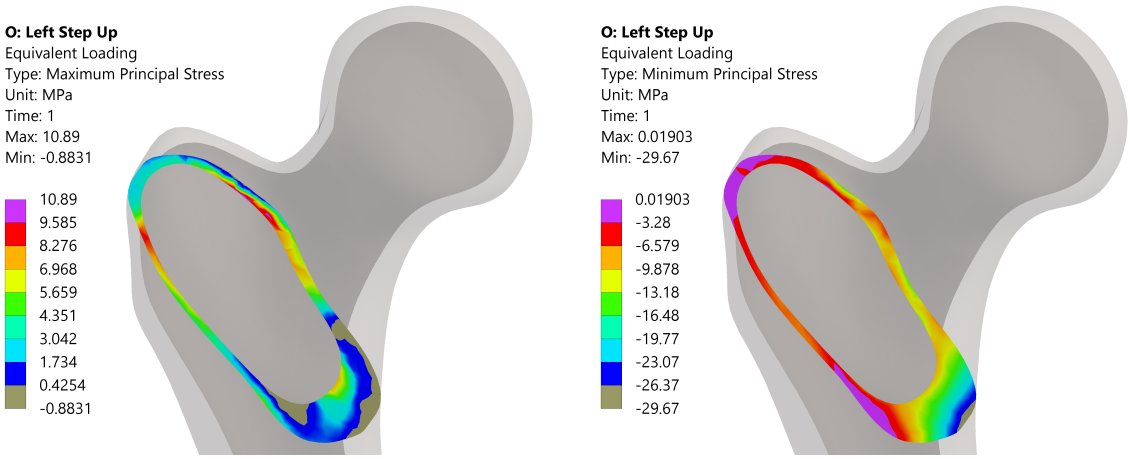

(a) Maximum Principal Stress **(b)** Minimum Principal Stress

Figure 4.37: Peak Principal Stresses of Experimental Loading Case During Left Step Up

4.4.5 Right Step Up (RSU)

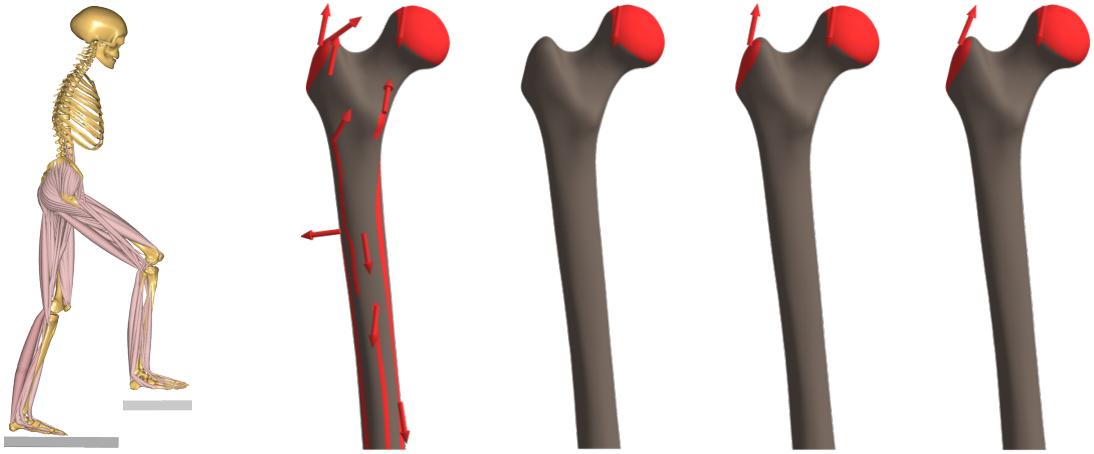

(a) Peak Stresses Position **(b)** Complete **(c)** Single **(d)** Significant **(e)** Equivalent

Figure 4.38: Right Step Up Loading of the Left Femur at the Peak Streeses Position

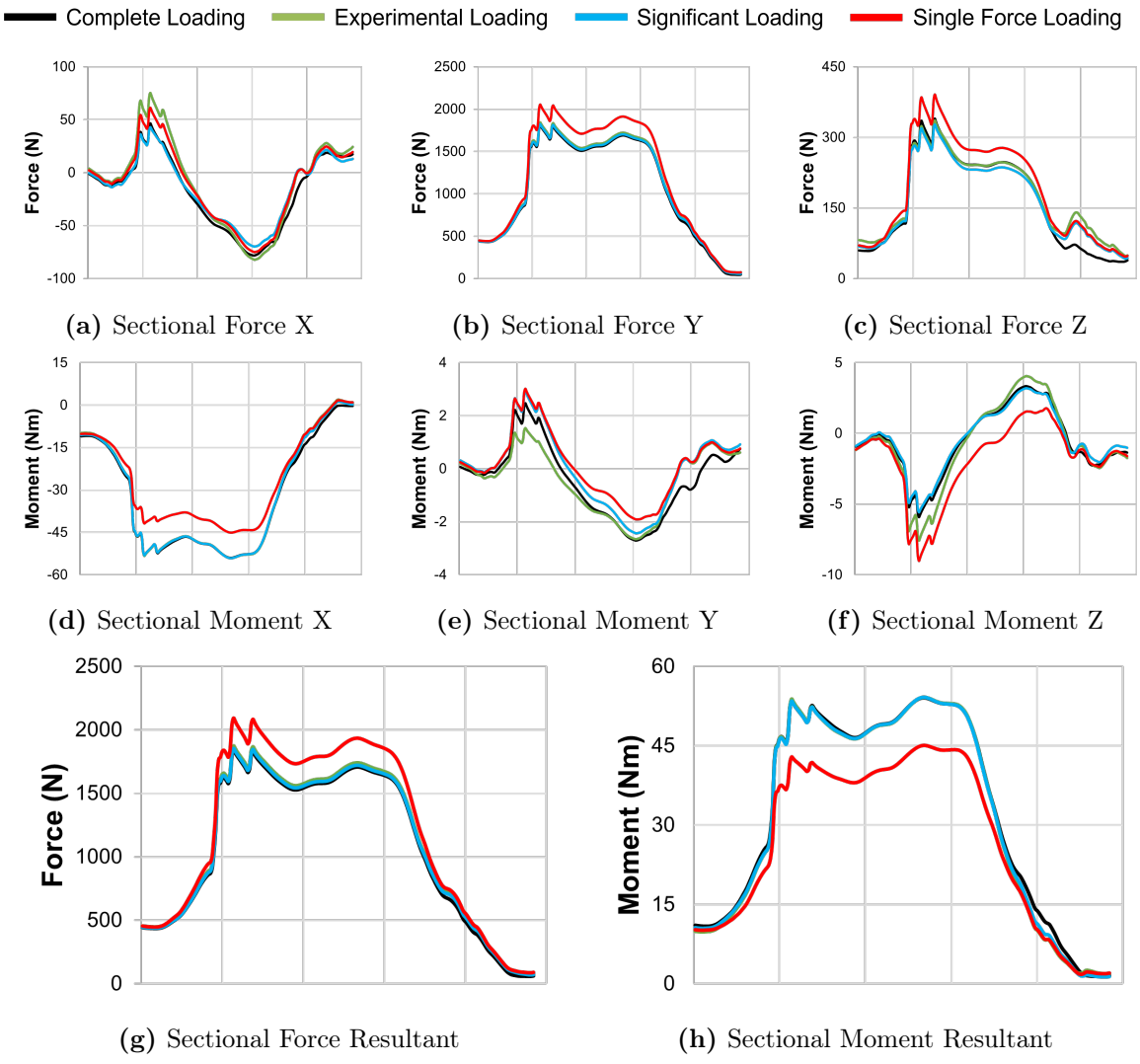

(a) Sectional Force X **(b)** Sectional Force Y **(c)** Sectional Force Z

(d) Sectional Moment X **(e)** Sectional Moment Y **(f)** Sectional Moment Z

(g) Sectional Force Resultant **(h)** Sectional Moment Resultant

Figure 4.39: Right Step Up Sectional Forces and Moments Comparison

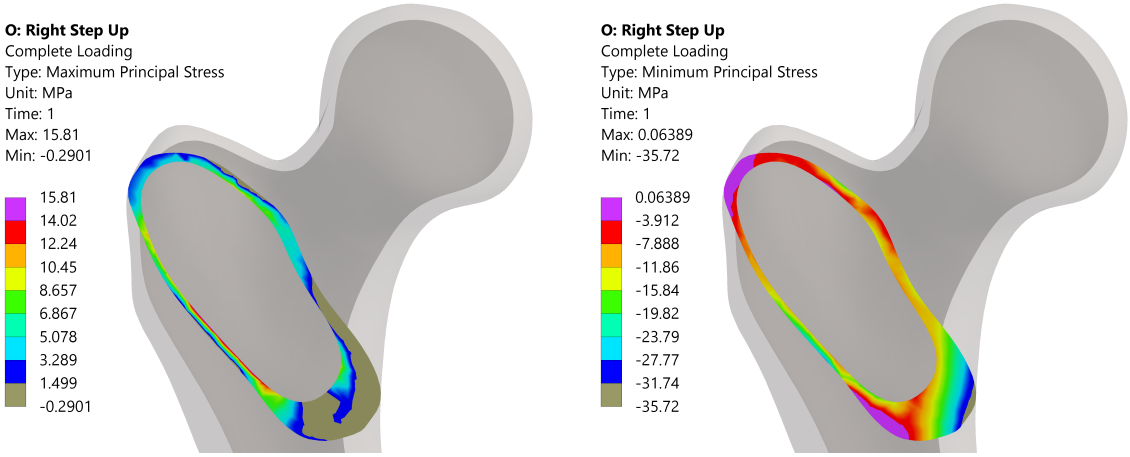

(a) Maximum Principal Stress **(b)** Minimum Principal of Stress

Figure 4.40: Peak Principal Stresses of Complete Loading Case During Right Step Up

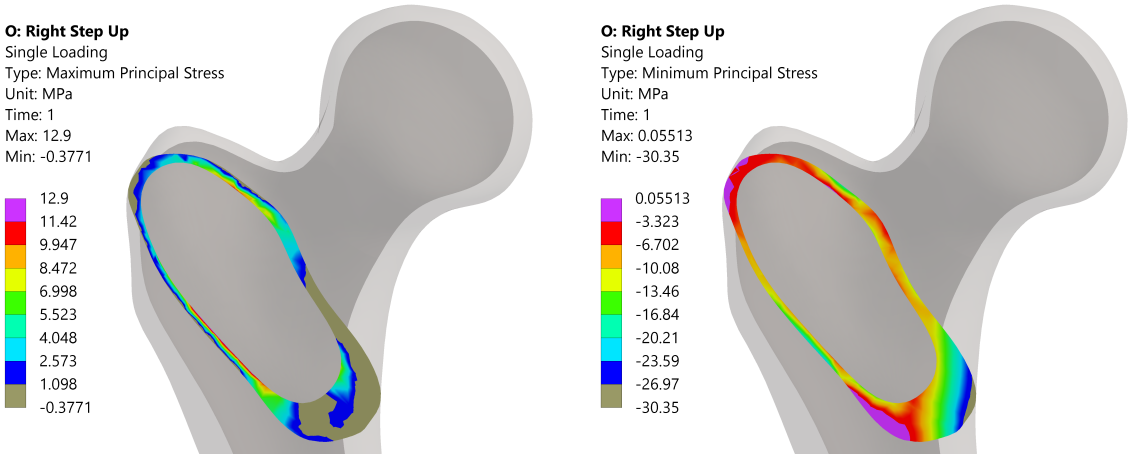

(a) Maximum Principal Stress **(b)** Minimum Principal Stress

Figure 4.41: Peak Principal Stresses of Single Force Loading Case During Right Step Up

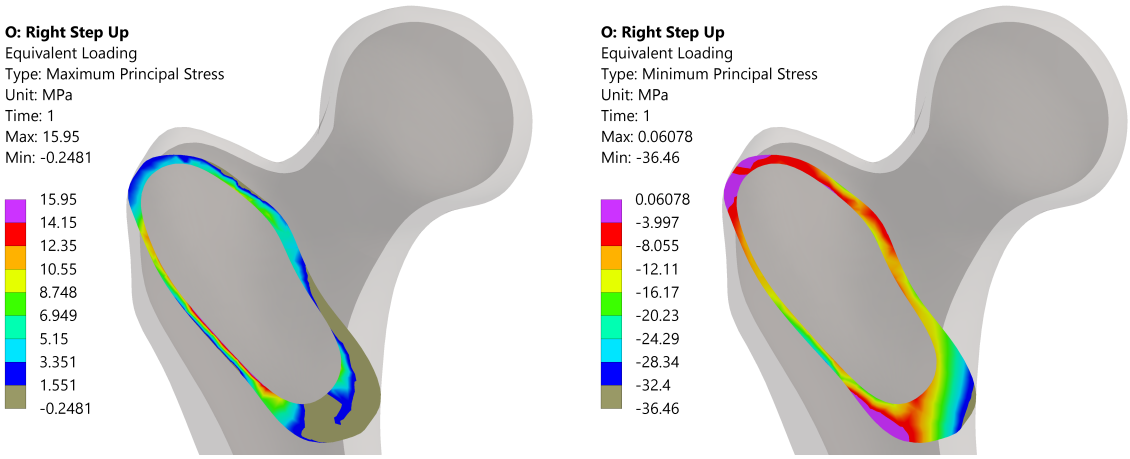

(a) Maximum Principal Stress **(b)** Minimum Principal Stress

Figure 4.42: Peak Principal Stresses of Experimental Loading Case During Right Step Up

4.4.6 Left Step Down (LSD)

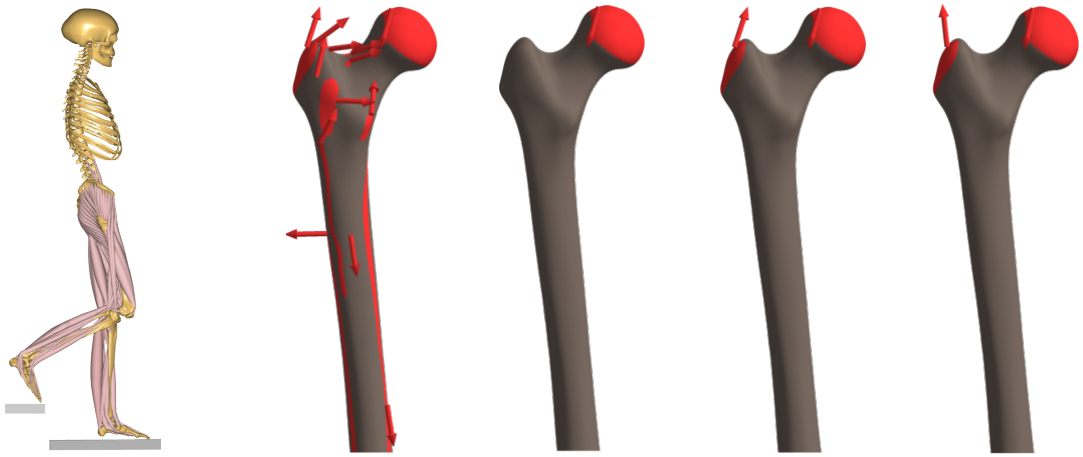

(a) Peak Stresses Position **(b)** Complete **(c)** Single **(d)** Significant **(e)** Equivalent

Figure 4.43: Left Step Down Loading of the Left Femur at the Peak Stresses Position

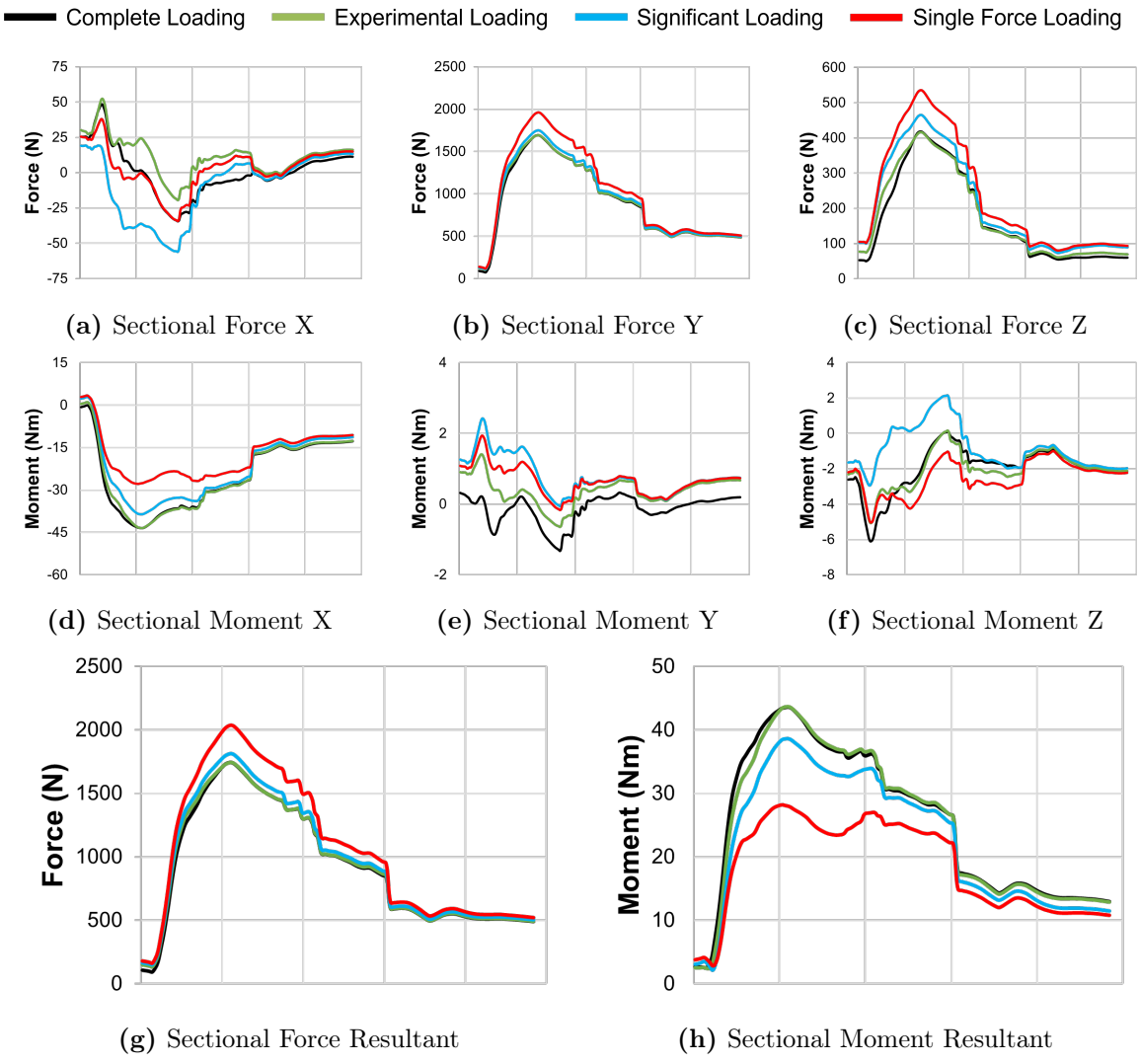

(a) Sectional Force X **(b)** Sectional Force Y **(c)** Sectional Force Z

(d) Sectional Moment X **(e)** Sectional Moment Y **(f)** Sectional Moment Z

(g) Sectional Force Resultant **(h)** Sectional Moment Resultant

Figure 4.44: Left Step Down Sectional Forces and Moments Comparison

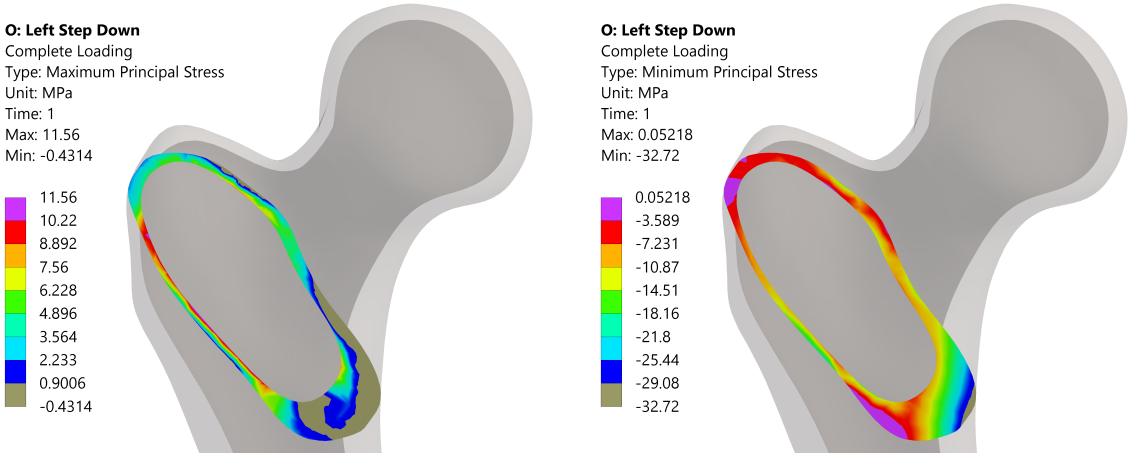

(a) Maximum Principal Stress **(b)** Minimum Principal of Stress

Figure 4.45: Peak Principal Stresses of Complete Loading Case During Left Step Down

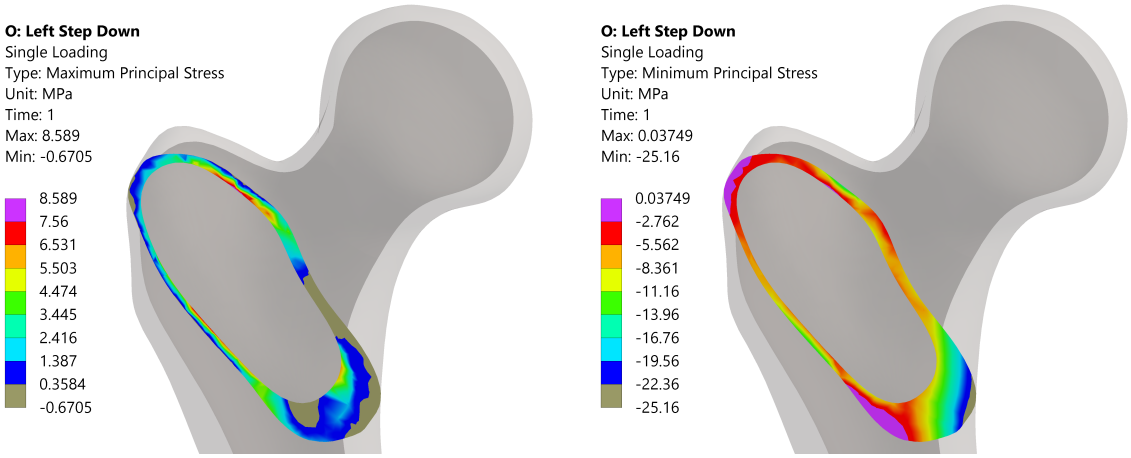

(a) Maximum Principal Stress **(b)** Minimum Principal Stress

Figure 4.46: Peak Principal Stresses of Single Force Loading Case During Left Step Down

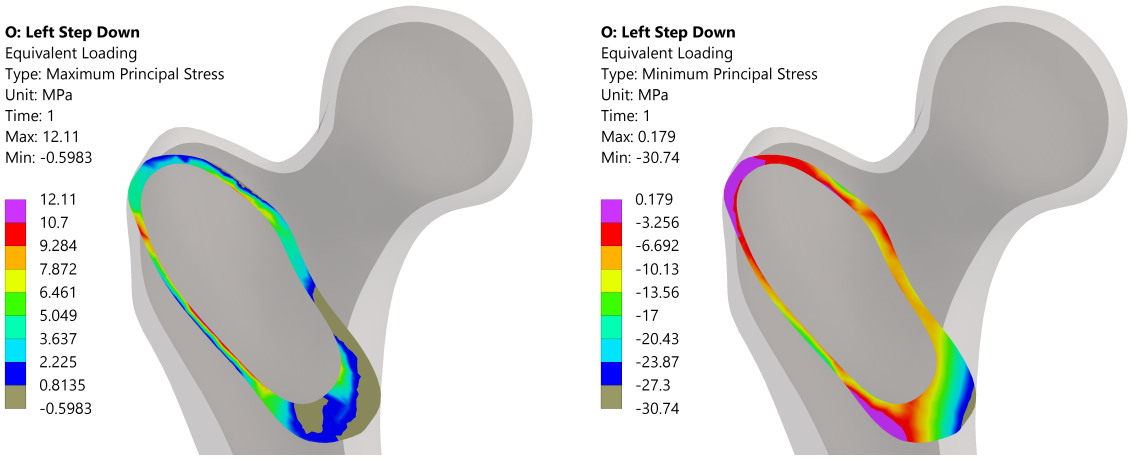

(a) Maximum Principal Stress **(b)** Minimum Principal Stress

Figure 4.47: Peak Principal Stresses of Experimental Loading Case During Left Step Down

4.4.7 Right Step Down (RSD)

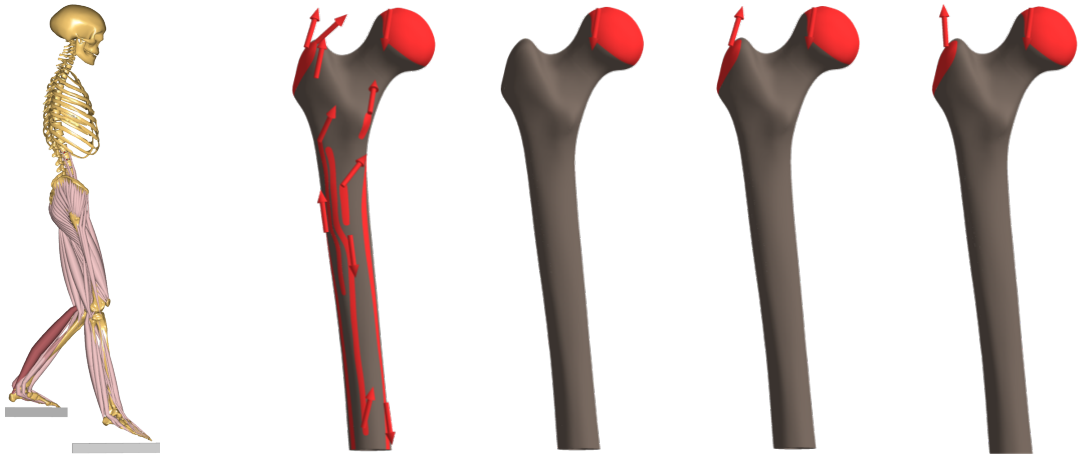

(a) Peak Stresses Position **(b)** Complete **(c)** Single **(d)** Significant **(e)** Equivalent

Figure 4.48: Right Step Down Loading of the Left Femur at the Peak Streeses Position

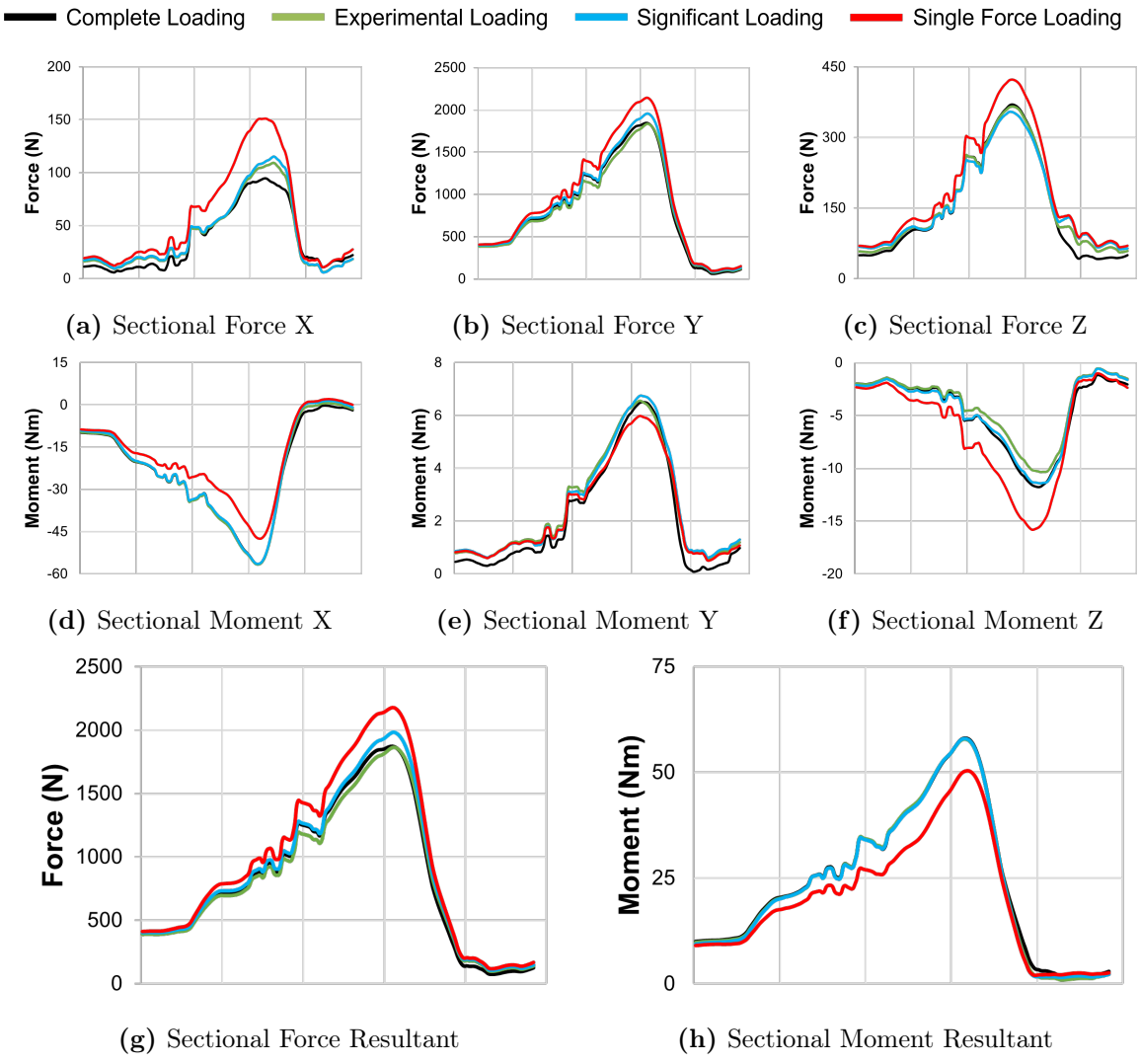

(a) Sectional Force X **(b)** Sectional Force Y **(c)** Sectional Force Z

(d) Sectional Moment X **(e)** Sectional Moment Y **(f)** Sectional Moment Z

(g) Sectional Force Resultant **(h)** Sectional Moment Resultant

Figure 4.49: Right Step Down Sectional Forces and Moments Comparison

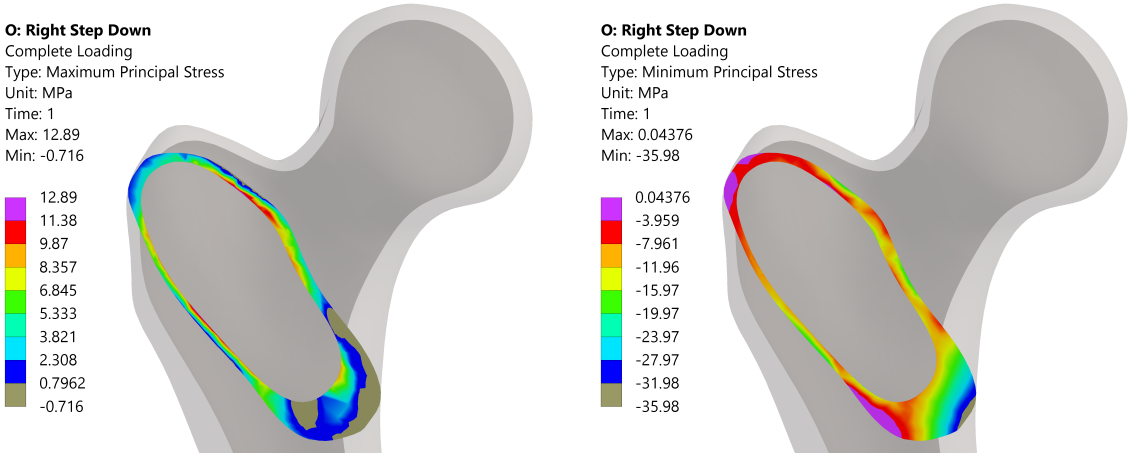

(a) Maximum Principal Stress **(b)** Minimum Principal of Stress

Figure 4.50: Peak Principal Stresses of Complete Loading Case During Right Step Down

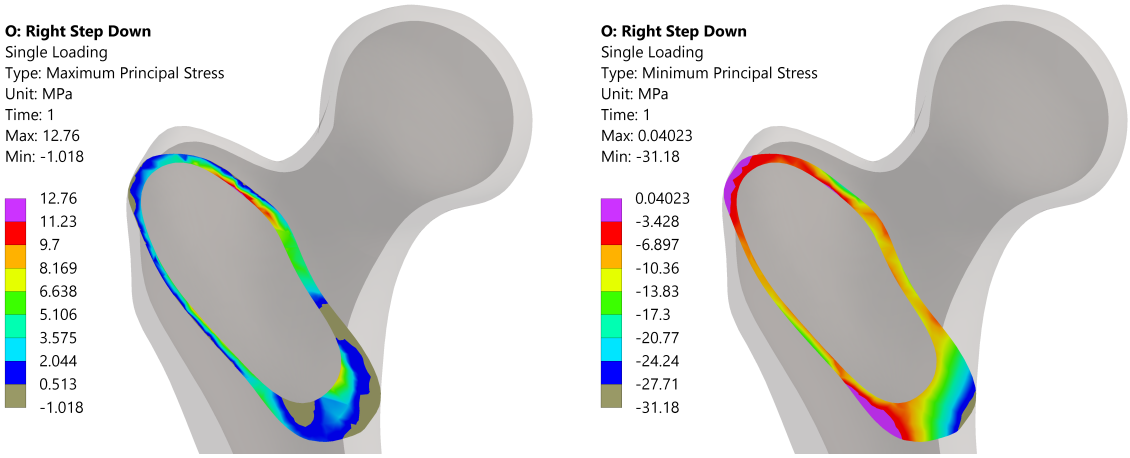

(a) Maximum Principal Stress **(b)** Minimum Principal Stress

Figure 4.51: Peak Principal Stresses of Single Force Loading Case During Right Step Down

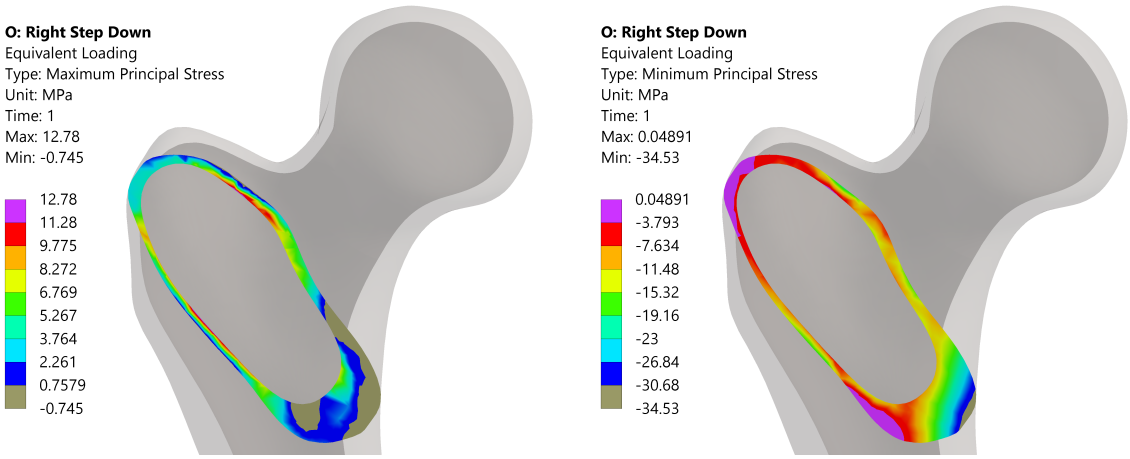

(a) Maximum Principal Stress **(b)** Minimum Principal Stress

Figure 4.52: Peak Principal Stresses of Experimental Loading Case During Right Step Down

4.5 Greyscale Quantitative Comparison

The comparison between different stress profiles is usually done on a qualitative level, because simply comparing the peak stress values without taking into consideration how it is distributed throughout the region of interest results on a misleading assessment. Therefore, the comparison is limited to logical observation, which is susceptible to subjectivity.

In order to complement the qualitative comparison between two distinctive stress profiles and produce a more objective assessment of their differences, the results were compared using an image processing algorithm. Two different stress profile results of a same region can be overlaid to create a composite image resulted from the difference of the original two. By plotting the stress profiles on greyscale, the image information can be recorded as a matrix with each element representing the numerical value of a pixel. For an 8-bit image, the pixel value ranges between 0 and 255, with pure black being represented by 0 and pure white by 255. Shades of grey are represented by the values in between going from darker to lighter shades as the value increases.

Once the image information is expressed as a matrix, the differences between two stress profiles can be easily quantified. By comparing each pixel of an image to its equivalent pixel on the correlating image, the numerical difference between their greyscale levels will generate an image with a deviation map based on pixel intensity. Therefore, the overall difference between two stress profiles can be quantified as the sum of the intensity level of all pixels from the deviation image.

This quantitative approach was used to compare both the **Single Force Loading** and the **Experimental Loading** to the reference (**Complete Loading** case). Therefore, a quantifiable value can be attributed to the difference of each one of them and be used to assess how much closer to the reference they are. The percentage difference of maximum and minimum principal stress states for the **Single Force Loading** and the **Experimental Loading** are respectively presented on Tables 4.14 and 4.15.

Table 4.14: Maximum Principal Stress Deviation From Reference

Factors	NG	LSU	RSU	LSD	RSD	SD	SU
Single Force	13.51%	17.71%	12.36%	14.75%	15.50%	13.54%	14.11%
Experimental	12.00%	6.60%	9.96%	12.90%	13.86%	7.55%	13.24%

Table 4.15: Minimum Principal Stress Deviation From Reference

Factors	NG	LSU	RSU	LSD	RSD	SD	SU
Single Force	28.01%	23.31%	21.14%	34.23%	22.90%	27.46%	24.40%
Experimental	18.87%	11.08%	18.42%	17.17%	22.96%	15.98%	17.36%

The side-by-side comparison of the maximum and minimum principal stress profiles and their respective deviation intensity maps are presented in Figures 4.53, 4.54, 4.55 and 4.56 for the movement scenario of Normal Gait (NG), while the stress profile comparison of the remaining movement scenarios are included in the Appendices.

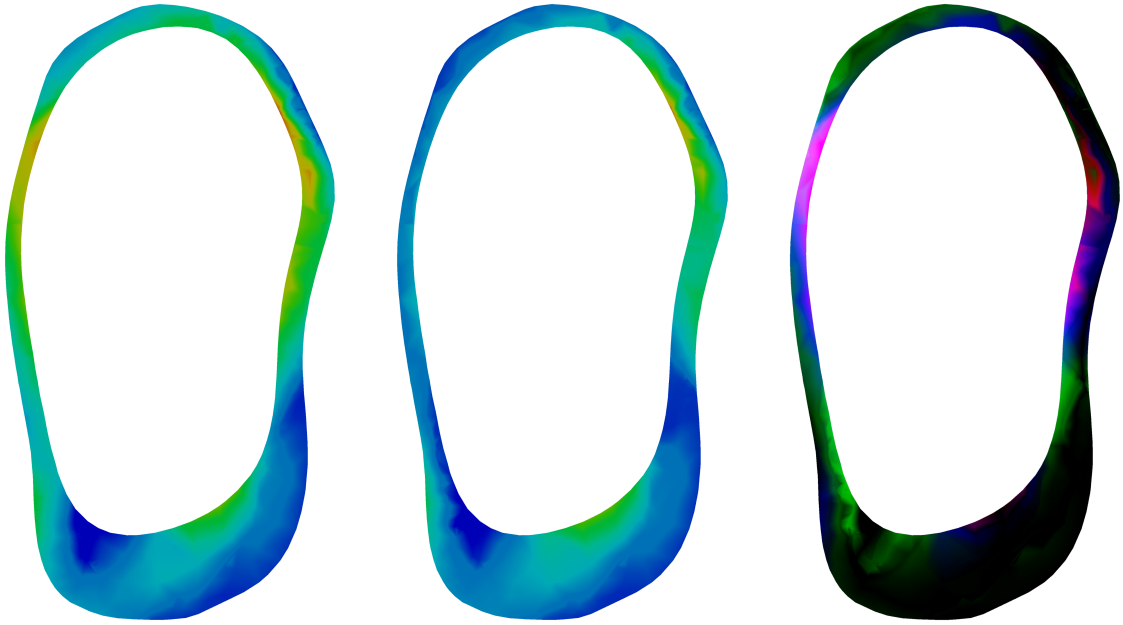

(a) Complete Loading Stress **(b)** Single Loading Stress **(c)** Deviation Intensity Map

Figure 4.53: NG Maximum Principal Stress Comparison - Complete Loading vs Single Force Loading

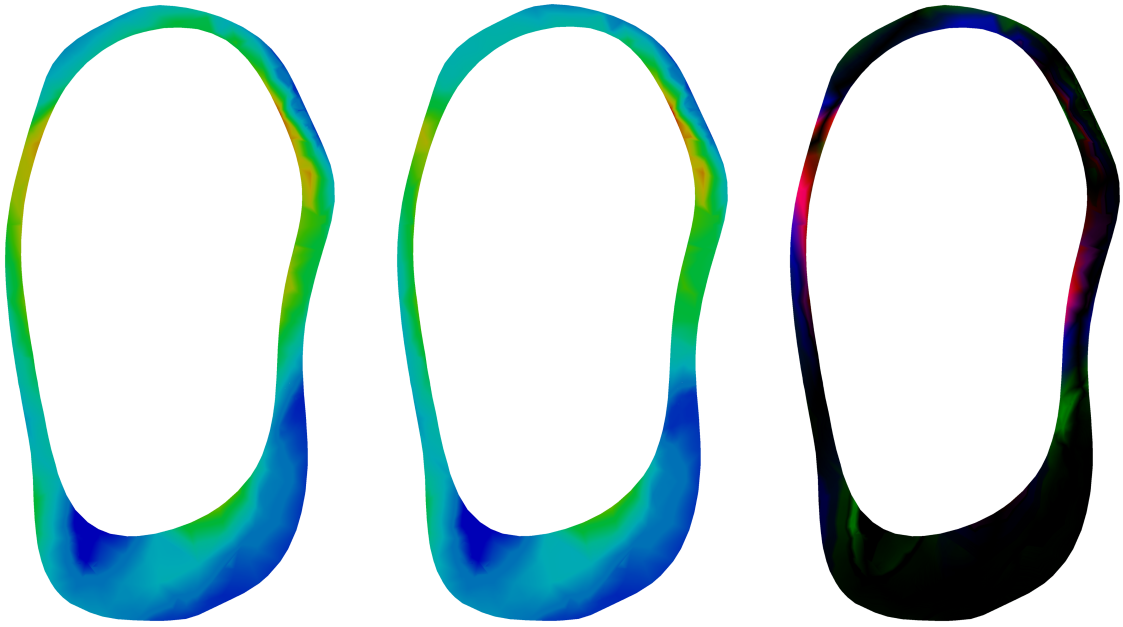

(a) Complete Loading Stress **(b)** Experimental Loading Stress **(c)** Deviation Intensity Map

Figure 4.54: NG Maximum Principal Stress Comparison - Complete Loading vs Experimental Loading

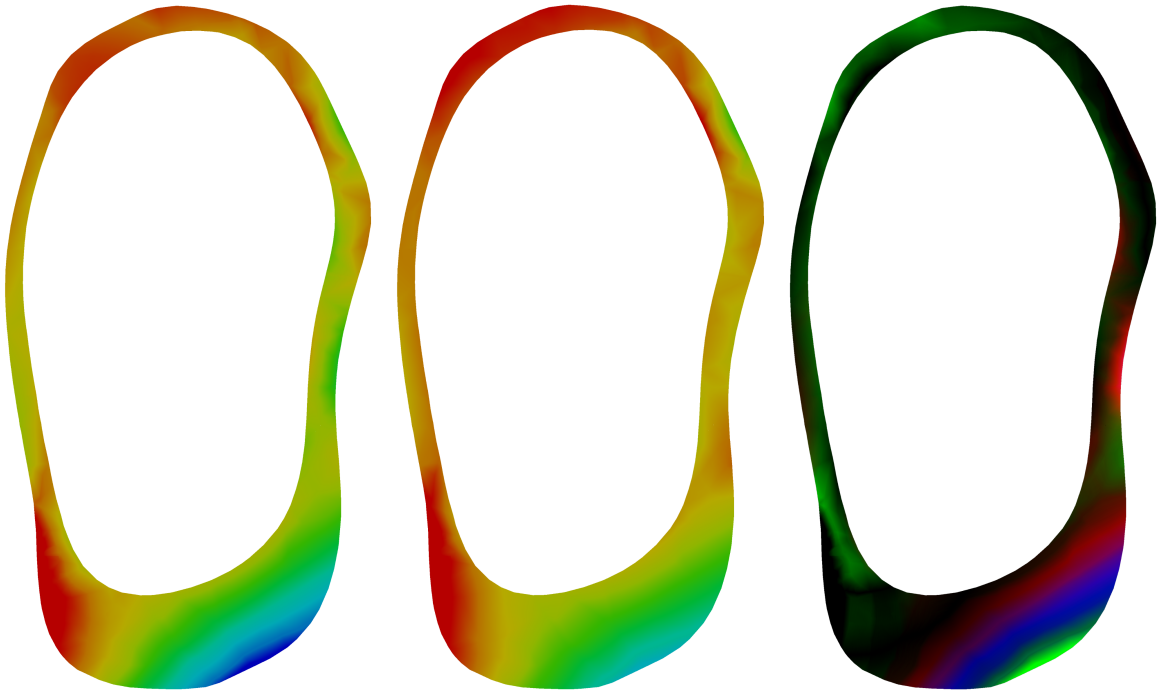

(a) Complete Loading Stress **(b)** Single Loading Stress **(c)** Deviation Intensity Map

Figure 4.55: NG Minimum Principal Stress Comparison - Complete Loading vs Single Force Loading

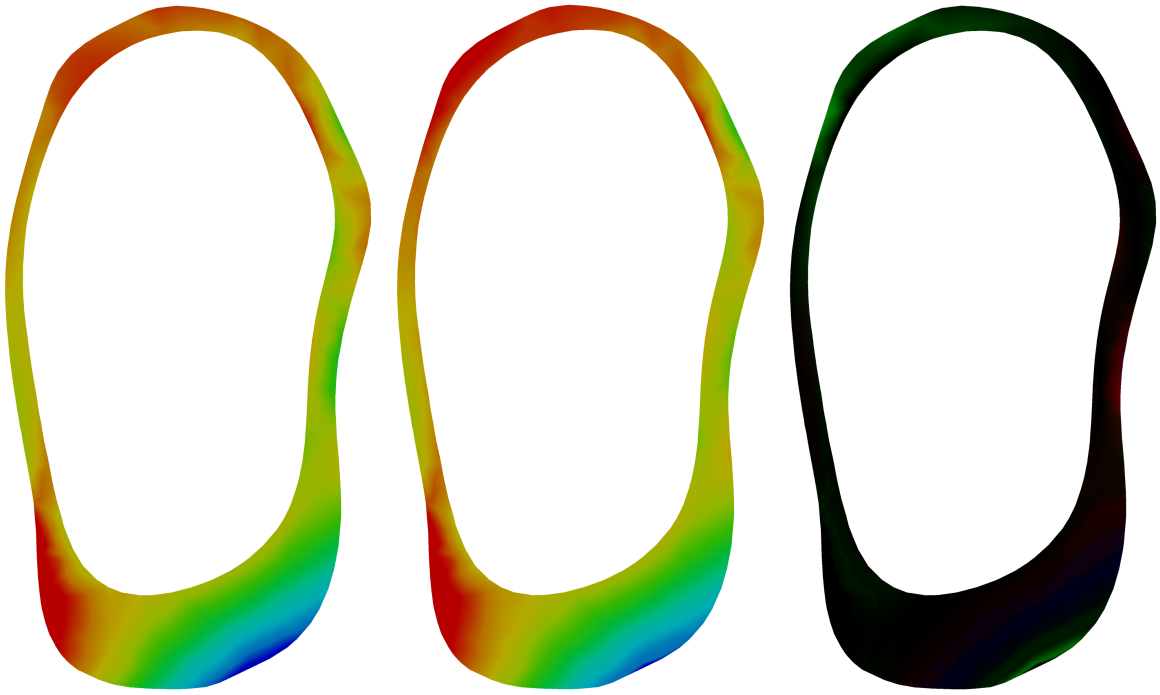

(a) Complete Loading Stress **(b)** Experimental Loading Stress **(c)** Deviation Intensity Map

Figure 4.56: NG Minimum Principal Stress Comparison - Complete Loading vs Experimental Loading

Chapter 5

Experimental Setup Design

Following the numerical simulations, experimental testing of the femur is necessary to adjust and validate the finite element models. However, since the experimental specimen, its loading and the multi-scenario proposed do not fit any standardised mechanical testing, a customised experimental setup needs to be designed and built.

Based on the results of the force significance study presented in Section 4.4, the Experimental Loading case can be considered a realistic alternative to the Complete Loading case. It is capable of generating sectional forces, moments and stresses at the proximal region of femur that are equivalent to the reference, while still being sufficiently simplified to be replicated within a laboratory setting.

The Experimental Loading cases proposed, independent of the movement scenario, require two different forces to be applied simultaneously to the femoral specimen. Of the seven movement scenarios, five of them (normal gait and all four stair climbing motions) have as statistically significant force sources the hip joint and the gluteus medius. The remaining two scenarios, sitting down and standing up, have the hip joint and the obturator externus. Additionally, since the objective is to be able to test all seven movements, the system needs to be adjustable to accommodate all scenarios.

5.1 Force Actuation

For all movement scenarios, the hip joint contact force is the primary source and is always applied to the femoral head in the downwards direction with varying inclination and magnitude for each scenario. The secondary force from the muscles on the other hand, is not homogeneous throughout the different movements, with most of the scenarios requiring a contribution coming from the gluteus medius, while the other coming from the obturator externus. Since the actuation area of the obturator externus is virtually inaccessible by a force actuator, a region at the lateral side of the greater trochanter was selected for the application of the secondary force for all movement scenarios.

In order to apply the necessary forces to the experimental specimens, an interface with attachment points needs to be created between the artificial bone and the force actuators. The primary force (hip joint) can be applied vertically to the femoral head. However, it is necessary to decouple both lateral components to guarantee that only the vertical force is being transferred. By using a flat platform fixed to the femoral head and transfer bearings at the extremity of the force actuator, a contact interface that prevents the transferring of lateral forces can be created, resulting on pure vertical motion between the bone and the actuator, as detailed in Figure 5.1. This flat platform is fixed to the femoral head by pouring resin within a casting pot that is included on its bottom side, as detailed in Figure 5.2a.

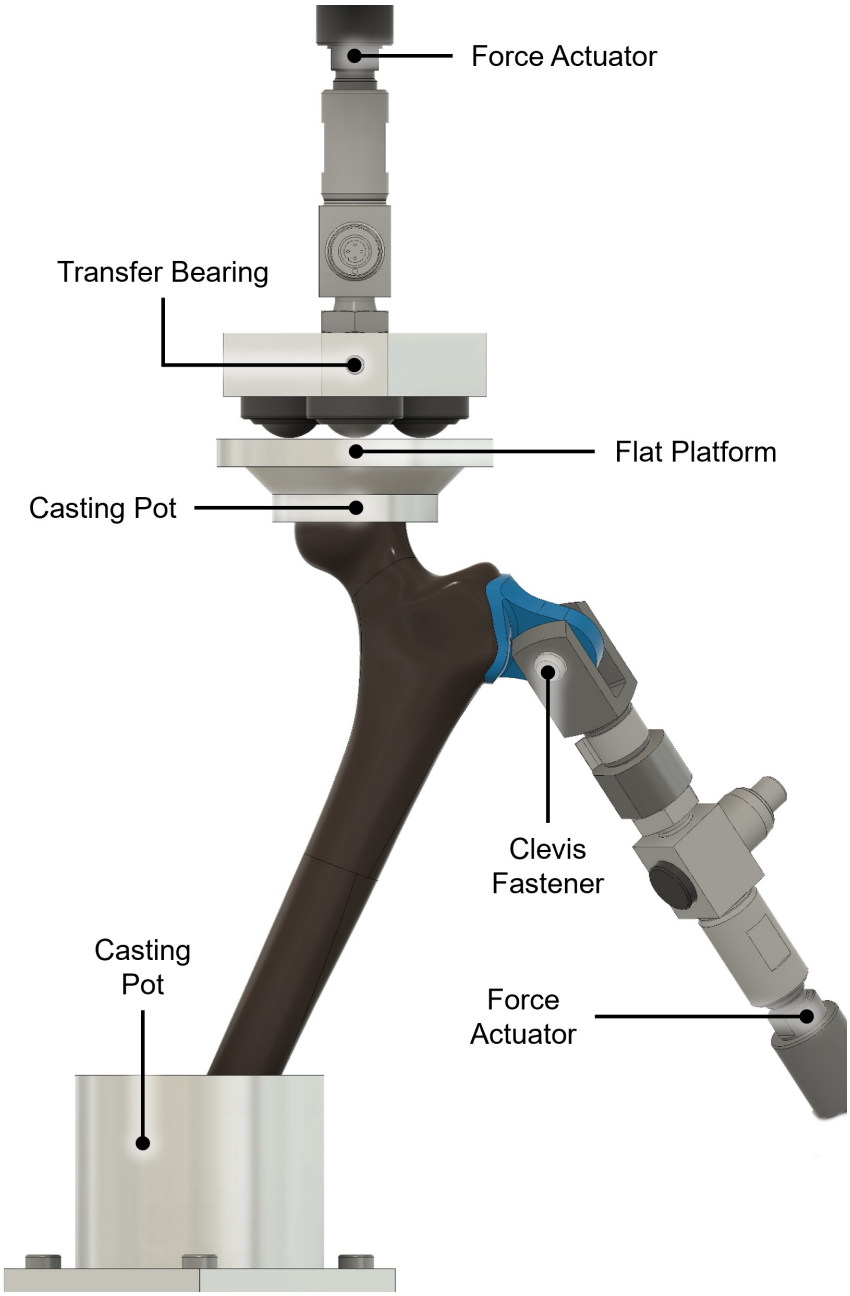

Figure 5.1: Force Actuation Setup

The application of the secondary force is done through a bracket that is glued to the bone and attached to the force actuator. By 3D printing this bracket, it is possible to accurately position it following the contour of the bone's surface, as shown in Figure 5.2b. To accommodate the deformation of the bone under load, spherical joints and clevis fasteners are used at each extremity of the actuator, as shown in Figure 5.1, to ensure that the force remains purely longitudinal throughout the movement cycle. The bone is secured in place to the test bench by its distal extremity by pouring resin within a casting pot bolted to the table, similarly to the flat platform on top of the head.

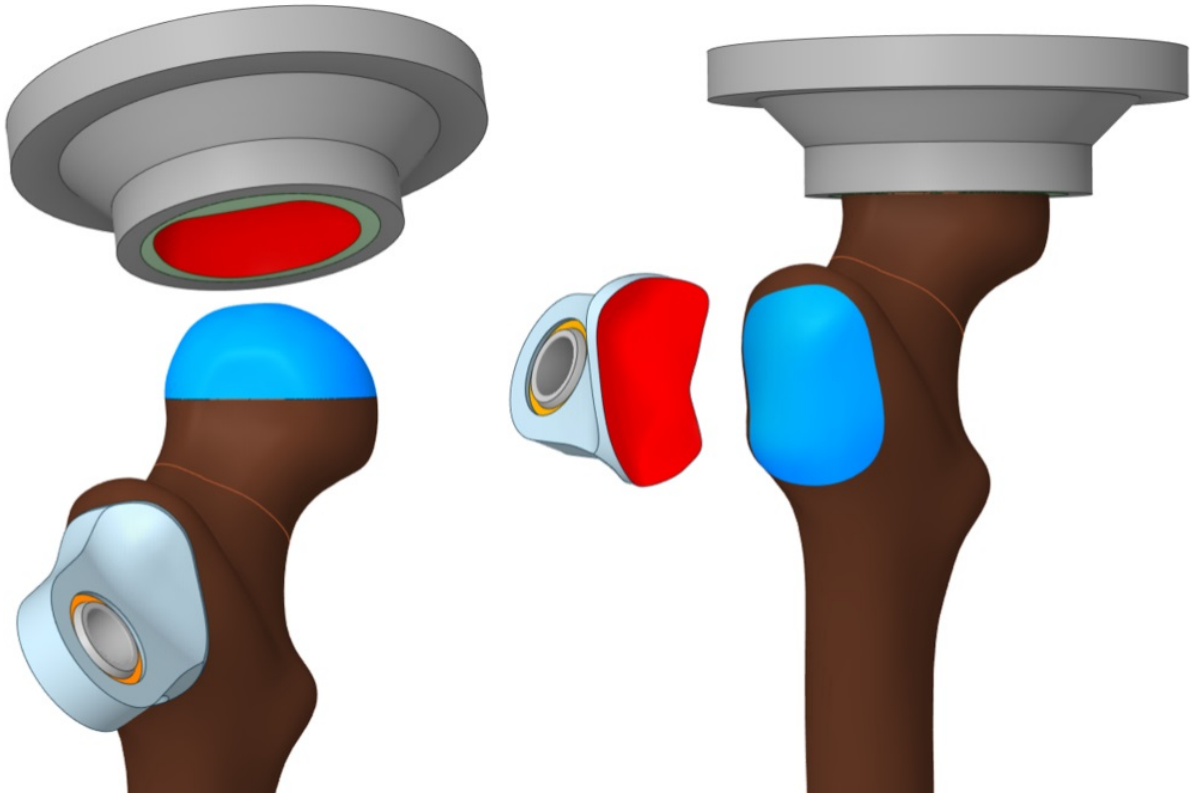

(a) Casting/Bone Surface Contour **(b)** Bracket/Bone Surface Contour

Figure 5.2: Force Input Attachment Interfaces

The forces being applied to the bone changes in magnitude and direction for every different movement scenario. Therefore, the test bench requires a certain degree of adjustability for the force actuators to be able to accommodate and perform all the proposed tests. In the case of the top actuator, that applies the primary force to the femoral head, no adjustment is possible due to it being completely fixed, thus relying on the positioning of the bone to define the force orientation, as it is detailed in Section 5.2.

The bottom actuator on the other hand is free to be oriented following the required direction of the force for any given scenario. In order to achieve an accurate positioning of the actuator, multiple different fixation points are needed to attach it on the base, as illustrated in Figure 5.3. The holes on the base plate were manufactured oblong in case minor adjustments are required while aligning the actuator to the specimen.

Additionally, since the force actuator has a significant length even when completely retracted, depending on its position in relation to the specimen, a considerable height difference between their bases is required. Most of the height gap can be mitigated by establishing separate bases at two different levels. However, some scenarios required an additional rising of the specimen, which was achieved by using a set of spacers, as shown in Figures 5.4, 5.5, 5.6 and 5.7.

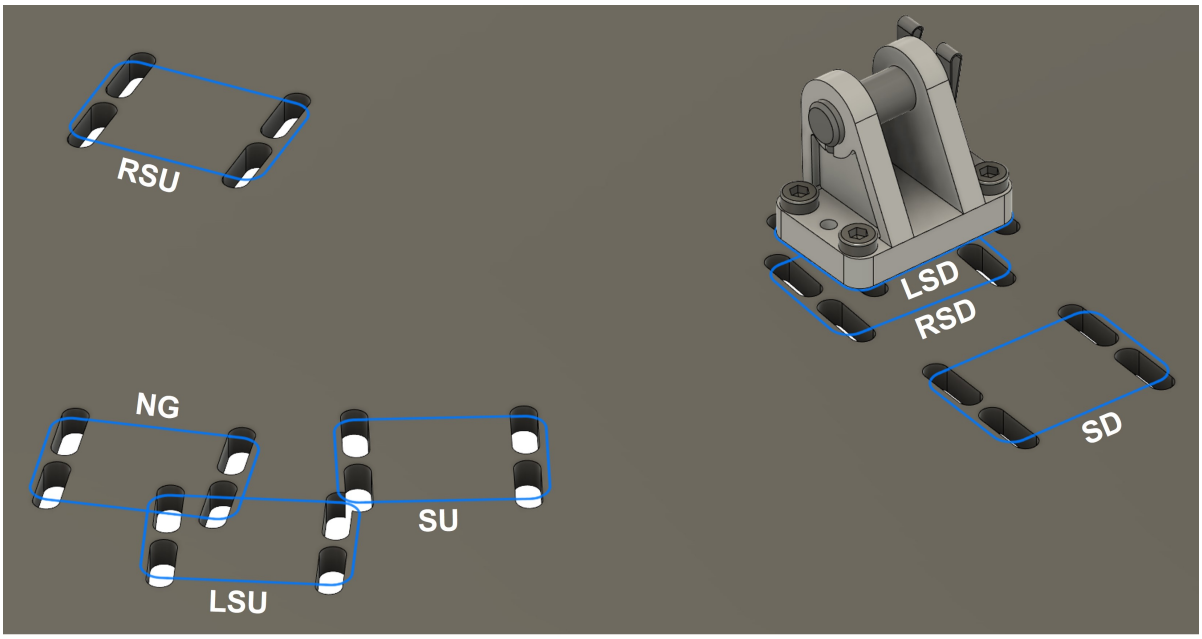

Figure 5.3: Adjustable Attachment Point of Secondary Actuator

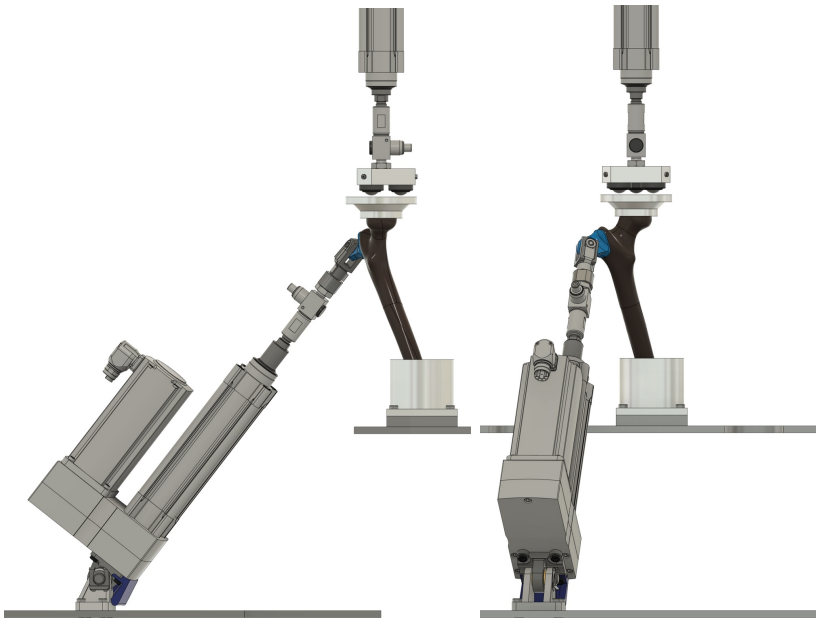

(a) NG Side View **(b)** NG Back View

Figure 5.4: Actuator and Specimen Positioning for The Walking Scenario

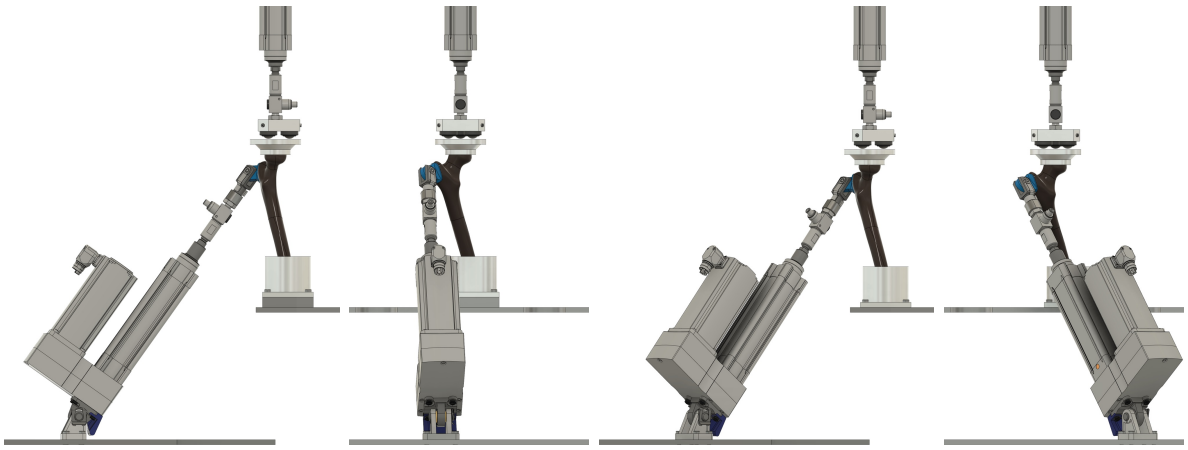

(a) SU Side View **(b)** SU Back View **(c)** SD Side View **(d)** SD Back View

Figure 5.5: Actuator and Specimen Positioning for the Sitting Scenario

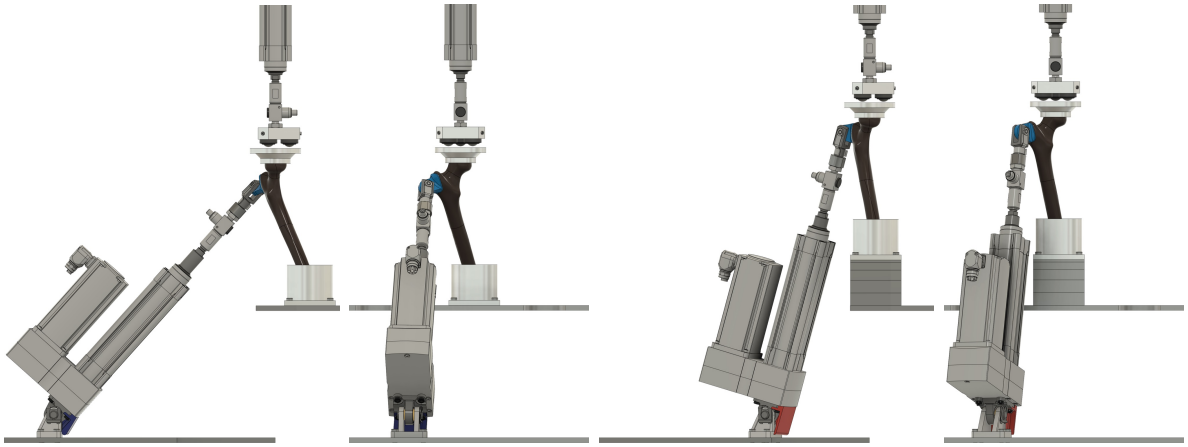

(a) LSU Side View **(b)** LSU Back View **(c)** RSU Side View **(d)** RSU Back View

Figure 5.6: Actuator and Specimen Positioning for the Stepping Up Scenario

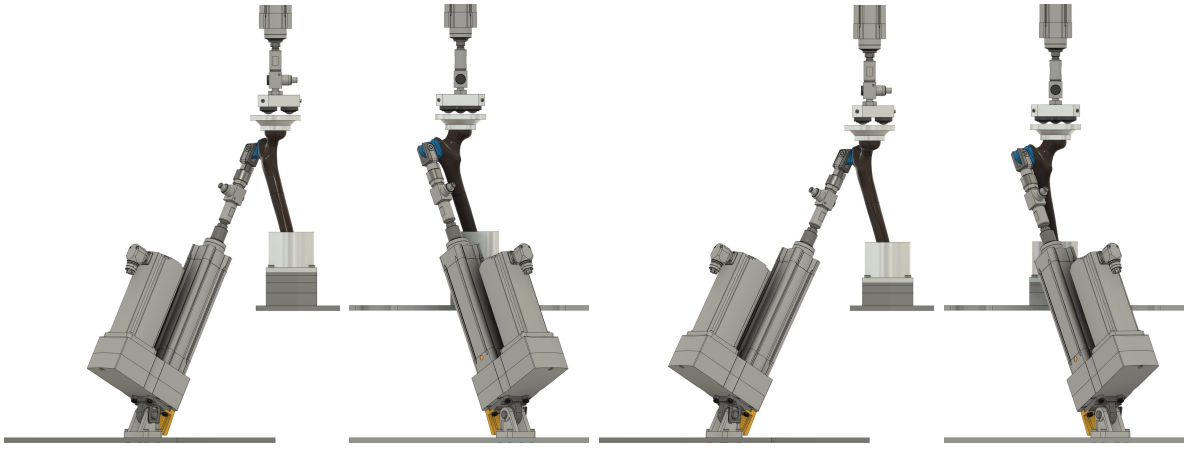

(a) LSD Side View **(b)** LSD Back View **(c)** RSD Side View **(d)** RSD Back View

Figure 5.7: Actuator and Specimen Positioning for the Stepping Down Scenario

5.2 Specimen Positioning

The top actuator, responsible for applying the hip joint force to the femoral head, is aligned with the vertical axis of the test stand with its inclination is fixed. Thus, the direction of the force is solely defined by the positioning of the specimen on the test bench. This limited adjustability of the top actuator makes the accurate positioning of the specimen a crucial step for correctly inputting the forces. For all movement scenarios, there are seven different positions for the specimen, as illustrated in Figure 5.8.

To guarantee accurate alignment of the specimen, a set of positioning jigs was designed to properly cast the bones in place. Using 3D printing, it is possible to manufacture positioning clamps containing the contour of the bone, as shown in Figure 5.9. Having the contour of the specimen printed on the clamps ensures that there is only one correct position for them to be mounted, making it a foolproof process. Once the femur is fastened between the clamps, the bone can be accurately positioned by fixing it at the correct height using threaded rods secured to a jig plate, as shown in Figure 5.10.

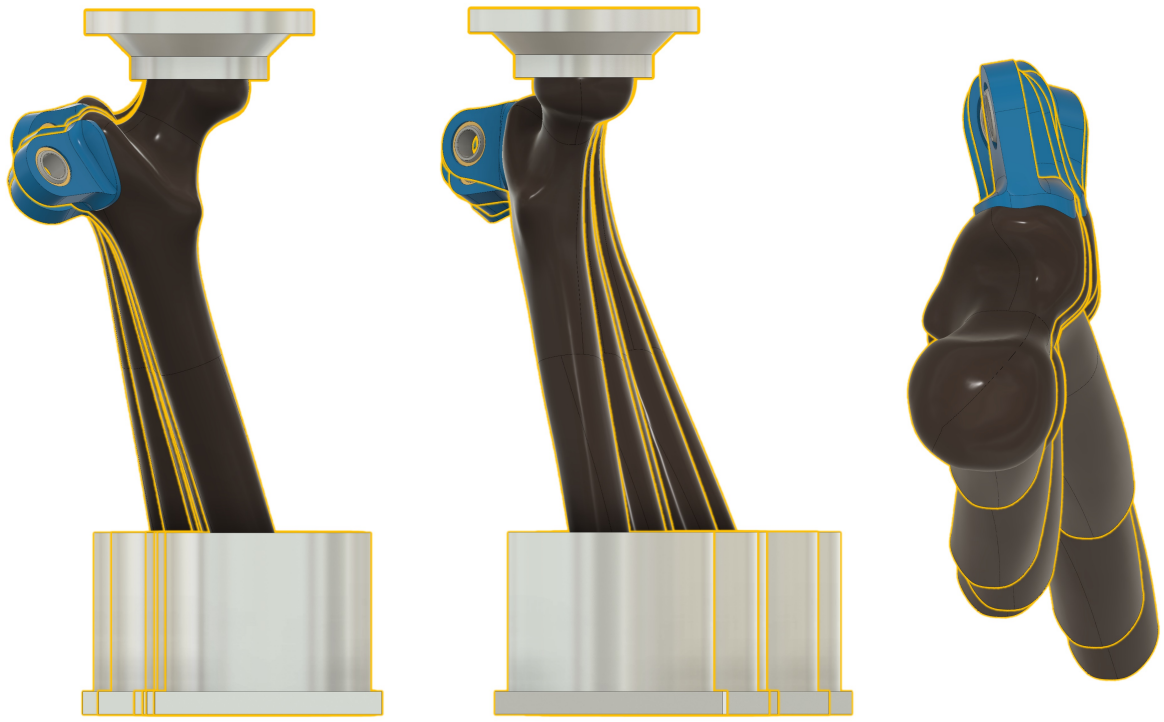

(a) Posterior View **(b)** Medial View **(c)** Superior View

Figure 5.8: Superposed Positioning of Specimens (All Seven Movement Scenarios)

With the specimen fixed in place, the casting pot is secured in the jig plate and the resin is poured in, as presented in Figure 5.10a. After the resin cures and the distal extremity of the bone is solidly bound within the casting pot, the same process is repeated for the proximal extremity, using a second jig plate to position the flat platform on the femoral head, as shown in Figure 5.10b.

(a) Anterior Clamp **(b)** Posterior Clamp

Figure 5.9: 3D Printed Contour Clamps

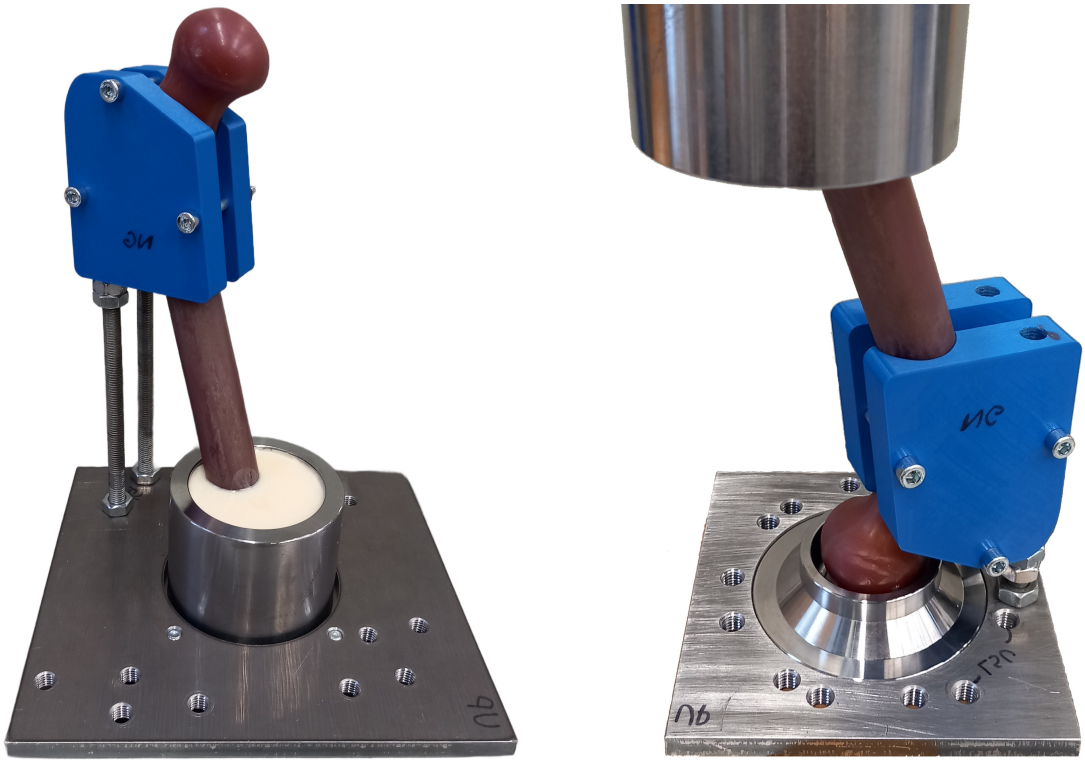

(a) Distal Extremity Positioning **(b)** Proximal Extremity Positioning

Figure 5.10: Positioning of Specimen for Casting

Once the resin is fully cured, the positioning clamps can be removed and the specimen will be correctly oriented, as presented in Figure 5.11a. Finally, the attachment bracket for the secondary force actuator is bonded to the bone using epoxy adhesive, as seen in Figure 5.11b. Since the bracket fixation surface is printed including the contour surface of the lateral greater trochanter, there is only one orientation in which the bracket can be fixed, guaranteeing accurate positioning and perfect alignment with the bottom force actuator.

(a) Specimen Cast in Position **(b)** Attachment Bracket Bonded in Position

Figure 5.11: Attachment Bracket Bonded to Experimental Specimen

5.3 Testing Machine

The experimental system was designed on top of an old testing machine frame, comprised of two vertical guide columns and a movable crosshead, as presented in Figure 5.12. The top actuator is secured at the crosshead, making it very stable and capable of having its height adjustable. The base plates, responsible for fixing the bottom actuator and the test specimen, were manufactured from thick steel sheets using laser cutting to make the different sets of fixation holes that allow for the setup of all seven predefined body movement scenarios.

Both actuators are equipped with force sensors at their extremities, which are used as feedback reference for the control of the system. The Experimental Loading cases, obtained from the force significance study detailed in Chapter 4, are used as input signals for the actuators. The force profiles can be discretised into finite time steps, describing the full cycle of each predefined body movement and allowing their complete range of motion to be replicated in the experiment for all scenarios.

Figure 5.12: Assembled Testing Machine

Conclusion

The objective of this study was to develop a methodology and experimental system capable of realistically replicating the loading of the femur to analyse the stability of fractures of its proximal region. Furthermore, it was proposed to expand on the state-of-the-art biomechanical tests observed in the literature, addressing their shortcomings of simplistic loading conditions and neglect of muscle forces contribution. Considering that these studies usually only apply a singular force to the femoral head based on a simplified single leg stance, the proposed design aimed to create a more complex multi loading system capable of replicating the full cycle of more complex body motions.

Using a methodology backed by numerical simulations and statistical studies, presented in Figure 6.1, a customized experimental test stand was designed and built to achieve the proposed goal. Musculoskeletal simulations were employed to realistically estimate the joint and muscle forces being applied to the femur during a diverse range of complex body movement scenarios based on motion capture recordings of human subjects. By adding the forces calculated with the musculoskeletal model into the finite element model, the realistic mechanical behaviour of the bone under load can be observed, using the results to statistically identify the most significant to be included on the experimental setup. Since the expected use of the proposed test stand is to compare the performance of different proximal femoral nail configurations and to create a guideline for their selection process, the design of the experimental setup was done based on artificial bones as test specimens, allowing for repeatable and reproducible test runs due to their consistency between samples.

For all the movement scenarios included in this study, the joint forces estimated using the musculoskeletal model resulted not only on the same order of magnitude of the empirical reference measured using instrumented implants, but it also revealed a similar force profile throughout the full cycle of each motion. The results obtained from the finite element simulations presented a reasonable equivalency between the stress states observed at the fracture section for the Complete Loading and the proposed Experimental Loading.

This simplified loading case, capable of producing results equivalent to the Complete Loading reference, was the basis for the design of the experimental setup. Two simultaneous forces being applied to the femur, representing the hip joint force and the

muscles respectively, is the configuration proposed to elevate the state-of-the-art currently present in the literature. Furthermore, the test stand was designed not only to replicate the full cycle of a complex loading, but also to be adjustable to a diversity of body movement scenarios, ranging from walking and sitting to stair climbing.

In conclusion, the methodology developed in this study was capable of producing an advanced customized experimental test stand that addresses the limitations of current biomechanical testing. That was achieved by introducing an additional source of force, that is representative of the muscles, and by making use of more complex loading scenarios that recreate relevant daily body movements.

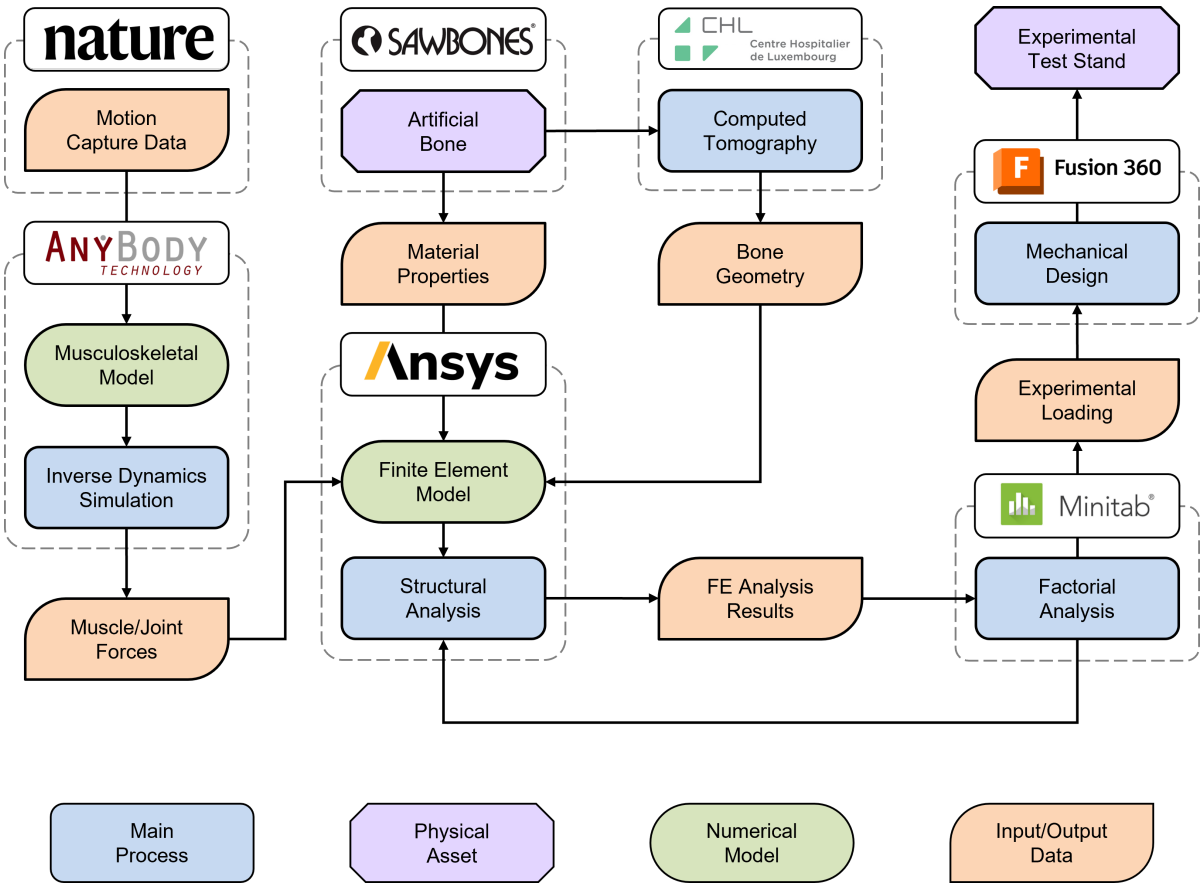

Figure 6.1: Methodology Flowchart

Research Prospective

The manufacturing of the test stand designed throughout the development of this project is an ongoing process close to completion. Even though its delay hindered the inclusion of experimental results in this study, it does not limit the future use of the test stand in other projects. Once the experimental setup is operational, a series of static tests should be performed using non fractured specimens of each movement scenario to fine-tune and validate the finite element models developed throughout this study.

After the initial validations, when the testing machine is fully functional and calibrated, it should be used for continuing this project. Considering that the original use proposed for this testing setup was the study of the stability of pertrochanteric fractures treated with proximal femoral nails, a comprehensive set of experiments encompassing implants with different diameters, would be a suitable starting point. With the goal of comparing the performance between tight and loose fitted implants, fractured osteoporotic artificial bones secured with theses respective proximal femoral nail configurations can be analysed on cyclic tests. By monitoring the spatial displacement of the femoral head, it is possible to assess the stability of the fracture measuring how much and how quickly the head collapses throughout the cycles of fatigue testing.

The quantitative data generated by the proposed biomechanical tests have the potential to shine a light on the mechanics of pertrochanteric fractures, providing surgeons with factual information that can be used as guidelines for implant selection prior to surgery. Hence effectively improving the chances of recovery for the patients.

References

[1] C. Milner, *Functional Anatomy for Sport and Exercise: Quick Reference*. 2008, vol. 1, ISBN: 9781134081660.

[2] S. Mader, *Understanding Human Anatomy and Physiology*. 2004, vol. 5, ISBN: 9780072935172.

[3] M. R. Feldesman, J. G. Kleckner, and J. K. Lundy, "Femur/Stature Ratio and Estimates of Stature in Mid- and Late-Pleistocene Fossil Hominids," *American Journal of Physical Anthropology*, vol. 83, no. 3, pp. 359–372, 1990, ISSN: 0002-9483. DOI: 10.1002/ajpa.1330830309.

[4] K. S. Saladin, S. J. Sullivan, and C. A. Gan, *Human Anatomy*. 2016, vol. 5, ISBN: 9780073403700.

[5] R. L. Drake, A. W. Vogl, and A. W. M. Mitchell, *Gray's Anatomy for Students*. 2020, vol. 4, ISBN: 9780323393041.

[6] A. Gilroy, B. Macpherson, and J. Wikenheiser, *Atlas of Anatomy*. 2013, vol. 4, ISBN: 9781684202034.

[7] E. Meinberg, J. Agel, C. Roberts, M. Karam, and J. Kellam, "Fracture and Dislocation Classification Compendium - 2018," *Journal of Orthopaedic Trauma*, vol. 32, no. 1, 2018, ISSN: 0890-5339. DOI: 10.1097/BOT.0000000000001063.

[8] M. Müller, P. Koch, S. Nazarian, and J. Schatzker, *The Comprehensive Classification of Fractures of Long Bones*. 1990, vol. 1, ISBN: 9783540181651.

[9] H. Song, S.-Y. Chen, and S.-M. Chang, "What Should Be Filled in the Blank of 31A2.1 in AO/OTA-2018 Classification," *Injury*, vol. 51, no. 6, pp. 1408–1409, 2020, ISSN: 0020-1383. DOI: 10.1016/j.injury.2020.02.069.

[10] K.-L. Ma, X. Wang, F.-J. Luan, *et al.*, "Proximal Femoral Nails Antirotation, Gamma Nails, and Dynamic Hip Screws for Fixation of Intertrochanteric Fractures of Femur: A Meta-Analysis," *Orthopaedics & Traumatology: Surgery & Research*, vol. 100, no. 8, pp. 859–866, 2014, ISSN: 1877-0568. DOI: 10.1016/j.otsr.2014.07.023.

[11] DePuy Synthes, *Instructions for Use - Intramedullary Nailing Implants*, 2018. [Online]. Available: http://emea.depuysynthes.com/hcp/reprocessing-care-maintenance.

[12] M. W. Whittle, *An Introduction to Gait Analysis*. 2007, vol. 4, ISBN: 9780750688833.

[13] C. Kirtley, *Clinical Gait Analysis: Theory and Practice*. Elsevier, 2006, vol. 1, ISBN: 9780443100093.

[14] J. Adams and K. Cerny, *Observational Gait Analysis: A Visual Guide*. 2018, vol. 1, ISBN: 9781630910402.

[15] I. Levadnyi, J. Awrejcewicz, Y. Zhang, and Y. Gu, "Comparison of Femur Strain Under Different Loading Scenarios: Experimental Testing," *Journal of Engineering in Medicine*, vol. 235, no. 1, pp. 17–27, 2021, ISSN: 0954-4119. DOI: 10.1177/0954411920951033.

[16] Z. Yosibash, A. Katz, and C. Milgrom, "Toward Verified and Validated FE Simulations of a Femur with a Cemented Hip Prosthesis," *Medical Engineering & Physics*, vol. 35, no. 7, pp. 978–987, 2013, ISSN: 1350-4533. DOI: 10.1016/j.medengphy.2012.09.007.

[17] J. Keyak, "Improved Prediction of Proximal Femoral Fracture Load Using Nonlinear Finite Element Models," *Medical Engineering & Physics*, vol. 23, no. 3, pp. 165–173, 2001, ISSN: 1350-4533. DOI: 10.1016/S1350-4533(01)00045-5.

[18] M. Mirzaei, M. Keshavarzian, and V. Naeini, "Analysis of Strength and Failure Pattern of Human Proximal Femur Using Quantitative Computed Tomography (QCT)-Based Finite Element Method," *Bone*, vol. 64, pp. 108–114, 2014, ISSN: 8756-3282. DOI: 10.1016/j.bone.2014.04.007.

[19] N. Trabelsi, Z. Yosibash, C. Wutte, P. Augat, and S. Eberle, "Patient-Specific Finite Element Analysis of the Human Femur - A Double-Blinded Biomechanical Validation," *Journal of Biomechanics*, vol. 44, no. 9, pp. 1666–1672, 2011, ISSN: 0021-9290. DOI: 10.1016/j.jbiomech.2011.03.024.

[20] R. Hambli and S. Allaoui, "A Robust 3D Finite Element Simulation of Human Proximal Femur Progressive Fracture Under Stance Load with Experimental Validation," *Annals of Biomedical Engineering*, vol. 41, no. 12, pp. 2515–2527, 2013, ISSN: 0090-6964. DOI: 10.1007/s10439-013-0864-9.

[21] H. Wille, E. Rank, and Z. Yosibash, "Prediction of the Mechanical Response of the Femur with Uncertain Elastic Properties," *Journal of Biomechanics*, vol. 45, no. 7, pp. 1140–8, 2012, ISSN: 1873-2380. DOI: 10.1016/j.jbiomech.2012.02.006.

[22] J. Kassi, M. Heller, U. Stoeckle, C. Perka, and G. Duda, "Stair Climbing is More Critical than Walking in Pre-Clinical Assessment of Primary Stability in Cementless THA in vitro," *Journal of Biomechanics*, vol. 38, no. 5, pp. 1143–1154, 2005, ISSN: 0021-9290. DOI: 10.1016/j.jbiomech.2004.05.023.

[23] M. Bessho, I. Ohnishi, T. Matsumoto, *et al.*, "Prediction of proximal femur strength using a CT-based nonlinear finite element method: Differences in predicted fracture load and site with changing load and boundary conditions," *Bone*, vol. 45, no. 2, pp. 226–231, Aug. 2009, ISSN: 87563282. DOI: 10.1016/j.bone.2009.04.241.

[24] J. Szivek, J. Benjamin, and P. Anderson, "An Experimental Method for the Application of Lateral Muscle Loading and its Effect on Femoral Strain Distributions," *Medical Engineering & Physics*, vol. 22, no. 2, pp. 109–116, 2000, ISSN: 1350-4533. DOI: 10.1016/S1350-4533(00)00020-5.

[25] J. Britton, L. Walsh, and P. Prendergast, "Mechanical Simulation of Muscle Loading on the Proximal Femur: Analysis of Cemented Femoral Component Migration with and without Muscle Loading," *Clinical Biomechanics*, vol. 18, no. 7, pp. 637–646, 2003, ISSN: 0268-0033. DOI: 10.1016/S0268-0033(03)00113-X.

[26] A. Dickinson, A. Taylor, H. Ozturk, and M. Browne, "Experimental Validation of a Finite Element Model of the Proximal Femur Using Digital Image Correlation and a Composite Bone Model," *Journal of Biomechanical Engineering*, vol. 133, no. 1, pp. 1–6, 2011, ISSN: 0148-0731. DOI: 10.1115/1.4003129.

[27] D. Dragomir-Daescu, J. Op Den Buijs, S. McEligot, *et al.*, "Robust QCT/FEA Models of Proximal Femur Stiffness and Fracture Load During a Sideways Fall on the Hip," *Annals of Biomedical Engineering*, vol. 39, no. 2, pp. 742–755, 2011, ISSN: 0090-6964. DOI: 10.1007/s10439-010-0196-y.

[28] K. Nishiyama, S. Gilchrist, P. Guy, P. Cripton, and S. Boyd, "Proximal Femur Bone Strength Estimated by a Computationally Fast Finite Element Analysis in a Sideways Fall Configuration," *Journal of Biomechanics*, vol. 46, no. 7, pp. 1231–1236, 2013, ISSN: 0021-9290. DOI: 10.1016/j.jbiomech.2013.02.025.

[29] L. Grassi, E. Schileo, F. Taddei, *et al.*, "Accuracy of Finite Element Predictions in Sideways Load Configurations for the Proximal Human Femur," *Journal of Biomechanics*, vol. 45, no. 2, pp. 394–399, 2012, ISSN: 0021-9290. DOI: 10.1016/j.jbiomech.2011.10.019.

[30] P. de Bakker, S. Manske, V. Ebacher, T. Oxland, P. Cripton, and P. Guy, "During Sideways Falls Proximal Femur Fractures Initiate in the Superolateral Cortex: Evidence from High-Speed Video of Simulated Fractures," *Journal of Biomechanics*, vol. 42, no. 12, pp. 1917–1925, 2009, ISSN: 0021-9290. DOI: 10.1016/j.jbiomech.2009.05.001.

[31] J. Keyak, S. Rossi, K. Jones, and H. Skinner, "Prediction of Femoral Fracture Load Using Automated Finite Element Modeling," *Journal of Biomechanics*, vol. 31, no. 2, pp. 125–133, 1997, ISSN: 0021-9290. DOI: 10.1016/S0021-9290(97)00123-1.

[32] J. Keyak and Y. Falkinstein, "Comparison of in situ and in vitro CT Scan-Based Finite Element Model Predictions of Proximal Femoral Fracture Load," *Medical Engineering & Physics*, vol. 25, no. 9, pp. 781–787, 2003, ISSN: 1350-4533. DOI: 10.1016/S1350-4533(03)00081-X.

[33] Y. Katz and Z. Yosibash, "New Insights on the Proximal Femur Biomechanics Using Digital Image Correlation," *Journal of Biomechanics*, vol. 101, pp. 1–11, 2020, ISSN: 1873-2380. DOI: 10.1016/j.jbiomech.2020.109599.

[34] E. Tayton, S. Evans, and D. O'Doherty, "Mapping the Strain Distribution on the Proximal Femur with Titanium and Flexible-Stemmed Implants Using Digital Image Correlation," *The Journal of Bone and Joint Surgery*, vol. 92-B, no. 8, pp. 1176–1181, 2010, ISSN: 0301-620X. DOI: 10.1302/0301-620X.92B8.23553.

[35] T. Rossman, S. Uthamaraj, A. Rezaei, *et al.*, "A Method to Estimate Cadaveric Femur Cortical Strains During Fracture Testing Using Digital Image Correlation," *Journal of Visualized Experiments*, vol. 2017, no. 127, pp. 1–7, 2017, ISSN: 1940-087X. DOI: 10.3791/54942.

[36] A. Bettamer, S. Allaoui, and R. Hambli, "Using 3D Digital Image Correlation to Visualise the Progress of Failure of Human Proximal Femur," *Computer Methods in Biomechanics and Biomedical Engineering*, vol. 5, no. 4, pp. 233–240, 2017, ISSN: 2168-1163. DOI: 10.1080/21681163.2015.1067152.

[37] V. Báča, Z. Horák, P. Mikulenka, and V. Dzupa, "Comparison of an Inhomogeneous Orthotropic and Isotropic Material Models Used for FE Analyses," *Medical Engineering & Physics*, vol. 30, no. 7, pp. 924–930, 2008, ISSN: 1350-4533. DOI: 10.1016/j.medengphy.2007.12.009.

[38] N. Knowles, J. Reeves, and L. Ferreira, "Quantitative Computed Tomography (QCT) Derived Bone Mineral Density (BMD) in Finite Element Studies: A Review of the Literature," *Journal of Experimental Orthopaedics*, vol. 3, no. 1, pp. 1–16, 2016, ISSN: 2197-1153. DOI: 10.1186/s40634-016-0072-2.

[39] Mindways Software INC, *BMD Spine, QCT Software Solutions*. [Online]. Available: https://www.qct.com/QCTSpine.html.

[40] M. Malekzadeh, S. Abbasi-Rad, M. Shahgholi, *et al.*, "Design and Validation of Synchronous QCT Calibration Phantom: Practical Methodology.," *Journal of Medical Imaging and Radiation Sciences*, vol. 50, no. 1, pp. 1–6, 2019, ISSN: 1876-7982. DOI: 10.1016/j.jmir.2018.10.002.

[41] B. Helgason, E. Perilli, E. Schileo, F. Taddei, S. Brynjólfsson, and M. Viceconti, "Mathematical Relationships Between Bone density and Mechanical Properties: A Literature Review," *Clinical Biomechanics*, vol. 23, no. 2, pp. 135–146, 2008, ISSN: 0268-0033. DOI: 10.1016/j.clinbiomech.2007.08.024.

[42] J. Elfar, R. Menorca, J. Reed, and S. Stanbury, "Composite Bone Models in Orthopaedic Surgery Research and Education," *Journal of the American Academy of Orthopaedic Surgeons*, vol. 22, no. 2, pp. 111–120, 2014, ISSN: 1067-151X. DOI: 10.5435/JAAOS-22-02-111.

[43] Sawbones, *Biomechanical Products Catalog*, 2021. [Online]. Available: https://www.sawbones.com/media/assets/product/documents/biomechanical_catalog2021.pdf.

[44] G. Bergmann, *Charité Universitaetsmedizin Berlin "OrthoLoad Database"*, 2008. [Online]. Available: https://orthoload.com/.

[45] D. Colgan, P. Trench, D. Slemon, *et al.*, "A Review of Joint and Muscle Load Simulation Relevant to in-vitro Stress Analysis of the Hip," *Strain*, vol. 30, no. 2, pp. 47–62, 1994, ISSN: 0039-2103. DOI: 10.1111/j.1475-1305.1994.tb00918.x.

[46] D. Robertson, G. Caldwell, J. Hamill, G. Kamen, and S. Whittlesey, *Research Methods in Biomechanics*. 2013, vol. 2, ISBN: 9780736093408.

[47] J. Challis, *Experimental Methods in Biomechanics*. 2021, vol. 1, ISBN: 9783030522551.

[48] M. Lund, S. Tørholm, C. Dzialo, and B. Jensen, *The AnyBody Managed Model Repository (AMMR)*, Jul. 2021. DOI: 10.5281/ZENODO.5060249. [Online]. Available: https://zenodo.org/record/5060249.

[49] AnyBody Technology, *AnyBody Modeling System 7.3*. [Online]. Available: https://www.anybodytech.com/software/.

[50] C. Falcinelli and C. Whyne, "Image-Based Finite-Element Modeling of the Human Femur," *Computer Methods in Biomechanics and Biomedical Engineering*, vol. 23, no. 14, pp. 1138–1161, 2020, ISSN: 1025-5842. DOI: 10.1080/10255842.2020.1789863.

[51] Z. Altai, E. Montefiori, B. van Veen, *et al.*, "Femoral Neck Strain Prediction During Level Walking Using a Combined Musculoskeletal and Finite Element Model Approach," *PLOS ONE*, vol. 16, no. 2, pp. 1–19, 2021, ISSN: 1932-6203. DOI: 10.1371/journal.pone.0245121.

[52] D. Wagner, K. Divringi, C. Ozcan, M. Grujicic, B. Pandurangan, and A. Grujicic, "Combined Musculoskeletal Dynamics/Structural Finite Element Analysis of Femur Physiological Loads During Walking," *Multidiscipline Modeling in Materials and Structures*, vol. 6, no. 4, pp. 417–437, 2010, ISSN: 1573-6105. DOI: 10.1108/15736101011095118.

[53] Z. Yosibash, N. Trabelsi, and C. Milgrom, "Reliable Simulations of the Human Proximal Femur by High-Order Finite Element Analysis Validated by Experimental Observations," *Journal of Biomechanics*, vol. 40, no. 16, pp. 3688–3699, 2007, ISSN: 0021-9290. DOI: 10.1016/j.jbiomech.2007.06.017.

[54] A. Diffo Kaze, S. Maas, P. Arnoux, C. Wolf, and D. Pape, "A Finite Element Model of the Lower Limb During Stance Phase of Gait Cycle Including the Muscle Forces," *BioMedical Engineering OnLine*, vol. 16, no. 1, pp. 138–157, 2017, ISSN: 1475-925X. DOI: 10.1186/s12938-017-0428-6.

[55] R. Bartoska, V. Baca, Z. Horak, *et al.*, "The Importance of Intramedullary Hip Nail Positioning During Implantation for Stable Pertrochanteric Fractures: Biomechanical Analysis," *Surgical and Radiologic Anatomy*, vol. 38, no. 5, pp. 577–585, 2016, ISSN: 0930-1038. DOI: 10.1007/s00276-015-1595-4.

[56] J. Op Den Buijs and D. Dragomir-Daescu, "Validated Finite Element Models of the Proximal Femur Using Two-Dimensional Projected Geometry and Bone Density," *Computer Methods and Programs in Biomedicine*, vol. 104, no. 2, pp. 168–174, 2011, ISSN: 0169-2607. DOI: 10.1016/j.cmpb.2010.11.008.

[57] R. Plackett and J. Burman, "The Design of Optimum Multifactorial Experiments," *Biometrika*, vol. 33, no. 4, pp. 305–325, 1946, ISSN: 0006-3444. DOI: 10.1093/biomet/33.4.305.

[58] L. Barrentine, *An Introduction to Design of Experiments*. 1999, vol. 1, ISBN: 9780873894449.

[59] V. Carbone, R. Fluit, P. Pellikaan, *et al.*, "TLEM 2.0 – A Comprehensive Musculoskeletal Geometry Dataset for Subject-Specific Modeling of Lower Extremity," *Journal of Biomechanics*, vol. 48, no. 5, pp. 734–741, 2015, ISSN: 0021-9290. DOI: 10.1016/j.jbiomech.2014.12.034.

[60] E. De Pieri, M. Lund, A. Gopalakrishnan, K. Rasmussen, D. Lunn, and S. Ferguson, "Refining Muscle Geometry and Wrapping in the TLEM 2 Model for Improved Hip Contact Force Prediction," *PLOS ONE*, vol. 13, no. 9, pp. 1–19, 2018, ISSN: 1932-6203. DOI: 10.1371/journal.pone.0204109.

[61] P. Liang, W. Kwong, A. Sidarta, *et al.*, "An Asian-Centric Human Movement Database Capturing Activities of Daily Living," *Scientific Data*, vol. 7, no. 1, pp. 290–303, Sep. 2020, ISSN: 2052-4463. DOI: 10.1038/s41597-020-00627-7.

[62] Vicon Motion Systems Limited, *Plug-in Gait Reference Guide*, 2016. [Online]. Available: https://docs.vicon.com/display/Nexus212/Plug-in+Gait+Reference+Guide.

[63] L. Raket, B. Grimme, G. Schöner, C. Igel, and B. Markussen, "Separating Timing, Movement Conditions and Individual Differences in the Analysis of Human Movement," *PLOS Computational Biology*, vol. 12, no. 9, J. Diedrichsen, Ed., Sep. 2016, ISSN: 1553-7358. DOI: 10.1371/journal.pcbi.1005092.

[64] F. Petitjean and P. Gançarski, "Summarizing a set of Time Series by Averaging: From Steiner Sequence to Compact Multiple Alignment," *Theoretical Computer Science*, vol. 414, no. 1, pp. 76–91, 2012, ISSN: 03043975. DOI: 10.1016/j.tcs.2011.09.029.

[65] Ansys Inc, *Ansys Workbench 2021 R1 - Simulation Integration Platform*. [Online]. Available: https://www.ansys.com/products/ansys-workbench.

[66] Centro de Tecnologia da Informação Renato Archer (CTI), *InVesalius 3.1*, 2017. [Online]. Available: https://invesalius.github.io/.

[67] Autodesk, *Meshmixer 3D Modeling Software*. [Online]. Available: https://www.meshmixer.com/.

[68] Ansys Inc, *SpaceClaim 3D CAD Modeling Software*. [Online]. Available: https://www.ansys.com/products/3d-design/ansys-spaceclaim.

[69] F. Netter, *Atlas of Human Anatomy*. 2003, vol. 3, ISBN: 1929007116.

[70] P. Tank and T. Gest, *Lippincott Williams & Wilkins Atlas of Anatomy*. 2009, vol. 1.

[71] Minitab LLC, *Minitab Support*. [Online]. Available: https://support.minitab.com/.

[72] M. Li, Z. Li, J. Li, *et al.*, "Three-Dimensional Mapping of Intertrochanteric Fracture Lines," *Chinese Medical Journal*, vol. 132, no. 21, pp. 2524–2533, Nov. 2019, ISSN: 0366-6999. DOI: 10.1097/CM9.0000000000000446.

Appendices

Standing Up Motion (SU)

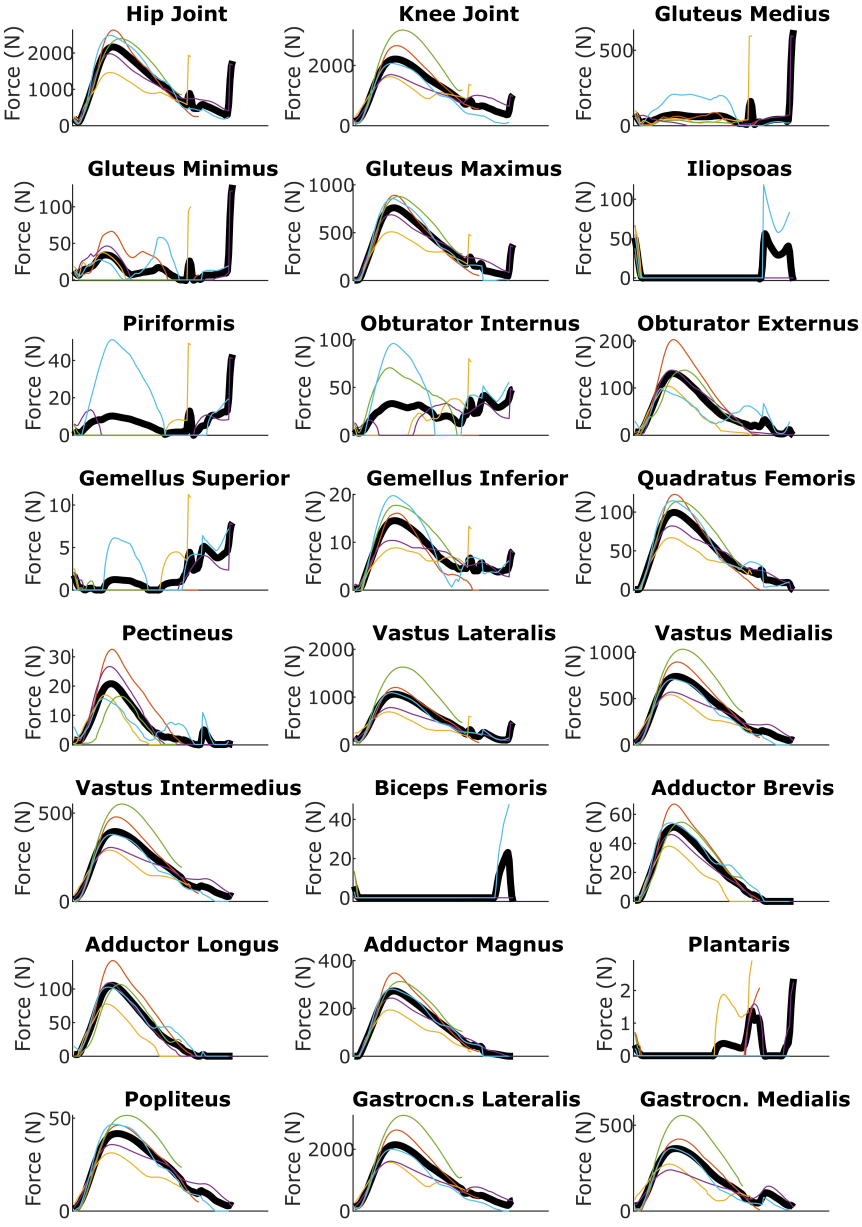

Figure A.1: DTW Averaging of Standing Up Forces

(a) Posterior View **(b)** Anterior View

Figure A.2: Standing Up Scenario Forces

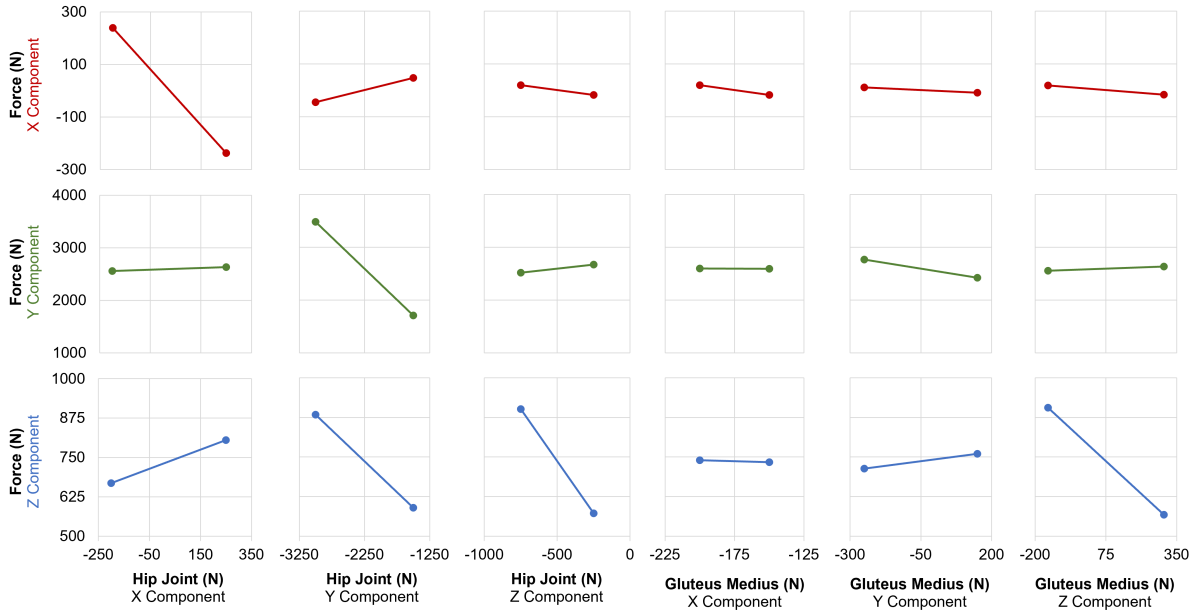

Figure A.3: Sectional Force Factorial Plots of Standing Up Movement Scenario

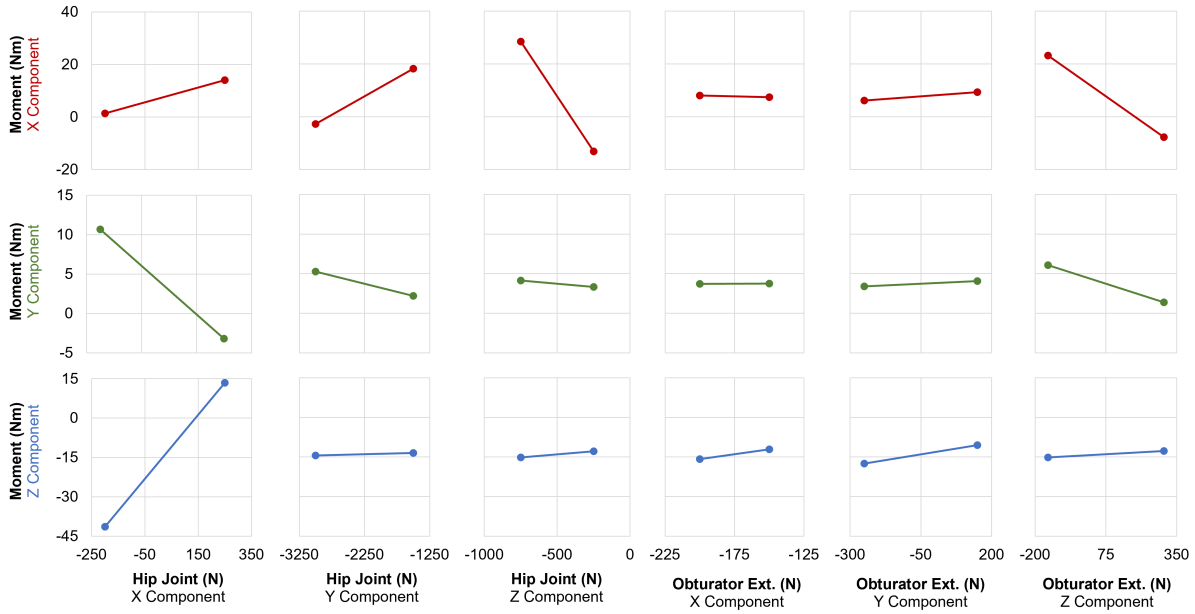

Figure A.4: Sectional Moment Factorial Plots of Standing Up Movement Scenario

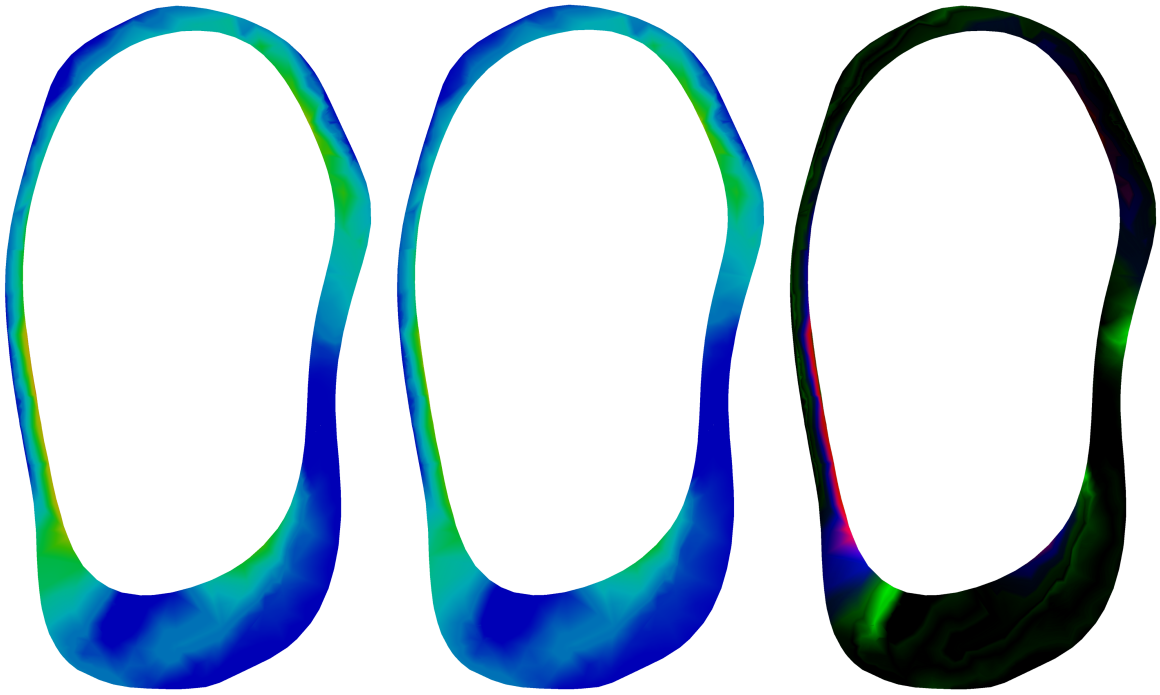

(a) Complete Loading Stress **(b)** Single Loading Stress **(c)** Deviation Intensity Map

Figure A.5: SU Maximum Principal Stress Comparison - Complete Loading vs Single Force Loading

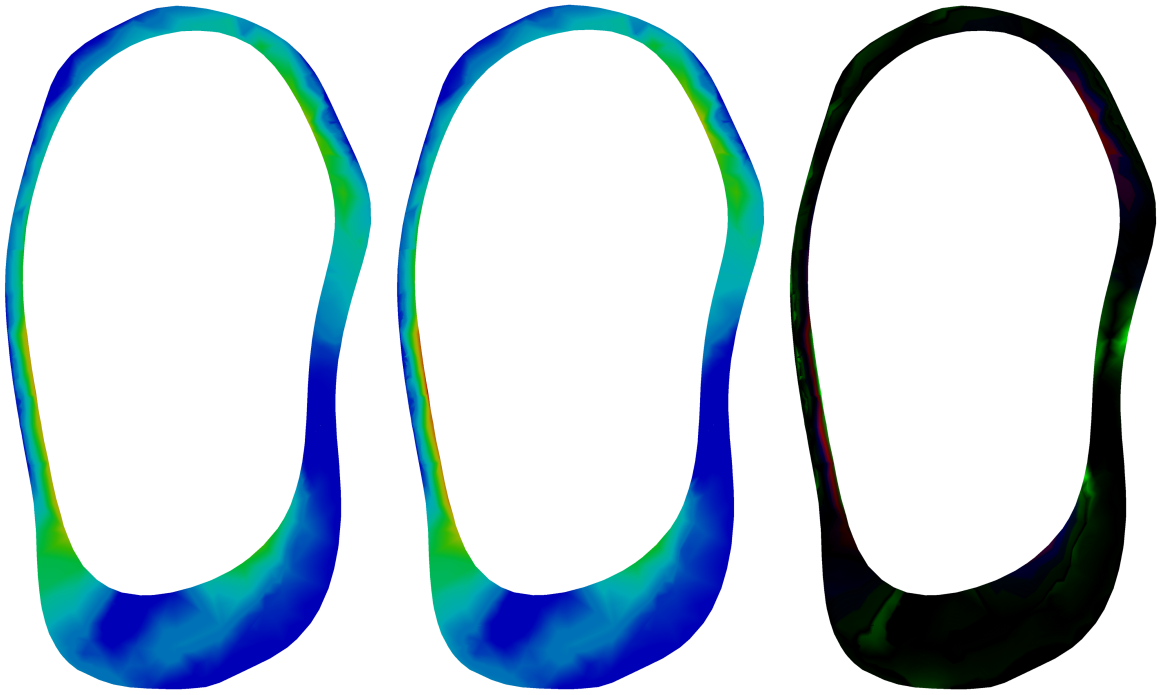

(a) Complete Loading Stress **(b)** Experimental Loading Stress **(c)** Deviation Intensity Map

Figure A.6: SU Maximum Principal Stress Comparison - Complete Loading vs Experimental Loading

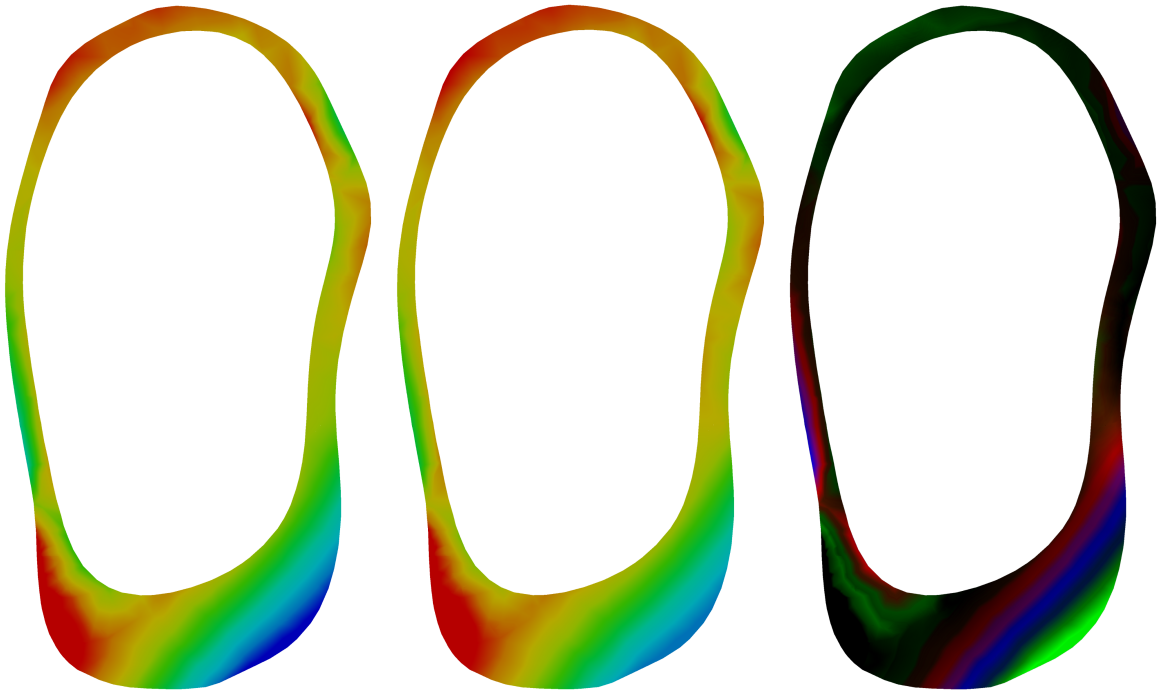

(a) Complete Loading Stress **(b)** Single Loading Stress **(c)** Deviation Intensity Map

Figure A.7: SU Minimum Principal Stress Comparison - Complete Loading vs Single Force Loading

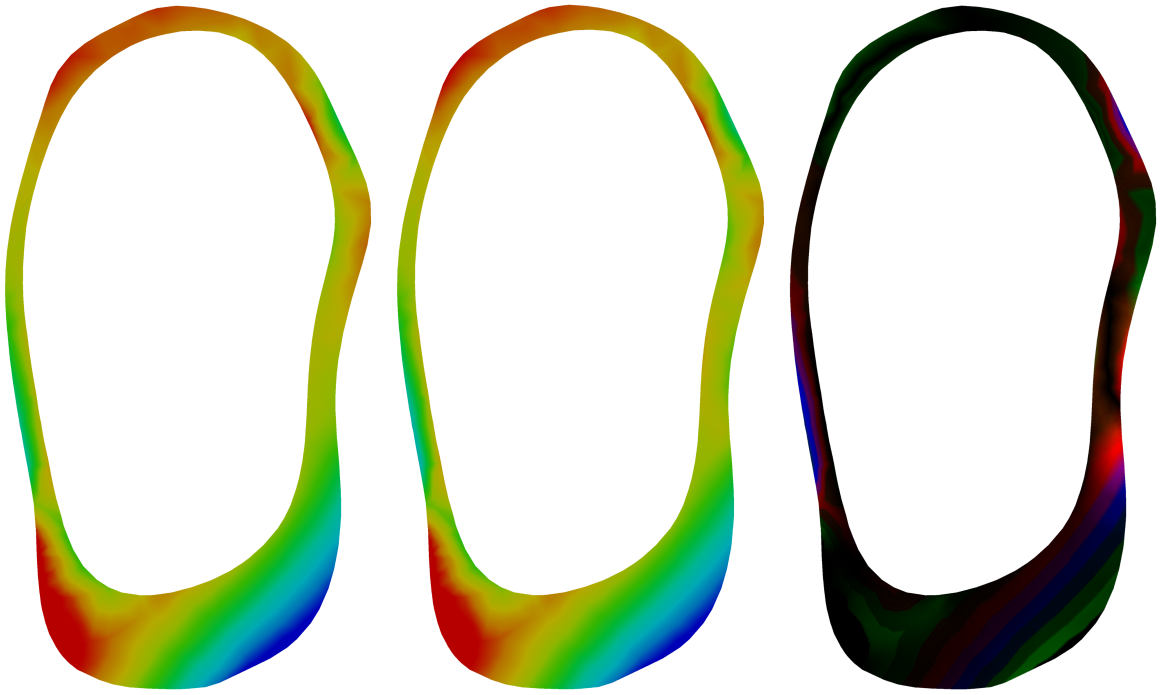

(a) Complete Loading Stress **(b)** Experimental Loading Stress **(c)** Deviation Intensity Map

Figure A.8: SU Minimum Principal Stress Comparison - Complete Loading vs Experimental Loading

Sitting Down Motion (SD)

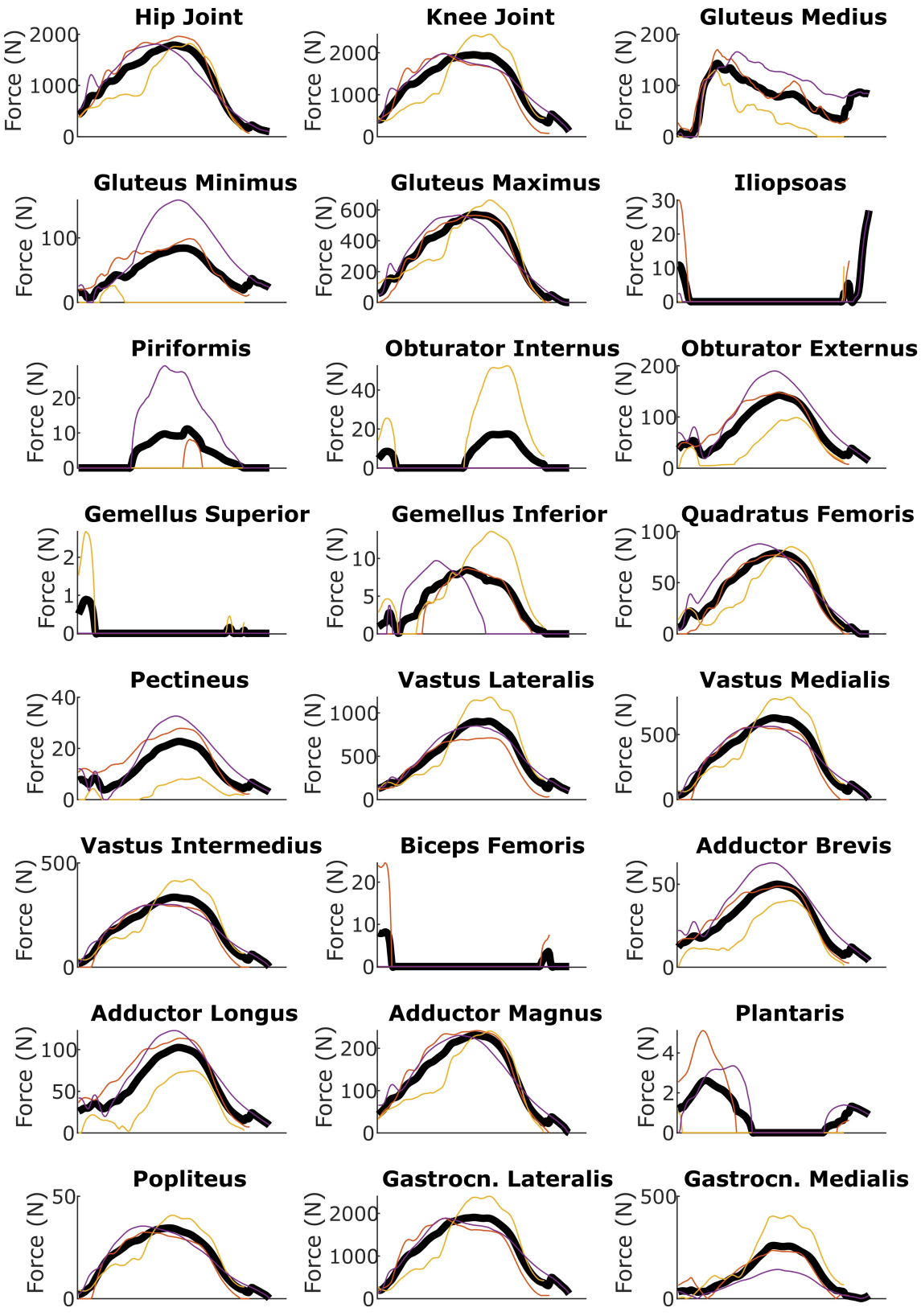

Figure A.9: DTW Averaging of Sitting Down Forces

(a) Posterior View **(b)** Anterior View

Figure A.10: Sitting Down Scenario Forces

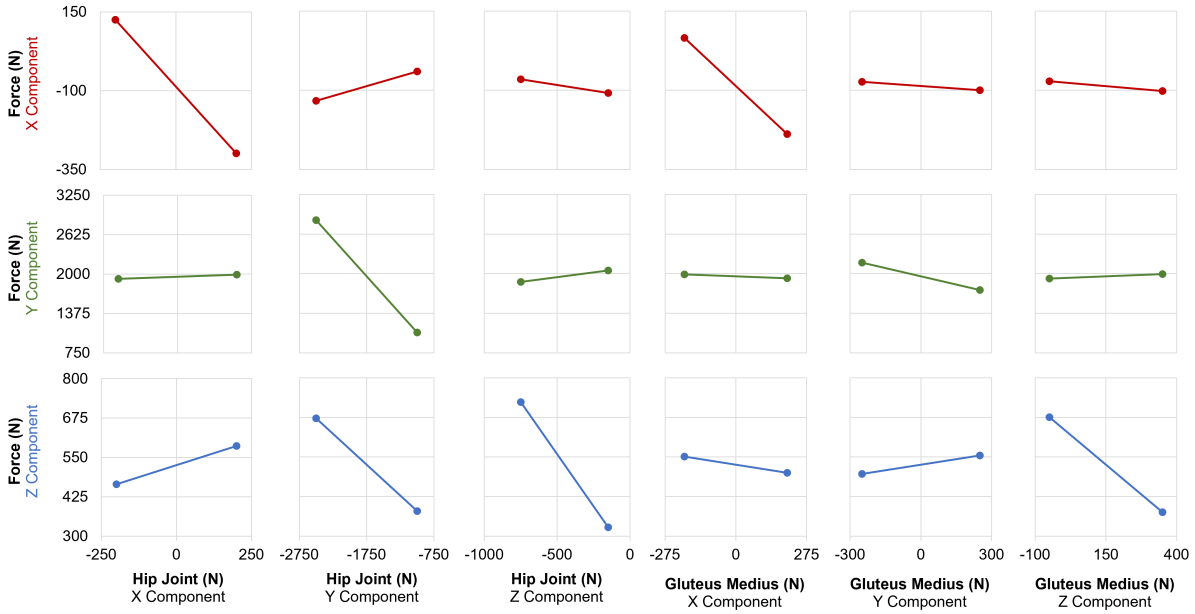

Figure A.11: Sectional Force Factorial Plots of Sitting Down Movement Scenario

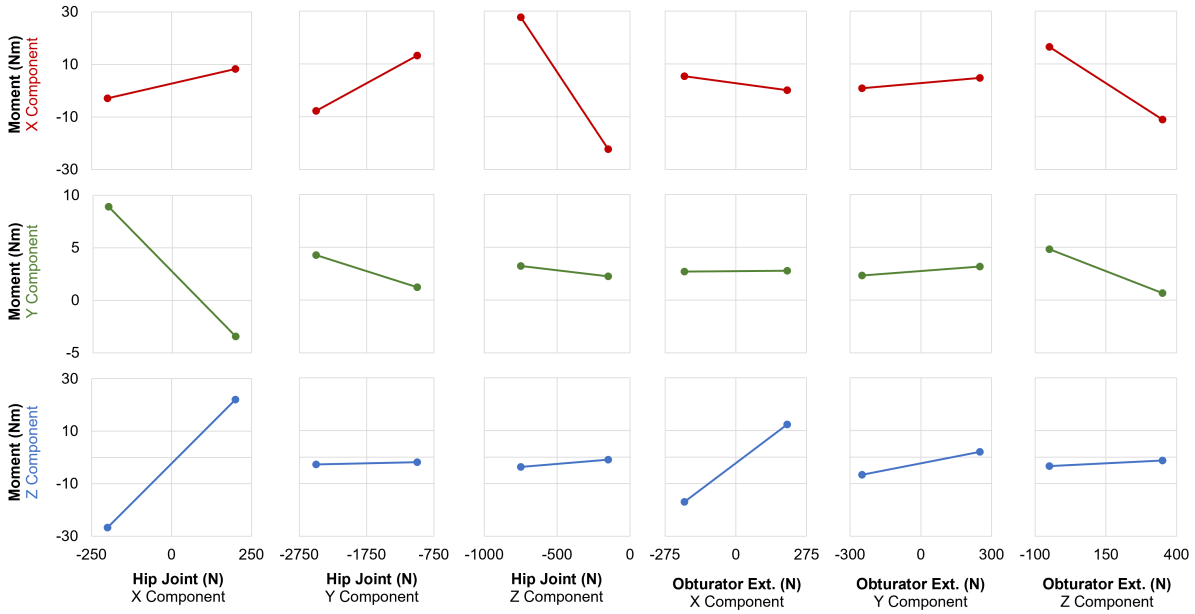

Figure A.12: Sectional Moment Factorial Plots of Sitting Down Movement Scenario

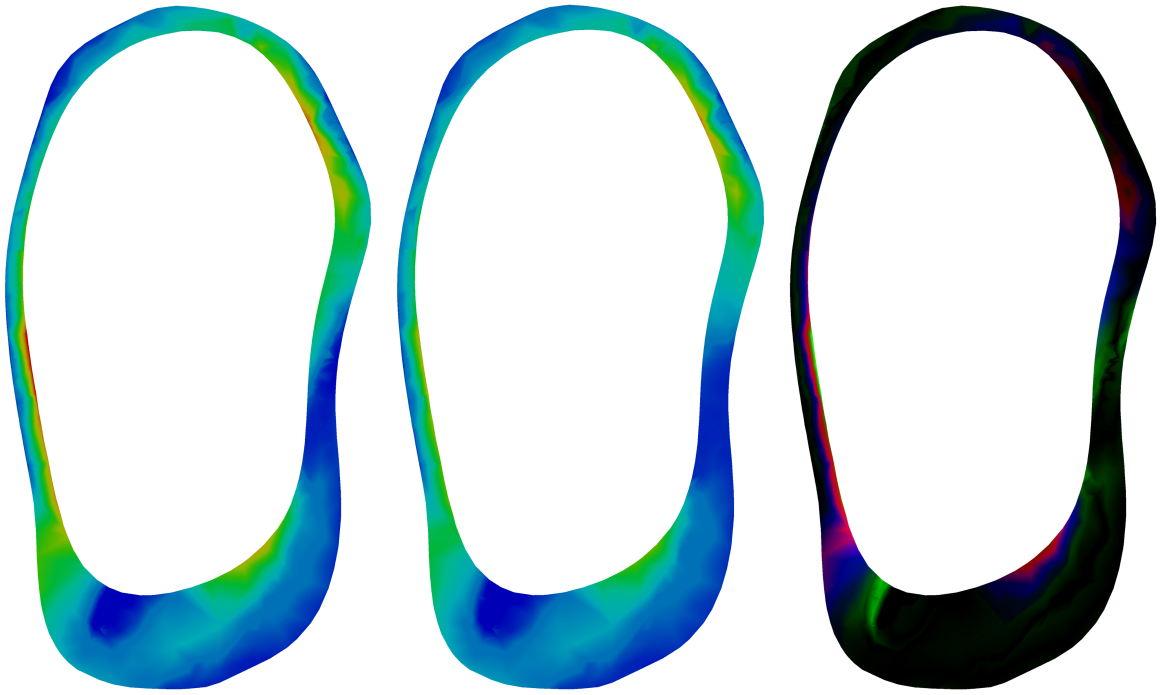

(a) Complete Loading Stress **(b)** Single Loading Stress **(c)** Deviation Intensity Map

Figure A.13: SD Maximum Principal Stress Comparison - Complete Loading vs Single Force Loading

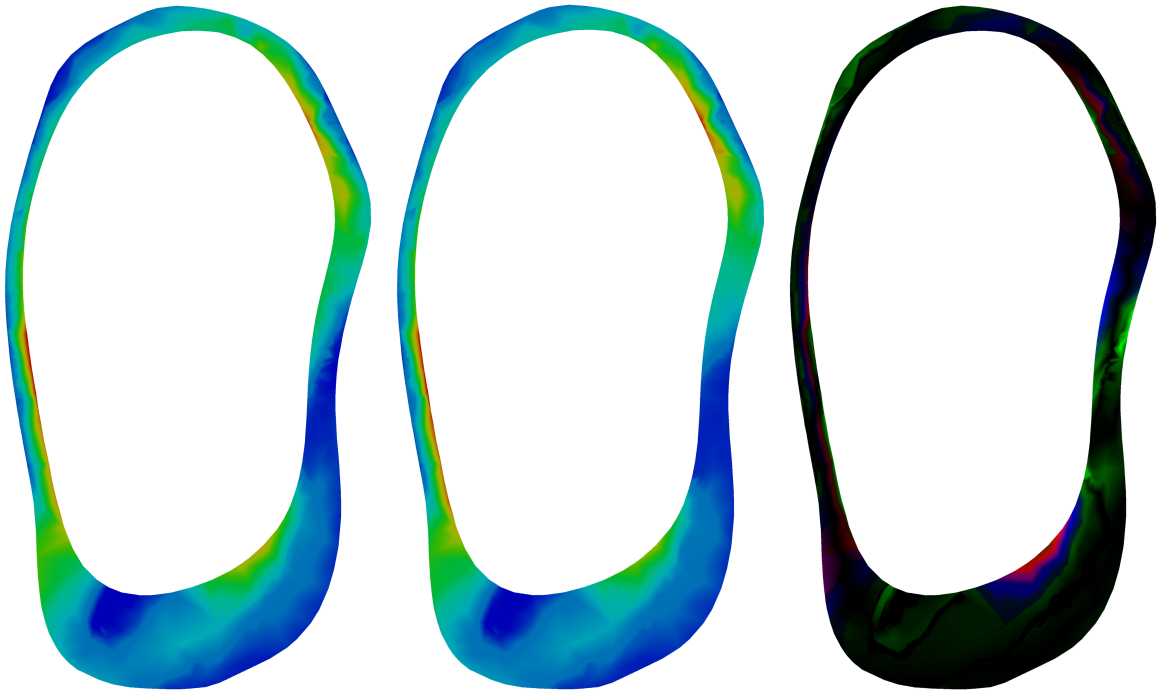

(a) Complete Loading Stress **(b)** Experimental Loading Stress **(c)** Deviation Intensity Map

Figure A.14: SD Maximum Principal Stress Comparison - Complete Loading vs Experimental Loading

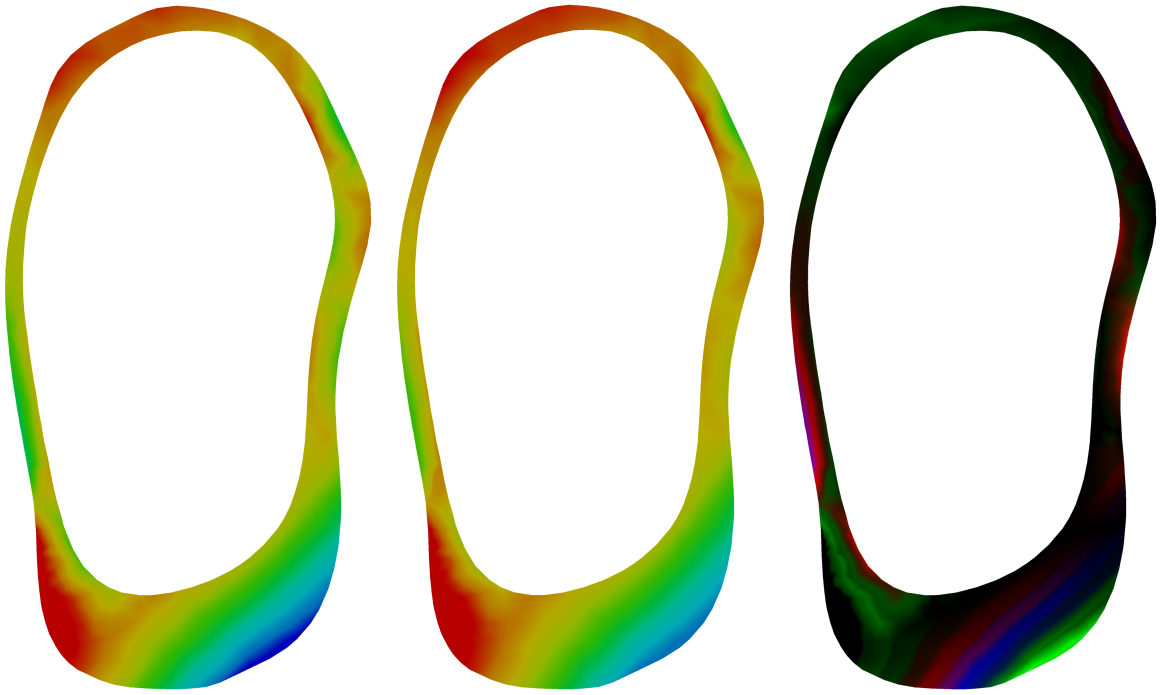

(a) Complete Loading Stress **(b)** Single Loading Stress **(c)** Deviation Intensity Map

Figure A.15: SD Minimum Principal Stress Comparison - Complete Loading vs Single Force Loading

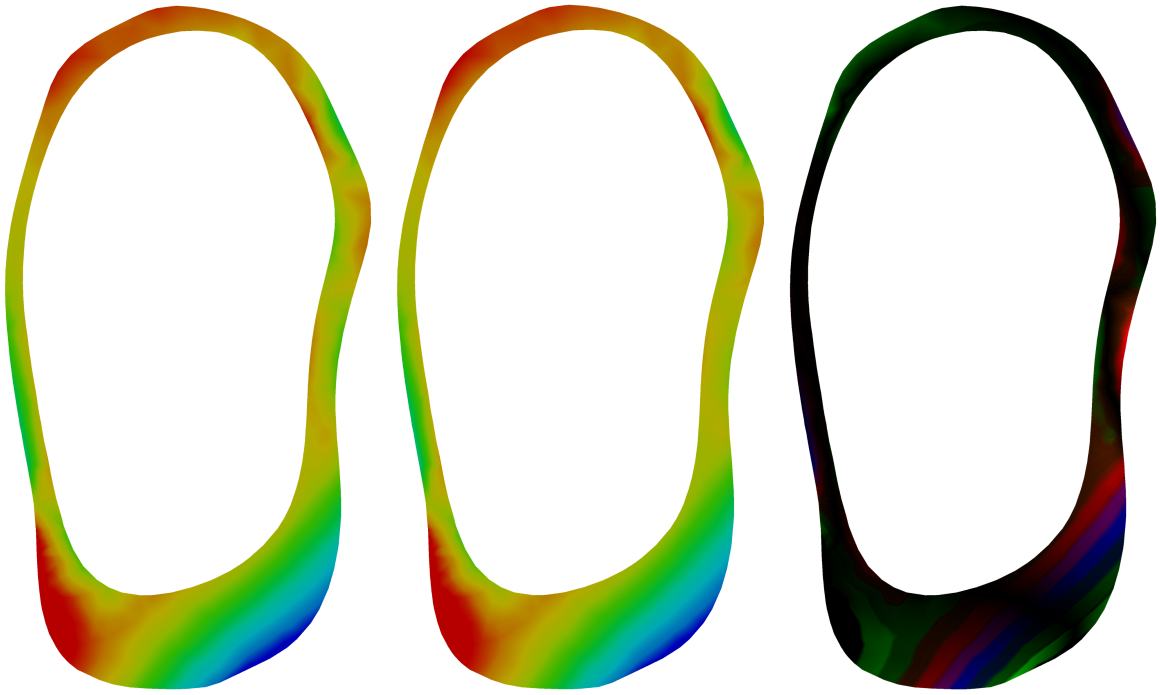

(a) Complete Loading Stress **(b)** Experimental Loading Stress **(c)** Deviation Intensity Map

Figure A.16: SD Minimum Principal Stress Comparison - Complete Loading vs Experimental Loading

Left Step Up Motion (LSU)

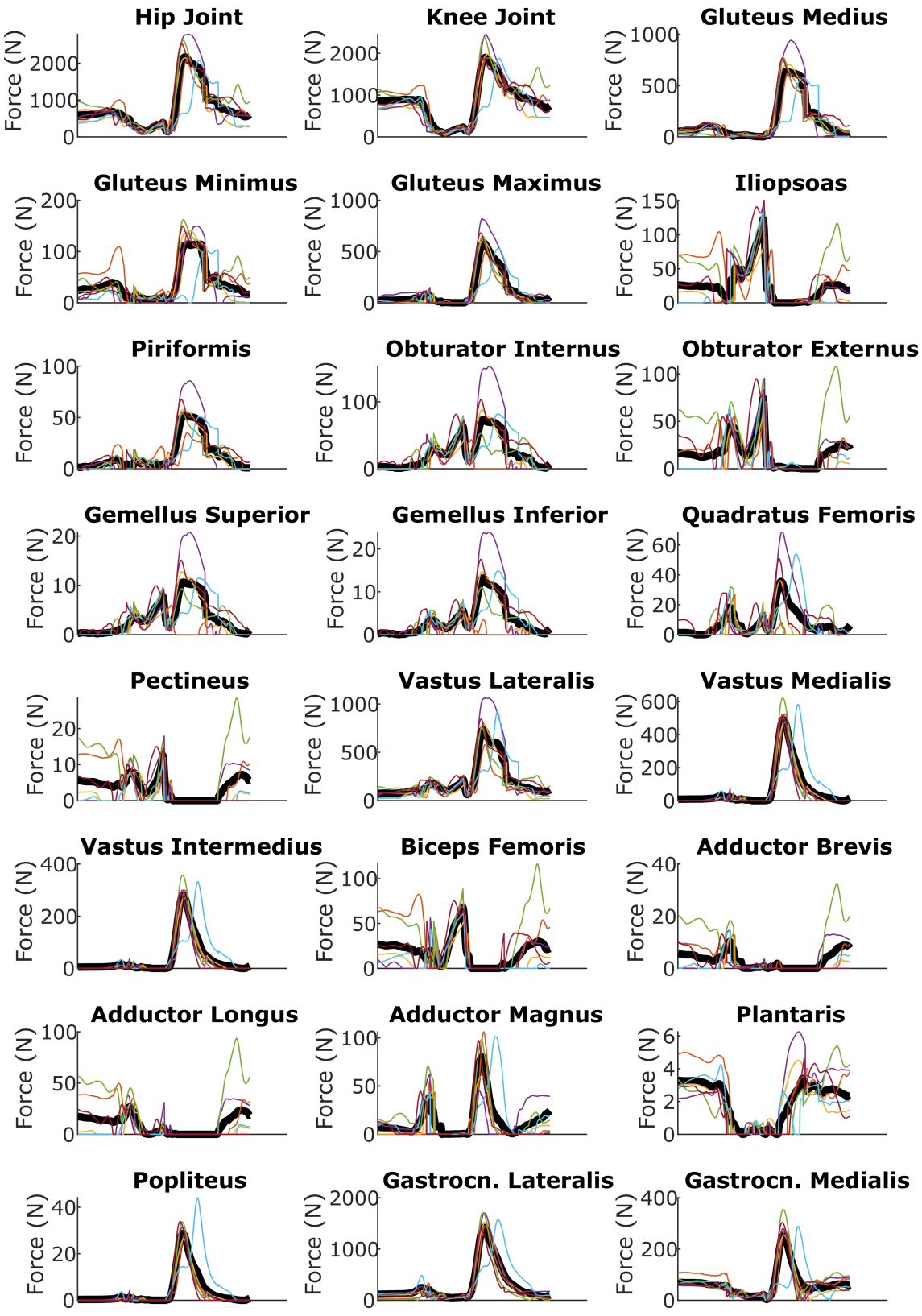

Figure A.17: DTW Averaging of Left Step Up Forces

(a) Posterior View **(b)** Anterior View

Figure A.18: Left Step Up Scenario Forces

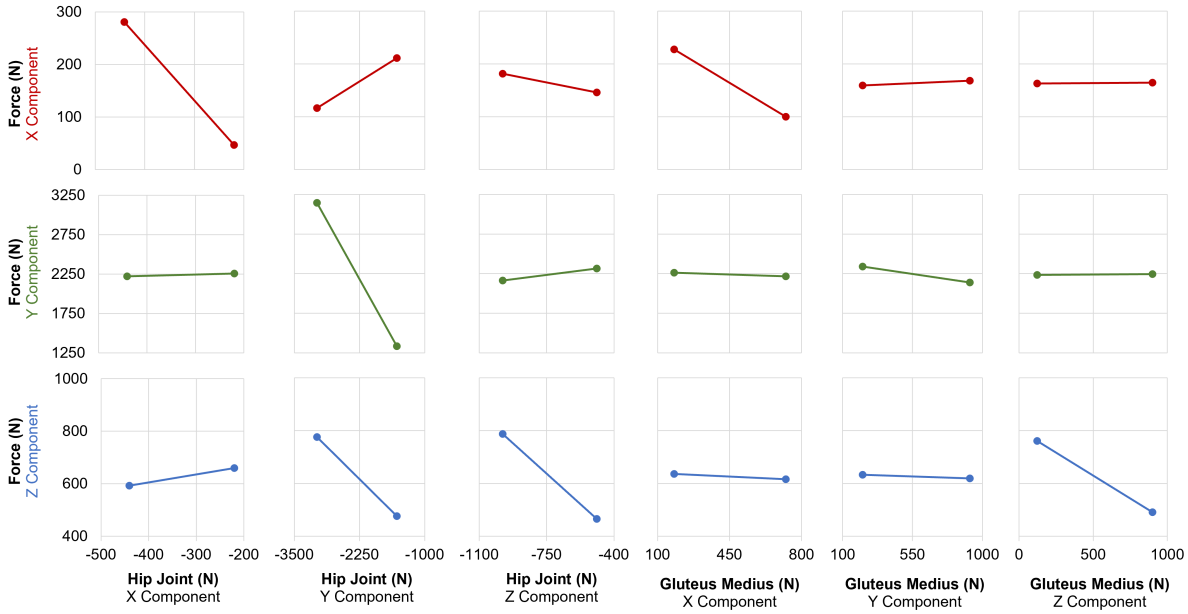

Figure A.19: Sectional Force Factorial Plots of Left Step Up Movement Scenario

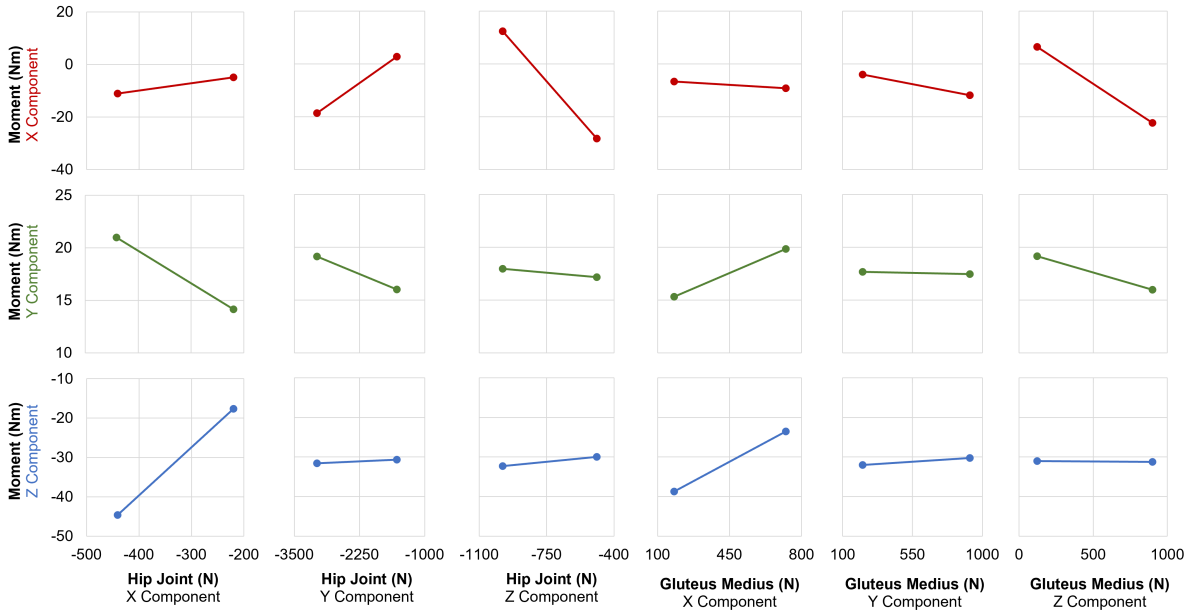

Figure A.20: Sectional Moment Factorial Plots of Left Step Up Movement Scenario

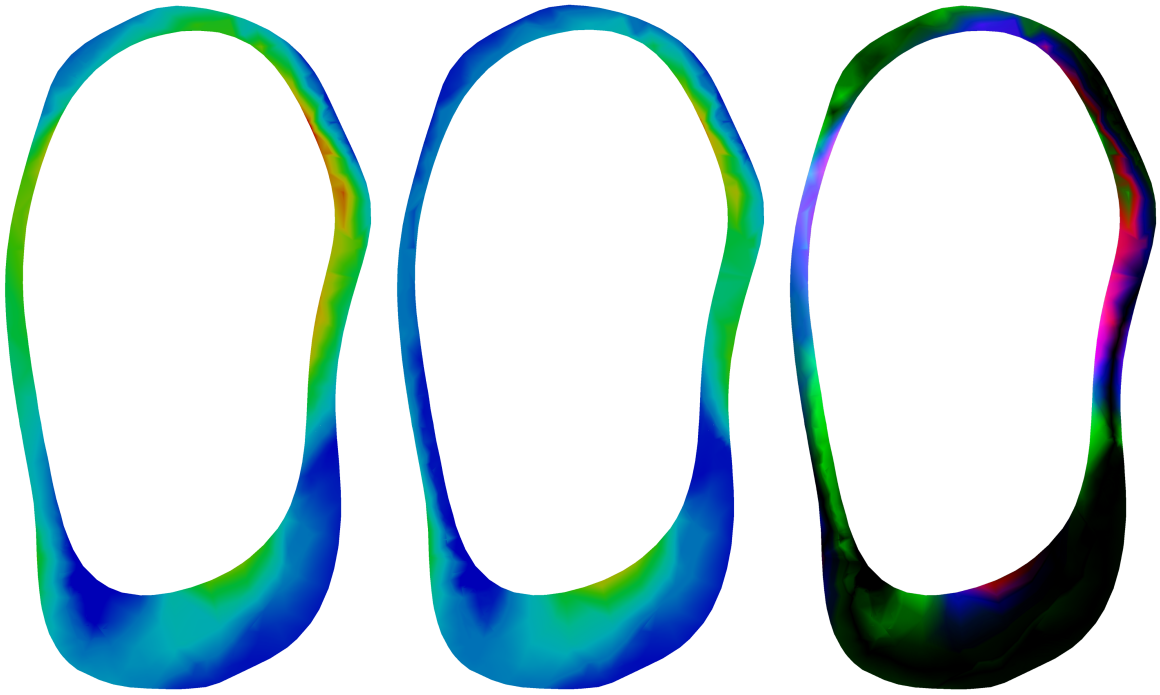

(a) Complete Loading Stress **(b)** Single Loading Stress **(c)** Deviation Intensity Map

Figure A.21: LSU Maximum Principal Stress Comparison - Complete Loading vs Single Force Loading

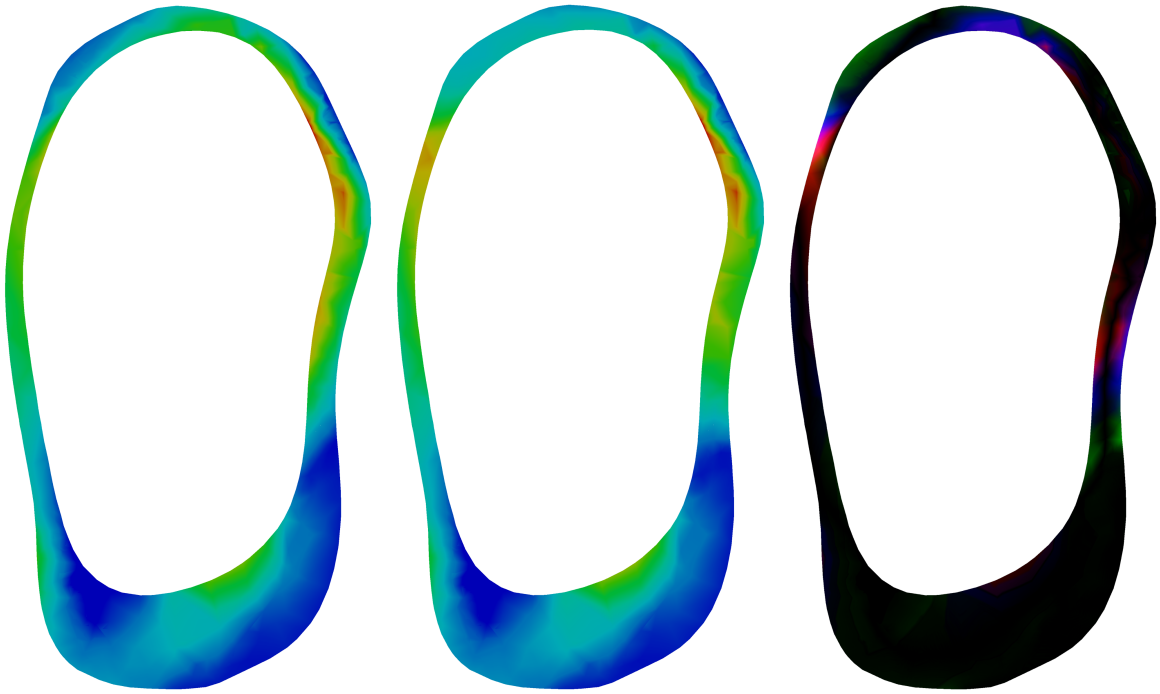

(a) Complete Loading Stress **(b)** Experimental Loading Stress **(c)** Deviation Intensity Map

Figure A.22: LSU Maximum Principal Stress Comparison - Complete Loading vs Experimental Loading

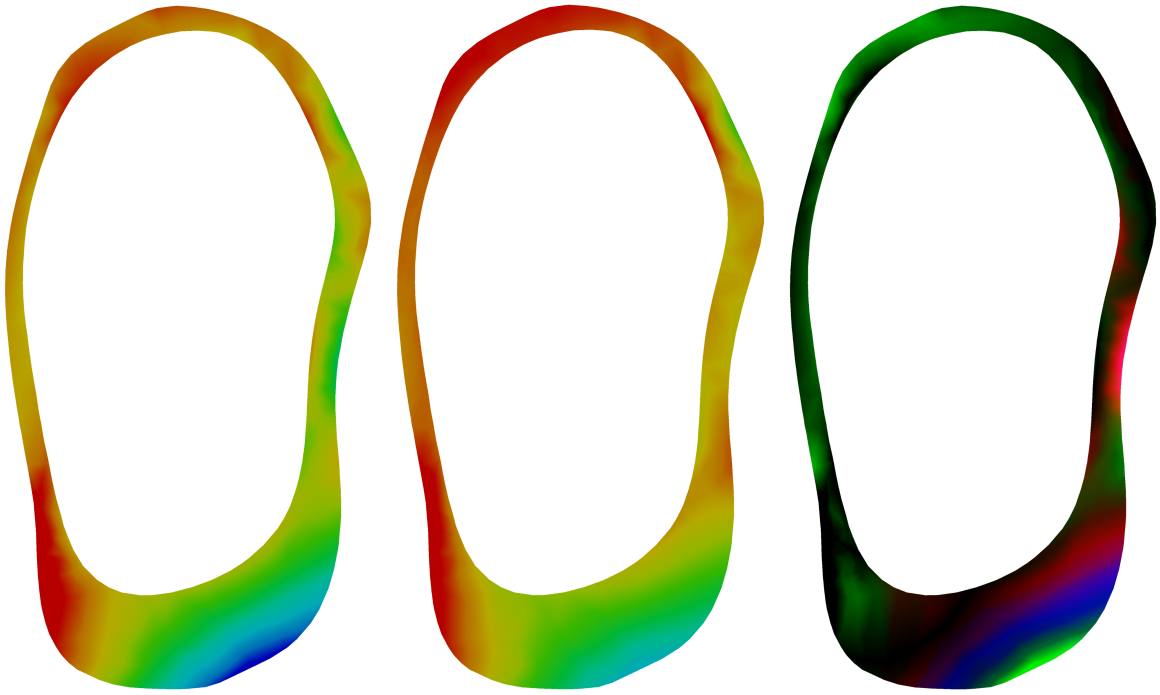

(a) Complete Loading Stress **(b)** Single Loading Stress **(c)** Deviation Intensity Map

Figure A.23: LSU Minimum Principal Stress Comparison - Complete Loading vs Single Force Loading

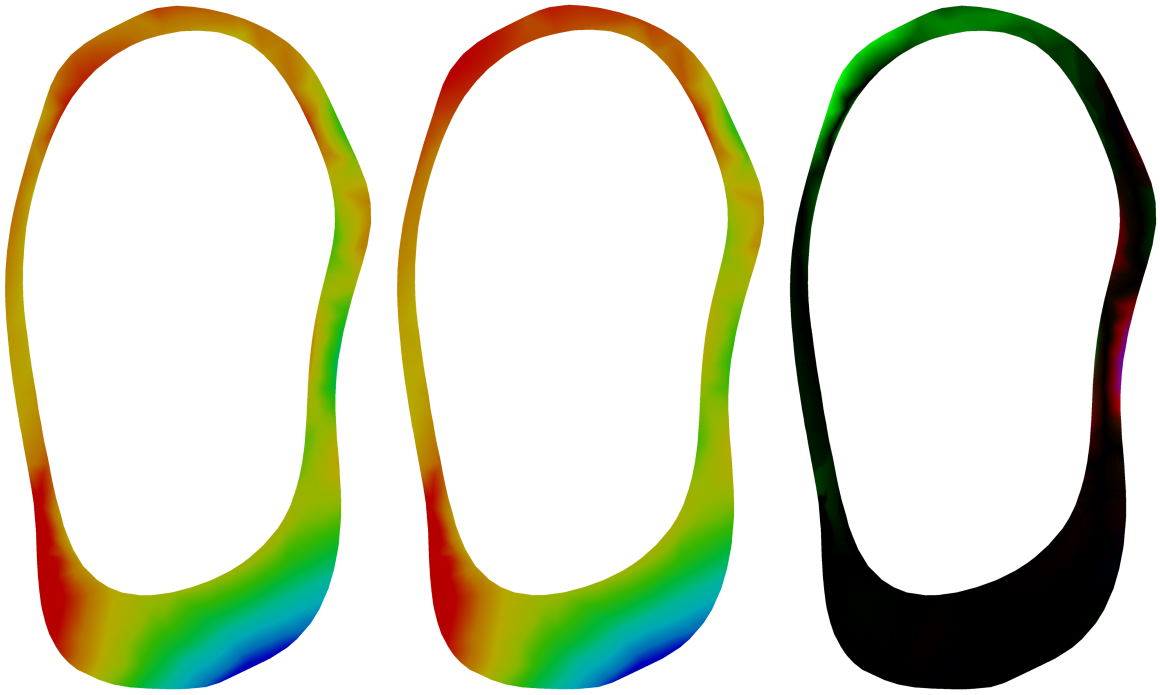

(a) Complete Loading Stress **(b)** Experimental Loading Stress **(c)** Deviation Intensity Map

Figure A.24: LSU Minimum Principal Stress Comparison - Complete Loading vs Experimental Loading

Right Step Up Motion (RSU)

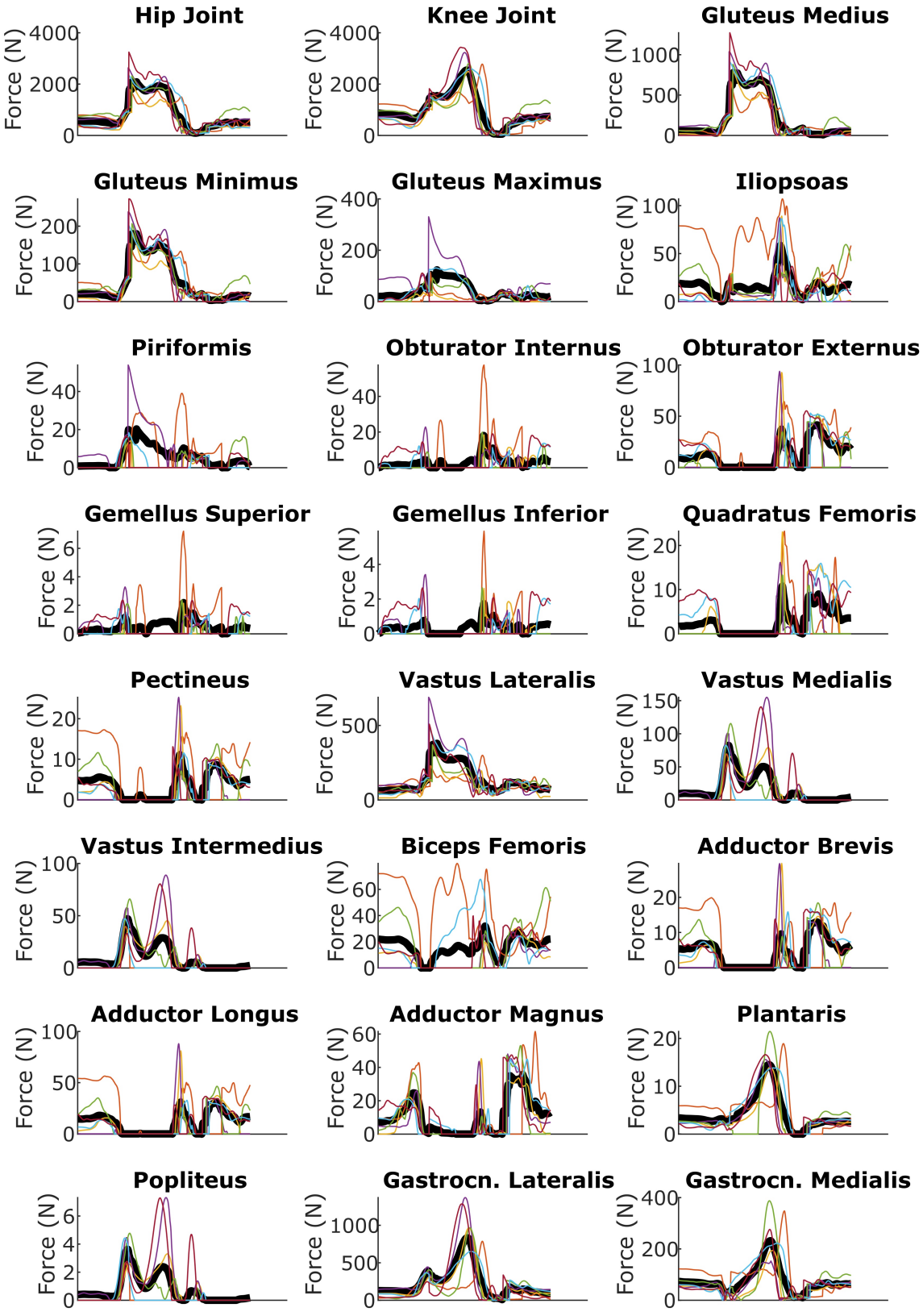

Figure A.25: DTW Averaging of Right Step Up Forces

(a) Posterior View **(b)** Anterior View

Figure A.26: Right Step Up Scenario Forces

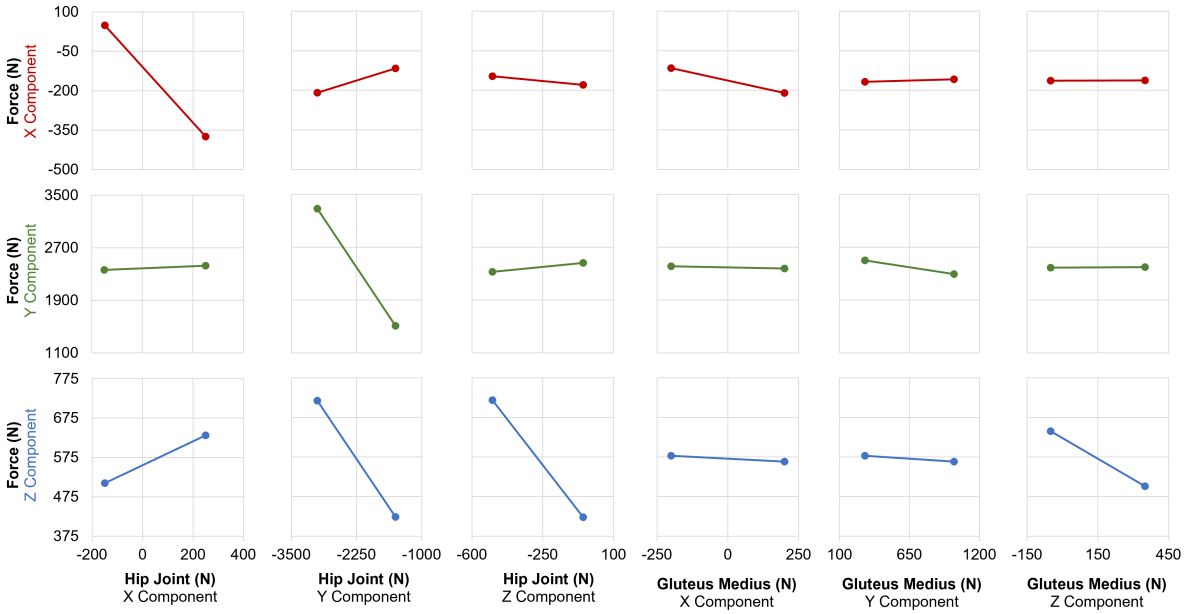

Figure A.27: Sectional Force Factorial Plots of Right Step Up Movement Scenario

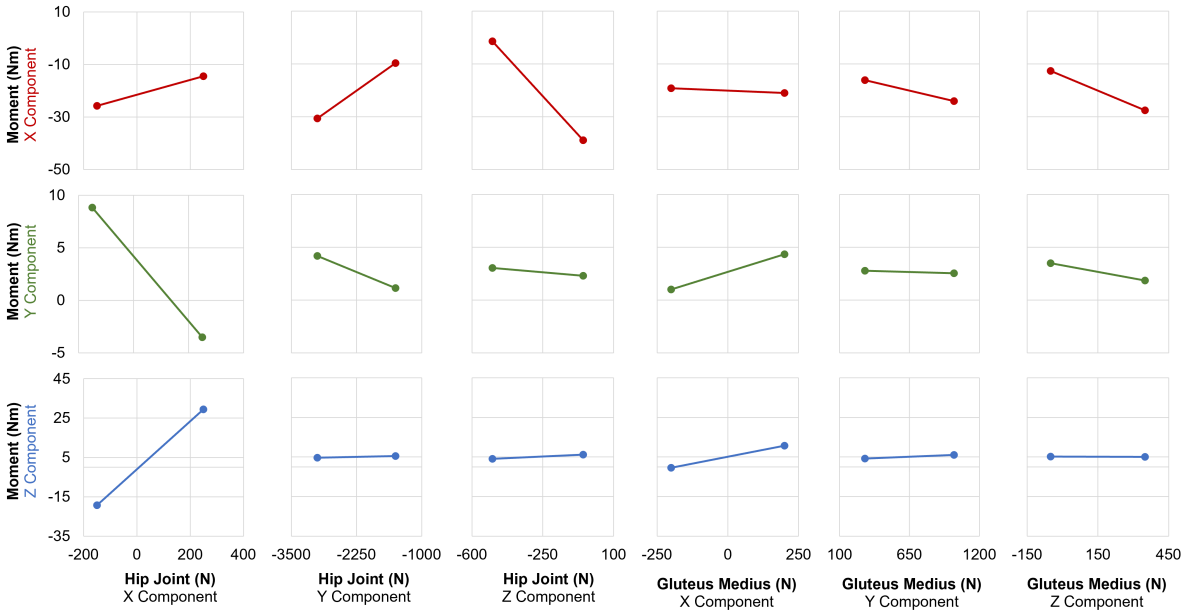

Figure A.28: Sectional Moment Factorial Plots of Right Step Up Movement Scenario

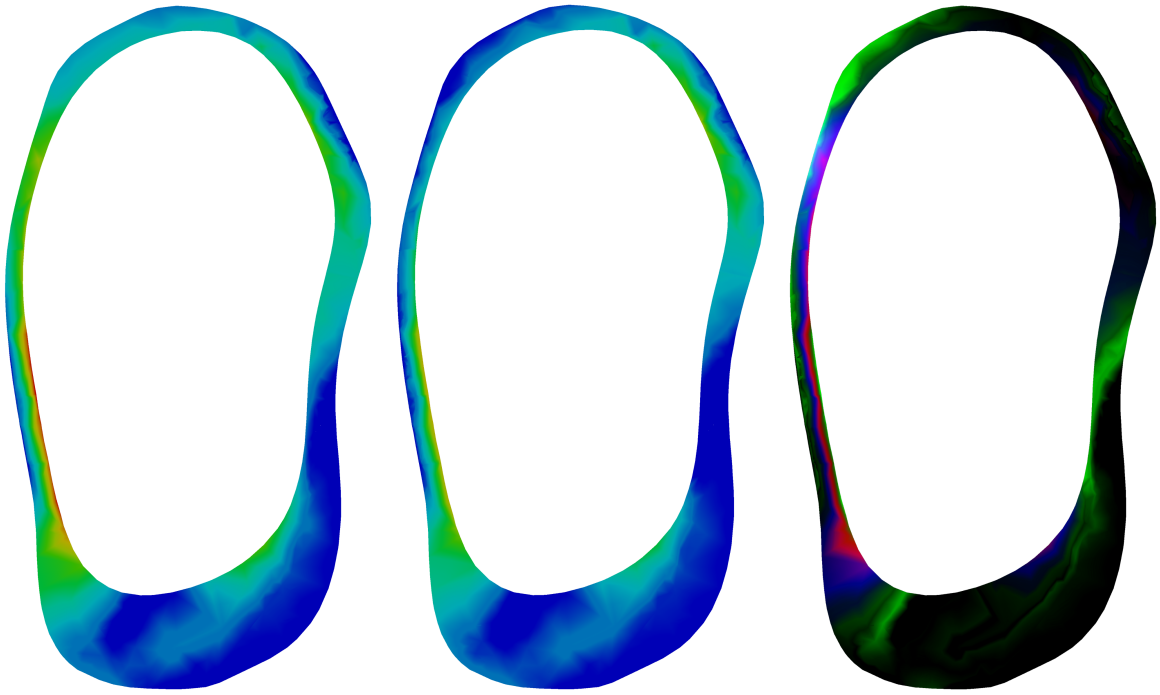

(a) Complete Loading Stress **(b)** Single Loading Stress **(c)** Deviation Intensity Map

Figure A.29: RSU Maximum Principal Stress Comparison - Complete Loading vs Single Force Loading

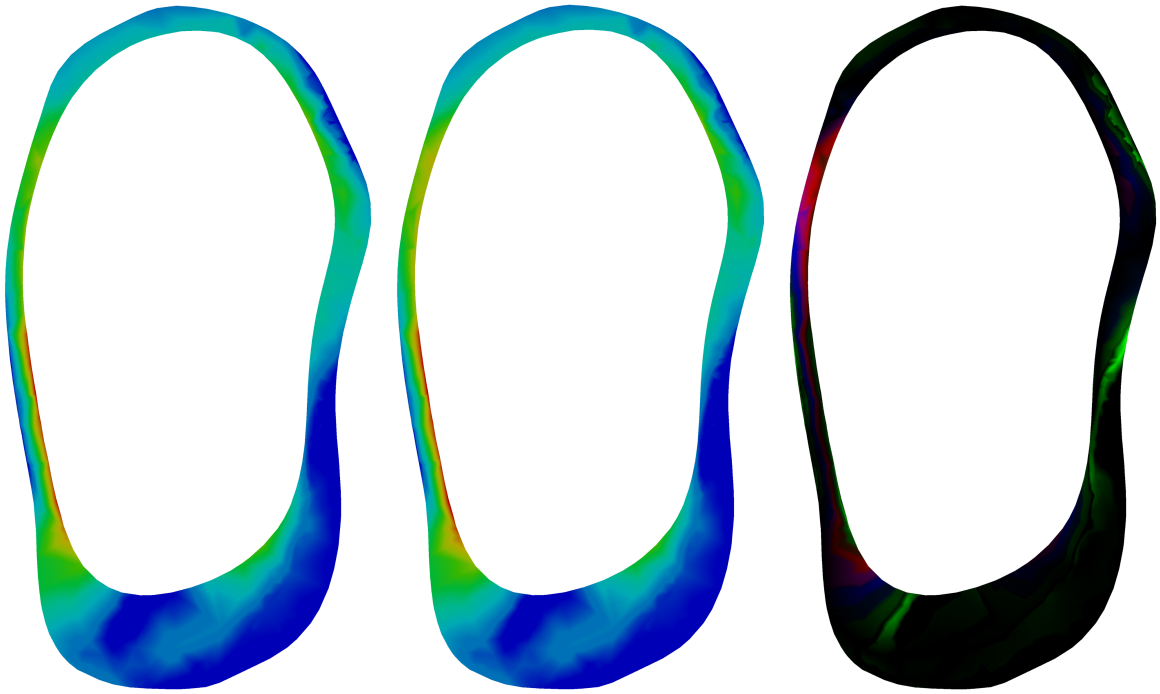

(a) Complete Loading Stress **(b)** Experimental Loading Stress **(c)** Deviation Intensity Map

Figure A.30: RSU Maximum Principal Stress Comparison - Complete Loading vs Experimental Loading

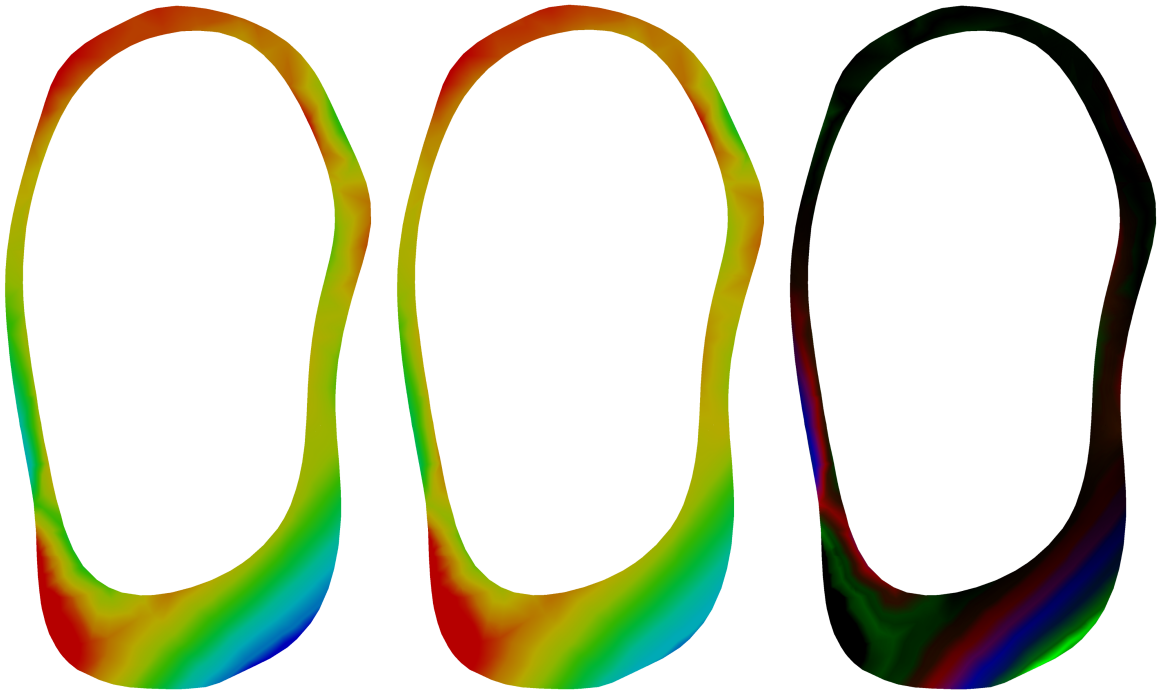

(a) Complete Loading Stress **(b)** Single Loading Stress **(c)** Deviation Intensity Map

Figure A.31: RSU Minimum Principal Stress Comparison - Complete Loading vs Single Force Loading

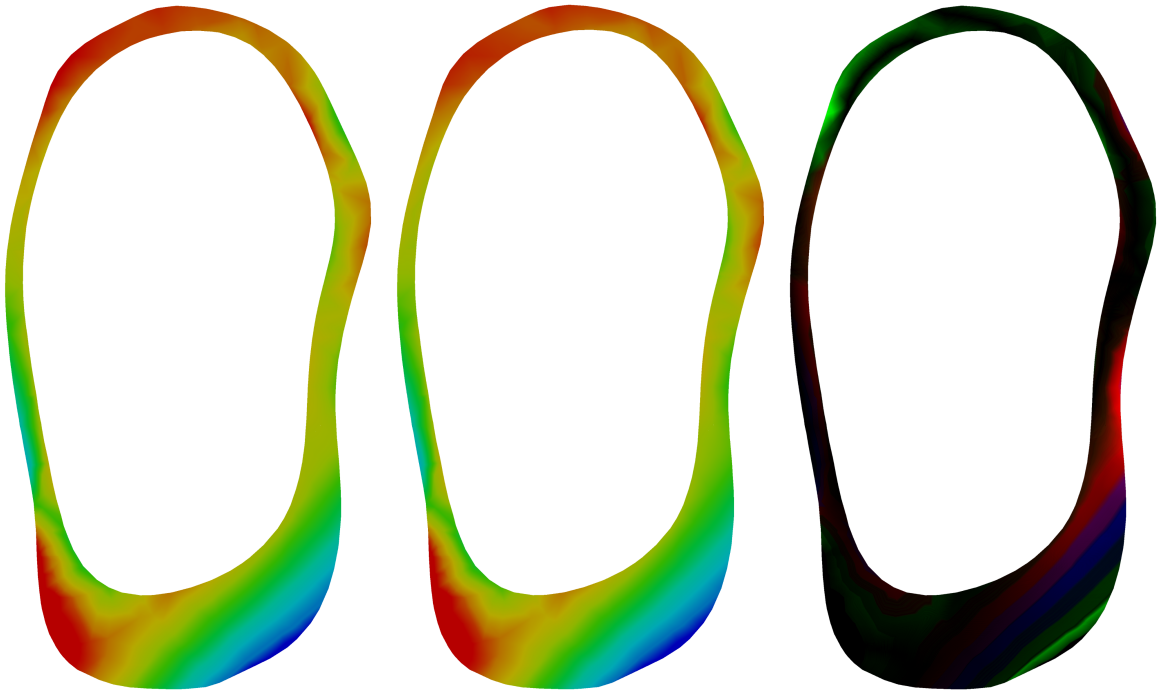

(a) Complete Loading Stress **(b)** Experimental Loading Stress **(c)** Deviation Intensity Map

Figure A.32: RSU Minimum Principal Stress Comparison - Complete Loading vs Experimental Loading

Left Step Down Motion (LSD)

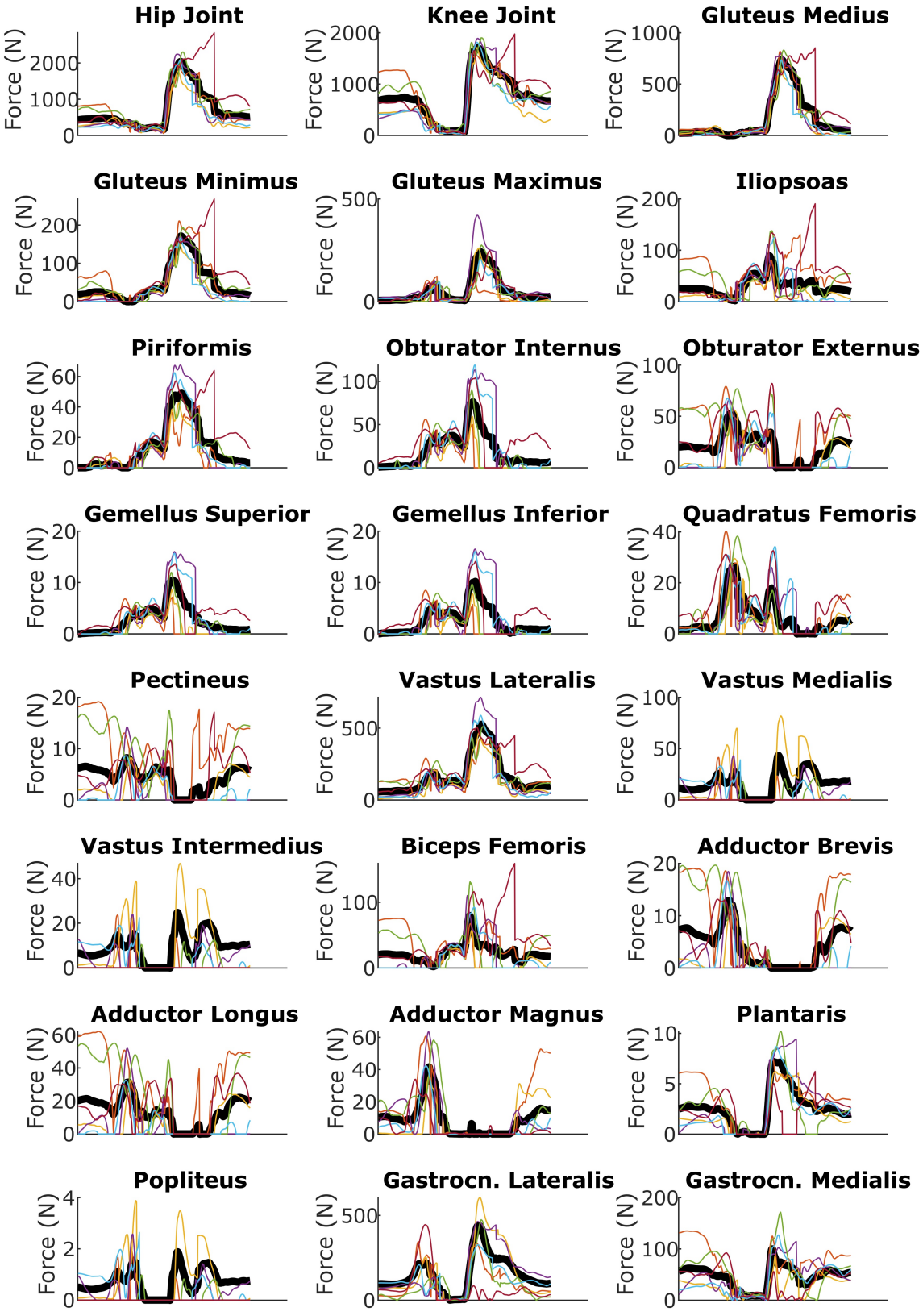

Figure A.33: DTW Averaging of Left Step Down Forces

(a) Posterior View **(b)** Anterior View

Figure A.34: Left Step Down Scenario Forces

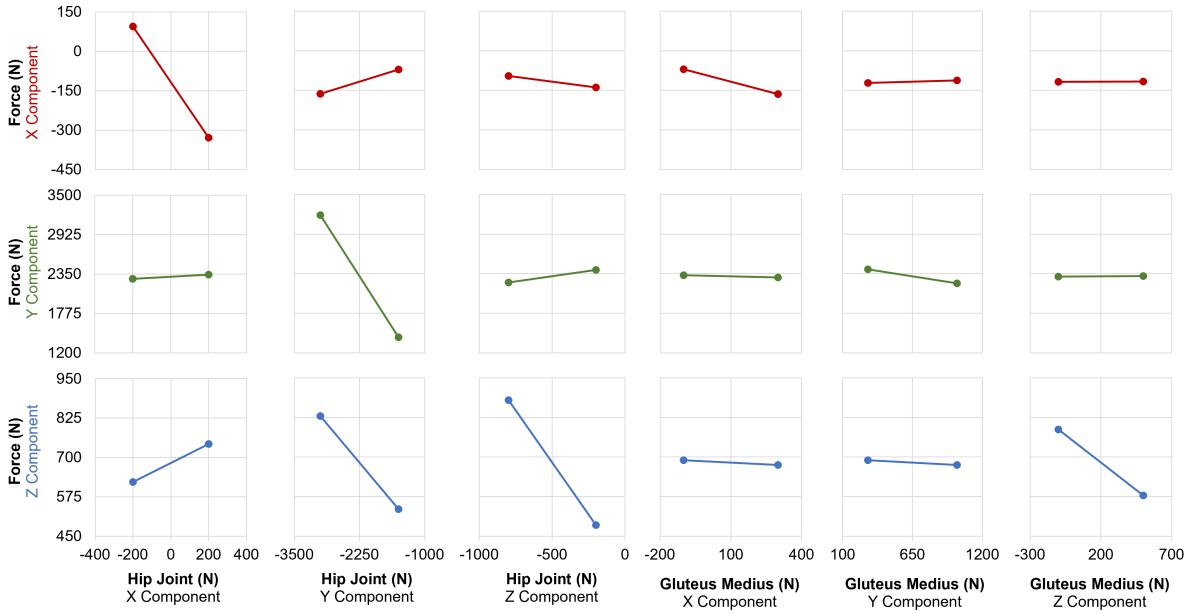

Figure A.35: Sectional Force Factorial Plots of Left Step Down Movement Scenario

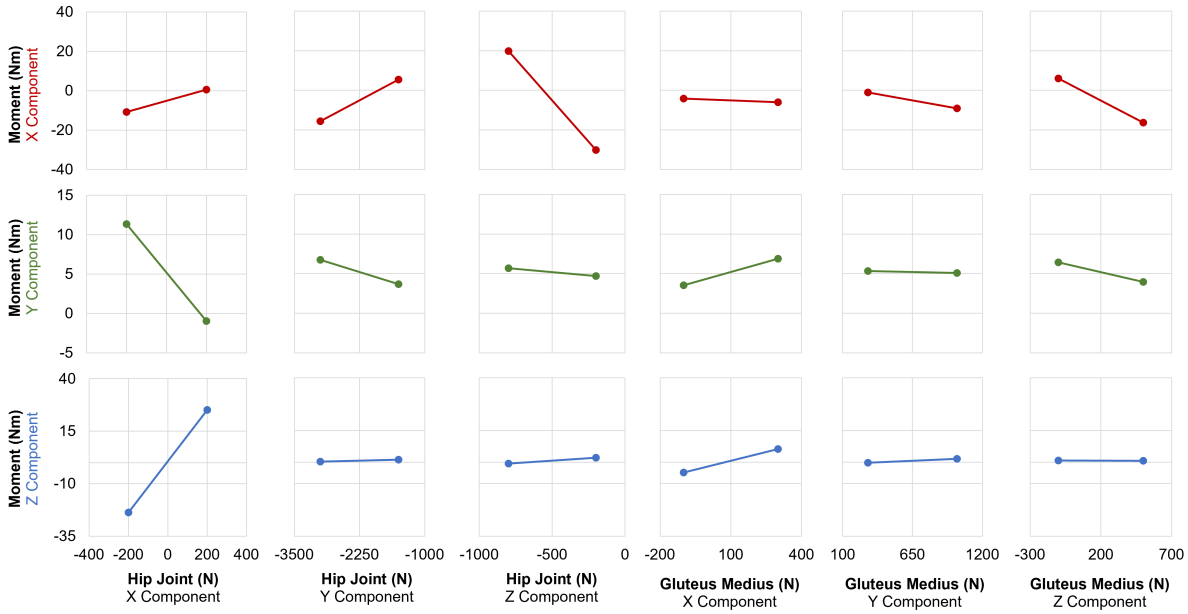

Figure A.36: Sectional Moment Factorial Plots of Left Step Down Movement Scenario

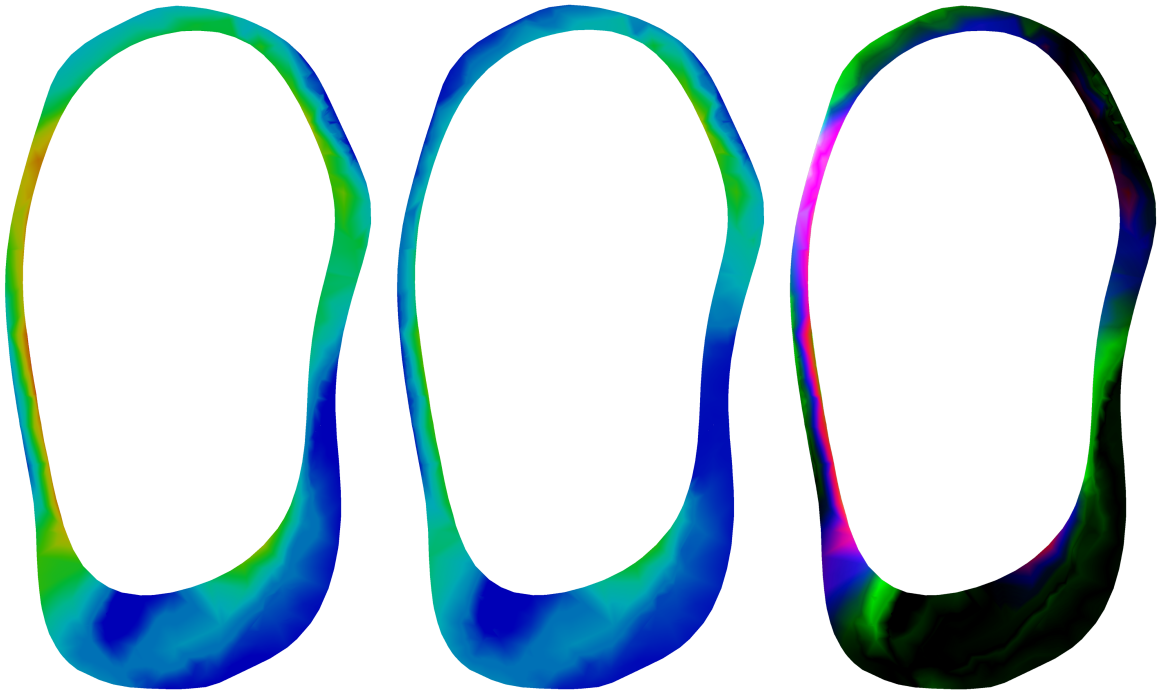

(a) Complete Loading Stress **(b)** Single Loading Stress **(c)** Deviation Intensity Map

Figure A.37: LSD Maximum Principal Stress Comparison - Complete Loading vs Single Force Loading

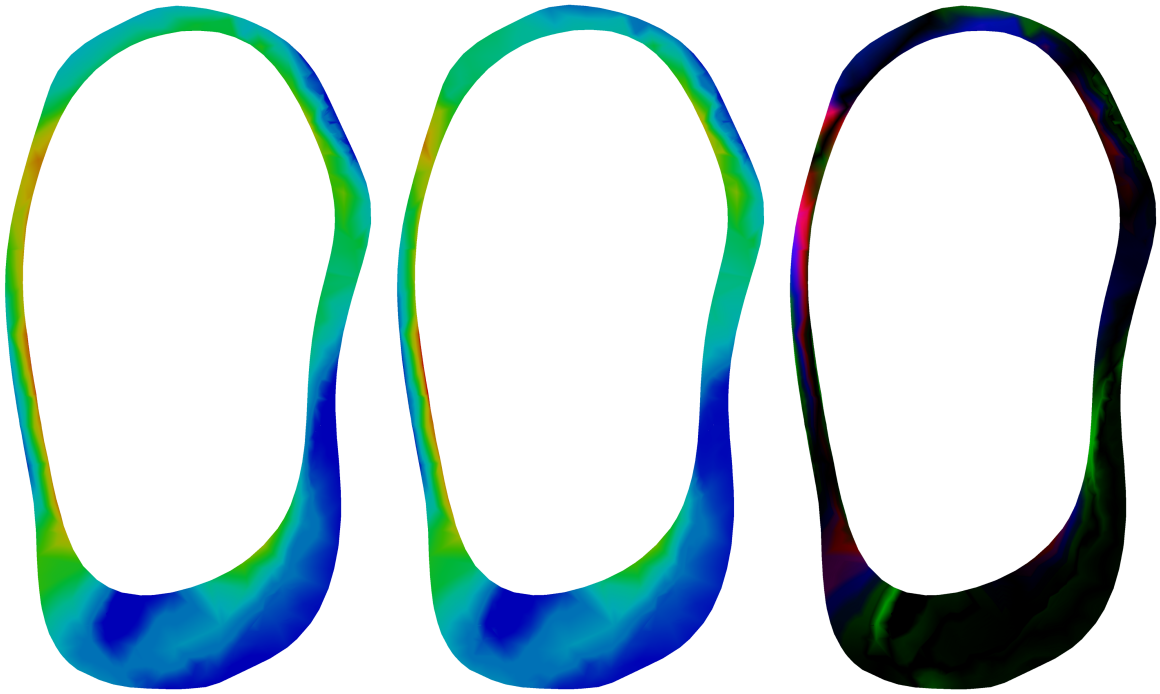

(a) Complete Loading Stress **(b)** Experimental Loading Stress **(c)** Deviation Intensity Map

Figure A.38: LSD Maximum Principal Stress Comparison - Complete Loading vs Experimental Loading

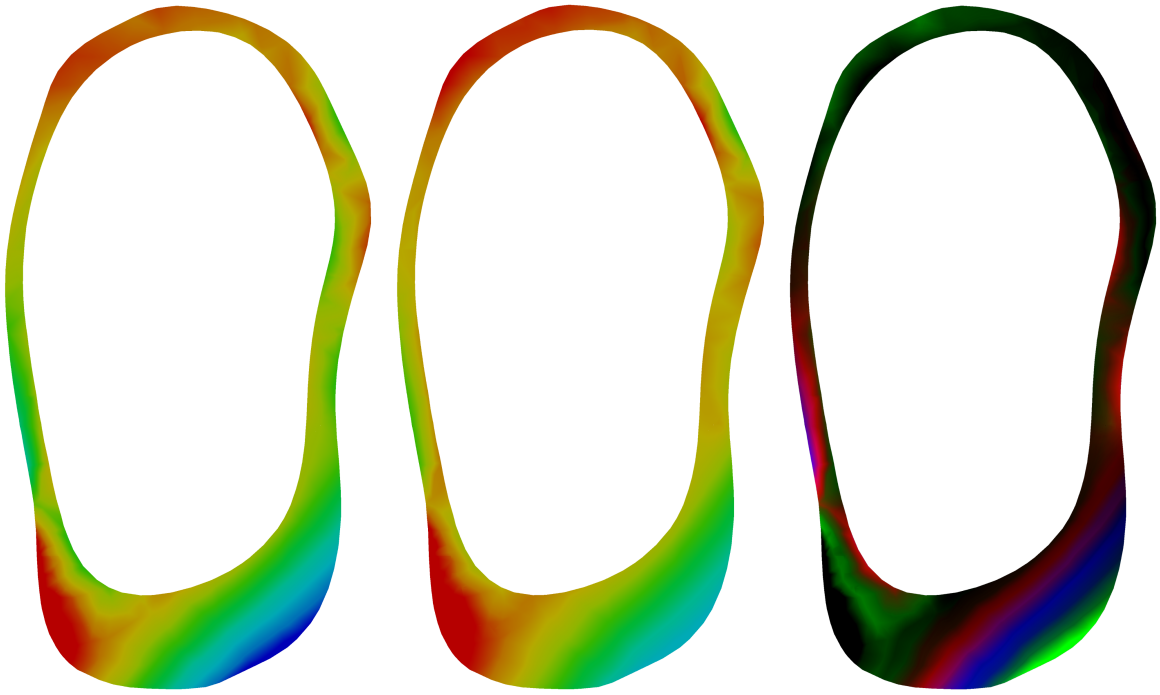

(a) Complete Loading Stress **(b)** Single Loading Stress **(c)** Deviation Intensity Map

Figure A.39: LSD Minimum Principal Stress Comparison - Complete Loading vs Single Force Loading

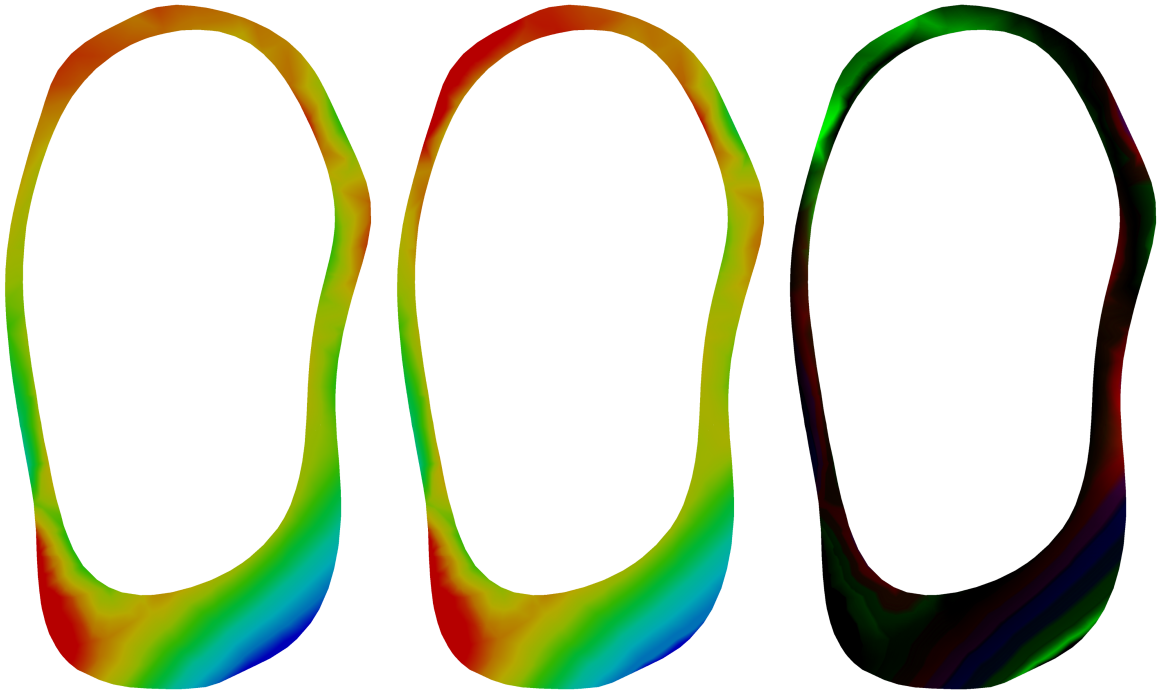

(a) Complete Loading Stress **(b)** Experimental Loading Stress **(c)** Deviation Intensity Map

Figure A.40: LSD Minimum Principal Stress Comparison - Complete Loading vs Experimental Loading

Right Step Down Motion (RSD)

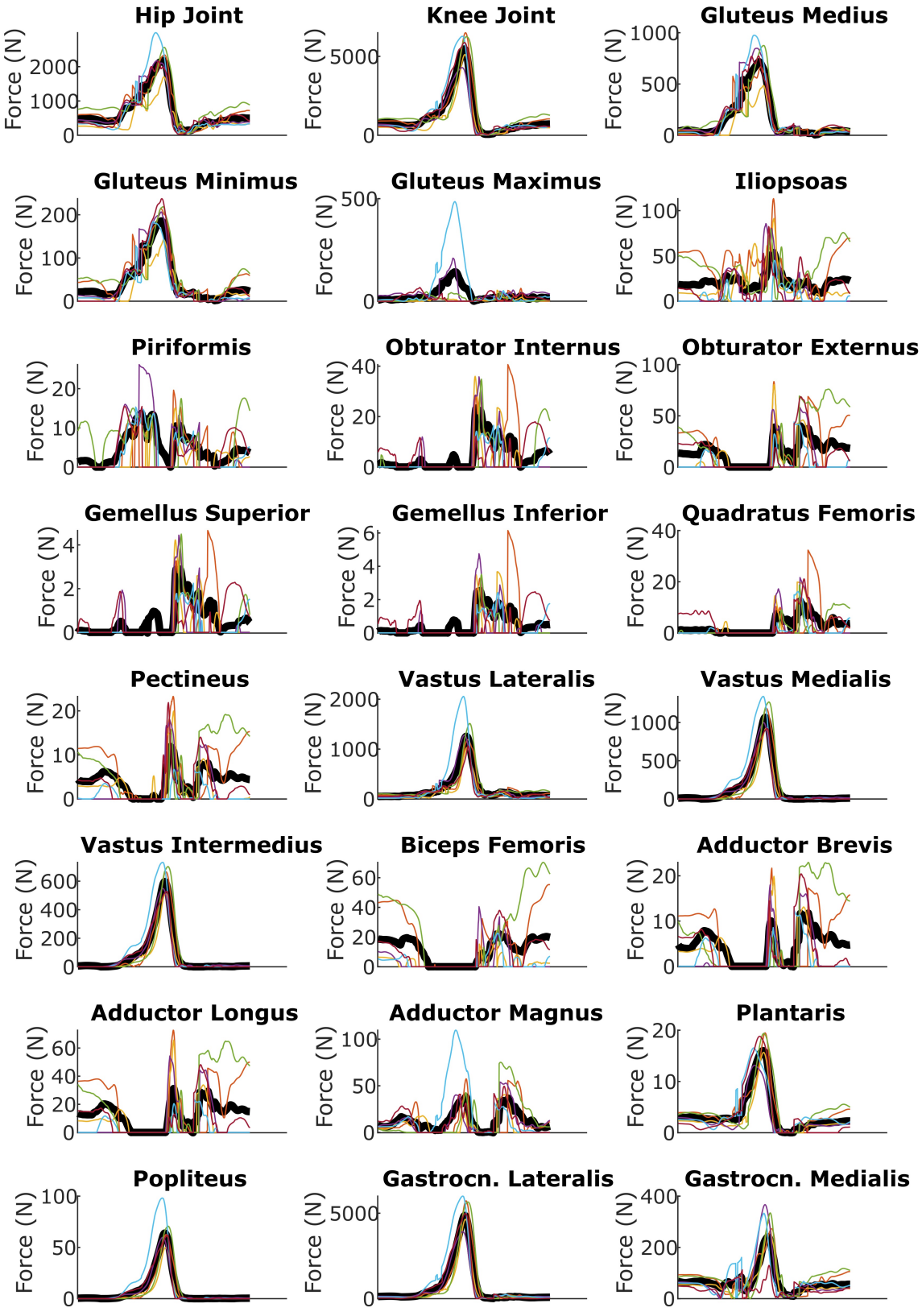

Figure A.41: DTW Averaging of Right Step Down Forces

(a) Posterior View **(b)** Anterior View

Figure A.42: Right Step Down Scenario Forces

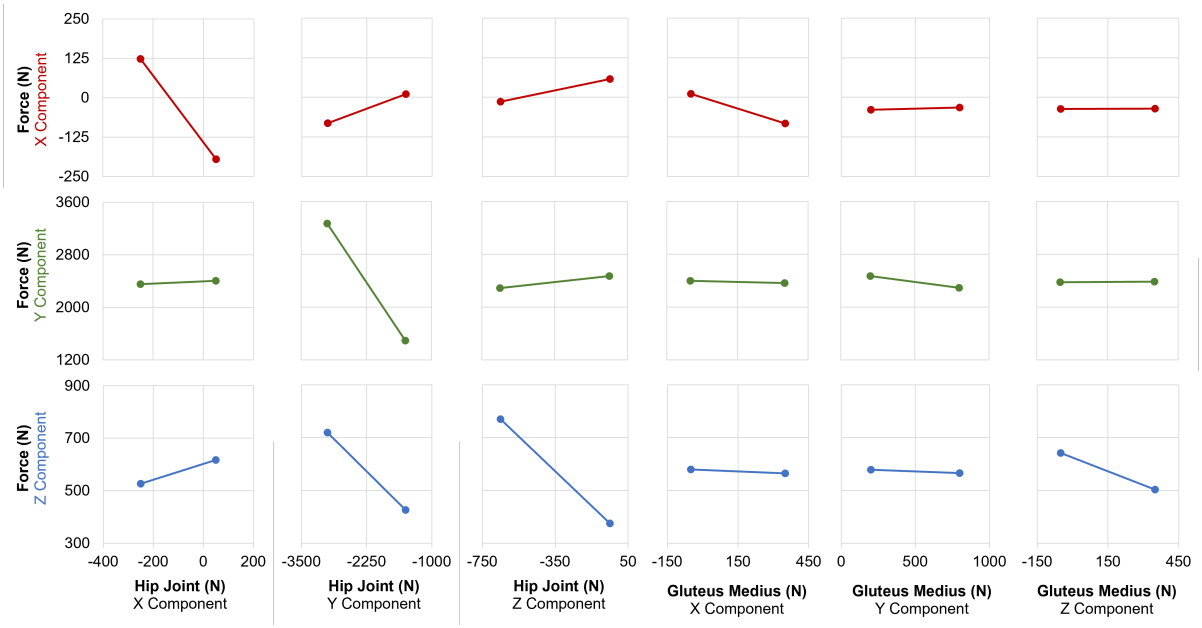

Figure A.43: Sectional Force Factorial Plots of Right Step Down Movement Scenario

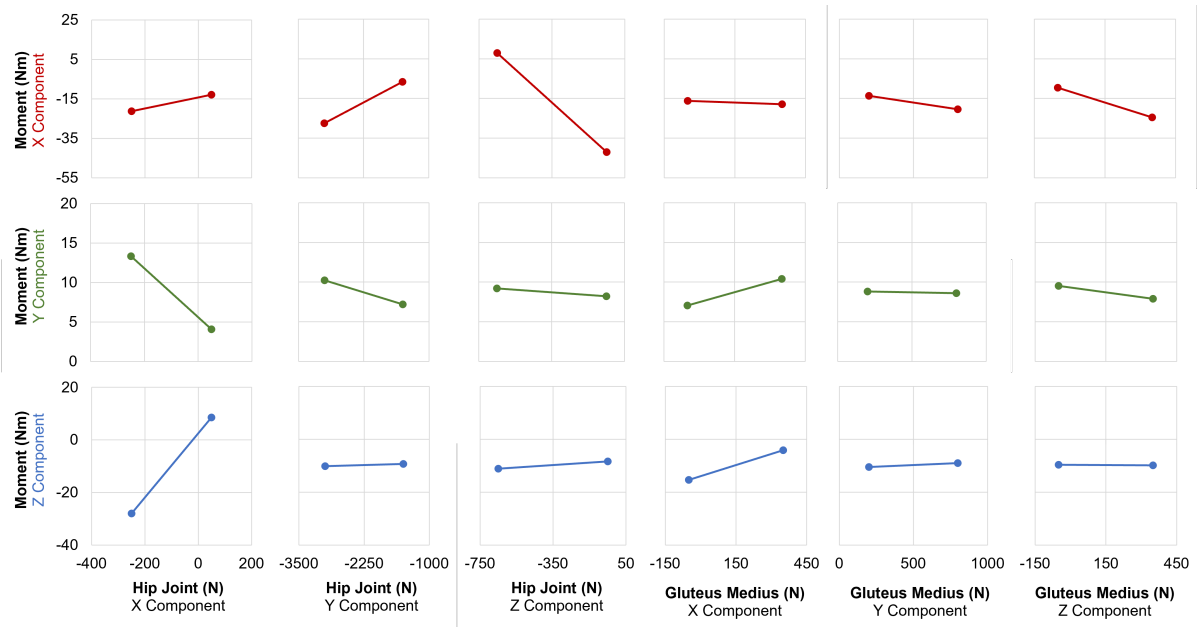

Figure A.44: Sectional Moment Factorial Plots of Right Step Down Movement Scenario

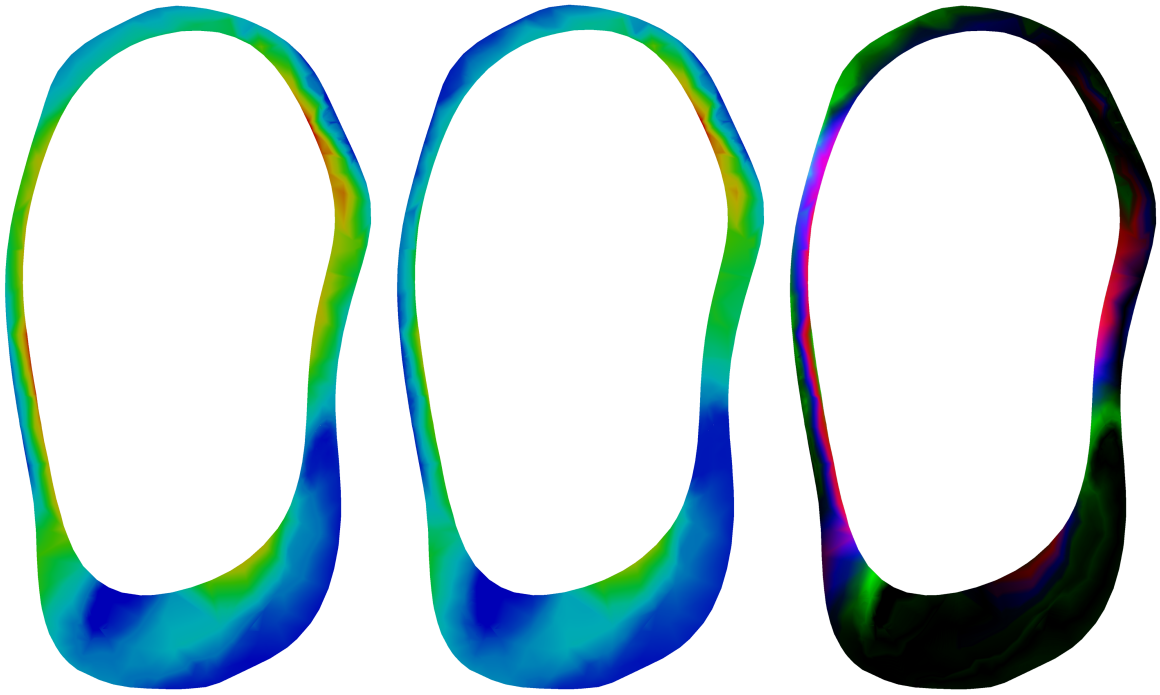

(a) Complete Loading Stress **(b)** Single Loading Stress **(c)** Deviation Intensity Map

Figure A.45: RSD Maximum Principal Stress Comparison - Complete Loading vs Single Force Loading

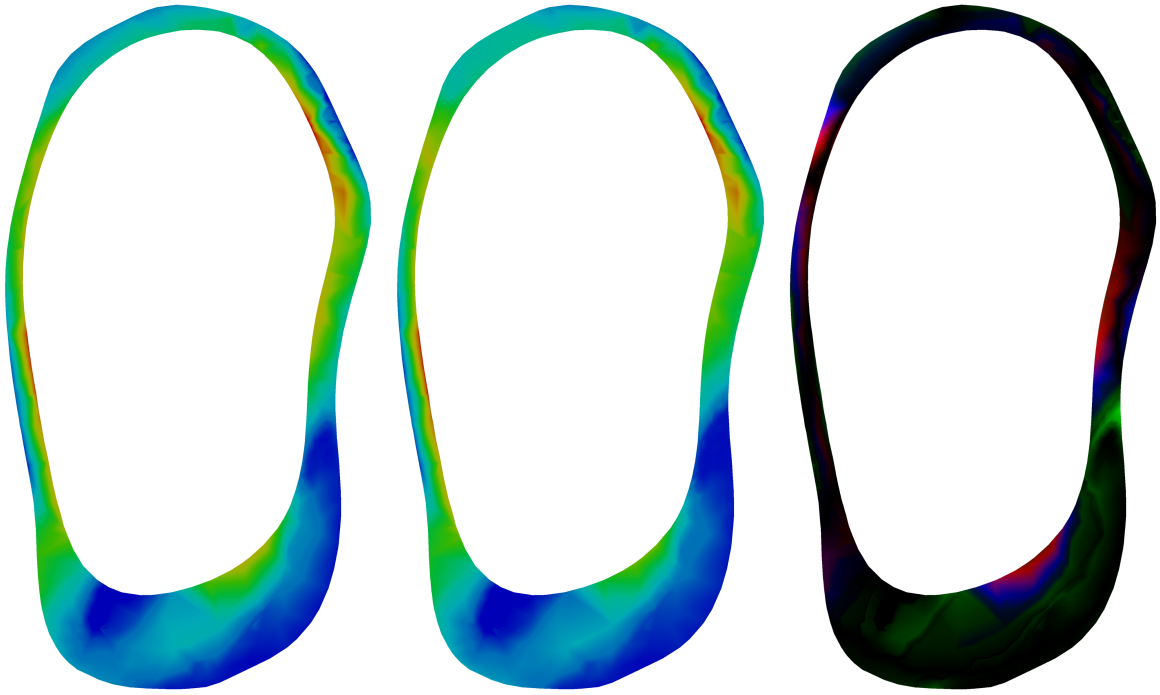

(a) Complete Loading Stress **(b)** Experimental Loading Stress **(c)** Deviation Intensity Map

Figure A.46: RSD Maximum Principal Stress Comparison - Complete Loading vs Experimental Loading

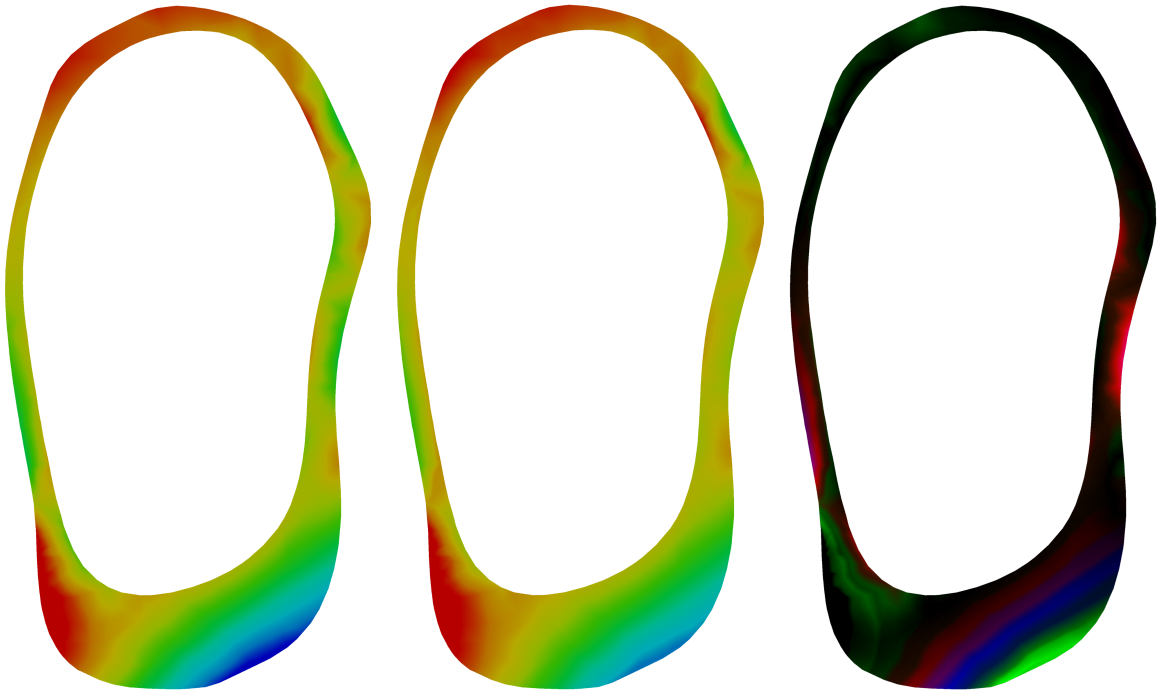

(a) Complete Loading Stress **(b)** Single Loading Stress **(c)** Deviation Intensity Map

Figure A.47: RSD Minimum Principal Stress Comparison - Complete Loading vs Single Force Loading

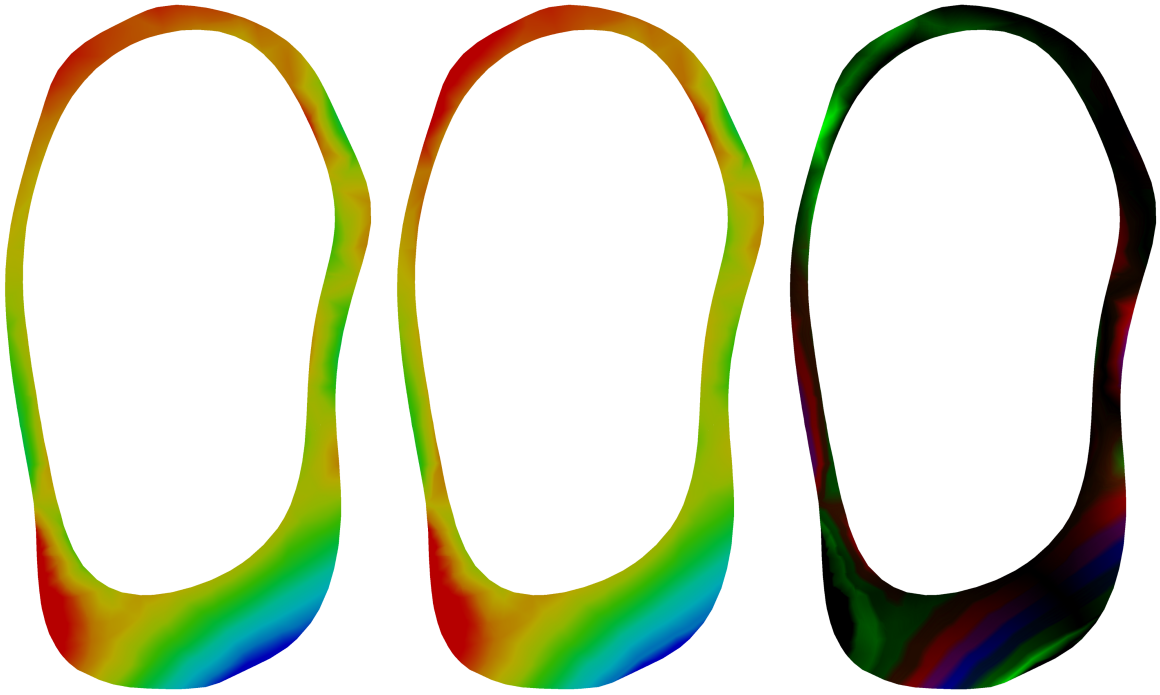

(a) Complete Loading Stress **(b)** Experimental Loading Stress **(c)** Deviation Intensity Map

Figure A.48: RSD Minimum Principal Stress Comparison - Complete Loading vs Experimental Loading